A Search for Gamma-ray Imprints of Annihilating Dark Matter in the Galaxy, and the Astrophysical Implications of Ultra-light Fundamental Vector Bosons

Dissertation zur Erlangung des Doktorgrades des
Department Physik der Universität Hamburg

vorgelegt von

Hannes-Sebastian Zechlin

aus Neunkirchen/Saar

Hamburg 2013

Gutachter der Dissertation: Prof. Dr. Dieter Horns
JProf. Dr. Alessandro Mirizzi

Gutachter der Disputation: Prof. Dr. Günter Sigl
Prof. Dr. Marcus Brüggen

Datum der Disputation: 08. Juli 2013

Vorsitzender des Prüfungsausschusses: PD Dr. Michael Martins

Vorsitzender des Promotionsausschusses: Prof. Dr. Peter Hauschildt

Dekan der Fakultät für Mathematik,
Informatik und Naturwissenschaften: Prof. Dr. Heinrich Graener

Nur wer bereit zu Aufbruch ist und Reise,
Mag lähmender Gewöhnung sich entraffen.

aus “Stufen” von Hermann Hesse

Abstract

Standard Model extensions imply new elementary particles that can lead to specific astrophysical signatures. In particular, weakly interacting massive particles (WIMPs) can constitute the unknown non-luminous cold dark matter, which contributes approximately 84% to the matter content of the Universe. Annihilation or decay of WIMPs may lead to high-energy gamma-rays. In this thesis, new methods of searching for gamma-ray signals from annihilating dark matter are developed and applied. Moreover, astrophysical imprints of new ultra-light hidden $U(1)$ gauge bosons in radio data are investigated.

Hierarchical structure formation predicts a variety of smaller bound dark matter subhalos in Milky-Way-like galactic hosts. It is shown that the *Fermi*-LAT is sufficiently sensitive for detecting up to a few nearby dark matter subhalos in terms of faint gamma-ray sources with a moderate angular extent. Searches in the first and second *Fermi*-LAT source catalogs reveal about ten candidate sources each. To discriminate the source candidates from conventional astrophysical objects, an analysis for spectral, spatial, positional, and temporal gamma-ray properties using 3.5 years of *Fermi*-LAT data is carried out. In addition, a multi-wavelength analysis of archival data or follow-up observations in the radio, infrared, optical, UV, X-ray, high-energy, and very-high energy gamma-ray bands is carried out. The broad-band spectra of all promising candidates are compatible with AGN, in particular high-energy peaked BL-Lac type objects (HBLs).

Dark matter annihilation can contribute to the small-scale angular anisotropy spectrum of the diffuse gamma-ray background (DGB). The detection capabilities of currently operating imaging atmospheric Cherenkov telescopes and the planned Cherenkov Telescope Array (CTA) are studied. With CTA, a relative gamma-ray contribution from annihilating dark matter of 10% to the extragalactic DGB can be resolved via angular anisotropies. In terms of the dark matter velocity-averaged self-annihilation cross section, the sensitivity of CTA corresponds to values below $3 \times 10^{-26}\,\mathrm{cm}^3\,\mathrm{s}^{-1}$ for WIMPs lighter than 200 GeV.

Standard Model extensions predict the existence of hidden sector $U(1)$ gauge bosons (hidden photons). It is shown how ultra-light hidden photons with masses below 10^{-14} eV can modify broad-band spectra of compact radio sources. The sensitivity of current and planned radio astronomical facilities is investigated. Radio observations are capable of probing mixing angles down to 10^{-3} in a mass range between 10^{-17} eV and 10^{-12} eV.

Zusammenfassung

Erweiterungen des Standardmodells beinhalten neue Elementarteilchen, die zu spezifischen astrophysikalischen Signaturen führen können. Insbesondere vermögen schwach-wechselwirkende massive Teilchen (WIMPs) die unbekannte, nicht-leuchtende Dunkle Materie zu bilden, welche ca. 84% der Materie des Universums ausmacht. Die Annihilation oder der Zerfall von WIMPs kann zur Entstehung hochenergetischer Gammastrahlung führen. In dieser Dissertation werden neue Methoden zur Suche nach Gammastrahlung annihilierender Dunkler Materie entwickelt und angewandt. Darüber hinaus werden astrophysikalische Signaturen neuer ultraleichter verborgener $U(1)$-Eichbosonen in Radiodaten untersucht.

Hierarchische Strukturbildung im Universum impliziert die Existenz einer Vielzahl kleinerer Subhalos Dunkler Materie innerhalb von Galaxien wie der Milchstraße. Es wird gezeigt, dass das *Fermi*-LAT ausreichende Sensitivität aufweist, um bis zu mehrere nahegelegene Dunkle-Materie-Subhalos als schwache Gammaquellen mit moderater Ausdehnung zu detektieren. Suchen im ersten und zweiten *Fermi*-LAT-Katalog ergeben jeweils ca. zehn Kandidaten. Zur ihrer Differenzierung von konventionellen astrophysikalischen Objekten wird eine Analyse der *Fermi*-LAT-Daten über 3,5 Jahre auf spektrale, räumliche, und zeitliche Eigenschaften sowie der genauen Position durchgeführt. Zudem wird eine Multiwellenlängenanalyse von Archivdaten und Folgebeobachtungen im Radioband, Infrarotband, optischen Band, UV-Band, Röntgenband, Hochenergieband sowie im sehr hochenergetischen Gammaband durchgeführt. Die spektralen Energieverteilungen aller interessanter Kandidaten sind mit AGNs kompatibel, insbesondere mit einer Klasse von BL Lacs, deren spektrale Maxima bei vergleichsweise hohen Energien liegen (HBLs).

Die Annihilation Dunkler Materie kann zum Spektrum kleinskaliger Winkelanisotropien des diffusen Gammastrahlungshintergrundes (DGB) beitragen. Die vorliegende Arbeit untersucht die Detektionsmöglichkeiten heutiger abbildender atmosphärischer Cherenkovteleskope und des geplanten Cherenkov Telescope Arrays (CTA). Mit Hilfe des CTA kann ein relativer Beitrag um 10% von annihilierender Dunkler Materie zum Gammastrahlungsfluss des extragalaktischen DGB nachgewiesen werden. In Bezug auf den geschwindigkeitsgemittelten Wechselwirkungsquerschnitt annihilierender Dunkler Materie entspricht die Sensitivität von CTA einem Wert unter $3 \times 10^{-26}\,\mathrm{cm}^3\,\mathrm{s}^{-1}$ für WIMPs, deren Masse kleiner als 200 GeV ist.

Einige Erweiterungen des Standardmodells beinhalten die Existenz verborgener $U(1)$-Eichbosonen (verborgene Photonen). Die Dissertation entwickelt, wie ultraleichte verborgene Photonen mit Massen unter $10^{-14}\,\mathrm{eV}$ breitbandige Spektren kompakter Radioquellen modifizieren können. Eine Sensitivitätsstudie aktueller und geplanter Radioteleskope wird beschrieben. Mit Radiobeobachtungen lassen sich Mischungswinkel bis zu Werten von 10^{-3} messen. Die nachweisbaren verborgenen Photonen umfassen einen Massenbereich zwischen 10^{-17} eV und 10^{-12} eV.

Contents

Chapter 1

Introduction

Modern telescopes cover a very broad frequency range of electromagnetic radiation. It extends from the radio band to the very-high energy (VHE; $E > 100\,\mathrm{GeV}$)[1] gamma-ray band, corresponding to an energy range of ∼20 orders of magnitude. Figure 1.1 shows a compilation of several currently operating and planned astronomical instruments utilized in this thesis. With such instruments, both the thermal and the non-thermal Universe can be addressed at galactic and cosmological distance scales. Apart from objects emitting thermal spectra, such as conventional stars, the Universe appears to be populated with sources accelerating charged particles up to PeV energies, such as supernova remnants, pulsar wind nebulae, or active galactic nuclei. Inverse-Compton scattering of relativistic electrons with target photon fields can cause these objects to emit gamma radiation up to TeV energies (see, e.g., Rieger *et al.* 2013 for a recent review). In addition, gamma rays can result from decays of π^0-mesons produced in hadronic interactions with ambient gas. Gamma-ray astronomy has emerged to be an important domain of observational astrophysics in the last three decades.

The various ground-based and space-borne instruments have enabled us to study the Universe in its entirety. Plenty of complementary observations on galactic and cosmological scales have demonstrated the existence of a new form of only gravitating matter, commonly referred to as *dark matter*. The dark matter of unknown physical nature accounts for ∼ 26% of the Universe's present-day energy content, while ordinary matter provides a fraction of ∼ 5% only. The dominating energy fraction (∼ 69%) is made of mysterious *dark energy* (Ade *et al.* 2013b). These remarkable theoretical and observational achievements of cosmological studies in the past decades now take us to an era of precision cosmology, where much deeper questions about the nature of dark matter and dark energy can be addressed.

The well-established Standard Model (SM) of particle physics describes nature on the microscopic scales of elementary quanta. Theoretical and experimental results, however, indicate that the model is far from complete. In particular, the SM fails at describing fundamental processes at energy scales above a few hundred GeV, which are nowadays accessible with particle accelerators such as the Large Hadron Collider (LHC). Beyond-SM theories commonly imply spectra of new particles at both low-mass scales and high-mass scales. Their signatures are anticipated in a variety of observations, among them astrophysical ones.

---

[1] Energy is denoted by E. The unit 1 eV (electron-volt) corresponds to an energy of $1\,\mathrm{eV} \approx 1.6022 \times 10^{-19}\,\mathrm{J}$. A more detailed account on units and conventions used in this thesis is given in Appendix A.

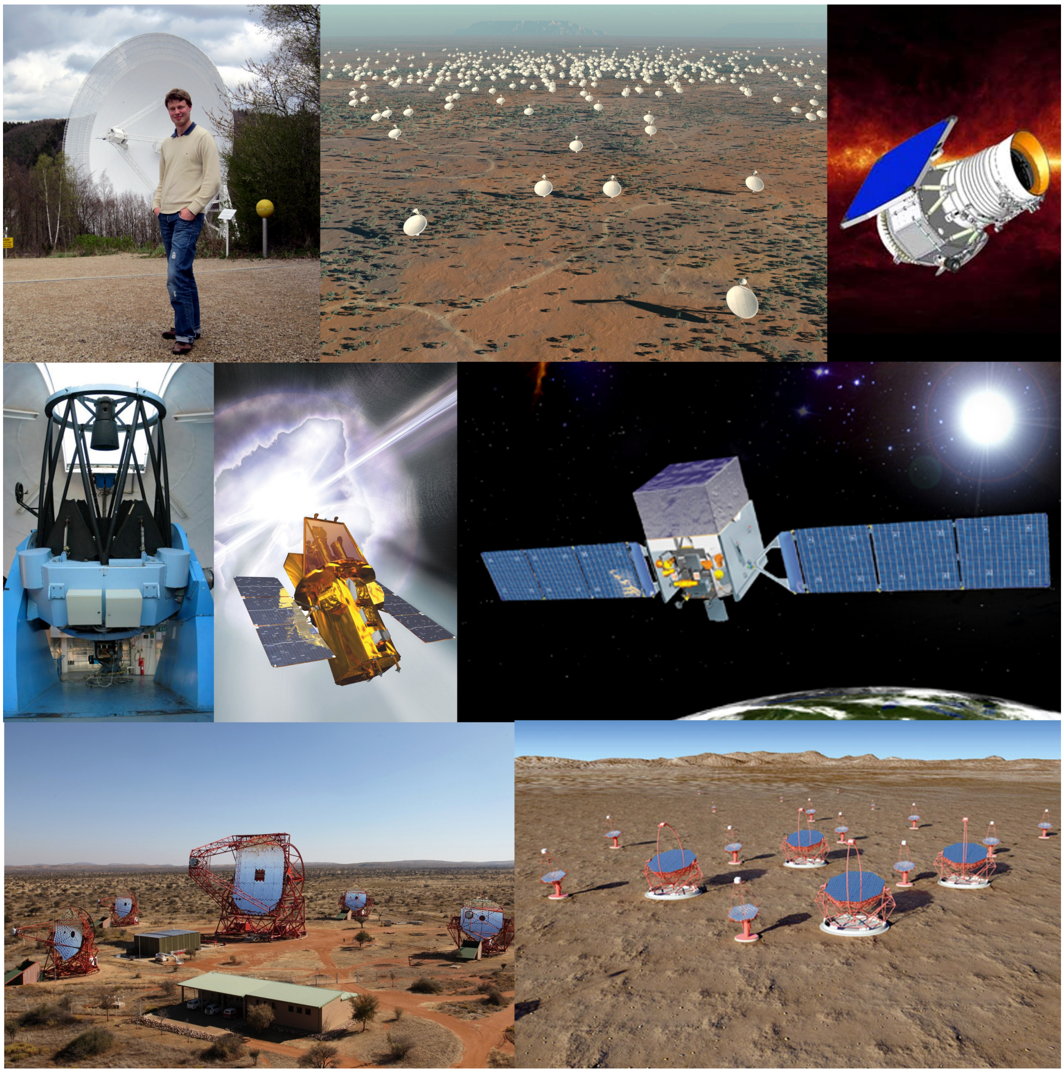

Figure 1.1: Pictures of several astronomical instruments covering various different wavelength ranges, from the radio band to the very-high energy gamma-ray band. From top to bottom and left to right: (i) the author in front of the Effelsberg 100-m radio telescope (Effelsberg, Germany), (ii) artist's view of the planned Square Kilometer Array (SKA), to be built in southern Africa and Australia, (iii) artist's view of the Wide Field Infrared Survey Explorer (WISE) satellite, (iv) the Nordic Optical Telescope (NOT) in La Palma, Canaries, Spain, (v) artist's view of the Swift satellite with the instruments UVOT, XRT, and BAT, (vi) artist's view of the Fermi Gamma-ray Space Telescope (Fermi) with the instruments GBM and LAT, (vii) the High Energy Stereoscopic System (H.E.S.S.-II) in the Khomas Highland, Namibia, (viii) artist's view of the planned Cherenkov Telescope Array (CTA). Image credit: *SKA*: SKA Organisation/TDP/DRAO/Swinburne Astronomy Productions; *WISE*: NASA/JPL-Caltech/UCLA; *NOT*: M. Gålfalk; *Swift*: Spectrum and NASA E/PO, Sonoma State University, Aurore Simonnet; *Fermi*: NASA/General Dynamics; *H.E.S.S.-II*: C. Medina; *CTA*: G. Pérez/IAC/SMM.

The observation of a dark matter constituent can be explained by cold dark matter, composed of an unknown non-baryonic type of electrically neutral and color neutral elementary particle. Interactions with the SM sector must be weak. Indeed, high-energy SM extensions predict weakly interacting massive particles (WIMPs) with masses of a few hundred GeV, providing well-motivated cold dark matter candidates. The annihilation or decay of WIMPs can eventually produce detectable signatures such as gamma radiation, charged light hadrons and leptons, and neutrinos (e.g., Bertone 2010b).

This thesis is dedicated to the search for astrophysical signatures of beyond-SM physics: With new observational campaigns and analyses, the emerged concordance cosmological model (ΛCDM) can now be probed by addressing increasingly more details in its predictions. One major aim of this thesis is the investigation of the existence of small-scale dark matter substructures in smooth galactic dark matter halos. The presence of these structures, commonly referred to as *dark matter subhalos* or *dark matter clumps*, is predicted by hierarchical structure formation of galaxies in a ΛCDM universe. Subhalos thus act as a probe of the ΛCDM model itself and enable new ways of searching for particle dark matter. Moreover, complementary imprints of WIMP dark matter in the diffuse gamma-ray background are investigated. Widening the search for beyond-SM physics, the astrophysical signatures of a class of new ultra-light particles are studied in addition. The paragraphs below provide a brief outline of this thesis.

Chapter 2 starts with a brief summary of standard cosmology in Section 2.1, in order to define important cosmological quantities referred to in the following sections. A review of various observational evidence for the existence of dark matter is presented in Section 2.2, beginning with a focus on dynamical constraints from observations of local galactic environments. The section proceeds with reviewing evidence from gravitational lensing observations of galaxy clusters as well as more constraining observations of large-scale structure and the cosmic microwave background. A summary of concordance ΛCDM cosmology is presented at the end of Section 2.2. The hierarchical formation of matter structures in the Universe is considered in Section 2.3. Starting with a glance over the basic analytical framework describing the growth of small-scale density perturbations and their subsequent collapse, recent results of numerical N-body simulations are discussed, i.e., the density profiles of dark matter halos and the basic properties of dark matter subhalos. Astrophysical implications of dark matter subhalos are considered as well. The section closes with an overview of particle dark matter candidates.

In **Chapter 3**, methods for dark matter detection and the current status of their results are introduced, focussing on approaches for indirect detection. In this thesis, new methods for indirect detection are developed, by examining the signatures of dark matter subhalos in the high-energy (HE; $E > 100\,\mathrm{MeV}$) and VHE gamma-ray sky, and by studying the general imprint of annihilating WIMPs in the diffuse gamma-ray background (DGB). Current instruments of HE and VHE gamma-ray astronomy are discussed.

The unique method and the search for dark matter subhalos developed in this thesis is presented in **Chapter 4**, Sections 4.1 and 4.2, in form of two articles (Zechlin *et al.* 2012; Zechlin & Horns 2012) published in peer-reviewed international journals. The all-sky survey of the Large Area Telescope aboard the Fermi Gamma-ray Space Telescope (*Fermi*-LAT, Nolan *et al.* 2012) offers unprecedented sensitivity for investigating the population of high-energy gamma-ray sources. The survey revealed ~1 900 detected gamma-ray sources, whereof about one third remain unassociated, i.e., lacking an astrophysical counterpart in another wavelength band. These sources may indeed harbor dark matter subhalos, and have been searched for candidates. Chapter 4 is concluded with the presentation of subsequent optical, UV, X-ray, and VHE investigations of promising candidate sources in Section 4.3.

Gamma-rays from annihilating or decaying WIMPs can influence the DGB. While *Fermi*-LAT data of the DGB have already been searched for such signals, imaging atmospheric Cherenkov telescopes (IACTs) offer the possibility of extending these searches to very-high energies. In particular, the specific imprint of dark matter in the DGB's small-scale angular anisotropy spectrum can be investigated. I participated in a project to study the sensitivity of current IACTs and the forthcoming Cherenkov Telescope Array (CTA) for detecting such anisotropies. The work has been published in Doro *et al.* (2013) and Ripken *et al.* (2012), and is reprinted in **Chapter 5**.

Beyond-SM physics predicts a class of new very light particles with masses in the sub-eV range (weakly interacting slim particles, WISPs). WISPs may also provide candidates for cold dark matter, depending on the specific particle parameters. The possibility of WISPs is addressed in **Chapter 6**, by the presentation of a study for investigating the astrophysical signatures of ultra-light hidden $U(1)$ gauge bosons (hidden photons) and the corresponding sensitivity of radio telescopes. I initiated and significantly contributed to this paper, which has been published as Lobanov *et al.* (2013).

A summary and conclusions of my work are presented in **Chapter 7**.

Chapter 2

Dark Matter

Compelling evidence has been reported for the existence of dark matter, even though its nature remains elusive. In this chapter, the theoretical framework of the current cosmological standard model is briefly reviewed in Section 2.1, in order to define important cosmological quantities. For a more comprehensive account on general relativity and modern cosmology see, for instance, Weinberg (1972), Misner, Thorne & Wheeler (1973), or Carroll (1997). An overview of observational dark matter evidence and concordance ΛCDM cosmology is given in Section 2.2. In the scaffold of concordance cosmology, structures have formed hierarchically from small scales to larger ones, discussed in Section 2.3 together with the properties of dark matter halos. A variety of differently motivated theoretical frameworks provide promising dark matter candidates, which are introduced in Section 2.4.

2.1 Standard cosmology

The *cosmological principle*, building the framework of modern cosmology, states that the Universe appears homogeneous and isotropic[1] on very large scales exceeding a few hundred Mpc. This directly implies that observers measure the same structural properties at arbitrary places and in arbitrary directions. The validity of the cosmological principle has been shown by a number of different observations, and measurements of the cosmic microwave background (CMB) now demonstrate that deviations from large-scale isotropy are very small ($\sim 10^{-5}$; Komatsu *et al.* 2011).

The cosmological principle allows us to derive the metric $g_{\mu\nu}$ of the 4D spacetime of the Universe. Determined by the fact that homogeneity and isotropy require the 3D space-manifold to be maximally symmetric, the line element $\mathrm{d}s$ is given by

$$\mathrm{d}s^2 = g_{\mu\nu}\mathrm{d}x^\mu \mathrm{d}x^\nu = -\mathrm{d}t^2 + a^2(t)\left[\frac{\mathrm{d}r^2}{1-kr^2} + r^2\left(\mathrm{d}\theta^2 + \sin^2\theta\,\mathrm{d}\phi^2\right)\right], \tag{2.1}$$

which is usually referred to as Robertson-Walker metric. Here, $a(t)$ denotes the scale factor as function of the time t and (r,θ,ϕ) denote the comoving spatial coordinates.[2] The only relevant choices for the parameter k are $k \in \{-1,0,1\}$, corresponding to a negatively

---

[1] Strictly speaking, homogeneity and isotropy are assumed in space but not in time, according to the observation of a dynamically evolving Universe (e.g., Hubble 1929; Hubble & Humason 1931).

[2] The scale factor relates the comoving coordinates to physical distances λ_p, i.e., $\lambda_\mathrm{p} = a\,r$ in a flat cosmology.

curved (open), flat, and positively curved (closed) universe, respectively. The arbitrary normalization of the scale factor is usually set to $a_0 \equiv a(t_0) = 1$, where t_0 is the age of the Universe today.

The different types of matter in the Universe can be described by a perfect fluid. Such a system is completely characterized by its rest-frame energy density ρ and isotropic rest-frame pressure p. Hence, its symmetric energy-momentum tensor is given by $T_{\mu\nu} = (\rho + p) U_\mu U_\nu + p g_{\mu\nu}$, where U^μ denotes the 4-velocity of the fluid. Perfect fluids important to cosmology are dust (collisionless, non-relativistic matter), radiation (highly relativistic matter), and the energy density of the vacuum (which is equivalent to a cosmological constant Λ). All of them obey the same form of the equation of state $p = w\rho$, where $w = 0$ for matter, $w = 1/3$ for radiation, and $w = -1$ for the vacuum. The fact that energy is conserved (i.e., $\nabla_\mu T^\mu{}_0 = 0$, where ∇_μ denotes the covariant derivative) determines the behavior of the density with the scale factor,

$$\rho \propto a^{-3(1+w)} . \tag{2.2}$$

The actual cosmological fluid can be described by the superposition of the individual components, i.e., $\rho = \sum_i \rho_i$ and $p = \sum_i p_i$. In an expanding universe, where the scale factor a increases with time, it is thus found that the energy density of matter decreases with time, $\rho_\mathrm{m} \propto a^{-3}$, while the energy density in radiation falls off faster, $\rho_\mathrm{r} \propto a^{-4}$. As we would expect, the energy density of the vacuum ρ_Λ is independent of a and thus constant in time. In terms of structure formation, the present-day ($t = t_0$) Universe is matter dominated with $\rho_\mathrm{m}/\rho_\mathrm{r} \approx 10^6$. As the past Universe was much smaller, the energy density in radiation dominated at early epochs, while the vacuum energy will dominate on the long term.

The time dependence of the scale factor is determined by the field equations of general relativity (Einstein 1916) for the Robertson-Walker metric,

$$R_{\mu\nu} - \frac{1}{2} R g_{\mu\nu} + \Lambda g_{\mu\nu} = 8\pi G_\mathrm{N} T_{\mu\nu} , \tag{2.3}$$

where $R_{\mu\nu}$ and R are the Ricci tensor and Ricci scalar, respectively, and G_N denotes Newton's gravitational constant. This results in two independent differential equations for a, known as Friedmann equations,

$$\frac{\ddot{a}}{a} = -\frac{4\pi G_\mathrm{N}}{3}(\rho + 3p) + \frac{\Lambda}{3} , \qquad \text{and} \qquad \left(\frac{\dot{a}}{a}\right)^2 = \frac{8\pi G_\mathrm{N}}{3}\rho + \frac{\Lambda}{3} - \frac{k}{a^2} . \tag{2.4}$$

The expansion rate is then characterized by the Hubble parameter $H \equiv \dot{a}/a$. Hubble's constant is $H_0 \equiv H(t_0) = 100\, h\, \mathrm{km\, s^{-1}\, Mpc^{-1}}$, where the value of h obtained from combined cosmological fits to CMB observations with WMAP and PLANCK is $h = 0.6780 \pm 0.0077$ (Ade *et al.* 2013b; see Section 2.2.4). Conveniently, the energy densities are normalized to a critical density $\rho_\mathrm{crit} \equiv 3H^2/(8\pi G_\mathrm{N})$, and the second Friedmann equation (Eq. 2.4) reads

$$\Omega + \Omega_\Lambda = 1 + \frac{k}{H^2 a^2} , \tag{2.5}$$

where $\Omega \equiv \rho/\rho_\mathrm{crit}$ and $\Omega_\Lambda \equiv \rho_\Lambda/\rho_\mathrm{crit}$, with $\rho_\Lambda = \Lambda/(8\pi G_\mathrm{N})$. Therefore, the curvature of the Universe (the sign of k) is determined by the measurable quantity $\Omega_\mathrm{tot} = \Omega + \Omega_\Lambda$, where $\Omega_\mathrm{tot} < 1$, $\Omega_\mathrm{tot} = 1$, and $\Omega_\mathrm{tot} > 1$ correspond to an open, flat, and closed Universe.

A measurable quantity related to the cosmological distance of an object (e.g., a galaxy) is its cosmological redshift $z = (\lambda_0 - \lambda_e)/\lambda_e$, where λ_e and λ_0 denote the wavelengths of light emitted in the rest-frame of the object (time t_e) and detected in the frame of the observer (time t_0), respectively. Considering geodesic motion in the Robertson-Walker Universe, one finds that the redshift is related to the scale factor as $z = a_0/a_e - 1$, i.e., $a = (1+z)^{-1}$ in the normalization used here.

From the observation of distant galaxies (in particular, type Ia Supernovae), significant evidence for an expanding Universe ($\dot{a} > 0$) has been reported (e.g., Hubble 1929; Riess *et al.* 1998; Perlmutter *et al.* 1999). Neglecting for the moment the effect of a non-zero cosmological constant (which only dominates on the long term) and considering fluids of positive energy ($\rho > 0$) and non-negative pressure ($p \geq 0$), Eq. (2.4) reveals $\ddot{a} < 0$, which means that the Universe is decelerating. We consequently conclude that the Universe must have evolved from a *Big Bang* at which $a \approx 0$. [3]

The thermal behavior of the Universe can be derived from temporal conservation of (comoving) entropy in thermal equilibrium. In the radiation-dominated epoch, the entropy density is given by $s = [\rho(T) + p(T)]/T = 2\pi^2/45\, g_{\rm eff} T^3$, where $g_{\rm eff}$ denotes the effective number of degrees of freedom. Therefore, the temperature T increases to earlier times (i.e., with decreasing a) as $T \propto g_{\rm eff}^{-1/3} a^{-1} = g_{\rm eff}^{-1/3}(1+z)$. Integrating the second equation in (2.4) using $H = \dot{s}/(3s)$ [from $\mathrm{d}(sa^3)/\mathrm{d}t = 0$] eventually results in

$$t \approx \left(\frac{T}{\mathrm{MeV}}\right)^{-2} \mathrm{sec}\,. \tag{2.6}$$

2.2 Observational evidence for dark matter

Determining the model of the Universe requires a measurement of the actual composition of the cosmological fluid (cf. Eq. 2.5). The total density parameter is given by $\Omega_{\rm tot} = \Omega_{\rm m} + \Omega_\Lambda$, since radiative contributions can be neglected in the matter-dominated epoch. Various astrophysical observations have resulted in strong evidence for two constituents contributing to $\Omega_{\rm m}$: ordinary *baryonic matter* ($\Omega_{\rm b}$) and a non-baryonic type of only gravitating matter, commonly referred to as *dark matter* ($\Omega_{\rm dm}$).

The early generation of baryons in the era of baryogenesis was followed by the production of light elements (D, ^{3}He, ^{4}He, ^{7}Li) during the first minutes of cosmological evolution (corresponding to temperatures down to ~ 0.01 MeV). Big-Bang nucleosynthesis (BBN; e.g., Sections 21 and 22 in Beringer *et al.* 2012) begins at temperatures of ~ 1 MeV, where neutrons and protons start to leave thermal equilibrium and freeze their number ratio to a constant value. Primarily, BBN leads to the production of ^{4}He with a primordial mass fraction of $Y_{\rm p}(^4\mathrm{He}) \approx 25\%$. The primordial abundances of light elements strongly depend on the baryon-to-photon ratio $\eta \equiv n_{\rm b}/n_\gamma$, and, therefore, their measurements serve as a unique tool for its determination. Astrophysical observations of the ^{4}He abundance in extragalactic H II-regions (Izotov *et al.* 1999) and the deuterium abundance D/H in high-redshifted, low-metallicity quasar absorption systems (Pettini *et al.* 2008) are compatible with $5.1 \times 10^{-10} < \eta < 6.5 \times 10^{-10}$. Note that the observed ^{7}Li abundance is still in poor agreement with these numbers. The baryon-to-photon ratio is linearly related to $\Omega_{\rm b}$. Standard BBN implies $0.019 < \Omega_{\rm b} h^2 < 0.024$.

---

[3] Note that the extrapolation to a singularity is not allowed within the validity range of general relativity. Rather, the Big Bang represents an initial state of highest energy density and temperature. A solution to the problem of the exact type of initial state of the Universe might be given once a consistent theory of quantum gravity has been found (see, e.g., Bojowald 2008; Bojowald & Paily 2012).

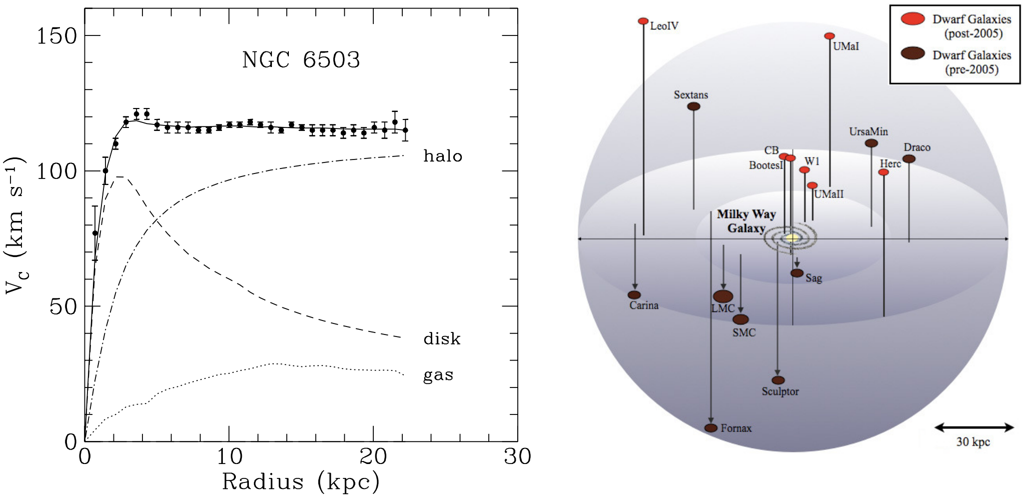

(a) (b)

Figure 2.1: (a): Rotation curve $v_c(r)$ of the spiral galaxy NGC 6503, including the contributions of gas (dotted line), the luminous disk (dashed line), and dark matter (dash-dotted line). From Begeman *et al.* (1991). **(b)**: Distribution of selected classical dSph galaxies and ultra-faint satellites in the Milky Way halo. Image credit: M. Geha

Below, it is shown that $\Omega_{\mathrm{dm}} \approx 5\Omega_{\mathrm{b}}$, meaning that dark matter prevails the matter content of the Universe. The most important evidence for dark matter is reviewed in the following section, beginning with evidence from galactic dynamics in Section 2.2.1, measurements of the gravitational potential of galaxy clusters with gravitational lensing and the temperature distribution of hot X-ray gas in Section 2.2.2, and finalizing with the most intriguing evidence from large-scale structure (Section 2.2.3) and cosmological observations of the CMB in Section 2.2.4. Section 2.2.4 presents a summary of concordance cosmology as well. Although some specific references will be given, details on most of the covered content can be found in a variety of excellent reviews, e.g., Jungman *et al.* (1996), Bertone *et al.* (2005), D'Amico *et al.* (2009), Bringmann (2011), or Strigari (2013).

2.2.1 Galactic kinematics

One of the historically first evidence for a missing mass component in galaxies was the observation that rotation curves of stars and gas (e.g., H I) remain flat in the outmost regions of spiral galaxies (Oort 1932; Babcock 1939; Kinman 1959; Rubin & Ford 1970; Sofue & Rubin 2001). In Newtonian dynamics, the circular velocity of a star around the center of a galaxy is expected to fall as $v_c(r) \propto 1/\sqrt{r}$ beyond the visible disk, where r denotes the galacto-centric radius. The observation of approximately flat rotation curves in outer regions can be reconciled with the existence of a large invisible ("dark") gravitating halo, with a total mass $M(r) \propto r$ and thus a mass-density profile $\rho(r) \propto r^{-2}$. For typical spiral galaxies, the observation of dark halos leads to a lower limit on the total mass fraction in dark matter of $\Omega_{\mathrm{dm}} \gtrsim 0.1$.[4] An example for a rotation curve of a spiral galaxy is presented in Fig. 2.1a.

---

[4] To account for a finite halo mass, the profile should drop faster than $\rho \propto r^{-3}$ beyond some outer point. However, this transition is not observed, implying the resulting Ω_{dm} estimate to be a lower limit.

Small satellite galaxies of the Milky Way turned out to be even more dark matter dominated systems. A population of nine *classical* dwarf spheroidal (dSph) galaxies (Sculptor, Fornax, Draco, Ursa Minor, Leo I, Leo II, Carina, Sextans, Sagittarius) have been discovered during the 20th century (Willman 2010), cf. Fig. 2.1b. Their luminosities spread over a range between $10^5\,\mathrm{L}_\odot$ and $10^7\,\mathrm{L}_\odot$, while their distances are distributed between 15 kpc and 250 kpc. Photometric and spectroscopic high-sensitivity sky surveys such as the Sloan Digital Sky Survey (SDSS; Aihara *et al.* 2011a,b) have led to the discovery of a fainter population of new *ultra-faint* satellites[5] with comparably smaller half-light radii and luminosities as low as $\sim 1\,000\,\mathrm{L}_\odot$. The mass-density profiles and total masses of dSphs can be determined from the line-of-sight velocity dispersion of stellar orbits. The radial component of the velocity dispersion is related to the gravitational potential of the galaxy by the radial Jeans equation, assuming spherical symmetry and hydro-dynamical equilibrium. Estimates of the total masses have resulted in values between $10^8\,\mathrm{M}_\odot$ and $10^9\,\mathrm{M}_\odot$, revealing mass-to-light ratios of the order of a hundred to a thousand in units of the Solar ratio $\mathrm{M}_\odot/\mathrm{L}_\odot$. Therefore, dSphs commonly show an impressively high dark matter content. While the mass-density profiles of the dark matter halos can in principle be measured, yet the lack in statistics of observed stellar orbits did not allow the determination of their central shape with sufficient precision (Mateo *et al.* 1993; Simon & Geha 2007; Strigari *et al.* 2008; Walker *et al.* 2009, 2010, 2011; Wolf *et al.* 2010).

2.2.2 Galaxy clusters

On much larger scales, first evidence for dark matter has been found in galaxy clusters. Galaxy clusters are gravitationally bound objects of hundreds to thousands of individual galaxies, with cluster diameters of $\mathcal{O}(\mathrm{Mpc})$. Observations have shown that galaxy clusters are embedded in hot X-ray emitting gas, making them one of the brightest object class populating the X-ray sky ($T \sim 1\,\mathrm{keV}$). From measurements of the velocity dispersion of galaxies in the Coma Cluster (Abell 1656), Zwicky (1933) concluded a mass-to-light ratio of $\sim 400\,\mathrm{M}_\odot/\mathrm{L}_\odot$ by applying the virial theorem. The mass-to-light ratio of the Coma Cluster thus exceeds the ratio of the Solar vicinity by about two orders of magnitude. Current dynamical estimates from clusters are well consistent with $0.2 \lesssim \Omega_\mathrm{m} \lesssim 0.3$.

Observations of gravitational lensing by clusters strengthen these conclusions. Lensing permits to infer the gravitational potential and thus the total mass of the lens (i.e., the galaxy cluster intervening the line-of-sight) from the distortion of optical images of background galaxies (e.g., Tyson *et al.* 1998).

In addition, consistent results on the cluster masses have been inferred from the radial pressure distribution $p(r) \propto n_e(r)T(r)$ of the hot X-ray gas. In hydro-static equilibrium, the pressure is related to the cluster mass $M(r)$ by $\mathrm{d}p/\mathrm{d}r = -G_\mathrm{N} M(r)\rho_\mathrm{gas}(r)/r^2$, and both the temperature profile $T(r)$ and the electron number density $n_e(r)$ can be measured with X-ray observations. Complementary constraints on the integral electron-gas distribution can be obtained from the inverse-Compton upscattering of CMB photons by the hot electrons (Sunyaev-Zel'dovich effect, Sunyaev & Zeldovich 1980).

---

[5] Examples are Willman I, Ursa Major I, Ursa Major II, Hercules, Leo IV, Canes Venatici I, Canes Venatici II, Coma Berenices, Segue I, and Bootes I, see Tab. 3 in Strigari (2013).

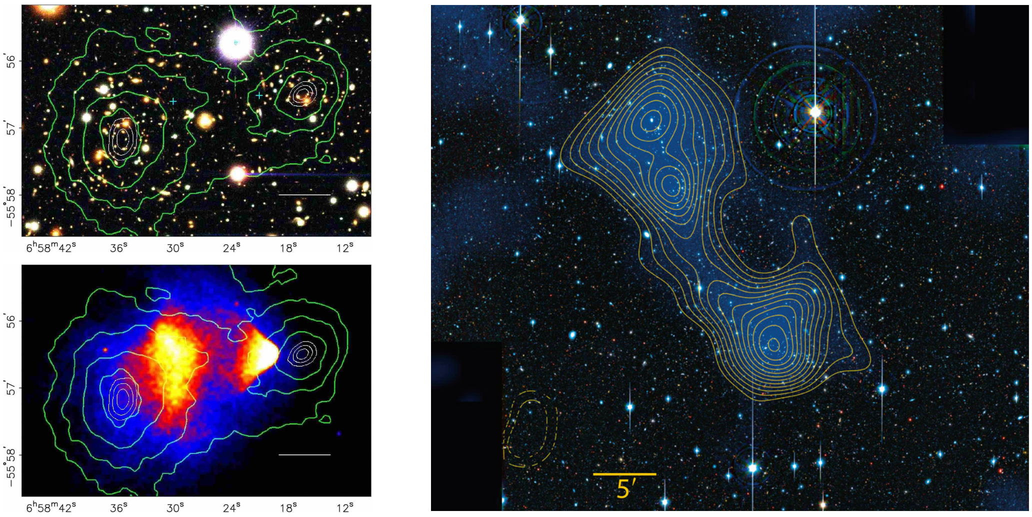

(a)

(b)

Figure 2.2: **(a)**: Images of the cluster 1E 0657–558 in the optical band (top) and the X-ray band (bottom). The green contours indicate the gravitational potential reconstructed from weak-lensing data, where the white contours show the $1\sigma, 2\sigma$, and 3σ errors on the peak positions. The white horizontal bar indicates a distance of 200 kpc at the position of the cluster. From Clowe *et al.* (2006). **(b)**: Mass distribution in the galaxy clusters A222 (south) and A223 (north), reconstructed from weak gravitational lensing. The background image shows a three-color-composite. The reconstructed surface mass density is overlaid in blue. Significance contours (yellow) are given above the mean field edge from 2.5σ in steps of 0.5σ. The filament bridge has been detected with a significance of 4.1σ and contributes a total mass comparable to an additional galaxy cluster to the system. The detection of X-ray emission (not shown in the figure) places an upper limit of ∼10% on the mass fraction of hot gas contained in the filament. From Dietrich *et al.* (2012).

Merging cluster systems. The famous cluster 1E 0657–558 ($z = 0.296$), commonly referred to as *Bullet Cluster* (Clowe *et al.* 2004, 2006; Bradač *et al.* 2006), was the first system where spatially segregated baryonic and dark matter components have been detected. The Bullet Cluster thus provides a substantial confirmation of dark matter in astrophysical environments.

The Bullet Cluster has formed from the collision of two galaxy clusters, which passed through each other ∼100 Myr ago (Fig. 2.2a). Before the collision, the three subcluster components, galaxies, hot plasma, and dark matter, are expected to follow their common spherically symmetric gravitational potentials. During the merging process, galaxies pass by each other without interaction, while the hot plasma fluid experiences ram pressure and spatially decouples from the galaxy stream.

The gravitational potential of the Bullet Cluster has been reconstructed from weak gravitational lensing data of optical background galaxies (Fig. 2.2a, top). The map reveals two separated, nearly spherical potentials, showing that the dominant fraction of matter must have been passed by each other collisionlessly. X-ray observations revealed that the two matter concentrations have moved ahead from their corresponding X-ray plasma accumulations, that were slowed down by ram pressure (Fig. 2.2a, bottom). Furthermore, the observations confirmed a subdominant contribution of galaxies (∼1%) and the X-ray plasma (∼10%) to the total cluster mass, stating that effectively collisionless dark matter contributes the main gravitating component of the cluster. Independent observations of other merging galaxy clusters have strengthened these results, e.g., MACS J0025.4-1222 (Bradač *et al.* 2008), A520 (Clowe *et al.* 2012), A1758 (Okabe & Umetsu 2008; Ragozzine *et al.* 2012), A2163 (Soucail 2012), A2744 (Merten *et al.* 2011), A754, A1750, A1914, A2034, and A2142 (Okabe & Umetsu 2008).

Observations of the Bullet Cluster confirmed the effectively collisionless nature of dark matter for the first time. They placed constraints on its self-interaction cross section (Randall *et al.* 2008) as well as on any hypothetical "5th force" in the dark sector (Springel & Farrar 2007; Farrar & Rosen 2007).

2.2.3 Large-scale structure

On larger scales, galaxy groups and clusters are gravitationally bound in a pattern of large-scale sheets, filaments and voids, forming the thread-like *cosmic web.* The structure of the local cosmic web has been precisely quantified by a new generation of galaxy redshift surveys, namely the Two-degree Field Galaxy Redshift Survey (2dFGRS; Colless *et al.* 2001) and the SDSS (York *et al.* 2000), illustrated in Fig. 2.3a.

Large-scale structures have hierarchically formed from small primordial density perturbations, generated in the early Universe by tiny quantum fluctuations of the vacuum before inflation (see Section 2.3 for details). If the Universe is indeed dark matter dominated, baryon-density fluctuations were rapidly increased at the epoch of recombination, while decoupled baryons were falling into gravitational wells created by dark matter. Then, the fluctuations have followed the evolution of the dark matter potentials and have grown with the expanding Universe. The CMB data shows that the density contrast in baryons was $\delta_{\mathrm{b}}(t_{\mathrm{rec}}) = 10^{-5}$ at recombination (Section 2.2.4). Without dark matter, linear growth would have resulted in $\delta_{\mathrm{b}}(t_0) \approx 10^{-2}$, not sufficient to initiate non-linear collapse (see Section 2.3). No structures would have formed by today.

Quantitatively, the statistical properties of galaxy clustering are described by correlation functions. The large data sets provided by redshift surveys constrain the galaxy power spectrum[6] remarkably well (Peacock *et al.* 2001; Tegmark *et al.* 2004; Cole *et al.* 2005; Eisenstein *et al.* 2005). The shape of the measured power spectrum depends on the properties of dark matter, due to the processing of the initial power spectrum of density fluctuations in the early Universe. Also, the coupling of baryons and photons via Thomson scattering in the early Universe introduces baryon acoustic oscillations (BAO), which imprint in the large-scale structure and serve as a cosmological standard ruler. As a result, the power spectrum of galaxy clustering strongly depends on Ω_{m}. BAO measurements are consistent with $\Omega_{\mathrm{m}} \approx 0.29$ (e.g., Anderson *et al.* 2012).

High-resolution N-body simulations (Frenk 1986; Springel *et al.* 2005, 2008a; Diemand *et al.* 2008a) provide a much more detailed picture of hierarchical structure formation, taking into account both the linear and non-linear regimes of evolution. Excellent agreement between the observed and simulated large-scale structure has been found, if and only if the bulk of dark matter was modeled to be cold (non-relativistic) and non-dissipative, cf. Fig. 2.3a. Vice versa, the observations only allow a small contribution of hot dark matter, having a free-streaming length too large to enable gravitational collapse on sufficiently small scales (e.g., the size of a gas cloud). The requirement of non-dissipative dark matter suppresses its cooling and therefore prevents overproduction of luminous structures.

---

[6] A Fourier transform relates the power spectrum and the two-point correlation function.

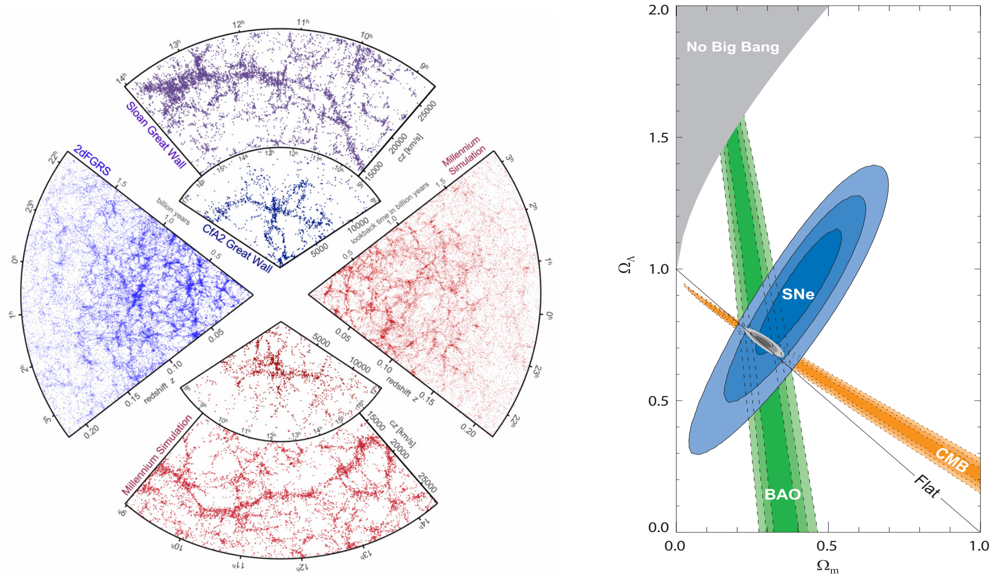

(a) (b)

Figure 2.3: **(a)**: Distribution of galaxies (blue wedge plots) detected in the spectroscopic redshift surveys SDSS, CfA2 (Geller & Huchra 1989), and 2dFGRS in comparison to mock maps generated with the Millennium Simulation (red wedge plots; Springel *et al.* 2005). See Springel *et al.* (2006) for details. **(b)**: Concordance cosmology: confidence contours (68.3%, 95.4%, and 99.7%) on Ω_m and Ω_Λ obtained from WMAP 5-yr measurements, BAO, and type Ia SNe data sets, as well as their combination (with $w = -1$). See Kowalski *et al.* (2008) for details.

Providing the underlying skeleton of the cosmic web, dark matter is distributed in large-scale structure filaments. Galaxy clusters occur at the intersections of the filaments (Bond *et al.* 1996), i.e., at the density peaks. Indeed, Dietrich *et al.* (2012) recently managed to detect a dark matter filament connecting the galaxy clusters A222 and A223, using the weak gravitational lensing signal of the system (see Fig. 2.2b).

2.2.4 Concordance cosmology

The most compelling evidence for Big Bang cosmology and non-baryonic dark matter is provided by the cosmic microwave background. After the first discovery by Penzias & Wilson (1965), it was the Cosmic Background Explorer (COBE) satellite which observed an almost perfectly isotropic black-body spectrum of microwave radiation at a temperature of $T = 2.73\,\mathrm{K}$ (Smoot *et al.* 1992). The CMB was released right after the ionized primordial plasma recombined to atoms ($T_\mathrm{r} \approx 0.26\,\mathrm{eV}$), corresponding to a redshift of the last scattering surface of $z_\mathrm{r} = 1090$ (see, e.g., Hu & Dodelson 2002 for a review). In comparison to galaxy clustering, the primordial tiny density fluctuations directly imprint in the CMB, whereas the matter distribution is changed by gravitational collapse. The fluctuations have led to small anisotropies $\delta T/T \approx 10^{-5}$ in the observed temperature map.

As a directly accessible picture of the primordial fluid at the time of last scattering, the temperature fluctuations provide characteristic length scales (the sound horizon of plasma oscillations) which serve as cosmological standard ruler. The observed features depend on the detailed composition of the cosmological fluid and the evolution history of the Universe. The observed angular diameter of the characteristic length scales is related to the large-scale geometry of the Universe since recombination.

High-resolution measurements of the CMB with the Wilkinson Microwave Anisotropy Probe (WMAP; Larson *et al.* 2011; Komatsu *et al.* 2011), the PLANCK satellite (Ade *et al.* 2013a), and other more specific instruments enabled us to observe the angular power spectrum[7] and to determine the cosmological parameters with high accuracy. The WMAP and PLANCK measurements are in agreement with the density parameters measured from BBN, dynamical estimates, gravitational lensing, and the large-scale structure, thus confirming the existence of a non-baryonic dark matter constituent. The CMB data is also in good agreement with an approximately flat geometry of the Universe, requiring a large contribution of dark energy. Evidence for dark energy has also been demonstrated with data from distant type Ia supernovae (SNe), that can only be reconciled with an accelerated expansion of the Universe and thus a non-vanishing cosmological constant (Riess *et al.* 1998; Perlmutter *et al.* 1999; Tonry *et al.* 2003). Highest precision of the cosmological parameters has been achieved with combined fits of complementary data (e.g., CMB, BAO, and type Ia SNe, see Komatsu *et al.* 2011), revealing a self-consistent model of the Universe. The most recent values obtained with CMB data from PLANCK are $\Omega_\mathrm{b} = 0.0482 \pm 0.0005$, $\Omega_\mathrm{dm} = 0.258 \pm 0.004$, and $\Omega_\Lambda = 0.692 \pm 0.010$ (Ade *et al.* 2013b), showing that the present-day Universe is made of approximately 5% baryons, 26% dark matter, and 69% dark energy. The high degree of complementarity is demonstrated in Fig. 2.3b, see Kowalski *et al.* (2008) for details. Following standard convention, the introduced concordance model is referred to as ΛCDM cosmology.

2.3 The hierarchical formation of structures

As shown in Section 2.2.3, the present Universe is populated by numerous large-scale structures, which contain highly overdense regions of dark and luminous matter. Let $\rho(\mathbf{x}, t)$ denote the mass density as function of space $\mathbf{x}$ and time t, and $\overline{\rho}(t)$ the average background density, then the density contrast is given by $\Delta = \delta\rho/\overline{\rho} \equiv (\rho - \overline{\rho})/\overline{\rho}$. Its value today in galaxies, clusters of galaxies, and in larger, gravitationally unbound systems of several galaxy clusters (superclusters) is about 10^6, 1000, and a few, respectively. These structures have emerged from small but finite initial perturbations of the primordial density field. The temporal evolution of $\overline{\rho}$ with $(1+z)^3$ demonstrates that these objects should have collapsed at late epochs of $z \ll 100$, $z < 10$, and $z < 1$, respectively, when the density contrast approached $\Delta \approx 1$. Before the time of collapse, the post-recombination density contrast of perturbations grew linearly to $\Delta \approx 1$.

Knowing its subsequent evolution, the spectrum of initial density fluctuations can be reconstructed from present-day galaxy clustering. Observations indicate a broad initial fluctuation spectrum without any preferred length scale. The initial power spectrum $P(k)$, which is the Fourier transform of the two-point correlation function $\xi(r) = \langle \Delta(\mathbf{x}) \Delta(\mathbf{x}+\mathbf{r}) \rangle$, takes the form of a power law, $P(k) = |\Delta_k|^2 \propto k^n$, where k denotes the norm of the wave vector and $\mathbf{r}$ the distance vector between two objects. Owing to an observationally required mass dependence of $\Delta(M) \propto M^{-2/3}$ and avoiding overproduction of excessively large-amplitude perturbations, $P(k)$ is anticipated to follow a Harrison–Zel'dovich spectrum with $n = 1$ (Harrison 1970; Zeldovich 1972).

---

[7] Conveniently, the observed temperature map is decomposed into spherical harmonics. The corresponding angular power spectrum is obtained from the variance distribution of their coefficients. Characteristic length scales manifest in enlarged power.

The following section describes the basic analytical framework of hierarchical structure formation, followed by a discussion of more detailed results from high-resolution numerical simulations. At the end, focus is given to the properties of small-scale substructure. A more comprehensive overview can be found in standard literature, e.g., the textbooks by Schneider (2006) and Longair (2008).

2.3.1 The growth of small density perturbations

The behavior of small gravitational instabilities in the post-recombination era ($z \lesssim 1000$) is governed by the dynamics of the fluid in the gravitational field. In the following, perturbations on scales much smaller than the horizon are considered after the epoch of radiation domination, i.e., a fluid in the non-relativistic regime. The evolution of density perturbations in an expanding universe is described by a set of coupled differential equations (Jeans 1902; Lifshitz 1946): (i) the equation of continuity, (ii) Euler's equation, and (iii) Poisson's equation. This leads to a differential equation in Δ,

$$\frac{\mathrm{d}^2\Delta}{\mathrm{d}t^2} + 2H\frac{\mathrm{d}\Delta}{\mathrm{d}t} + \left(k^2 c_\mathrm{s}^2 - 4\pi G_\mathrm{N}\bar{\rho}\right)\Delta = 0\,, \tag{2.7}$$

where the given representation reflects the Fourier transform for plane waves with a proper wave vector $\mathbf{k}$, and $c_\mathrm{s}^2 := \partial p / \partial \rho$ is the adiabatic sound speed. Depending on the overall sign of the third term, Eq. (2.7) takes the form of a damped harmonic oscillator (in the case of a positive sign) or describes instability (in the case of a negative sign). Thus, the Jeans wavelength

$$\lambda_\mathrm{J} = \frac{2\pi}{k_\mathrm{J}} = c_\mathrm{s}\left(\frac{\pi}{G_\mathrm{N}\bar{\rho}}\right)^{1/2} \tag{2.8}$$

defines the length scale of a growing density perturbation: stable oscillations are found for wavelengths $\lambda < \lambda_\mathrm{J}$, while the modes become instable if $\lambda > \lambda_\mathrm{J}$. For instable modes, Eq. (2.7) has a decaying and a growing solution. As the latter quickly starts to dominate, the decaying solution is of little importance. The general solutions of Eq. (2.7) depend on the composition of the cosmic fluid (Heath 1977; Carroll *et al.* 1992). For an *Einstein-de Sitter* universe ($\Omega_\mathrm{m} = 1, \Omega_\Lambda = 0$), for instance, which serves as a good approximation for the composition of the early ΛCDM Universe, the density contrast for perturbations with $\lambda \gg \lambda_\mathrm{J}$ grows with the expansion of the Universe as

$$\Delta \propto t^{2/3} \propto a \propto (1+z)^{-1}\,. \tag{2.9}$$

A full relativistic treatment allows the generalization of the previous approach for the case of an ultra-relativistic gas or photon gas during the radiation-dominated era. Again, for perturbations with $\lambda \gg \lambda_\mathrm{J}$ but smaller than the horizon scale, one finds a growing solution: $\Delta \propto t \propto a^2 \propto (1+z)^{-2}$.

2.3.2 Non-linear gravitational collapse

Once the density contrast has grown to $\Delta \approx 1$, the evolution of density perturbations enters a non-linear phase, where the overdensity starts to collapse under its self-gravity. The basic principles of gravitational collapse can be derived from the ideal situation of the *spherical top-hat collapse*, assuming a uniform spherical density perturbation embedded in a homogeneous background fluid.

Spherical top-hat collapse. The enhanced gravitational potential of a spherical overdensity drives its expansion to lower rates than the expansion rate of the surrounding background. Thus, the density contrast is increased. Locally, the region can be described with the same dynamics as those for a closed universe with $\Omega_\mathrm{m} > 1$. For such a system, the Friedmann equations (2.4) for the scale factor a_p are solved by a cycloidal, which depends on the exact value of the effective Ω_m of the region. The cycloidal solution implies that the expansion of the sphere stops at a turnaround time t_max of maximum expansion, and the sphere will collapse to infinite density at $t_\mathrm{c} = 2t_\mathrm{max}$. Assuming Einstein–de Sitter cosmology, the overdensity of the sphere at the time t_max is $\rho_\mathrm{max}/\overline{\rho}(t_\mathrm{max}) = 9\pi^2/16 \approx 5.55$. Since the scale factor evolves with $a \propto t^{2/3}$, the subsequent gravitational collapse occurs quite rapidly, $1 + z_\mathrm{c} = (1 + z_\mathrm{max})/2^{2/3}$.

In a more realistic situation, the overdensity field will deviate from homogeneity and particles will not move on exactly radial orbits. Scattering and fragmentation of density fluctuations prevent the sphere from collapsing to a singularity; instead, the system will virialize, residing in a gravitationally bound state in dynamical equilibrium with a final radius $r_\mathrm{c} = r_\mathrm{max}/2$. This process of *violent relaxation* (Lynden-Bell 1967) is essentially completed at t_c.

The mean density of the virialized object after collapse is given by $\rho_\mathrm{vir} = \Delta_c(z)\rho_\mathrm{crit}(z)$ at redshift z (Eke *et al.* 1996; Bullock *et al.* 2001). In general, $\Delta_\mathrm{c}(z)$ depends on the cosmological model, see Bryan & Norman (1998) for details. For an Einstein–de Sitter cosmology, $\Delta_\mathrm{c} \approx 178$ for all redshifts, while $\Delta_\mathrm{c} \approx 100$ in the concordance ΛCDM model at $z = 0$. A virialized dark matter mass concentration of this type is referred to as *dark matter halo*. By definition, the virial mass M_vir of a dark matter halo is given by $M_\mathrm{vir} := 4\pi/3\,\Delta_\mathrm{c}\rho_\mathrm{crit}R^3_\mathrm{vir}$, where R_vir denotes the halo's virial radius. The virial theorem can be used to estimate the collapse redshift, revealing that galaxies must have formed at redshifts less than 7, and galaxy clusters at redshifts less than 1.

It remains worth emphasizing that the previous arguments also hold for a sphere with a density profile radially decreasing to outward regions. Owing to correspondingly higher density contrasts, inner regions collapse faster, resulting in halos of low initial mass. With the collapse of outer regions, these halos then grow to later times by further accretion of matter, building up massive dark matter halos in the final stages of evolution.

Number density of dark matter halos: the Press–Schechter model. The process of hierarchical clustering was quantified by Press & Schechter (1974), who developed an analytical model predicting the number density of dark matter halos as a function of mass and redshift. Despite its strong limitations and too simple assumptions, the Press-Schechter model turned out to describe the basic process and observational results of structure formation in remarkable detail.

In this model, the density contrast of primordial perturbations is assumed to follow a Gaussian distribution, centered on $\overline{\Delta} = 0$ with a variance $\sigma^2(M) = \langle\Delta^2\rangle$. Gaussian fluctuations are expected for a variety of reasons, and are, so far, compatible with CMB observations (Ade *et al.* 2013c). Their statistical properties are completely characterized by the power spectrum $P(k) \propto k^n$.

Density perturbations rapidly grew to bound objects of mass M once they had reached a critical overdensity Δ_c. The fraction of bound objects at a given epoch is determined by the Gaussian distribution of fluctuations, utilizing the fact that $\sigma^2(M) \propto M^{-(3+n)/3}$. Thus, the differential mass function of dark matter halos (in an Einstein–de Sitter universe)

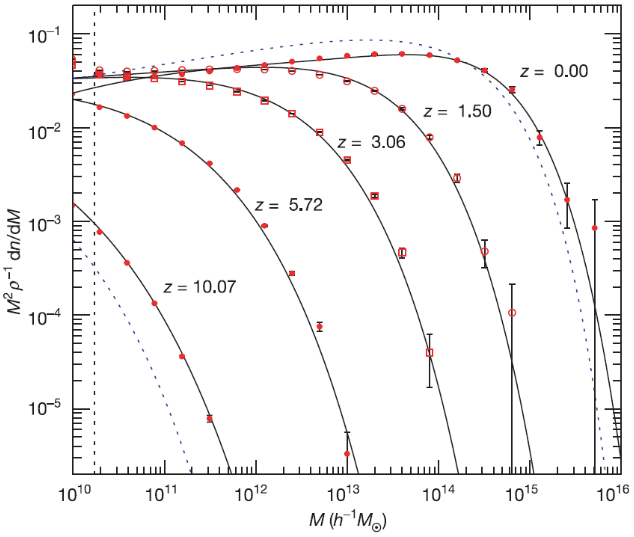

Figure 2.4: Differential number density of dark matter halos as function of mass and redshift. In the figure, $n(M, z)$ denotes the comoving number density of halos with masses less than M, and $\rho \equiv \overline{\rho}$. Red symbols depict data from the Millennium simulation, while the vertical dashed line marks its resolution limit. Solid black lines refer to an analytical fitting function. Predictions of the Press-Schechter model are shown with dashed blue lines. From Springel *et al.* (2005).

is given by[8]

$$N(M) = \frac{\overline{\rho}}{\sqrt{\pi}} \frac{\gamma}{M^2} \left(\frac{M}{M^*}\right)^{\gamma/2} \exp\left[-\left(\frac{M}{M^*}\right)^{\gamma}\right], \tag{2.10}$$

where $\gamma = 1 + (n/3)$ and $M^* = M^*(t_0)(t/t_0)^{4/(3\gamma)}$. For small masses, the processed power spectrum $P(k)$ can be approximated with power laws with indices from $n = -1.5$ to $n = -3$, going from comparably large to smallest length scales. The characteristic mass scale M^* of the exponential cutoff grows with time and marks the transition region between the non-linear and linear regime of the distribution.

Fig. 2.4 illustrates the Press–Schechter mass function (blue dashed lines) in comparison with results from the *Millennium Simulation* (see Section 2.3.3) for selected redshifts between 10.07 and 0 (red data points). The agreement between the simple model and the simulation is obvious. The evolution of the mass distribution in Fig. 2.4 demonstrates the bottom-up scenario of hierarchical structure formation: starting from early-forming low-mass halos, the formation of massive dark matter halos in later epochs is driven by merging of initially formed low-mass objects. This behavior originates in the form of the initial power spectrum $P(k)$. The predictions of hierarchical structure formation are in good agreement with the observed redshift distribution of galaxies and galaxy clusters.

2.3.3 Numerical N-body simulations

Analytical calculations only provide a coarse approximation of the highly non-linear collapse of density perturbations and their subsequent hierarchical clustering. Higher precision can be achieved with numerical simulations of late-time structure formation. The constantly growing computing capabilities have permitted a significant improvement of the resolution over the last two decades.

---

[8] Eq. (2.10) has been corrected by a factor of 2, accounting for the symmetry of the Gaussian distribution around 0.

Numerical simulations aim at tracking the gravitational clustering in late epochs from $z \approx 100$ to $z = 0$, in representative volumes chosen to be sufficiently large to describe the properties of the largest observable structures and the periodicity of the cosmic web. Most of the current high-resolution simulations focus on the dynamics of dissipationless dark matter only, which dominates structure formation. Although dissipative processes of the baryon fluid, such as radiative cooling, are critical for star formation, galaxy formation, and even the formation of dark matter halos themselves, their inclusion still remains beyond the scope of most modern projects. Yet, baryon physics can be included afterwards by post-hoc semi-analytical modeling (Springel *et al.* 2005).

Initial simulation conditions are chosen according to the considered cosmology and are set at a highly redshifted epoch. The processed power spectrum $P(k, z)$ governs the initial particle distribution. Available computing power and memory do not allow us to simulate every single dark matter particle. Rather, the gravitational forces are computed for macroscopic particle clumps of minimal mass m_{min}, and their trajectories are discretized following an underlying regular spatial grid (particle-mesh method). Therefore, the mass resolution of a simulation is driven by m_{min}, while the grid-spacing determines the spatial resolution. Usually, the grid-spacing meets the gravitational softening length, which corrects the law of gravitation for strong collisions introduced by the macroscopic nature of simulated particles.

Recent results. For a ΛCDM cosmology, the large-scale cosmic web has been studied with the *Hubble Volume Simulations* (Evrard *et al.* 2002), with a side length of $3000h^{-1}$ Mpc. While the simulation is perfectly suited for investigating large-scale structures, higher resolution is required to resolve smaller galaxy groups or even galactic scales. This has been one of the major achievements of the *Millennium Simulation* (Springel *et al.* 2005), which currently provides the largest simulation of the overall cosmological structure at a length scale of $500h^{-1}$ Mpc. The Millennium Simulation follows $\sim 10^{10}$ particles from a redshift of $z = 127$, providing a mass resolution of $\sim 1.7 \times 10^{10} h^{-1}\,\mathrm{M}_{\odot}$ and a spatial resolution of $5h^{-1}$ kpc. Figs. 2.3a and 2.5 show the complex topology of the simulated cosmic web. A tight network of cold dark matter filaments and voids can be seen in the bottom panels. Galaxy clusters form at the filament's intersections. The characteristic size of clusters and filaments is $\sim 100h^{-1}$ Mpc, while the distribution appears homogeneous and isotropic on larger scales. Each stacked panel in Fig. 2.5 depicts a zoom-in by a factor of 4 on a selected rich galaxy cluster. The final zoom clearly shows hundreds of accreted cold dark matter substructures orbiting in the cluster halo. The substructures have been resolved as independently bound objects and are remnants of earlier halo merging (Springel *et al.* 2005).

The high-resolution N-body simulations have inevitably demonstrated the success of the ΛCDM model in reproducing the observed structure on large scales, see Section 2.2.3. However, high-resolution tests of small-scale predictions, i.e., galactic and sub-galactic length scales, remained missing. In the recent years, this issue has been addressed by two independent projects: the Aquarius Project (Springel *et al.* 2008a,b), which was carried out by the Virgo Consortium[9], and the Via Lactea Project[10] (Diemand *et al.* 2007a, 2008a; Zemp *et al.* 2009).

---

[9] The Virgo Consortium is a collaboration of scientists in the UK, Germany, Netherlands, Canada, the USA, and Japan, see `http://www.virgo.dur.ac.uk`. [10] The Via Lactea Collaboration includes scientists from Switzerland and the USA, see `http://www.ucolick.org/~diemand/vl/`.

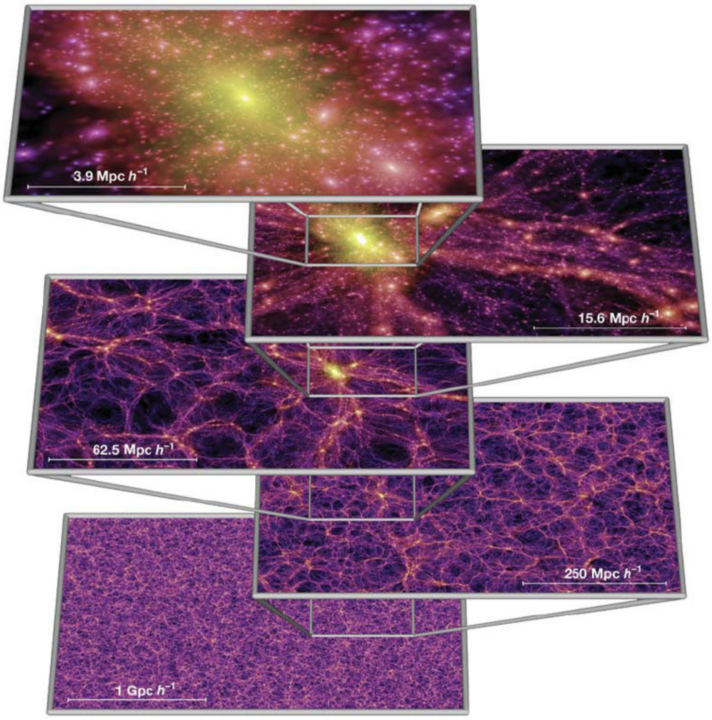

Figure 2.5: Millennium Simulation: the cosmic web of cold dark matter structures on five different length scales. The images, each zoomed by a factor of 4, depict the projected dark matter density field in a slice of $15h^{-1}$ Mpc thickness. The color code represents the density and local velocity dispersion. From Springel *et al.* (2005).

To achieve sufficient resolution on sub-galactic scales within a reasonable amount of computing time, both the Aquarius and the Via Lactea II (VL-II) simulation employed a two-phase approach: at first, low-resolution runs resolving large scales were used to select fiducial Milky-Way-sized halos for re-simulation. Embedded in the low-resolution web, the selected halos were re-simulated with a significantly improved mass and spatial resolution. Selected halos were required to match a mass of $\sim 2 \times 10^{12}\,\mathrm{M}_{\odot}$, to be without a massive nearby neighbor, to have had no recent merger, and to be suitable for hosting late-type galaxies (Springel *et al.* 2008b). To prove convergence, six individual halos have been investigated by the Aquarius Project, each of them with different resolutions. One single halo has been studied in the VL-II simulation. Fig. 2.6 illustrates the structure of the highest-resolution Aquarius halo (Aq-A-1) and the VL-II halo. Corresponding characteristic parameters are listed in Tab. 2.1.

As demonstrated in the figure, the prediction of hierarchical structure formation has been clearly verified on small scales: A large number of gravitationally bound substructures appear on sub-galactic scales, orbiting in an underlying smooth galactic host halo. Similar to larger scales (see above), these dark matter substructures have formed earlier and have been accreted to form a larger host in later epochs. Small-scale dark matter substructures of this type are commonly referred to as *dark matter subhalos* (DM subhalos) or *dark matter clumps*. I will refer to the former term in this thesis. The simulations predict DM subhalos to exist on a variety of mass scales, and they allow us to study the properties of DM subhalos with high precision. Details on DM subhalos are presented in Section 2.3.4.

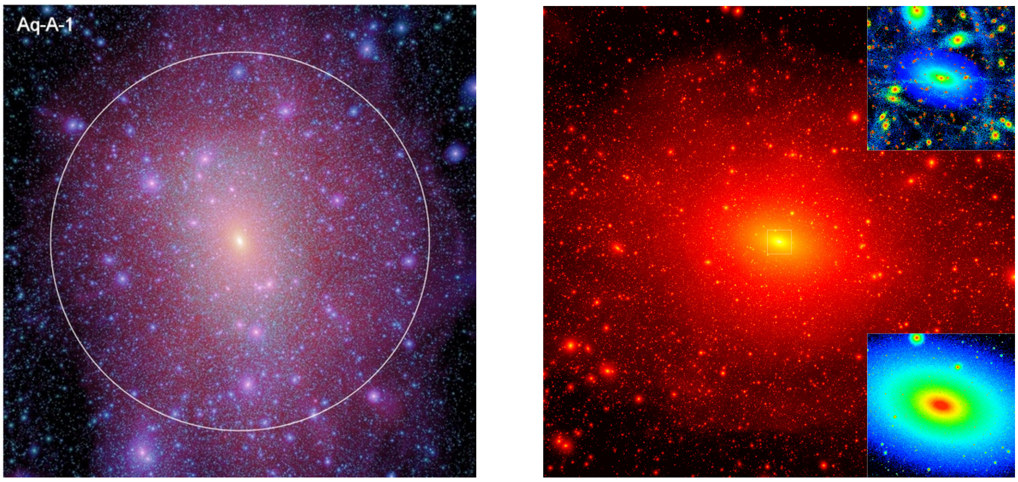

(a) Aquarius **(b)** Via Lactea II

Figure 2.6: **(a)**: Aquarius Simulation, Aq-A-1 halo: projected dark matter density at $z = 0$, in a slice of 13.7 Mpc thickness. The brightness of the image reflects the squared dark matter density projected along the line of sight, while the color code represents the weighted local velocity dispersion. The radius of the circle is $r_{50} = 433$ kpc. From Springel *et al.* (2008b). **(b)**: Via Lactea II Simulation: projected squared dark matter density at $z = 0$. The image shows a cube of 800 kpc side length. See Diemand *et al.* (2008a) for the meaning of the insets.

Density profile of dark matter halos. Up to now, no consensus has emerged with regard to the mass-density profile(s) of dark matter halos. As initially deduced by Navarro, Frenk, and White from numerical simulations (Navarro *et al.* 1997), dark matter halos are well fit by a universal, spherically symmetric density profile. Lacking sufficiently precise measurements (see Section 2.2.1), however, a general agreement on the detailed halo shape has not yet been achieved. Most of the usually considered mass-density profiles can be parameterized as

$$\rho(r) = \frac{\rho_s}{(r/r_s)^\gamma\,[1+(r/r_s)^\alpha]^{(\beta-\gamma)/\alpha}}\,, \tag{2.11}$$

where r denotes the halo-centric radius, and r_s and ρ_s the characteristic profile radius and density, respectively. Numerical simulations show that such a profile indeed fits smooth dark matter halos on various scales, i.e., cluster halos, galaxy halos, and subhalos. The original Navarro-Frenk-White (NFW) profile is given by $(\alpha,\beta,\gamma) = (1,3,1)$, thus having a central cusp scaling as r^{-1} for $r \ll r_s$. The profile falls as r^{-3} to outer regions $r \gg r_s$. A steeper profile was claimed by Moore *et al.* (1998) with $(1.5,3,1.5)$, while various follow-up investigations resulted in a mean inner slope of $(1,3,\gamma)$, with $\gamma = 1.16 \pm 0.14$ (Diemand *et al.* 2004). Note that this would be consistent with a cusp of $\gamma = 1.3$ found in analytical calculations (Ahn & Shapiro 2005). Better agreement with galactic rotation curves – but in disagreement with simulations – is achieved with cored profiles, such as the isothermal profile $(2,2,0)$, see Begeman *et al.* (1991), or the Burkert profile (Burkert 1995).

Halo	m_{min} $[\mathrm{M}_\odot]$	ϵ [pc]	z_{i}	M_{200} $[\mathrm{M}_\odot]$	R_{200} [kpc]	M_{50} $[\mathrm{M}_\odot]$	R_{50} [kpc]
Aq-A-1	1.712×10^3	20.5	127	1.839×10^{12}	245.76	2.523×10^{12}	433.48
VL-II	4.098×10^3	40.0	104.3			1.93×10^{12}	402

Table 2.1: Characteristic parameters of the Aq-A-1 and VL-II halos. The mass resolution for subhalos is given by $M_{\mathrm{min}} \approx 20\, m_{\mathrm{min}}$, where m_{min} denotes the mass of simulated particles. The spatial resolution is determined by the gravitational softening length ϵ. Re-simulations were started at an initial redshift z_{i}. When available, the virial mass and virial radius are listed for two choices of Δ_{c}, i.e., 200 and 50. Note the different definition of Δ_{c} in Diemand *et al.* (2008a). The numbers have been adapted to the definition used here. See Springel *et al.* (2008b) and Diemand *et al.* (2008a) for details.

More recent simulations (Navarro *et al.* 2004), including Aquarius (Navarro *et al.* 2010), have shown that a better empirical description of halo profiles is provided by the Einasto profile (Einasto 1965), which has a smoothly changing logarithmic slope and no singularity at the halo center:

$$\rho_{\mathrm{Ein}}(r) = \rho_{-2} \exp\left\{ -\frac{2}{\alpha_{\mathrm{E}}} \left[\left(\frac{r}{r_{-2}} \right)^{\alpha_{\mathrm{E}}} - 1 \right] \right\}, \tag{2.12}$$

where α_{E} is a shape parameter, r_{-2} denotes the radius where the local logarithmic slope $\mathrm{d}\ln\rho/\mathrm{d}\ln r|_{r_{-2}} = -2$, and $\rho_{-2} \equiv \rho(r_{-2})$. More precisely, Navarro *et al.* (2010) find that the Aq-A-1 halo is best matched with an Einasto profile with $\alpha_{\mathrm{E}} = 0.17$, $r_{-2} = 15.14\,\mathrm{kpc}$, and $\rho_{-2} = 3.976 \times 10^{15}\,\mathrm{M}_\odot\,\mathrm{Mpc}^{-3}$. In addition, the Einasto profile fits significantly better than a cusped profile with $(1, 3, 1.24)$, which, contradictingly, provides the best fit of the VL-II halo (Diemand *et al.* 2008a).

Given the shape of the dark matter profile, the actual parameters of the Milky Way halo can be deduced from overall Galaxy mass models matching a variety of dynamical observables. This allows the determination of the local dark matter density in the vicinity of the Solar system, being of the order of $0.4\,\mathrm{GeV\,cm}^{-3}$ (see, e.g., Catena & Ullio 2010; Nesti & Salucci 2013).

In comparison to r_{s} and ρ_{s}, the concentration $c_{\mathrm{vir}} := R_{\mathrm{vir}}/r_{-2}$ provides a more robust quantity to parameterize dark matter halo profiles. Note that for the NFW profile $r_{-2} \equiv r_{\mathrm{s}}$ holds. The quantities r_{s} and ρ_{s} can be expressed in terms of the concentration and the virial halo mass M_{vir}. Simulations and observations show that the concentration strongly depends on M_{vir} (Navarro *et al.* 1997; Bullock *et al.* 2001; Eke *et al.* 2001): due to earlier formation times of lighter halos at epochs when the Universe was denser, massive halos generally have lower concentrations than lighter ones.

As part of this thesis, a more detailed account on the phenomenological modeling of dark matter halos and DM subhalos is presented in Chapter 4.

Effects of baryons. Accumulated baryons can affect the density profiles of dark matter halos in various ways, mediated through dissipative processes (see Diemand & Moore 2011 for an overview). Adiabatic contraction can steepen the inner dark matter density profiles. However, the overall total density profile of dark matter and baryons may resemble an isothermal sphere – consistent with the observations from galactic rotation curves (Blumenthal *et al.* 1986; El-Zant *et al.* 2001; Gnedin *et al.* 2004).

The growth of supermassive black holes in the centers of galaxies can dynamically flatten or steepen the central cusp, depending on their formation histories (Gondolo & Silk 1999; Merritt 2004; Gnedin & Primack 2004). Hydro-dynamical simulations have shown that halos of $M \gtrsim 10^6\,\mathrm{M}_\odot$ are sufficiently massive to accrete and radiatively cool baryonic gas, thus allowing for considerably efficient star formation (Madau *et al.* 2008 and references therein). Feedback processes, such as baryon ejection by supernovae, can redistribute dark matter by central re-virialization (Gnedin & Zhao 2002; Mashchenko *et al.* 2008), while stellar bars can transfer angular momentum by dynamical friction (Weinberg & Katz 2007). Simulations carried out by Kuhlen *et al.* (2013) recently showed evidence for a bar-halo interaction that significantly shifts the density peak of the dark matter halo out of the nominal galaxy center.

2.3.4 Dark matter subhalos

The early formation of low-mass dark matter halos from density perturbations at high redshift ($z \approx 60$), i.e., in a very dense Universe, has resulted in light halos with comparably high density concentrations. Pioneering works by Kauffmann *et al.* (1993) and Zentner & Bullock (2003), for instance, have demonstrated that the high core densities allow small-scale subhalos to survive merging processes to later-forming large-scale halos. As a result, a significant fraction of these objects has not been destroyed by strong tidal forces acting during merger events and subhalo evolution in the host. The existence of DM subhalos on sub-galactic scales results as a clear implication of this scenario.

Despite the fact that early simulations of dark matter substructures suffered strong resolution limits (Klypin *et al.* 1999a; Moore *et al.* 1999; Diemand *et al.* 2005), results on the subhalo abundance and mass-density profiles of current high-resolution simulations are in remarkable consistency with early simulations. Below, the basic properties of DM subhalos are discussed on the example of the Aquarius simulation, following Springel *et al.* (2008b). In the case of contradiction, the results from the Via Lactea simulation will be mentioned separately. In the framework of this thesis, Chapter 4 discusses the quantitative modeling of subhalo properties.

Mass function. Approximately 300 000 gravitationally bound subhalos have been resolved to orbit within the virialized region of the Aq-A-1 halo (see Fig. 2.6). Above the mass-resolution limit of the simulation, $M_\mathrm{res}^\mathrm{Aq} = 3.24 \times 10^4\,\mathrm{M}_\odot$, the abundance of subhalos with mass M decreases to higher masses with a power law $\mathrm{d}N/\mathrm{d}M \propto M^{-\alpha}$, where $\alpha = 1.9$ (VL-II: $\alpha \rightarrow 2.0$). This corresponds to a clumpiness factor f_sh of 13.2% in subhalos within R_{50}, where f_sh denotes the ratio of the total mass in subhalos and the virial mass of the host. To the low-mass end, the subhalo distribution is anticipated to have a sharp cutoff at M_min, which is determined by the free-streaming limit of dark matter particles in the early Universe. The cutoff mass M_min may vary between $10^{-12}\,\mathrm{M}_\odot$ and $10^{-3}\,\mathrm{M}_\odot$, depending on the dark matter particle (Berezinsky *et al.* 2003, 2006; Green *et al.* 2005; Bringmann 2009). The resolution limit of current simulations is well above these mass bounds. Assuming the power-law distribution to continue to M_min, the total clumpiness factor of the host would be ~18%. The subhalo abundance found in the VL-II run is ~31% lower than the mean abundance of the six simulated Aquarius halos.

Spatial distribution. Subhalos follow a spatial distribution which is "anti-biased" to the smooth dark matter distribution of the host halo, i.e., the vast majority of subhalos populates outer halo regions ($r > 100\,\mathrm{kpc}$). The number-density profile is well fit by an Einasto profile (Eq. 2.12) with $\alpha_\mathrm{E} = 0.678$ and $r_{-2} = 199\,\mathrm{kpc} = 0.81\,R_{200}$, independent of the considered mass threshold. Assuming this behavior to continue down to M_min, the smooth dark matter host halo dominates the inner part of galactic halos, while substructures guide the outer regions.

Sub-substructure. The simulations resolve up to four levels of sub-substructure within subhalos, validating the expectation from hierarchical formation. In contradiction to claims that the sub-subhalo number-density profile should be self-similar to the one for subhalos (Shaw *et al.* 2007; Diemand *et al.* 2008a), the fractional abundance of sub-subhalos resolved in the Aquarius simulation is a factor of 2 to 3 lower than the abundance anticipated from self-similarity. The suppression of higher level substructure can be explained with tidal stripping of halos while falling into the larger host system and becoming subhalos: tidal forces of the host's gravitational potential (see, e.g., Binney & Tremaine 2008) truncate the subhalo-rich outer regions of infalling halos and, therefore, reduce the abundance of subhalos. This process continues with ongoing evolution in the corresponding host halo.

Mass-density profile. Consistently, both the Aquarius and the VL-II project have found the mass-density profiles of subhalos to be similar to the profile of their galactic host halos. While Diemand *et al.* (2008a) suggest a cuspy $(1, 3, 1.24)$-profile, Aquarius subhalos are best fit by an Einasto profile. Even further, Springel *et al.* (2008b) conclude that a Moore profile with an inner slope of $\rho \propto r^{-1.5}$ appears to be significantly disfavored, while an NFW profile cannot be ruled out.

Concentration. Subhalos generally appear to be more concentrated than isolated field halos of comparable mass. In addition, the concentration increases with decreasing subhalo mass, which is related to the earlier formation of smaller structures in environments with comparably higher densities. Tidal mass loss of accreted subhalos finally results in a concentration which depends on the position of the subhalo in the host. The concentration increases towards the halo center (Diemand *et al.* 2007b, 2008b).

2.3.5 The search for dark matter subhalos

The previous discussion of dark matter and concordance cosmology has clearly demonstrated the agreement between the predictions of hierarchical structure formation and the observations of the cosmic web, on length scales of galaxy clusters down to the scales of small galaxies. However, no convincing observational confirmation of the small-scale predictions of hierarchical structure formation has been achieved yet. A full test or even confirmation of the ΛCDM scenario requires the discovery of the predicted amount of small-scale substructures, which is also related to the specific properties of the dark matter constituents themselves.

As introduced in Section 2.2.1, a number of $\sim$20 dSph galaxies have been discovered as satellites gravitationally bind to the Milky Way system. Strong evidence has emerged for the stellar kinematics of these objects to be dominated by dark matter. This observation results in the hypothesis that dSphs are the luminous counterparts of massive DM subhalos. A comparison to the subhalo mass function predicted by numerical simulations, however, reveals that ∼350 dark matter subhalos[11] are assumed to be sufficiently massive to form stars and, therefore, reside as dSph galaxies in the Milky Way halo. The apparent mismatch by about one order of magnitude has emerged to an extensively discussed problem over the last decade, referred to as the *Missing Satellites Problem* (Klypin *et al.* 1999b; Moore *et al.* 1999), see Bullock (2010) for a recent review. Basically, proposed solutions to the Missing Satellites Problem fall in two different categories:

(i) *Sample bias.* The sample of known dSphs obeys a high degree of incompleteness with regard to sky-coverage, luminosity bias, and surface brightness limits (Tollerud *et al.* 2008). Estimates corrected for these effects result in the prediction of ∼400 massive dSph galaxies brighter than $1\,000\,\mathrm{L}_\odot$ within ∼400 kpc of the Sun, consistent with the expectation of the ΛCDM scenario. While maybe alleviating the Missing Satellites Problem, in particular the low-mass extrapolation of the satellites's luminosity function (Strigari *et al.* 2008) remains to be clarified. The latter is directly related to the fate and the detection prospects of the much more abundant low-mass subhalos. A strict lower limit for star formation in DM subhalos might obviously be a subhalo mass of a few ten to a few hundred Solar masses, while the exact order of the cutoff mass is presumably higher. In particular, Bullock *et al.* (2010) have predicted a population of low-luminosity dwarf galaxies with a peak surface brightness fainter than $30\,\mathrm{mag\,arcsec}^{-2}$, which is well below the sensitivities of current star-count surveys for identifying them as dwarf galaxies. These galaxies resemble ultra-faint dSphs with regard to their total luminosities and stellar velocity dispersions, but their surface brightness is reduced by a radially more extended stellar distribution. Low-luminosity dwarf galaxies can be hosted by less massive DM subhalos, explaining the larger extend of the stellar distribution. A discovery of these objects might be in reach of next generation survey projects.

    Brown *et al.* (2012) have recently demonstrated that the stellar content of at least three (presumably five) ultra-faint dSph galaxies is as old as the ancient globular cluster M92 (which is one of the oldest known globular cluster of the Milky Way). The result implies that star formation in ultra-faint dSphs must have been truncated by an early global event such as re-ionization, strengthening the hypothesis that ultra-faint dSphs are fossil remnants of the early Universe.

(ii) *Different dark matter models.* The standard assumption of a cold dark matter scenario can be modified in order to reduce the expected number of low-mass halos. Among currently discussed models are warm dark matter (Bode *et al.* 2001; Lovell *et al.* 2012), self-interacting dark matter (Spergel & Steinhardt 2000), and also modified inflation models changing the cutoff in the primordial density fluctuation spectrum (Kamionkowski & Liddle 2000; Zentner & Bullock 2003).

Yet another possibility which has been invoked to probe for DM subhalos is provided by strong gravitational lensing (see Zackrisson & Riehm 2010 for a recent review). Objects of the mass-scale of dwarf galaxies have been shown to give rise to millilensing in the images of background galaxies. Lensing induced by subhalos with masses between $10^5\,\mathrm{M}_\odot$ and

---

[11] The number depends on the definition of the lower mass bound. Here, a minimal subhalo mass of $3.4 \times 10^7\,\mathrm{M}_\odot$ was assumed, see Bullock (2010).

$10^{10}\,\mathrm{M}_\odot$ leads to a couple of observable second-order effects, such as flux-ratio anomalies, astrometric effects, small-scale structure in macroimages, and time-delay effects. In particular, radio-loud lensed quasar systems serve as promising objects in order to search for substructures in the lens system, since radio observations are capable of providing the high spatial resolution required. While evidence for the existence of small-scale substructure has already been found in these systems, so far lacking resolution has prevented current observations to give rise to strong constraints (Zackrisson & Riehm 2010 and references therein). However, significant improvement of the detection prospects will be in reach of next generation telescopes such as the Large Synoptic Survey Telescope (LSST; Abate *et al.* 2012), the Joint Dark Energy Mission (JDEM; Gehrels 2010), the James Webb Space Telescope (JWST; Gardner *et al.* 2006), and the Atacama Large Millimeter Array (ALMA; Hodge *et al.* 2013).

Small-scale tribulations of ΛCDM. Apart from the missing detection of small-scale substructures, other tribulations seem to appear between current observational results and small-scale predictions of ΛCDM (see Primack 2012 for a recent review). Stellar motion indicates a flatter shape of the inner dark matter density profile of dSph galaxies, such as for Sculptor and Fornax, than predicted by the cuspy NFW profile (Walker & Peñarrubia 2011; Amorisco & Evans 2012). The effect is even more pronounced in standard low surface brightness (LSB) galaxies. However, the flattening of the inner profile in the centers of dwarf galaxies can be consistently explained by recent hydro-dynamical simulations including baryon physics: strong outflows from supernovae rapidly drive out inner gas, leading to a significant reduction of the inner dark matter density and eventually forming cored profiles (Governato *et al.* 2010). Notwithstanding, supernova feedback might not be sufficient to explain the flat profiles of LSB galaxies, owing to their reduced stellar content (Kuzio de Naray & Spekkens 2011).

Other challenges for the ΛCDM model have arisen in form of the "too big to fail" (TBTF) problem or from an observationally missing class of dwarf galaxies (see Kroupa 2012).

The TBTF problem manifests as follows: Boylan-Kolchin *et al.* (2011) found the most massive simulated subhalos to be apparently too concentrated to host visible dwarf galaxies with a luminosity larger than $10^5\,\mathrm{L}_\odot$ (also, cf. Boylan-Kolchin *et al.* 2012). The result has been obtained comparing the observed circular velocity curves $v_\mathrm{c}(r)$ of dSph galaxies to the ones of simulated Aquarius and VL-II subhalos. While these subhalos might be inhabited by ultra-faint dSphs, the result contradicts the established monotonic rise of the luminosity function with mass: star formation in massive halos is not expected to be significantly suppressed. In that sense, the most massive subhalos are *too big to fail* star formation. Consequently, the absence of such subhalos in the Milky Way would put the small-scale predictions of ΛCDM to question (baryonic feedback processes are presumably not capable of reducing the inner concentrations in a sufficiently large manner, see di Cintio *et al.* 2011).

Recently, Wang *et al.* (2012) claimed that the TBTF problem can be alleviated if the virial halo mass of the Milky Way is lower than previously thought ($\lesssim 1 \times 10^{12}\,\mathrm{M}_\odot$). Another solution has been deduced by di Cintio *et al.* (2013) from dark matter only and full hydro-dynamical simulations of the local Universe: the authors conclude that the radial dark matter density profile of subhalos is best described with an Einasto profile, with a slope parameter strongly correlated with the total subhalo mass. Adopting such a non-universal density profile alleviates the TBTF problem.

2.4 Dark matter candidates

The fundamental nature of dark matter remains unknown. The non-observation of dark matter constituents puts severe constraints on its nature, summarized as follows: to satisfy the BBN and CMB observations, dark matter must be *non-baryonic*. Because no electromagnetic radiation has been detected from dark matter, it must be *electrically neutral*, and if it was not *color-neutral*, it would have spoiled BBN and the CMB. The coupling of dark matter to weak gauge bosons should be very small, given its non-detection in direct detection experiments (see Section 3.2). Large-scale structure requires dark matter to be dissipationless with a small free-streaming length, i.e., dark matter has to be *cold*. Merging galaxy clusters such as the Bullet Cluster imply it to behave as a *collisionless* fluid. Below, a brief summary of dark matter candidates in accordance with these constraints is given. For more comprehensive accounts on the content, see, e.g., Jungman *et al.* (1996), Bertone *et al.* (2005), Bertone (2010a), Bringmann (2011), and references therein.

The established properties are sufficient to exclude standard astronomical massive compact halo objects (MACHOs) as dark matter candidates, such as brown dwarfs, Jupiter-sized planets, stellar black-hole remnants, white dwarfs, or neutron stars. MACHOs have also been excluded by direct searches, which are sensitive to a broad mass range between $10^{-7}\,\mathrm{M}_\odot$ and $15\,\mathrm{M}_\odot$ (Tisserand *et al.* 2007).

As dark matter manifests through gravitational interactions only, the assumption that the theory of gravitation looses validity on large scales might be a natural conclusion. This possibility has been addressed in the framework of Modified Newtonian Dynamics (MOND; Milgrom 1983a,b,c), see Bekenstein (2010) for a recent review. Even though this model works in explaining the flat rotation curves of galaxies and clusters, problems emerged while trying to consistently describe all observed phenomena.

Almost all remaining dark matter candidates belong to the category of currently unknown non-baryonic elementary particles. This case has gained most of the research interest over the last decades, and is considered in the framework of this thesis.

Neutrinos are the only candidates within the Standard Model (SM) of particle physics that satisfy the above criteria. The detection of neutrino oscillations has clearly demonstrated that neutrinos carry a small mass and contribute to the relic density Ω_{dm}. However, CMB observations constrain the sum of the three mass-eigenstates to $\sum m_\nu < 0.23\,\mathrm{eV}$ (95% CL), corresponding to a maximum contribution of $\Omega_\nu h^2 < 0.0025$ (Ade *et al.* 2013b). Additionally, the free-streaming length of hot neutrino dark matter is not in agreement with large-scale structure. It would also imply a “top-down” structure formation scenario, which has been ruled out by observations.

The phenomenology of the SM is not suited for describing physical processes on energy scales significantly larger than a few hundred GeV. Theoretical problems, such as the hierarchy problem and the related fine-tuning problem, as well as experimental results like the strong-CP problem or non-vanishing neutrino masses require SM extensions, implying beyond-SM physics. Most of the currently proposed models contain particles which fulfill the observational constraints on cold dark matter. It is worth emphasizing that most SM extensions comprise dark matter candidates in a natural way, i.e., the models have not been developed to specifically address the nature of dark matter, but to solve general SM shortcomings.

Particle candidates for cold dark matter predicted by common SM extensions can basically be grouped into two categories, distinguishing them by their masses: *weakly interacting massive particles* (WIMPs) at a mass scale of $\mathcal{O}(100)\,\mathrm{GeV}$ and very light *weakly interacting slim particles* (WISPs) with masses $< 1\,\mathrm{eV}$. Popular WIMP candidates are discussed in Section 2.4.2, while WISPs are introduced in Chapter 6, Section 6.1. It should be mentioned that the following discussion omits various other models, e.g., warm dark matter scenarios based on sterile neutrinos (Merle 2013), given that this thesis is centered on indirect searches for WIMPs and WISPs.

2.4.1 WIMPs as cold thermal relics

Let the main dark matter constituent be a new, stable WIMP χ with a mass m_χ. As demonstrated below, the thermal evolution of the Universe indeed implies a cosmological relic abundance of these particles (e.g., Lee & Weinberg 1977; Gunn *et al.* 1978; Ellis *et al.* 1984; Scherrer & Turner 1986). The time evolution of the cosmological number density $n_\chi(t)$ is described by the Boltzmann equation

$$\dot{n}_\chi + 3Hn_\chi = -\langle\sigma_\mathrm{A} v\rangle\left[(n_\chi)^2 - (n_\chi^\mathrm{eq})^2\right], \tag{2.13}$$

where $\langle\sigma_\mathrm{A} v\rangle$ denotes the thermally-averaged effective cross section for annihilating $\chi\overline{\chi}$ pairs times their relative velocity v. WIMP pairs can annihilate to lighter final-state particles $f\overline{f}$, which commonly cover quark-antiquark, lepton-antilepton, and, for a sufficiently large m_χ, gauge boson or Higgs boson pairs. In the early Universe ($T \gg m_\chi$), WIMPs reside in thermal equilibrium, which is maintained by the equilibrium process $\chi\overline{\chi} \rightleftarrows f\overline{f}$. While the Universe cools with expansion, the equilibrium number density decreases exponentially as $n_\chi^\mathrm{eq} \propto T^{2/3}\exp(-m_\chi/T)$ after T falls below m_χ. This causes a corresponding drop in the annihilation rate $\Gamma = \langle\sigma_\mathrm{A} v\rangle n_\chi$, which eventually falls below the Universe's expansion rate H: $\Gamma \lesssim H$.[12] WIMP annihilation then starts to *freeze out*, the particles leave thermal equilibrium, and, consequently, a constant relic cosmological abundance remains in the late Universe. Details of this process of chemical decoupling are demonstrated in Fig. 2.7, which shows the actual solution of Eq. (2.13) for the comoving number density $a^3 n_\chi$ as a function of the dimensionless quantity $x = m_\chi/T \propto t$. For typical weak-scale numbers, the freeze-out temperature is given by $T_\mathrm{cd} \simeq m_\chi/20$.

The figure shows that the relic density depends on the annihilation cross section, which itself depends on energy and can be approximated as $\langle\sigma_\mathrm{A} v\rangle \approx a + bv^2$. Here, the first term a originates from s-wave annihilation, while the second term bv^2 includes contributions of both s-wave and p-wave annihilation. Assuming energy independence and conservation of comoving entropy reveals that the WIMP relic density is inversely proportional to $\langle\sigma_\mathrm{A} v\rangle$,

$$\Omega_\chi h^2 \simeq \frac{3\times 10^{-27}\,\mathrm{cm^3\,s^{-1}}}{\langle\sigma_\mathrm{A} v\rangle}, \tag{2.14}$$

using the values of the entropy density and the critical density at $z = 0$. Given the observed $\Omega_\chi h^2 \approx 0.1$, one immediately concludes that the annihilation cross section satisfying the relic density constraint should be of the order of $\langle\sigma_\mathrm{A} v\rangle \approx 3\times 10^{-26}\,\mathrm{cm^3\,s^{-1}}$. This value is in remarkable consistency with the value expected for a new particle with weak-scale

---

[12] In many considered models the WIMP is a Majorana particle, i.e., $\overline{\chi} = \chi$. Majorana particles are self-annihilating, and the annihilation rate reads $\Gamma = \langle\sigma_\mathrm{A} v\rangle n_\chi^2/2$.

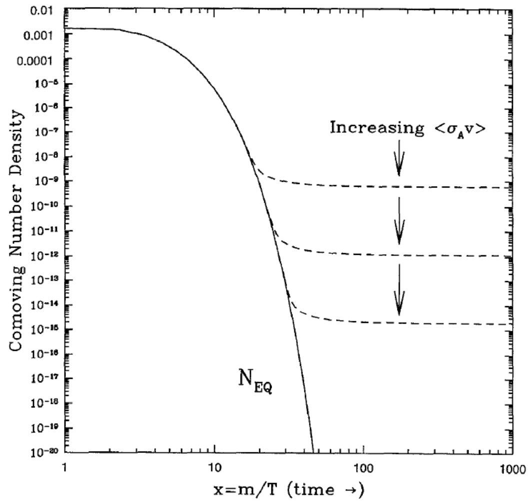

Figure 2.7: Comoving number density of WIMPs in the early Universe as function of time ($x \propto t$). The solid line shows the equilibrium abundance, while the dashed lines give the actual abundances for different $\langle \sigma_{\mathrm{A}} v \rangle$. From Jungman *et al.* (1996).

interactions: $\langle \sigma_{\mathrm{A}} v \rangle \approx \alpha^2/m_\chi^2 \approx 10^{-25}\,\mathrm{cm}^3\,\mathrm{s}^{-1}$ (for $m_\chi = 100\,\mathrm{GeV}$ and a coupling constant $\alpha = 10^{-2}$), linking the cosmological density parameter to a particle physics nature, a fact which is often referred to as the *WIMP miracle*.

In general, the annihilation cross section is a decreasing function of the WIMP mass, revealing the relic density to increase with m_χ. Unitarity places a strict upper bound on the slope of this function, $\langle \sigma_{\mathrm{A}} v \rangle \propto m_\chi^{-2}$, which translates into a model-independent lower bound on the relic density, $\Omega_\chi h^2 \gtrsim [m_\chi/(3\,\mathrm{TeV})]^2$. Here, a weak-coupling strength $\alpha = 10^{-2}$ has been used (Griest & Kamionkowski 1990; Hall *et al.* 2013). The measured value of the relic density then places an upper bound on the WIMP mass of $m_\chi < \mathcal{O}(\mathrm{TeV})$.

Note that scattering processes between WIMPs and SM particles leave the WIMPs to stay in contact with the thermal bath for a given time after chemical decoupling. Only after the time of kinetic (or thermal) decoupling, when these processes have lost their efficiency, WIMPs and SM particles remain completely decoupled (Bringmann 2009).

2.4.2 WIMP candidates

Supersymmetric candidates. Supersymmetry (SUSY; e.g., Jungman *et al.* 1996; Martin 1998) belongs to the most promising high-energy extensions of the SM. SUSY establishes a fundamental connection between bosons and fermions, by introducing a Lie algebra combining the Poincaré group and internal symmetry groups. Every SM particle gets an equivalent supersymmetric particle (superpartner) with the same quantum numbers except for the spin, which differs by 1/2. Therefore, gauge bosons have fermionic superpartners (*gauginos*), while scalar partners are associated to fermions (*sfermions*). SUSY contains five physical Higgs states. Stated in a more formal way, the new generators Q of the Lie algebra map fermionic states $|F\rangle$ to bosonic states $|B\rangle$, and vice versa: $Q|F\rangle = |B\rangle$ and $Q|B\rangle = |F\rangle$.

SUSY provides solutions to the main SM shortcomings: (i) The introduction of superpartners would solve the hierarchy problem. In the SM, the hierarchy problem manifests in quadratically divergent radiative corrections to the scalar mass (the mass of the Higgs boson), destroying the stability of the electroweak scale. In SUSY, these divergences cancel out by both fermionic and bosonic loops, owing to the opposite sign of their contributions. (ii) SUSY would lead to a unification of the gauge couplings at an energy scale of $\sim 2 \times 10^{16}\,\mathrm{GeV}$, as expected in a grand unified theory (GUT).

The broad framework of SUSY results in different models, where one of the most appealing is the Minimal Supersymmetric Model (MSSM), providing the minimum field content required for a self-consistent SM extension. To suppress proton decay, the MSSM additionally assumes conservation of R-parity, which is a multiplicative quantum number assigned to SM and SUSY fields. All SM particles get $R = 1$, while SUSY particles have $R = -1$. Hence, the lightest supersymmetric particle (LSP) is stable. A pair of LSPs can annihilate to SM states. Furthermore, the MSSM requires an electrically neutral and color neutral LSP, making the LSP an excellent dark matter candidate.

Collider experiments have shown that no superpartner with the same mass as its SM partner exists. That means that SUSY must be broken. The specific breaking mechanism also determines the characteristics of a SUSY model.

LSP candidates are sneutrinos, gravitinos, axinos, and the neutralino, which is the most popular candidate discussed in the literature. Note that sneutrinos have been excluded by direct detection experiments (see Section 3.2). The lightest neutralino, henceforth *the* neutralino $\chi \equiv \tilde{\chi}^0_1$, is the lightest state of four Majorana mass eigenstates, which are linear combinations of superpartners to the SM gauge bosons B, W_3, and the neutral Higgs bosons H^0_1 and H^0_2:

$$\chi = N_{11}\tilde{B} + N_{12}\tilde{W}_3 + N_{13}\tilde{H}^0_1 + N_{14}\tilde{H}^0_2\,, \tag{2.15}$$

where the tilde marks the superpartners and N_{1i}, $i = 1, \ldots, 4$, denote the mixing coefficients.

The generic MSSM can be further constrained by additional theoretical arguments, leading to specific models which reduce the more than hundred parameters of the MSSM to an experimentally constrainable number. Among the most considered models are the constrained MSSM (cMSSM) and the even more constrained mSUGRA model (Kane *et al.* 1994). In the cMSSM, for instance, a variety of well-motivated theoretical assumptions at the GUT scale reduce the free parameters to four plus one sign: the ratio of the vacuum expectation values of the Higgs fields, $\tan\beta$, the universal gaugino mass $m_{1/2}$, the universal scalar mass m_0, the universal trilinear coupling A_0, and the sign of the higgsino mass parameter $\mathrm{sgn}\,\mu$.

The experimental signatures of neutralinos, e.g., their self-annihilation to SM states $\chi\chi \to f\bar{f}$, are used for a variety of searches. Colliders, direct detection experiments, and astrophysical observations have placed strong bounds on the cMSSM and the mSUGRA model, which are discussed in Chapter 3. Models with small R-parity breaking and a gravitino LSP are consistent with concordance cosmology as well (Buchmüller *et al.* 2007). Gravitinos can decay to SM final states and therefore lead to detectable signatures. The theoretically expected livetimes are of the order of 10^{27} s or larger, that can be constrained observationally (see Bertone *et al.* 2007, Buchmüller *et al.* 2009, and references therein).

Extra dimensions. Though no experiment has indicated that the world has more than 3+1 (three space and one time) dimensions, higher-level theories such as string theory point to additional compactified dimensions. Such dimensions could exist as long as they are sufficiently small to evade current instrumental resolution. The scenario would imply our macroscopic spacetime *brane* to be embedded in a higher dimensional spacetime *bulk*.

In the frame of a macroscopic observer, particles propagating along compactified extra-dimensions of size R gain quantized additional mass, $m_n^2 = m^2 + n^2/R^2$. The mode number n corresponds to the state in the infinite Kaluza-Klein (KK) tower, which is attributed to each bulk field. Different models of extra-dimensions have been studied, depending on considered topologies and types of extra-dimensions (e.g., Arkani-Hamed *et al.* 1998; Randall & Sundrum 1999). By reducing the size of the Planck scale, extra-dimensions could provide a solution to the hierarchy problem.

In the model of Universal Extra Dimensions (UED; Appelquist *et al.* 2001), allowing all particles to propagate freely in the bulk dimension, compactification on the orbifold $\mathbb{S}^1/\mathbb{Z}_2$ is chosen. This implies a conserved KK-parity $(-1)^n$, ensuring stability of the lightest KK particle (LKP), which thus provides a viable dark matter candidate. The LKP is represented by the first KK excitation $B^{(1)}$ of the weak hypercharge boson (Cheng *et al.* 2002), revealing the correct relic density for $R^{-1} \approx 1.3\,\mathrm{TeV}$ (Servant & Tait 2003; Bélanger *et al.* 2011). Yet, this value is in good agreement with otherwise strong collider constraints (Section 4.5 in Baak *et al.* 2012b) in combination with the measured value of the Higgs mass (Baak *et al.* 2012a). Essentially, $B^{(1)}$ annihilation results in charged lepton pairs (~60%) and quark pairs (~35%).

Other models. Various other models for WIMP dark matter have appeared in the literature, with some addressing the primary aim to solve the hierarchy problem, while others just provide minimum SM extensions (see, e.g., Bertone 2010a). For instance, Little Higgs models (Schmaltz & Tucker-Smith 2005) extend the SM with a large global symmetry group, which is spontaneously broken at a scale $f \approx 1\,\mathrm{TeV}$. Tackling the hierarchy problem, the SM Higgs appears as a pseudo-Nambu-Goldstone boson. Particles carry T-parity, yielding the heavy photon B_H as dark matter candidate. B_Hs dominantly annihilate to W^+W^-, ZZ, and $t\bar{t}$. Their mass is between 80GeV and 500GeV.

Other examples include Mirror dark matter (Barbieri *et al.* 2005), Singlet scalar models (Burgess *et al.* 2001), and Minimal dark matter (Cirelli *et al.* 2006).

Chapter 3

Approaches to Particle Dark Matter Detection

Laboratory dark matter production and the detection of its constituent(s) are required to confirm the existence of dark matter and to investigate its properties. Feasible approaches for experimental or observational WIMP dark matter searches cover three complementary ways: production of WIMPs at colliders (Section 3.1), direct detection of their scattering with heavy nuclei (Section 3.2), and indirect detection of annihilation (or decay) products (Section 3.3). Final confirmation of dark matter would require its detection in all three channels, given that the methods are sensitive to partly different properties. Meaningful constraints can eventually be made by fitting the combination of all observables with candidate theoretical frameworks. Recent success in the development of combining fit algorithms has led to strong constraints on the cMSSM and the mSUGRA model (Buchmueller *et al.* 2007, 2012; Nguyen *et al.* 2012; Bechtle *et al.* 2012).

The following sections aim at glancing over the various experimental and observational searches discussed in the literature, and summarize the current results. In between, Section 3.3.1 focusses on current instruments of gamma-ray astronomy, which are also used for the indirect searches conducted in this thesis. The case for WISPs is highlighted in the second part of the thesis, see Section 6.1. Further information can be found in various recent reviews, e.g., Bertone (2010a), Porter *et al.* (2011), Bringmann & Weniger (2012), or Strigari (2013).

3.1 Production at colliders

Dark matter in form of WIMPs can be directly produced with particle accelerators, once the center-of-mass energy of the colliding beams is sufficiently large. While a small coupling and temporal stability make a subsequent detection of WIMPs themselves nearly impossible at colliders, the general imprints of SUSY or other beyond-SM physics can be robustly identified (e.g., Nath *et al.* 2010). Recent searches with detectors at the LHC, in particular with ATLAS and CMS, have focussed on various signatures such as *jets + missing transverse energy* ($\not{E}_T$) and *leptons + jets +* $\not{E}_T$, investigating the data provided by the $\sqrt{s} = 7$ TeV run with a total integrated luminosity of up to $\sim 5\,\mathrm{fb}^{-1}$ (e.g., Aad *et al.* 2012d,c, 2013a; CMS Collaboration 2012b; Chatrchyan *et al.* 2013a; CMS Collaboration 2013b). In combination with other highly sensitive observables[1] and the mass of the recently discovered Higgs boson (Aad *et al.* 2012a,b; CMS Collaboration 2012a; Chatrchyan *et al.* 2013b), the non-observations of any potential signal have resulted in strong constraints on SUSY, in particular on the cMSSM and mSUGRA, by pushing the lower mass limits on gluinos and squarks (or m_0 and $m_{1/2}$ in the cMSSM/mSUGRA) to values above the TeV level (Aad *et al.* 2013b; CMS Collaboration 2013a,c).

3.2 Direct detection

WIMPs can be directly detected by their scattering signatures with heavy nuclei. In the last decades, a variety of low-noise detectors have been deployed in underground laboratories, with the purpose of resolving nuclear recoils from scattering WIMPs from the Galactic halo. The interaction rate of a WIMP flux nv (where n is the number density in the vicinity of the Sun) with a number of target nuclei N_T is given by $R = N_\mathrm{T}\sigma n v$. Owing to the low scattering cross section of WIMPs, anticipated to be at the order of $\sigma \approx 10^{-44}\,\mathrm{cm}^2$, experimental setups face the challenge of efficient shielding from external electromagnetic and nuclear backgrounds. For typical WIMP and target properties, the recoil energy transferred to target nuclei is between ten and one hundred keV.

Usual target materials used in current detectors are germanium and silicon, as in CDMS-II (Ahmed *et al.* 2011), EDELWEISS-II (Armengaud *et al.* 2011), and CoGeNT (Aalseth *et al.* 2011), the noble gas xenon as in ZEPLIN-III (Akimov *et al.* 2012) and XENON100 (Aprile *et al.* 2012), and calcium tungstate $\mathrm{CaWO_4}$ as in CRESST-II (Angloher *et al.* 2012). Such detector setups are most sensitive to the spin-independent part of the cross section. Signal-to-background discrimination is achieved by measuring at least two of three possible signal channels that are differently triggered by nuclear recoil and electromagnetic backgrounds: phonons, charge deposit, and light yield.

Direct detection experiments focus on three different signals: the mean event rate, annular modulation, and the recoil direction. While DAMA/LiBRA (Bernabei *et al.* 2008) reported a significant annular modulation, CRESST-II claimed the detection of 67 events in its acceptance region. However, these detections correspond to a rather high scattering cross section, different WIMP masses, and are in conflict with bounds from other experiments, see Fig. 3.4a on page 39 for details. So far, various efforts to explain the discrepancies have not resulted in convincing explanations. The current best bounds on the spin-independent cross section have resulted from an exposure of $224.6\,\mathrm{d} \times 34\,\mathrm{kg}$ with XENON100, with a minimum upper limit of $2 \times 10^{-45}\,\mathrm{cm}^2$ (90% CL) for a WIMP mass of 55 GeV (Aprile *et al.* 2012).

The spin-dependent cross section can be measured with threshold detectors, e.g., SIMPLE (Felizardo *et al.* 2012), PICASSO (Archambault *et al.* 2012), and COUPP (Behnke *et al.* 2012). Highest sensitivity is reached with large-scale neutrino detectors such as Super-Kamiokande (Tanaka *et al.* 2011), IceCube (Abbasi *et al.* 2012a), and ANTARES (Adrián-Martinez *et al.* 2013), constraining the neutrino flux emitted by annihilating WIMPs captured in the Sun.

---

[1] Especially beyond-SM physics, such as SUSY, should reflect in the rate of rare B-meson decays (Aaij *et al.* 2012) and the anomalous magnetic moment of the muon.

3.3 Indirect detection

WIMPs can annihilate or decay to SM particles: Higgs bosons H, gauge bosons (W, Z, g, γ), quarks (t, b, c, s, u, d), or leptons $(\tau, \mu, e, \nu_\tau, \nu_\mu, \nu_e)$, cf. Section 2.4.2. Individual channels f, weighted with their branching ratios B_f, combine to a total final state spectrum. Subsequent hadronization or rapid decay of the final state products eventually yield a spectrum of stable particles and their antiparticles: deuterium $(D, \overline{D})$, protons $(p, \overline{p})$ and electrons $(e^{\pm})$, high-energy neutrinos $(\nu_\tau, \nu_\mu, \nu_e)$, and gamma-ray photons (γ). All of these secondary particles may then be emitted by astrophysical halos and objects of high dark matter density, providing various opportunities for the indirect detection of WIMPs with astrophysical instruments. Separation between dark matter powered and conventional astrophysical sources is facilitated by the characteristically hard spectra of secondary particles from WIMP annihilation. In addition, energy conservation requires a distinct spectral cutoff to the WIMP mass m_{dm} (see Cirelli *et al.* 2011, 2012 for details).

Detection prospects for charged particles are generally improved by focussing on the antiparticles, given comparably lower astrophysical backgrounds. However, the trajectories of charged particles propagating in the Galaxy are quickly randomized by their scattering on interstellar magnetic fields. Light charged particles also quickly loose their energy via synchrotron radiation and inverse-Compton scattering on interstellar radiation fields, producing additional low-energy photons. While these effects challenge experimental detection, the emission of gamma-ray photons and high-energy neutrinos offers the possibility to directly pinpoint the origin of dark matter powered sources.[2]

Annihilating WIMPs produce gamma-ray photons via three processes: (i) Hadronization of final-state gauge bosons and quarks results in particle jets dominated by π-mesons. The subsequent decay of neutral pions ($\pi^0 \to \gamma\gamma$) produces a continuous spectrum of high-energy gamma-rays, cf. Fig 3.1a (see Baltz *et al.* 2007 for details). This also partly holds for τ final states, which can kinematically decay to π-mesons. (ii) Internal Bremsstrahlung (IB) can give rise to additional spectral features peaking at energies just below m_{dm}, cf. Fig 3.1b. Two different processes contribute to the IB spectrum, i.e., final state radiation from external legs and virtual internal Bremsstrahlung from charged virtual particles (Bringmann *et al.* 2008; Essig *et al.* 2009). (iii) Providing the "smoking gun" signal, dark matter can directly annihilate to two gamma-ray photons with energy $E \approx m_{\mathrm{dm}}$, cf. Fig 3.1c. The annihilation to monochromatic gamma-ray lines is, however, loop-suppressed with a branching-ratio of $B_\gamma \approx 10^{-3}$ (Ullio & Bergström 1998). Some models do also allow annihilation in γZ at $E = m_{\mathrm{dm}}[1 - m_Z^2/(4m_{\mathrm{dm}}^2)]$.

The differential gamma-ray flux per unit energy interval $[E; E + \mathrm{d}E]$ of a source driven by self-annihilating WIMPs reads

$$\frac{\mathrm{d}\phi(E, \Delta\Omega)}{\mathrm{d}E} = \frac{1}{4\pi} \frac{\langle \sigma_{\mathrm{A}} v \rangle}{2m_{\mathrm{dm}}^2} \sum_f \left(\frac{\mathrm{d}N_f}{\mathrm{d}E} B_f \right) \int_{\Delta\Omega} \mathrm{d}\Omega \int_{\mathrm{los}} \rho^2[r(l)]\mathrm{d}l \tag{3.1}$$

(Gunn *et al.* 1978; Zeldovich *et al.* 1980; Bergström *et al.* 1998), where $\mathrm{d}N_f/\mathrm{d}E$ denotes the differential photon yield per annihilation into SM particles f, $\Delta\Omega$ the solid angle covered

---

[2] The Galactic attenuation of photons vanishes for energies below a few 10 TeV (Moskalenko *et al.* 2006). However, extragalactic photons above a few hundred GeV may suffer significant pair-production losses on the extragalactic background light (EBL; e.g., Meyer *et al.* 2012).

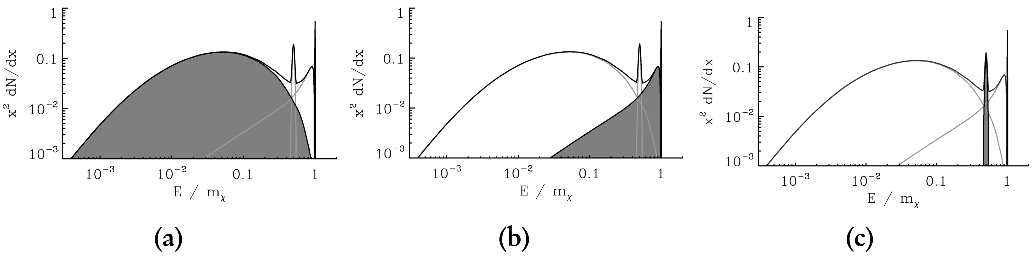

Figure 3.1: Schematic representation of the different contributions to the differential gamma-ray yield $x^2 \mathrm{d}N/\mathrm{d}x$ of annihilating WIMPs, where $x = E/m_{\mathrm{dm}}$ (here, $m_\chi \equiv m_{\mathrm{dm}}$): **(a)** continuous contribution from final state fragmentation, **(b)** internal Bremsstrahlung radiation, and **(c)** monochromatic lines. Adapted from Kuhlen (2010).

with the detector, and the last term is the line-of-sight integral of the squared dark matter mass-density profile ρ. [3]

A vast variety of different observations in secondary channels have been used to search for dark matter signals. The non-detections made so far have been interpreted in terms of constraints on the annihilation cross section $\langle \sigma_{\mathrm{A}} v \rangle$ or the decay rate Γ_{d} as functions of the WIMP mass. Below, a brief review of recent results is given in Sections 3.3.2, 3.3.3, and 3.3.4, following up on a description of current instruments of gamma-ray astronomy in Section 3.3.1. Details can be found in up-to-date reviews, e.g., Kuhlen (2010), Porter *et al.* (2011), Bringmann & Weniger (2012), or Strigari (2013).

3.3.1 Gamma-ray astronomy and instruments

The interplay between space-based and ground-based instruments of gamma-ray astronomy has pushed observations to offer unprecedented sensitivity in a broad energy range, down to ~ 20 MeV and up to ~ 100 TeV. The discovery of currently ~ 1 900 gamma-ray sources with *Fermi*-LAT in the GeV range (Nolan *et al.* 2012) and more than 100 TeV-sources with IACTs (Rieger *et al.* 2013) opened the opportunity of studying the non-thermal gamma-ray sky in remarkable detail.

The population of gamma-ray sources consists of both extragalactic and Galactic emitters. The major fraction (~ 1 000) of discovered GeV gamma-ray sources can be associated with active galactic nuclei (AGN) in cosmological distances, in particular with *blazars* (BL Lacs and flat spectrum radio quasars). Blazars provide a subclass of AGN, where the jet of relativistic plasma directly points in the direction to the observer.[4] Blazars contribute ~ 50% to the population of TeV emitters (Rieger *et al.* 2013). Apart from some other extragalactic emitters (e.g., starburst galaxies), the remaining source population divides into Galactic sources and objects of unknown origin (unassociated sources). Unassociated sources provide the second most of the GeV emitters (~ 600), while the TeVCat[5] catalog lists about 25 TeV-emitters of unknown origin. In distinction to AGN, which are distributed over the whole sky, Galactic gamma-ray sources align with the Galactic plane and mainly consist of supernova remnants, pulsar wind nebulae, gamma-ray pulsars (in the GeV range), compact binary systems, and others.

---

[3] The equivalent expression for decaying dark matter is given by substituting Eq. (3.1) with $\langle \sigma_{\mathrm{A}} v \rangle/(2m_{\mathrm{dm}}^2) \rightarrow \Gamma_{\mathrm{d}}/m_{\mathrm{dm}}$, where Γ_{d} denotes the decay rate, and $\rho^2[r(l)] \rightarrow \rho[r(l)]$. [4] In AGN, two oppositely directed jets are believed to be ejected by a system of a central supermassive black hole surrounded by an accretion disk. [5] `http://tevcat.uchicago.edu/`

Conventional gamma-ray sources are powered by charged light leptons (electrons) or hadrons (protons), which are stochastically accelerated up to highest (PeV) energies while crossing plasma shock fronts (Fermi 1949). Once a particle has crossed the termination shock, back scattering is facilitated by plasma magnetic fields. In a leptonic scenario, gamma-rays are produced by inverse-Compton scattering of accelerated electrons with target photon fields, while non-thermal radiation at lower energies results from synchrotron emission (e.g., Meyer, Horns & Zechlin, 2010). In hadronic scenarios, gamma-rays result from the decay of π^0-mesons produced in hadronic interactions of protons with ambient gas. In general, this leads to broad-band gamma-ray spectra, which can be locally approximated with power laws $\mathrm{d}\phi/\mathrm{d}E \propto E^{-\Gamma}$, where Γ denotes the photon index ($\Gamma > 0$ in this notation). See Horns (2008) and Rieger *et al.* (2013) for recent reviews.

The Earth's atmosphere is opaque to gamma-rays, thus requiring space-based instruments for their direct detection. Launched in June 2008, the Large Area Telescope (LAT) aboard the *Fermi* satellite (Atwood *et al.* 2009) provides the currently most sensitive instrument in the energy range between ∼20 MeV and more than 300 GeV. Observations with *Fermi*-LAT are complemented by AGILE (Tavani *et al.* 2008), which was launched in 2007. The *Fermi*-LAT is an imaging pair-conversion telescope with a wide field of view (FoV) of $\sim 2.4\,\mathrm{sr}$. Its effective area is however limited to $\sim 0.8\,\mathrm{m}^2$, due to restricted capacities of satellites. A sketch of the LAT is presented in Fig. 3.2a: The telescope consists of a 4×4 array of 16 precision tracker modules, each of them mounted on top of an electromagnetic calorimeter. Each tracker module comprises 16 planes of high-Z converter material (tungsten), where gamma-ray photons hitting the LAT can convert to e^+e^- pairs. The direction of incident gamma-rays can be reconstructed from the corresponding $e^\pm$ tracks, measured with position-sensitive single-sided silicon strip detectors, which interleave the converter planes (see Fig. 3.2b for details). This setup thus determines the point-spread function (PSF) of the LAT, which is very broad to low energies but approaches a value below $\sigma_{\mathrm{psf}} \approx 0.15^\circ$ for photon energies above ∼30 GeV (see Section 6 in Ackermann *et al.* 2012c). The primary photon energy can be reconstructed from the energy deposition of the electromagnetic showers evolving in the calorimeter. Each calorimeter consists of layers of 96 CsI(Tl) crystals, comprising a vertical depth of 8.6 radiation lengths[6], and allows energy measurements up to ∼ 1 TeV. The corresponding energy resolution is between 8% and 15% (see Section 7 in Ackermann *et al.* 2012c). The total array of trackers and calorimeters is covered with a segmented anti-coincidence detector to reject charged-particle background. *Fermi* usually operates in survey mode, i.e., the *Fermi*-LAT reaches an almost uniform all-sky exposure after ∼ 3 h (corresponding to two orbits). The sensitivity of the instrument for detecting point-like gamma-ray sources is shown in Fig. 3.3a. The integrated sensitivity improves to higher energy thresholds, approaching a value of $\sim 2 \times 10^{-10}\,\mathrm{cm}^{-2}\,\mathrm{s}^{-1}$ for energies above 10 GeV and a survey exposure of one year.

Due to power-law-shaped spectra, the flux from gamma-ray sources quickly drops with increasing energy. A detection of gamma-rays in the VHE band requires instruments with large effective detection areas, which cannot be mounted in space. However, gamma-rays with energies above ∼ 10 GeV can be indirectly detected through particle showers induced by their atmospheric absorption (in heights between 10 km and 20 km), i.e., e^+e^- pair-production in the electromagnetic field of atmospheric nuclei (essentially nitrogen and oxygen). The resulting electromagnetic showers of highly relativistic electrons can ei-

---

[6] The total system of tracker and calorimeter has a depth of 10.1 radiation lengths.

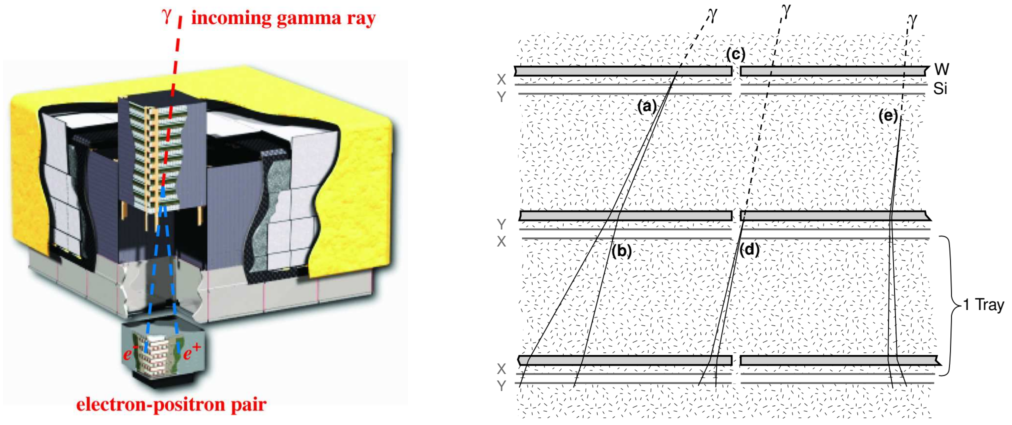

(a) (b)

Figure 3.2: **(a)**: Sketch of the *Fermi*-LAT. The scheme focusses on one of the tracker and calorimeter units. The dimensions of the total system are 1.8 m × 1.8 m × 0.72 m. From Atwood *et al.* (2009). **(b)**: Schematic principles of the tracker system as explained in the text. The bracketed letters refer to different conversion situations. See Atwood *et al.* (2009) for details.

ther be directly detected with ground-based scintillation techniques (EAS arrays) or by short (∼10 ns) pulses of emitted Cherenkov light. The light emission allows us to image the air shower with ground-based imaging atmospheric Cherenkov telescopes (IACTs), that are usually equipped with a segmented primary mirror of ∼ 10 m in diameter. Small arrays of (e.g., four) identical telescopes separated by ∼ 100 m allow stereoscopic reconstruction of the primary gamma-ray direction from shower images obtained under different viewing angles (Aharonian *et al.* 2006c). The images are recorded with fast optical cameras consisting of an array ∼ 1 000 photo-multiplier tubes. The total number of detected Cherenkov photons is related to the energy of the primary photon. Complementing *Fermi*-LAT, IACTs extend the energy range of observable gamma rays to the interval between ∼ 50 GeV and ∼ 100 TeV. IACTs offer large energy-dependent effective detection areas up to $10^5\,\mathrm{m}^2$, but their small FoV of ∼ 5° in diameter in combination with short duty cycles of ∼1 000 h of observation time per year restrict them to dedicated pointed observations. Their energy resolution between 15% and 20% and spatial resolution of ∼ 0.1° are comparable to *Fermi*-LAT. IACTs suffer a dominating background of hadronic showers induced by cosmic rays. However, the shape of the recorded shower image enables separation between hadronic and electromagnetic showers (gamma-hadron separation). With IACTs, a point-like source with an integrated flux of 1% of the Crab Nebula's VHE flux can be detected in ∼ 25 h. In Fig. 3.3b, the differential flux sensitivities of current and planned IACTs are compared to the sensitivity of *Fermi*-LAT. See Horns (2008) and Rieger *et al.* (2013) for further details.

Currently operating IACTs are H.E.S.S. (Aharonian *et al.* 2006c), located in the southern hemisphere in Namibia, Africa (23°16′18″S, 16°30′00″E), while the northern hemisphere is covered by MAGIC-II (Albert *et al.* 2008b; Tridon *et al.* 2010) on the Canary island of La Palma, and VERITAS (Aliu *et al.* 2011) in southern Arizona, USA. Very recently, the H.E.S.S. array has been extended with a much larger fifth telescope (H.E.S.S.-II, see Fig. 1.1; Vincent 2005, Becherini & Punch 2012), reducing the energy threshold to

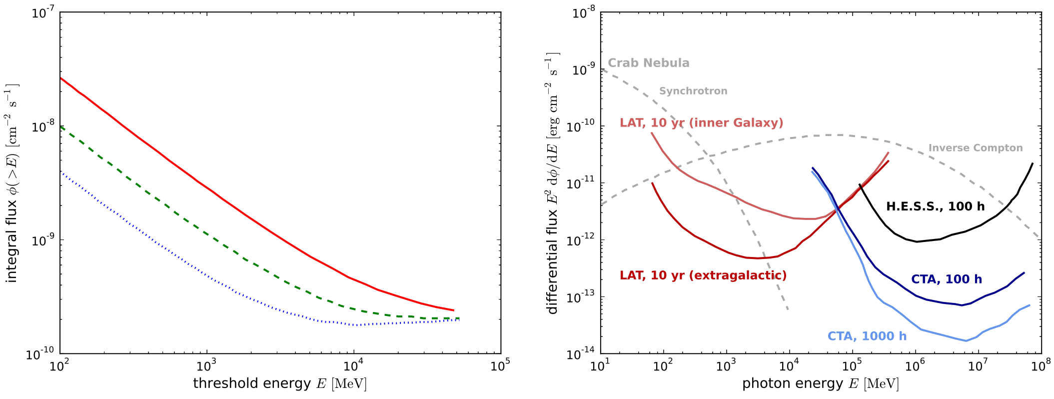

(a) **(b)**

Figure 3.3: **(a)**: Integrated sensitivity of *Fermi*-LAT for a 5σ detection of a point source (power-law index $\Gamma = 2.0$) with one-year sky survey exposure. The three curves correspond to different (uniform) background values, resembling typical diffuse backgrounds at high galactic latitudes (dotted blue line), intermediate latitudes (dashed green line), and on the Galactic plane (solid red line). Adapted from Atwood *et al.* (2009). **(b)**: Differential sensitivity curves for a significance threshold of 5σ in each bin for feasible observations with *Fermi*-LAT, H.E.S.S., and CTA. The two curves for *Fermi*-LAT correspond to typical backgrounds in the inner Galaxy and at high galactic latitudes. For comparison, the gamma-ray spectrum of the Crab Nebula is shown. Adapted from Funk & Hinton (2013).

~50 GeV. In the near future, the sensitivity of IACTs will be significantly improved with the planned Cherenkov Telescope Array (CTA, see Fig. 1.1; Actis *et al.* 2011, The CTA Consortium 2013). CTA will profit from the combination of different types of Cherenkov telescopes in one array, i.e., large-scale telescopes, reducing the energy threshold, and widely separated small-scale telescopes, improving the sensitivity to high energies. The array will consist of up to 80 telescopes.

Monitoring of VHE sources and an extension of the sensitivity to even higher energies can be achieved with extensive air-shower (EAS) arrays, offering large FoVs. Among current instruments are MILAGRO (Atkins *et al.* 2004) and TIBET-III (Amenomori *et al.* 2009), while the newly built HAWC (Abeysekara *et al.* 2012) will enter data-taking phase soon. Unique sensitivity in the energy range between ~10 TeV and several PeV will be provided by the planned HiSCORE (Tluczykont *et al.* 2011, 2012, 2013) and the planned LHAASO arrays (Zha & LHAASO Collaboration 2012) in the near future.

3.3.2 Indirect detection with gamma rays

The distinctive central density peak of the large spatially extended dark matter halos manifests secondary gamma-ray emission from dark matter annihilation in point or moderately extended sources with a characteristic gamma-ray spectrum. Dark matter annihilation in the overall halo also gives rise to diffuse gamma-ray background emission. The complementary energy coverage and FoV of *Fermi*-LAT and modern IACTs permit the search for WIMPs in the mass range between ~10 GeV and ~10 TeV. In the following, various different astrophysical targets for indirect dark matter searches are discussed.

Galactic Center. The anticipated high dark matter density and its proximity to the Solar system make the Galactic Center (GC) one of the prime targets for indirect dark matter searches. The gamma-ray emission of the GC has been well measured with *Fermi*-LAT and IACTs (see Chernyakova *et al.* 2011 and references therein), enabling us to search and constrain dark matter annihilation in this region (Horns 2005; Aharonian *et al.* 2006b; Morselli *et al.* 2010; Hooper & Linden 2011; Linden & Profumo 2012). However, the GC gamma-ray spectrum is dominated by the point source HESS J1745–290 (Aharonian *et al.* 2004, confirmed by MAGIC (Albert *et al.* 2006) and *Fermi*-LAT) and by diffuse foreground emission of secondary gamma-rays from inelastic cosmic-ray interactions with interstellar H I and molecular clouds. Even after careful subtraction of these components (Aharonian *et al.* 2006a; Porter *et al.* 2008), large systematic uncertainties on all components make the extraction of a dark matter signal difficult. However, model uncertainties can be heavily reduced using observations of a nearby region, i.e., the field between annuli with angles of 0.3 deg and 1.0 deg from the nominal GC position (Abramowski *et al.* 2011c). Fig. 3.4c shows the resulting limits on $\langle\sigma_A v\rangle$ derived from VHE observations with H.E.S.S. These bounds are among the most constraining and most robust upper limits obtained with IACT observations so far.

Much harder to mimic by conventional astrophysical processes are gamma-ray lines (Aharonian *et al.* 2012). Vertongen & Weniger (2011) as well as the *Fermi*-LAT Collaboration (Ackermann *et al.* 2012a) published upper limits on gamma-ray line emission from the Galaxy, that have been extended by the H.E.S.S. Collaboration (Abramowski *et al.* 2013) to higher energies (see Fig. 3.4d). Recently, Bringmann *et al.* (2012) and Weniger (2012) found evidence for a line-like feature with an energy at ∼130 GeV in the region around the GC. A variety of follow-up studies have investigated the details and possible systematics of this gamma-ray line (e.g., Su & Finkbeiner 2012a,b; Tempel *et al.* 2012; Hektor *et al.* 2012, 2013; Hooper & Linden 2012; Mirabal 2013; Finkbeiner *et al.* 2013; Ackermann *et al.* 2013), which may point to the long-sought dark matter signal. In conclusion, its reality and origin are still under debate and have to be investigated both by longer *Fermi*-LAT observations and complementary instruments. Here, the recently inaugurated H.E.S.S.-II array serves as a promising opportunity (Bergström *et al.* 2012).

Dwarf spheroidal galaxies, globular clusters, and galaxy clusters. With high mass-to-light ratios (see Section 2.2.1), strict constraints on star formation (Grcevich & Putman 2009, 2010), and a relatively low distance, dSph galaxies contribute a highly promising class of targets with almost no astrophysical background emission. Additionally, the uncertainties on their dark matter profile are sufficiently low to provide a reliable base for the interpretation of the gamma-ray measurements (cf. Strigari 2013). *Fermi*-LAT observations of individual dSphs combined with a joint likelihood stacking of all dSph data provide the currently best constraints on dark matter annihilation for WIMP masses below a few hundred GeV, see Fig. 3.4b (Ackermann *et al.* 2011; Geringer-Sameth & Koushiappas 2011). For WIMPs lighter than ∼30 GeV, the constraints fall below the relic-density constraint of $3 \times 10^{-26}\,\mathrm{cm}^3\,\mathrm{s}^{-1}$. Recently, Geringer-Sameth & Koushiappas (2012) also published upper limits on gamma-ray lines from *Fermi*-LAT observations of dSphs. To constrain higher dark matter masses, dSphs have been observed with IACTs, see Aharonian *et al.* (2008b, 2009a, 2010); Abramowski *et al.* (2011a); Albert *et al.* (2008a); Aliu *et al.* (2009); Aleksić *et al.* (2011); Acciari *et al.* (2010), providing $\langle\sigma_A v\rangle$ constraints as low as a few times $10^{-24}\,\mathrm{cm}^3\,\mathrm{s}^{-1}$ (Aliu *et al.* 2012). Other observations of potentially dark matter

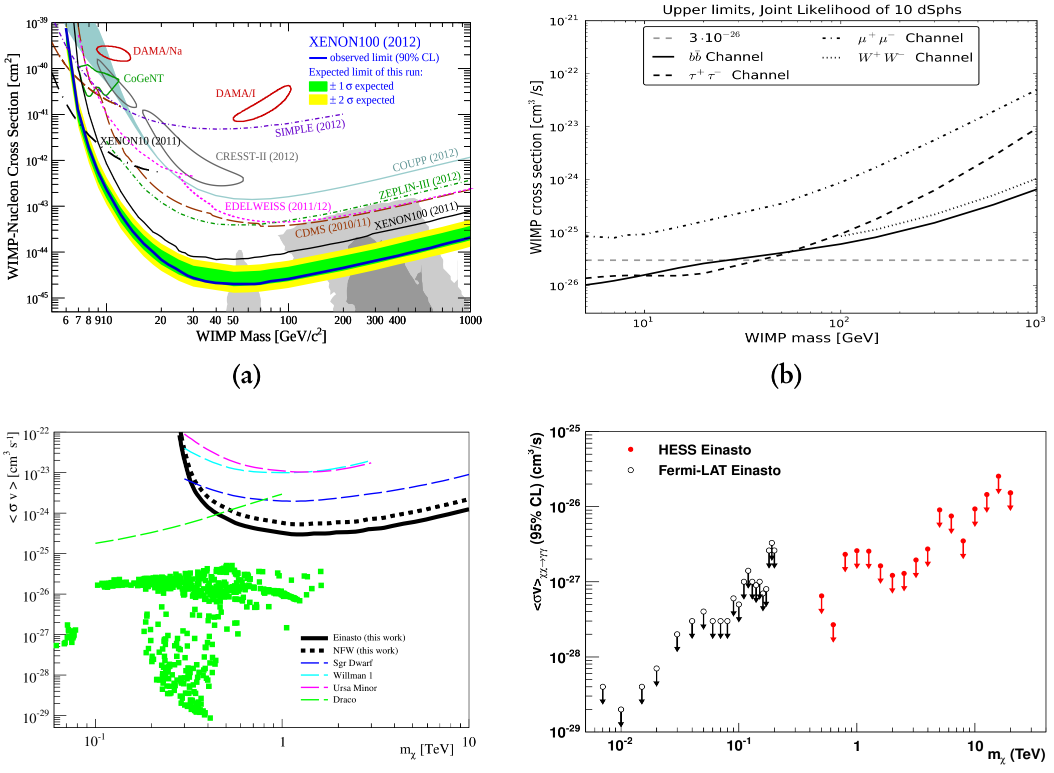

(a) (b)

(c) (d)

Figure 3.4: **(a)**: Detection claims and upper bounds on the spin-independent WIMP-nucleon scattering cross section from various experiments, in comparison to regions preferred by SUSY models ($1\sigma/2\sigma$, dark/light gray). In particular, the solid blue line shows the upper bound (90% CL) from XENON100. See Aprile *et al.* (2012) for details. **(b)**: Upper limits (95% CL) on $\langle\sigma_{\mathrm{A}} v\rangle$ as derived from the likelihood stacking of 10 dSphs observed with *Fermi*-LAT. Limits are given for different annihilation channels. From Ackermann *et al.* (2011). **(c)**: Upper limits (95% CL) on $\langle\sigma_{\mathrm{A}} v\rangle$ as function of the WIMP mass m_χ derived from H.E.S.S. data of the GC halo (for annihilation in quark pairs). The dark matter halo of the Milky Way was modeled with an Einasto and NFW profile, demonstrating a negligible impact of the profile modeling on the analysis of an annular region around the GC. The figure also depicts current VHE limits obtained from dSph galaxies. The green points show a scan of viable mSUGRA models, which are consistent with CMB and collider constraints. From Abramowski *et al.* (2011c). **(d)**: Upper limits (95% CL) on $B_\gamma \times \langle\sigma_{\mathrm{A}} v\rangle$ for direct annihilation into two photons $[\mathrm{d}N_\gamma/\mathrm{d}E = 2\delta(E - m_\chi)]$ as function of m_χ. Limits obtained from *Fermi*-LAT data are plotted with black open points, while the H.E.S.S. limits are marked with red filled circles. An Einasto profile was used for the dark matter distribution of the Milky Way. From Abramowski *et al.* (2013).

dominated targets include globular clusters (Abramowski *et al.* 2011b) and galaxy clusters (Aleksić *et al.* 2010; Ackermann *et al.* 2010a).

Targets addressed in this thesis. Nearby Galactic DM subhalos imply significant dark matter overdensities and should be visible as point or slightly extended gamma-ray sources, given common dark matter annihilation models. The motivations for observational subhalo searches are then two-fold, i.e., probing the ΛCDM scenario and testing for dark matter annihilation products. Within the framework of this thesis, this topic is investigated in Chapter 4.

Moreover, the dissection of the diffuse Galactic and extragalactic gamma-ray emission provides a promising alternative to search for clues on dark matter annihilation or decay. In principle, two different methods have been considered in the literature: one resolving individual components of the total diffuse flux, while the other relies on the specific imprint of the dark matter signal in the power spectrum of spatial anisotropies in the photon arrival directions. With the former approach, current analyses have a sensitivity of a few times $10^{-25}\,\mathrm{cm}^3\,\mathrm{s}^{-1}$ for a 100 GeV WIMP annihilating to $b\overline{b}$ (Abdo *et al.* 2009a, 2010a; Abazajian *et al.* 2010; Cirelli *et al.* 2010; Papucci & Strumia 2010; Calore *et al.* 2013). In the framework of this thesis, the latter approach is discussed in Chapter 5.

3.3.3 Indirect detection with neutrinos

Large-volume neutrino detectors such as IceCube and Super-Kamiokande offer the possibility of searching for neutrino emission from dark matter. The IceCube Collaboration reported limits from observations of the diffuse Galactic halo and the GC (Abbasi *et al.* 2011, 2012b) at the level of $\langle\sigma_\mathrm{A} v\rangle \approx 10^{-22}\,\mathrm{cm}^3\,\mathrm{s}^{-1}$ (for annihilation into $\nu\overline{\nu}$ and $200\,\mathrm{GeV} \lesssim m_\mathrm{dm} \lesssim 10\,\mathrm{TeV}$).

3.3.4 Indirect detection with electrons, anti-protons, and anti-deuterium

Relativistic electrons and positrons give rise to synchrotron emission at radio frequencies when propagating through ambient magnetic fields. The presence of considerable interstellar radiation fields would also lead to inverse-Compton emission in the X-ray regime. Strong constraints on $\langle\sigma_\mathrm{A} v\rangle$ have been derived from GC and Galactic diffuse radio emission (e.g., Regis & Ullio 2008; Bergström *et al.* 2009; Borriello *et al.* 2009; Hooper *et al.* 2012; Fornengo *et al.* 2012a,b; Laha *et al.* 2013), while dSph galaxies approve as promising targets as well (Colafrancesco *et al.* 2006, 2007; Jeltema & Profumo 2012; Spekkens *et al.* 2013). Likewise, dark matter annihilation has been invoked to explain the WMAP haze (Finkbeiner 2004) with its corresponding gamma-ray counterpart, the *Fermi* haze (Dobler *et al.* 2010), see, e.g., Hooper *et al.* (2007), Carlson *et al.* (2013), and Hooper & Slatyer (2013).

Dark matter might imprint in the direct cosmic-ray electron (CRE) flux. In particular, measurements of the CRE spectrum with the balloon-borne instruments ATIC (Chang *et al.* 2008) and PPB-BETS (Torii *et al.* 2008), the space-borne *Fermi*-LAT (Abdo *et al.* 2009c; Ackermann *et al.* 2010b,c), and the IACT systems H.E.S.S. (Aharonian *et al.* 2008a, 2009b) and MAGIC (Borla Tridon *et al.* 2011) revealed an unexpectedly hard electron-positron flux at energies above ∼20 GeV, with a significant steepening above 1 TeV. In addition, PAMELA (Adriani *et al.* 2009, 2011), *Fermi*-LAT (Ackermann *et al.* 2012b), and AMS-02 (Aguilar *et al.* 2013) have measured an increase in the positron fraction $\phi(e^+)/[\phi(e^-)+\phi(e^+)]$ between several GeV and ∼350 GeV. A diffuse CRE flux is produced by Galactic supernova remnants with additional contributions from secondary electrons from inelastic cosmic-ray collisions with the interstellar medium. The most natural explanation of the hard CRE spectrum and the rising positron fraction is given by one or more local (within 1 kpc) astrophysical electron-positron emitters (with distinct cutoffs to TeV energies) on top of the diffuse background emission (Grasso *et al.* 2009; di Bernardo *et al.* 2011). Such sources are naturally provided by local middle-aged ($\tau \approx 10^5$ yr) pulsars such as Monogem and Geminga. However, another viable scenario might be dark matter annihilation, and both the smooth Galactic halo (Grasso *et al.* 2009; Meade *et al.* 2010) and nearby DM subhalos (see Brun *et al.* 2009 and Chapter 4) have been considered as possibilities. Although large boost factors have to be invoked, these scenarios remain of general interest.[7]

Efficient constraints on dark matter setups can also be deduced from the anti-proton flux (see Bringmann & Salati 2007, Donato *et al.* 2009, and references therein). However, a discrimination between dark matter candidates might be hard to achieve with antiprotons. A very low astrophysical background is also anticipated for anti-deuterium, which might therefore provide a promising alternative to detect particle dark matter with AMS-02 (Ibarra & Wild 2013).

---

[7] The different hypotheses on the origin of CREs can be discriminated combining future measurements of the slope of the positron fraction at high energies and the measurement of spatial anisotropies in the arrival directions of CREs (Ackermann *et al.* 2010c; di Bernardo *et al.* 2011). The release of new AMS-02 data in the near future might have significant impact on this topic (e.g., Hooper & Xue 2013).

Chapter 4

The Indirect Search for Dark Matter Subhalos

In Chapter 2 it is demonstrated that the scenario of hierarchical structure formation in a ΛCDM universe requires the presence of DM subhalos on sub-galactic scales. The main part of this thesis is dedicated to the investigation of the gamma-ray and multi-wavelength properties of small-scale DM subhalos for self-annihilating dark matter scenarios. The study motivated the development of a new method of searching for DM subhalos, leading to in-depth searches for gamma-ray candidates and their interpretation. The results have been published in two peer-reviewed journal articles, which are presented in Sections 4.1 and 4.2.

Prior to the work on Publication I, detector simulations on the prospects of *Fermi*-LAT for detecting DM subhalos have been carried out in collaboration with S. Januschek in her diploma thesis (Januschek 2010). The diploma thesis was prepared under my co-supervision.

4.1 Publication I

The publisher's version of Publication I (Zechlin *et al.* 2012) is presented below. The publication also contains archival ROSAT data that were analyzed by K. Borm in her bachelor's thesis, which was prepared under my co-supervision (Borm 2010). The publication was accompanied by a proposal for X-ray observations of 1FGL J0030.7+0724 with *Swift*-XRT, which is presented in Appendix C.1.

Parts of the publication have also been published as conference proceeding to the *3rd Fermi Symposium, Rome, Italy, May 09-12, 2011*, see Zechlin *et al.* (2011).

My contributions. The initial idea for Publication I was created by both my supervisor D. Horns and myself. I developed most parts of this publication: the phenomenological modeling of DM subhalos, the extraction of their relevant gamma-ray characteristics, the sensitivity study, and the design of the method to search for them. I developed and conducted all catalog searches, simulations, and data analyses (except for the analysis of the raw gamma-ray data resulting in Table 5 and 6), and most of the interpretation. The manuscript was written mainly by myself and I prepared all figures.

Publication I

Dark matter subhaloes as gamma-ray sources
and candidates in the first Fermi-LAT catalogue

H.-S. Zechlin, M. V. Fernandes, D. Elsässer, and D. Horns

Astronomy & Astrophysics **538**, A93 (2012)

A&A 538, A93 (2012)
DOI: 10.1051/0004-6361/201117655

Astronomy & Astrophysics

Dark matter subhaloes as gamma-ray sources and candidates in the first *Fermi*-LAT catalogue

H.-S. Zechlin[1], M. V. Fernandes[1], D. Elsässer[2], and D. Horns[1]

[1] University of Hamburg, Institut für Experimentalphysik, Luruper Chaussee 149, 22761 Hamburg, Germany
e-mail: `hzechlin@physik.uni-hamburg.de`
[2] University of Würzburg, Institut für Theoretische Physik und Astrophysik, Am Hubland, 97074 Würzburg, Germany

Received 7 July 2011 / Accepted 3 November 2011

ABSTRACT

The standard paradigm of hierarchical structure formation in a ΛCDM universe predicts the presence of dark matter subhaloes, hosted by Milky Way-sized galaxies. Anticipated subhalo masses range from 10^{10} down to a cut-off mass between 10^{-3} and $10^{-11}\,M_\odot$. If dark matter is composed of heavy self-annihilating or decaying particles, these subhaloes could be visible in the γ-ray band as faint and temporally constant sources without astrophysical counterparts. Based upon realistic subhalo models and current observational constraints on annihilating dark matter scenarios, we predict that one massive Galactic subhalo between 10^6 and $10^8\,M_\odot$ may already be present in the 11-month catalogue of *Fermi*-LAT. Indeed, at least twelve objects in the first *Fermi* catalogue qualify as candidates. The most promising object, 1FGL J0030.7+0724, is investigated in detail using a dedicated *Swift* X-ray follow-up observation and a refined positional analysis of the 24-month *Fermi*-LAT data. With the new observations, seven point-like X-ray sources have been discovered, of which SWIFT J003119.8+072454, which coincides with a faint radio source (12 mJy at 1.4 GHz), serves as a counterpart candidate of 1FGL J0030.7+0724. The broad-band spectral energy distribution is consistent with a high-energy-peaked blazar. However, flux and extent of 1FGL J0030.7+0724 may also be compatible with a dark matter subhalo. Detection of temporal variability or improved astrometry of 1FGL J0030.7+0724 are necessary to rule out or confirm an astrophysical origin. We discuss strategies to identify γ-ray sources that are associated with self-annihilating dark matter subhaloes.

Key words. dark matter – Galaxy: halo – Galaxy: structure – gamma rays: general

1. Introduction

Several astrophysical observations indicate that in the early as well as in the present Universe a non-baryonic form of dark matter (DM) prevails over the baryonic matter content. Structure formation favours a cold dark matter (CDM) scenario (for recent reviews see, e.g., Bertone et al. 2005; D'Amico et al. 2009; Bertone 2010). However, the nature of DM remains unknown. A class of promising candidates for CDM are stable, weakly interacting, massive particles (WIMPs) with masses between 10 and 10^5 GeV, predicted by theories that extend the standard model of particle physics. The most prominent extensions encompass those based on supersymmetry and universal extradimensions, which were invented to solve inconsistencies of the standard model at high energy scales [$\mathcal{O}$(TeV)], and which deliver adequate DM candidates in this way. These particles can self-annihilate or decay, producing detectable signatures in the final states such as energetic photons (γ rays), antimatter, and leptons.

Unravelling the nature of DM remains a challenging problem for astronomy and particle physics, and a variety of attempts to detect signals have been made, using both direct and indirect detection techniques. For instance, multi-wavelength observations of astrophysical targets have constrained the self-annihilation rate of DM, which is related to the thermally averaged annihilation cross section. In particular, regions with high DM densities such as the Galactic Centre (Aharonian et al. 2006a,b; Morselli et al. 2010; Abramowski et al. 2011b), Galactic Ridge (Aharonian et al. 2006d), dwarf spheroidal galaxies (dSphs; Colafrancesco et al. 2007; Albert et al. 2008b; Aharonian et al. 2008, 2009; Aliu et al. 2009; Aharonian et al. 2010; Abdo et al. 2010c; Acciari et al. 2010; Aleksić et al. 2011, H.E.S.S. Collaboration 2011), as well as globular (Colafrancesco et al. 2006; Wagner 2009; Abramowski et al. 2011a) and galaxy clusters (Aleksić et al. 2010; Ackermann et al. 2010) serve as excellent targets. Furthermore, DM annihilation in the entire Galactic halo as well as its subhalo population produces a diffuse γ-ray flux, which contributes to the overall diffuse signal of the Galaxy. Comparatively stringent upper limits on the annihilation cross section have been obtained from the combination of both dedicated observations and bounds obtained from the diffuse γ-ray flux (Abazajian et al. 2010; Cirelli et al. 2010; Meade et al. 2010; Papucci & Strumia 2010; Zaharijas et al. 2010).

Based on the theory of hierarchical structure formation, DM haloes of Milky Way-sized galaxies are anticipated to host numerous DM subhaloes with masses between a cut-off scale 10^{-11}–10^{-3} and $10^{10}\,M_\odot$ (e.g., Bringmann 2009), where $M_\odot$ denotes the solar mass. This expectation is a consequence of the early collapse of overdensities in the expanding Universe (Diemand et al. 2005), leading to the formation of initially low-mass haloes, which subsequently serve as building-blocks for larger haloes by merging at later times. Besides analytical calculations (e.g., Berezinsky et al. 2003, 2006, 2008), recent numerical high-resolution N-body simulations of structure formation in a ΛCDM cosmology (Komatsu et al. 2011), such as the Aquarius Project (Springel et al. 2008a,b) or the Via Lactea II simulation (Diemand et al. 2008b; Zemp et al. 2009), allow us to study substructures in detail. For a Milky Way-type galaxy, these simulations predict a large number of subhaloes (up to 10^{16}) with masses distributed following a power law, $\mathrm{d}N/\mathrm{d}M \propto M^{-\alpha}$, where $\alpha \in [1.9; 2.0]$. The DM density profiles of large-mass subhaloes are found to be similar to the host's, which results in high central densities (Springel et al. 2008a). The spatial distribution of subhaloes is "anti-biased", i.e., the dominant fraction is placed far away from the host-halo's centre.

In self-annihilating DM scenarios, subhaloes are expected to appear as weak point-like or moderately extended γ-ray sources, and a small fraction of them could be detectable with current high- or very high-energy (VHE) γ-ray telescopes (e.g., Pieri et al. 2005, 2008, 2011; Springel et al. 2008b; Kuhlen et al. 2008; Ando 2009; Buckley & Hooper 2010; Brun et al. 2011; Zechlin et al. 2011). Examples for currently operating telescopes are the *Fermi*-LAT (20 MeV−300 GeV, Atwood et al. 2009) and imaging air Cherenkov telescopes (IACTs; $E \gtrsim 100\,\mathrm{GeV}$) such as H.E.S.S. (Aharonian et al. 2006c), MAGIC (Albert et al. 2008a; Tridon et al. 2010), and VERITAS (Weekes et al. 2002). In the near future, a significant improvement in the overall sensitivity and lower energy threshold will be achieved by upcoming experiments such as H.E.S.S.-II (Vincent 2005) and CTA (Hermann 2010; the CTA consortium 2010; Doro 2011). Such instruments are possibly sufficiently sensitive to detect nearby large-mass subhaloes of $\mathcal{O}(10^6)\,M_\odot$ within distances of $\mathcal{O}(1)$ kpc.

This paper consists of two separate parts, which can in principle be read independently. The first part (Sects. 2 to 4) investigates the detectability of subhaloes with *Fermi*-LAT, where the basic framework for predicting the γ-ray properties of subhaloes is laid out in Sects. 2 and 3. In Sect. 4, properties of detectable subhaloes are investigated by means of a fiducial source. In the second part, Sect. 5 discusses the search for DM subhaloes in the first *Fermi*-LAT point-source catalogue (1FGL) and subsequent multi-wavelength studies of the most promising candidate, 1FGL J0030.7+0724. A discussion of the physical origin of 1FGL J0030.7+0724 and prospects for IACTs are presented in Sect. 6.

Throughout this paper, Hubble's constant is $H_0 = 73\,\mathrm{km\,s^{-1}\,Mpc^{-1}}$, yielding the present value of the Universe's critical density $\rho_\mathrm{crit} = 3H_0^2/(8\pi G_\mathrm{N}) \simeq 1.48 \times 10^{11}\,M_\odot\,\mathrm{Mpc^{-3}}$, where G_N denotes Newton's gravitational constant (e.g., Spergel et al. 2007).

2. Gamma rays from DM subhaloes

In the following, the γ-ray flux from DM subhaloes will be derived, based upon current theoretical models of the corresponding radial density distribution.

With respect to undisturbed, isolated galactic haloes, henceforth field haloes, the general formation history of (embedded) subhaloes differs significantly. Analytical models and numerical N-body simulations of structure formation found their physical properties to depend on particular evolutionary conditions, i.e., formation time, evolution, and orbit (see Diemand et al. 2007, 2008a, and references therein). Tidal interaction with the gravitational potential of the host halo leads to tidal stripping and heating, and can therefore truncate the outer region of subhaloes. In the following, two different approaches will be discussed. On the one hand, subhaloes are modelled assuming negligible tidal effects and are therefore considered to be in a genuine virialised state. Because this approximation is (at least) valid for field haloes, this model will be tagged as *field-halo model* (FHM). On the other hand, a second and more realistic model is considered to account for subhalo evolution, henceforth referred to as *subhalo model* (SHM).

2.1. Density profile

The subhalo's DM density profile $\rho(r)$ is assumed to follow

$$\rho(r) = \frac{\rho_\mathrm{s}}{(r/r_\mathrm{s})^\gamma\,(1+r/r_\mathrm{s})^2} \begin{cases} 1 & \text{for } r \le r_\mathrm{cut}, \\ 0 & \text{for } r > r_\mathrm{cut}, \end{cases} \qquad (1)$$

where r denotes the distance to the subhalo's centre. In general, the profile cuts at an outer radius r_cut, which is the virial or tidal radius (R_vir or R_t), respectively. Given $\gamma = 1.0$ for the remainder, the profile follows the universal spherically symmetric Navarro-Frenk-White (NFW) profile, well-fitting haloes resolved in numerical simulations[1] (Navarro et al. 1997). The profile is defined by two parameters: a characteristic inner radius r_s, where the effective logarithmic slope of the profile is −2, and an inner density $\rho_\mathrm{s} = 4\rho(r_\mathrm{s})$. In case of FHM haloes, which are not subject to tides, both parameters are related to each other by the virial halo mass M_vir. This quantity is defined as the mass inside the sphere of radius R_vir, which encloses a mean density of Δ_c times the critical density of the Universe at the considered redshift z (Navarro et al. 1997; Bullock et al. 2001), $M_\mathrm{vir} := 4\pi/3\,\Delta_\mathrm{c}\rho_\mathrm{crit}R_\mathrm{vir}^3$. The virial overdensity at $z = 0$ is $\Delta_\mathrm{c} \approx 100$, as suggested by models of the dissipationless spherical top-hat collapse (Eke et al. 1996; Bryan & Norman 1998) and assuming present concordance cosmology. In general, the subhalo mass M is given by a volume integration of Eq. (1), revealing $M = 4\pi\rho_\mathrm{s}r_\mathrm{s}^3 f(c)$, where $f(c) \equiv \ln(1+c) - c/(1+c)$ and c denotes the concentration parameter of the subhalo. For non-disturbed haloes, the concentration is then given by the virial concentration $c_\mathrm{vir} \equiv R_\mathrm{vir}/r_\mathrm{s}$. Generally, the concentration depends on the subhalo mass and redshift, $c = c(M, z)$, where lighter haloes have higher concentrations (Navarro et al. 1996, 1997; Bullock et al. 2001). Since observational estimates are lacking (see Sect. 2.2.1 in Lavalle et al. 2008, and references therein), $c(M)$ is adopted from N-body simulations. For the FHM, the toy model of Bullock et al. (2001)[2] is used, where the halo's (average) virial concentration at redshift z is connected with the density of the Universe at the halo's (mass-dependent) collapse redshift $z_\mathrm{c}(M)$, $c_\mathrm{vir} = K(1+z_\mathrm{c})/(1+z)$. The contraction parameter K is constant and independent of cosmology. To determine the mass dependence of z_c and, therefore, of c_vir at $z = 0$, the low-mass extrapolation of the Bullock model by Lavalle et al. (2008) is adapted. Because c_vir implicitly depends on Δ_c (see also Sect. 2.2), a conversion of c_vir to $\Delta_\mathrm{c} = 100$ was applied[3] with the relation of Hu & Kravtsov (2003). The concentration-to-mass relation is well-fitted by the polynomial form

$$\ln(c_\mathrm{vir}^\mathrm{FHM}) = \sum_{i=0}^{4} c_i^\mathrm{FHM} \times \left[\ln\left(\frac{M}{M_\odot}\right)\right]^i, \qquad (2)$$

$c_i^\mathrm{FHM} = \{4.265, -0.0384, -3.91\times10^{-4}, -2.2\times10^{-6}, -5.5\times10^{-7}\}$. Note that this model almost equals the relation derived by Pieri et al. (2011) for a cosmology as used in the Aquarius simulation. Regarding the concentration of SHM haloes, the low-mass extrapolation of the Bullock model provides a conservative estimate (cf., Pieri et al. 2008).

---

[1] Note that details on the very inner slope of halo profiles remain to be clarified, by simulations as well as observationally (e.g., Walker et al. 2011; Salucci et al. 2007).

[2] This model extends a proposal by Navarro et al. (1997).

[3] Lavalle et al. chose $\Delta_\mathrm{c} = 81.6$.

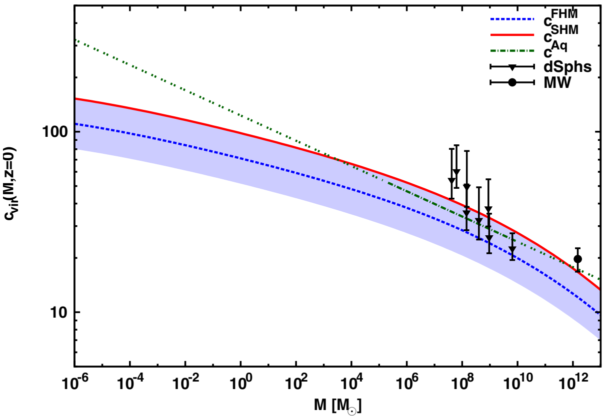

Fig. 1. Concentration-to-mass relation for subhaloes at $z = 0$. The dashed blue line depicts the concentration predicted by the Bullock model (FHM), while its corresponding scatter is given by the blue-shaded area. The mean concentration corrected for subhalo evolution (SHM) is shown by the solid red line for a galactocentric distance of 74 kpc, the average distance of the dSph galaxies included from Abdo et al. (2010c) (black triangles). For comparison, the concentration derived for Aquarius subhaloes is indicated by the dot-dashed dark green line within its validity range, the low/high-mass extrapolation by the double-dotted green line. The black filled circle marks the virial concentration of the MW.

However, because subhalo formation differs from that of field haloes and includes tidal truncation at R_t, the virial concentration is not well defined for subhaloes[4] (Diemand et al. 2007). Therefore, the SHM incorporates an empirical correction of c_{vir}. Indicated by numerical simulations, the concentration of subhaloes increases with decreasing distance to the host's centre D_{gc},

$$c_{vir}^{SHM}(M, D_{gc}) = c_{vir}^{FHM}(M)\left(\frac{D_{gc}}{R_{vir}^{MW}}\right)^{-\alpha_D}, \tag{3}$$

see Diemand et al. (2007, 2008a) and Kuhlen et al. (2008). The galactocentric distance is $D_{gc} = (R_0^2 + D^2 - 2R_0 D \cos l \cos b)^{1/2}$, where D denotes the subhalo's distance to the Sun, (l, b) its position in galactic coordinates, and $R_0 = (8.28 \pm 0.29)$ kpc the Sun's distance to the Galactic Centre (Catena & Ullio 2010). The virial radius of the Milky Way (MW) is $R_{vir}^{MW} = c_{vir}^{MW} r_s^{MW} \approx (288 \pm 61)$ kpc, where $c_{vir}^{MW} = 19.70 \pm 2.92$ and $r_s^{MW} = (14.65 \pm 2.24)$ kpc (Catena & Ullio 2010). The power-law slope $\alpha_D = 0.237$ is adopted as fitting subhaloes resolved in the Aquarius simulation (Pieri et al. 2011).

Intrinsic to the stochastic process of halo formation, the concentration of individual haloes scatters around the median $\bar{c}$ provided by the quantities $c_{vir}^{FHM}(M)$ and $c_{vir}^{SHM}(M, D_{gc})$, respectively. The corresponding probability distribution follows a lognormal,

$$P(c, \bar{c}) = \frac{\log_{10} e}{\sqrt{2\pi}\sigma_{\log_{10} c}\, c} \exp\left[-\frac{1}{2}\left(\frac{\log_{10} c - \log_{10} \bar{c}}{\sigma_{\log_{10} c}}\right)^2\right], \tag{4}$$

where $\sigma_{\log_{10} c} = 0.14$ (Bullock et al. 2001; Wechsler et al. 2002).

The concentration-to-mass relations are shown in Fig. 1. For the FHM, the scatter is also depicted (68% c.l. of $\log_{10} c$), see Eq. (4). In addition to the concentration of the MW, Fig. 1 contains a selection of eight dSphs that are associated with sufficiently precise stellar data, which allow a conclusive modelling of the DM distribution (see Abdo et al. 2010c). Each dSph is modelled with a NFW profile with parameters chosen to fit measurements of stellar line-of-sight velocities and their distributions (see also Martinez et al. 2009). The dSph's virial concentration is given by its characteristic density, $\rho_s = \Delta_c \rho_{crit} c_{vir}^3 / [3 f(c_{vir})]$, where tidal effects on the inner system are assumed to be negligible. The SHM is depicted for $D_{gc} = 74$ kpc, the average galactocentric distance of the dSph subset. Additionally, the models are confronted with direct predictions of the Aquarius simulation, derived from scaling relations fitting subhaloes observed in the simulation. Details are provided in Appendix A.

Within its scatter, the concentration model of FHM haloes consistently describes the DM profile of dSph galaxies and the MW itself. However, the median values c_{vir}^{FHM} underpredict dSphs, whereas the subhalo model SHM provides convincing agreement (as expected by N-body simulations). The concentration derived directly from the Aquarius simulation confirms the SHM within the validity range, see Fig. 1. Note that the mean distance of subhaloes resolved in Aquarius is 64 kpc.

2.2. DM annihilation in subhaloes

For self-annihilating particles, the total rate of photons (or particles) emitted by a DM subhalo with energy E in the interval $[E_1; E_2]$ is

$$\mathcal{L} = \frac{\langle \sigma v \rangle_{eff} N_\gamma}{2 m_\chi^2} \int dV \rho^2(r) \propto \frac{M^2}{r_s^3 f(c)^2}, \quad N_\gamma = \int_{E_1/m_\chi}^{E_2/m_\chi} dx \frac{dN_\gamma}{dx}, \tag{5}$$

where $\langle \sigma v \rangle_{eff}$ is the thermally averaged annihilation cross section times the relative velocity, m_χ the WIMP mass, and dN_γ/dx, $x \equiv E/m_\chi$, denotes the differential spectrum of photons per annihilation. Assuming $r_s \ll D$, the produced photon flux is given by $\phi = \mathcal{L}/(4\pi D^2)$. The solution of the integral holds for $\gamma = 1.0$ and $c \gg 1$. In Eq. (5), a small, flat core replacing the unphysical singularity at the halo centre (Berezinsky et al. 1992) is safely neglected (given the NFW profile used here). For $\gamma = 1.0$, Eq. (5) simplifies via $r_s = [3M/(4\pi \Delta_c \rho_{crit} c_{vir}^3)]^{1/3}$:

$$\mathcal{L} = \frac{\langle \sigma v \rangle_{eff} N_\gamma \Delta_c \rho_{crit}}{18 m_\chi^2} \frac{M c_{vir}^3}{f(c_{vir})^2}. \tag{6}$$

For a $\gamma = 1.2$ profile (Eq. (1)) the photon rate increases by a factor of ~1.5 for subhaloes above $10^3\ M_\odot$. DM annihilation in subhaloes may be additionally boosted by sub-substructure populations (see Strigari et al. 2007; Kuhlen et al. 2008; Martinez et al. 2009). Conveniently, the value of $\langle \sigma v \rangle_{eff}$ is normalised to the value $\langle \sigma v \rangle_0 = 3 \times 10^{-26}\ \mathrm{cm^3\ s^{-1}}$, which leads to the correct relic density. An increase of the annihilation rate, a so-called boost factor $\langle \sigma v \rangle_{eff} / \langle \sigma v \rangle_0$, could in principle be related to the underlying particle physics framework (e.g., Fornengo et al. 2004) and effects such as Sommerfeld enhancement (e.g., Arkani-Hamed et al. 2009; Kuhlen et al. 2009).

We considered DM to be composed of self-annihilating heavy WIMPs of mass $m_\chi = 500$ GeV and investigated three distinct annihilation models: two of them with total annihilation in heavy quarks or gauge bosons ($b\bar{b}$ and W^+W^-) and a

---

[4] In general, the physical subhalo radius R_t is smaller than the formally defined virial radius R_{vir}, implying the physical subhalo mass M_t to be smaller than M_{vir}. For massive subhaloes, the $M_t(M_{vir})$ relation is approximately linear, where $M_t/M_{vir} \approx 0.2$ (see Appendix A). Given the empirical model correction discussed below, the formal virial quantities will be used in the remainder of the paper.

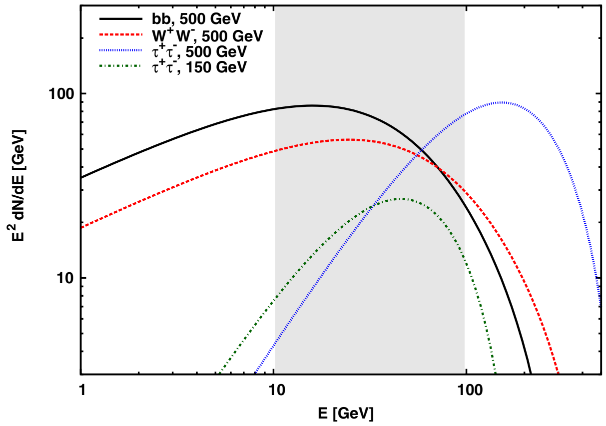

Fig. 2. Differential γ-ray energy spectra $E^2\frac{\mathrm{d}N}{\mathrm{d}E}$ originating from final-state fragmentation of WIMP annihilation. Four different WIMP models are depicted: mass $m_\chi = 500\,\mathrm{GeV}$, final states: $b\bar{b}$ (solid black line), W^+W^- (dashed red line), $\tau^+\tau^-$ (dotted blue line); mass $m_\chi = 150\,\mathrm{GeV}$, final state $\tau^+\tau^-$ (dot-dashed green line). The parametrisations are valid down to $E/m_\chi \approx 0.01$. The grey-shaded area indicates the considered energy range $E \in [10; 100]\,\mathrm{GeV}$.

model with total annihilation in the leptons $\tau^+\tau^-$. Additionally, we considered WIMPs of $m_\chi = 150\,\mathrm{GeV}$ for annihilation in $\tau^+\tau^-$ final states. Particles of this type are, for instance, provided by supersymmetric theories, e.g., manifested in the neutralino. The WIMP masses chosen are compatible with WIMPs which might explain the recently observed cosmic-ray electron and positron excess, see, e.g., Meade et al. (2010). In general, *heavy* WIMPs are also supported by collider searches such as the non-detection of supersymmetric particles in the 7 TeV run of the Large Hadron Collider (for an integrated luminosity of $35\,\mathrm{pb}^{-1}$) (Aad et al. 2011; CMS Collaboration 2011, and references therein).

Given these final annihilation states, hadronisation and the subsequent decay of π^0-mesons lead to a continuous γ-ray spectrum. The resulting photon spectra $\mathrm{d}N_\gamma/\mathrm{d}x$ were modelled using parametrisations provided by Fornengo et al. (2004), see Fig. 2. Note that photons produced by final state radiation (FSR) and virtual internal bremsstrahlung (VIB) (Bergström et al. 2005a,b; Bringmann et al. 2008) are neglected, because a significant contribution of FSR is only expected for W^+W^- at high energies ($E > 0.6\,m_\chi$) and possible contributions of VIB are highly model-dependent.

3. Candidate gamma-ray sources

Given a high WIMP mass, a DM subhalo will show up as steady (very) high-energy γ-ray source. The differential photon spectrum follows a hard power law (index $\Gamma \lesssim 1.5$) that cuts off exponentially at energies beyond 10 GeV, see Fig. 2.

Candidate sources are selected according to their possibility to originate from DM subhaloes based on their observational quantities flux and angular extent. Note that the detailed spectral shape of faint sources is observationally rather unconstrained. Via Eq. (6), the effective self-annihilation cross section $\langle\sigma v\rangle_{\mathrm{eff}}$ required to obtain a given flux ϕ for the intrinsic source extent θ_s is determined by $\mathcal{L} = 4\pi D^2\phi$, where θ_s constrains the distance D to the subhalo. For feasible candidate sources the required $\langle\sigma v\rangle_{\mathrm{eff}}$ should comply with current observational constraints.

Conveniently, the characteristic profile radius r_s (see Eq. (1)) traces the intrinsic extent of a DM subhalo, because for an NFW profile 87.5% of the total luminosity is produced within r_s (see Table 1 for values of r_s). Therefore, the distance to the subhalo is $D \approx r_\mathrm{s}/\theta_\mathrm{s}$, where θ_s denotes the angle corresponding to r_s. Owing to the centrally peaked profile, about 68% of the total luminosity is emitted within the angle $\theta_{68} \simeq 0.46\,\theta_\mathrm{s}$. The following relations are given with respect to θ_s and can easily be adjusted for θ_{68}, which is more convenient for a comparison with observational data. With $r_\mathrm{s} = [3M/(4\pi\Delta_\mathrm{c}\rho_{\mathrm{crit}}c_{\mathrm{vir}}^3)]^{1/3}$, the distance to a subhalo with given θ_s is related to its mass and concentration. In the FHM,

$$D_{\mathrm{FHM}}(M;\theta_\mathrm{s}) \simeq 3.8\left(\frac{M}{10^6\,M_\odot}\right)^{1/3}\left(\frac{c_{\mathrm{vir}}^{\mathrm{FHM}}}{37.9}\right)^{-1}\left(\frac{\theta_\mathrm{s}}{\mathrm{deg}}\right)^{-1}\,\mathrm{kpc}. \tag{7}$$

Note that the concentration depends on the subhalo mass via Eq. (2) as well as, in the SHM, on the object's position (l, b).

For a given WIMP model $\langle\sigma v\rangle_{\mathrm{eff}}$ is then fully determined by the subhalo mass (Eq. (6)) and the observed quantities flux and extent:

$$\langle\sigma v\rangle_{\mathrm{eff}}(M;\phi,\theta_\mathrm{s}) = 96\,\pi^{\frac{1}{3}}\,\frac{m_\chi^2}{N_\gamma}\left(\frac{3}{4\Delta_\mathrm{c}\rho_{\mathrm{crit}}}\right)^{5/3}\frac{\phi}{\theta_\mathrm{s}^2}\,\frac{M^{-1/3}f(c_{\mathrm{vir}})^2}{c_{\mathrm{vir}}^5}\cdot \tag{8}$$

Additional contributions to the DM signal from annihilation in the smooth halo as well as the entire subhalo population were neglected[5]. The required $\langle\sigma v\rangle_{\mathrm{eff}}$ is highly sensitive to the (observationally unconstrained) concentration, because Eq. (8) roughly depends on c_{vir}^{-5}.

4. Interpretation of *Fermi* sources as DM subhaloes

Based on the study of a fiducial candidate source in Sect. 4.1, the properties of *Fermi*-LAT detectable subhaloes are investigated in Sect. 4.2.

4.1. A fiducial candidate

4.1.1. Observational properties

In combination with improving (integrated) sensitivity at high energy (Atwood et al. 2009, and cf., Fig. 7), the expected energy spectrum of DM subhaloes (Sects. 2 and 3) favours a detection at the high-energy band of *Fermi*-LAT. In Appendix B, we investigate the detection sensitivity for faint, moderately extended ($\theta_\mathrm{s} \lesssim 1°$, corresponding to $\theta_{68} \lesssim 0.5°$), and high-latitude ($|b| > 20°$) sources between 10 and 100 GeV in detail. We find that a spectrally hard high-energy source with a flux $\phi(10{-}100\,\mathrm{GeV}) = 1.4\times10^{-10}\,\mathrm{cm}^{-2}\,\mathrm{s}^{-1}$ and moderate extent[6] $\theta_\mathrm{s} = 1°$ can be detected as a point-source with a reconstructed flux $\phi_\mathrm{p}(10{-}100\,\mathrm{GeV}) = 0.9\times10^{-10}\,\mathrm{cm}^{-2}\,\mathrm{s}^{-1}$, with a sky-survey exposure of one year. With respect to the true flux ϕ emitted by the entire source, the reconstructed flux ϕ_p fitted by the point-source analysis in general decreases with increasing θ_s. To account for this effect, the scaling relation $\phi(\theta_\mathrm{s}) = h(\theta_\mathrm{s})\,\phi_\mathrm{p}$ is used in Eq. (8), where $h(\theta_\mathrm{s}) = 1$ for $\theta_\mathrm{s} \ll 2\,\sigma_{\mathrm{PSF}}$ and

---

[5] For the fiducial candidate in Sect. 4 this additional contribution is less than 1%.

[6] In comparison with the point spread function of *Fermi*-LAT, $\theta_\mathrm{s} = 1°$ (as implying $\theta_{68} \approx 0.5°$) corresponds to about $3\,\sigma_{\mathrm{PSF}}$, where $\sigma_{\mathrm{PSF}} \approx 0.15°$ for energies beyond 10 GeV (see `http://www-glast.slac.stanford.edu/software/IS/glast_lat_performance.htm`).

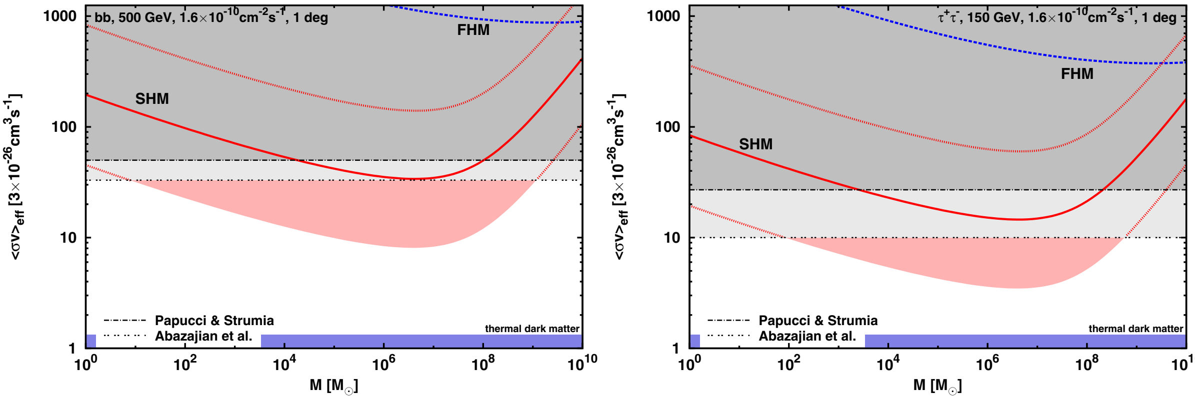

Fig. 3. Effective self-annihilation cross section $\langle\sigma v\rangle_{\rm eff}$ required for a moderately extended, faint *Fermi*-LAT source to originate from a DM subhalo of mass M. Assumed source parameters are $\phi(10{-}100\,{\rm GeV}) = 1.6\times10^{-10}\,{\rm cm^{-2}\,s^{-1}}$, an intrinsic extent $\theta_{\rm s} = 1^\circ$ ($\theta_{68}\approx 0.5^\circ$), and the Galactic position $(l,b) = (114^\circ, -55^\circ)$. The dashed blue and solid red lines indicate the average prediction considering the FHM and SHM, respectively. The intrinsic SHM scatter is shown by the red-shaded area and the dotted red lines. The *left panel* depicts WIMPs of $m_\chi = 500\,{\rm GeV}$ totally annihilating in $b\bar{b}$, while the *right panel* considers $m_\chi = 150\,{\rm GeV}$ with total annihilation in $\tau^+\tau^-$. Current contraints on $\langle\sigma v\rangle_{\rm eff}$ from Papucci & Strumia (2010) (grey-shaded) and Abazajian et al. (2010) (light grey-shaded) are plotted in combination with the expectation from thermal freeze-out (blue-shaded).

$h(\theta_{\rm s})\approx 0.72\,(\theta_{\rm s}/{\rm deg}) + 0.89$ for extended sources up to ~1° (see Appendix B for details).

The high-energy flux of the fiducial source above 10 GeV has been chosen to be at the level of the detection sensitivity, $\phi_{\rm p}^{\rm fid}(10{-}100\,{\rm GeV}) = 10^{-10}\,{\rm cm^{-2}\,s^{-1}}$, assuming an extent of $\theta_{\rm s}^{\rm fid} = 1^\circ$. Given the dependence of the SHM concentration on the galactocentric distance (see Eq. (3)), the fiducial source is placed on a particular line-of-sight chosen to match the location of 1FGL J0030.7+0724 (investigated in Sect. 5). In general, this line-of-sight serves as an appropriate (conservative) benchmark, because it points to (anticentric) positions where the majority of subhaloes is located.

4.1.2. Subhalo interpretation

Adopting the properties of the fiducial source, Fig. 3 depicts the effective enhancement factors $\langle\sigma v\rangle_{\rm eff}/\langle\sigma v\rangle_0$ required to generate the emission $\phi_{\rm p}^{\rm fid}$ by DM annihilation (obtained via Eq. (8)). In the left panel, WIMPs of $m_\chi = 500\,{\rm GeV}$ are considered to totally annihilate in $b\bar{b}$, while the right panel assumes $m_\chi = 150\,{\rm GeV}$ and annihilation in $\tau^+\tau^-$. For a given WIMP model, the resulting enhancement factors of the FHM and SHM are widely different. With respect to the FHM, much less enhancement is required in the SHM, which is manifested in generically higher concentrations of SHM subhaloes. Within the scatter of the concentration intrinsic to the stochastic nature of halo formation (Eq. (4)), which is shown for the SHM, the necessary enhancement spans about one order of magnitude. Only moderate enhancement is required for massive subhaloes between 10^6 and $10^7\,M_\odot$, where the lowest $\langle\sigma v\rangle_{\rm eff}$ is needed for $m_\chi = 150\,{\rm GeV}$ and $\tau^+\tau^-$ final states (amongst the WIMP models considered here). The lowest possible enhancement factors within the concentration scatter of a $10^6\,M_\odot$ subhalo are listed in Table 1 for the different subhalo and the WIMP models of Sect. 2.

The distance to the fiducial candidate anticipated in the FHM and the SHM is shown in Fig. 4. The intrinsic concentration scatter implies a corresponding distance scatter for a given halo mass and angular extent. Note that a similar scatter is present for the FHM, but is not shown in the figure. Compared with the FHM, tidal effects lead to higher concentrated subhaloes. This in turn favours a closer distance at the same mass and angular extent for SHM subhaloes than for FHM.

4.1.3. Consistency with observational constraints

The resulting values of $\langle\sigma v\rangle_{\rm eff}$ can now be checked for consistency with the diffuse extragalactic γ-ray background (EGB; Abdo et al. 2010b). *Fermi*-LAT measurements of the overall diffuse γ-ray flux allow the derivation of the isotropic high-energy EGB, which is shown to be compatible with a featureless power-law spectrum ($\Gamma = 2.41 \pm 0.05$) and integrated diffuse flux $\phi_{\rm EGB}(>100\,{\rm MeV}) = (1.03\pm0.17)\times10^{-5}\,{\rm cm^{-2}\,s^{-1}\,sr^{-1}}$ (Abdo et al. 2010b). The diffuse γ-ray flux anticipated from DM annihilation in the Galactic halo as well as the entire subhalo population is shown in Fig. 5 (see Appendix C for details), in comparison with the EGB. Both FHM and SHM subhaloes are depicted for $m_\chi = 150\,{\rm GeV}$ and annihilation in $\tau^+\tau^-$. In this model, the nearly isotropic diffuse flux from the subhalo population contributes about 1% to the EGB (assuming SHM subhaloes and no sub-substructure) and is fainter than the contribution of the smooth halo ($\gtrsim$3%). Note that the flux from the extragalactic halo population is lower than the contribution of Galactic subhaloes, see, e.g., Abazajian et al. (2010).

Table 1. Enhancement factors $\langle\sigma v\rangle_{\rm eff}/\langle\sigma v\rangle_0$ required to explain the fiducial γ-ray source with a DM subhalo of $10^6\,M_\odot$.

Model	$m_\chi = 500\,{\rm GeV}$ $b\bar{b}$	W^+W^-	$\tau^+\tau^-$	150 GeV $\tau^+\tau^-$	$r_{\rm s}^{\rm n}$ [kpc]	$g_r(c_{\rm vir})$
FHM	$\gtrsim$321	$\gtrsim$479	$\gtrsim$1386	$\gtrsim$138	0.067	$\left(\frac{c_{\rm vir}^{\rm FHM}}{37.86}\right)^{-1}$
SHM^a	$\gtrsim$8	$\gtrsim$ 12	$\gtrsim$35	$\gtrsim$3	0.029	$\left(\frac{c_{\rm vir}^{\rm SHM}}{86.56}\right)^{-1}$

Notes. The factors correspond to the WIMP models discussed in the text. The respective photon yields are $N_\gamma^{bb\,(WW)\,[\tau\tau]}(10{-}100\,{\rm GeV}) = 6.95\,(4.66)\,[1.46]$ for $m_\chi = 500\,{\rm GeV}$ and $N_\gamma^{\tau\tau}(10{-}100\,{\rm GeV}) = 1.61$ for $m_\chi = 150\,{\rm GeV}$. We list the minimum values within the c-scatter. In addition, the subhalo's (average) characteristic radius $r_{\rm s}(M) = r_{\rm s}^{\rm n}[M/(10^6\,M_\odot)]^{1/3}g_r(c_{\rm vir})$ is depicted. $^{(a)}$ The normalisation of $c_{\rm vir}^{\rm SHM}$ implies the Galactic position $(114^\circ, -55^\circ)$ and intrinsic extent $\theta_{\rm s} = 1^\circ$, corresponding to $D\approx1.7\,{\rm kpc}$ ($D_{\rm gc}\approx 8.8\,{\rm kpc}$).

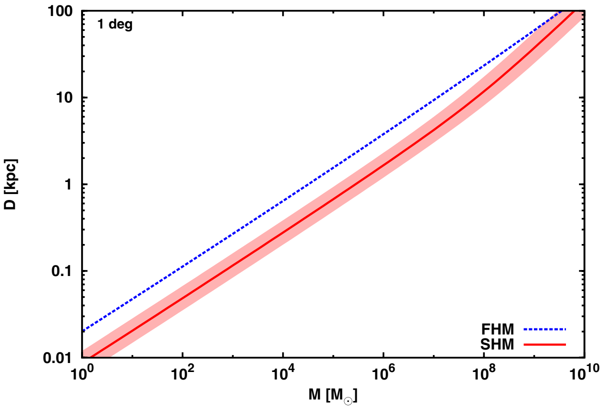

Fig. 4. Distance to the fiducial subhalo in the FHM (dashed blue line) and SHM (solid red line), respectively, as function of the subhalo mass M. The scatter of the SHM distance is indicated by the red-shaded area. An extent of $\theta_s = 1°$ ($\theta_{68} \approx 0.5°$) and a source position $(l, b) = (114°, -55°)$ are assumed.

Table 2. Upper limits on $\langle\sigma v\rangle_{\rm eff}/\langle\sigma v\rangle_0$ from the EGB.

WIMP model		Upper limit on $\langle\sigma v\rangle_{\rm eff}/\langle\sigma v\rangle_0$			
Channel	m_χ [GeV]	FHM	SHM	FHM	SHM
$b\bar{b}$	500	1650	530	1875	605
W^+W^-	500	2096	673	2381	769
$\tau^+\tau^-$	500	3490	1121	3964	1279
$\tau^+\tau^-$	150	378	121	429	139
$M_{\rm min}$		$10^{-10}\,M_\odot$		$10^{-6}\,M_\odot$	

Notes. We assumed a subhalo mass fraction of $f_{\rm sh} = 15\%$ for a cut-off mass $M_{\rm min} = 10^{-6}\,M_\odot$. Upper limits are listed for the cut-off masses bordering a 500 GeV neutralino scenario (see Bringmann 2009) and with respect to $\psi = 180°$ and $E = 40$ GeV. See text and Appendix C for details.

The contribution from the smooth halo peaks at the Galactic Centre, where a high astrophysical foreground is also present, and can therefore not be isotropic. Given that the EGB has been derived assuming isotropy, the most robust upper limits on $\langle\sigma v\rangle_{\rm eff}$ are determined by the subhalo contribution and are listed in Table 2, depending on the WIMP model and cut-off mass. The bounds were obtained requiring that the specific intensity of the subhalo population $\langle I_\nu(180°, E)\rangle$ does not exceed the EGB, where $\langle I_\nu(\psi, E)\rangle$ depends on the angle ψ between the Galactic Centre direction and line-of-sight, and the γ-ray energy E (see Appendix C).

However, more stringent constraints have been provided by a more detailed modelling of the EGB, including all DM components. To evaluate a possible DM origin of the fiducial source, the results of Abazajian et al. (2010) and Papucci & Strumia (2010)[7] are included in Fig. 3. As stated in the introduction, competitive and similar constraints have been also provided by the non-detection of various objects with high (central) DM densities. Note, for instance, that the constraints used here are consistent with recent bounds from dSph galaxies (Abdo et al. 2010c).

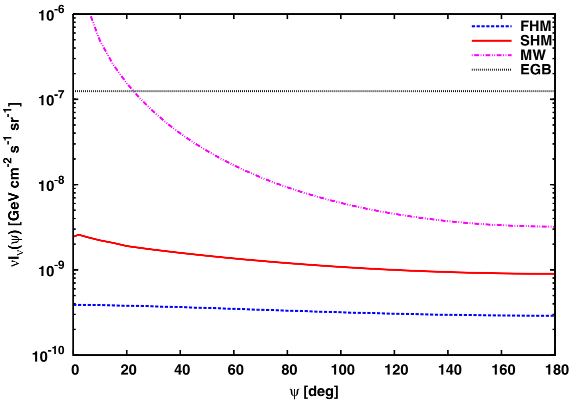

Fig. 5. Average diffuse γ-ray flux from DM annihilation in the Galaxy as function of the angle between the observational and Galactic Centre direction ψ. The fluxes from the host halo (double-dot-dashed magenta line), FHM (dashed blue line), and SHM subhaloes (solid red line) are depicted. Each curve was derived at the peak energy of $\nu I_\nu(E)$ (40 GeV) assuming total annihilation in $\tau^+\tau^-$ with $m_\chi = 150$ GeV and $\langle\sigma v\rangle_{\rm eff} = \langle\sigma v\rangle_0$. The minimum subhalo mass used was $M_{\rm min} = 10^{-6}\,M_\odot$ (see Appendix C). The EGB at 40 GeV is shown by the dotted black line.

4.2. Fermi-LAT detectable subhaloes

4.2.1. Expected number

Integrating over the mass and spatial distribution (Eq. (C.2)) reveals the total number of detectable subhaloes with masses $M_{\rm I} \in [M; M + \Delta M]$, solar distances $D_{\rm I} \in [D; D + \Delta D]$, concentrations $c_{\rm I} \in [c; c + \Delta c]$, galactic latitudes $b_{\rm I} \in [b, b + \Delta b]$, and galactic longitudes $l \in [0; 2\pi]$, $N = N(M_{\rm I}, D_{\rm I}, c_{\rm I}, b_{\rm I})$,

$$N = \int_{M_{\rm I}} {\rm d}M \int_{D_{\rm I}} {\rm d}D\, D^2 \int_{c_{\rm I}} {\rm d}c \int_{b_{\rm I}} {\rm d}b\, \cos b \int_0^{2\pi} {\rm d}l\, P(c, \bar{c})\, \frac{{\rm d}n_{\rm sh}(D_{\rm gc}, M)}{{\rm d}M} \qquad (9)$$

$$= a_N \int_{M_{\rm I}} {\rm d}M\, M \int_0^{\theta_{\rm s}^{\rm max}} {\rm d}\theta_{\rm s} \frac{\cos^2\theta_{\rm s}}{\sin^4\theta_{\rm s}} \int_{c_{\rm min}(\theta_{\rm s}, M)}^{\infty} {\rm d}c\, c^{-3} \int_{b_{\rm I}} {\rm d}b\, \cos b \int_0^{2\pi} {\rm d}l\, P(c, \bar{c})\, \frac{{\rm d}n_{\rm sh}}{{\rm d}M},$$

using $D = r_{\rm s}/\tan\theta_{\rm s}$ (see Sect. 3) and $a_N \equiv 3/(4\pi\Delta_{\rm c}\rho_{\rm crit})$. Parameters defining the subhalo distribution were taken to match the Aquarius simulation (Appendix C). In total, this resulted in about 6.4×10^{14} Galactic subhaloes residing in the Galaxy. For every single $\theta_{\rm s}$ and M, the integral counts detectable subhaloes only, i.e., their concentration is sufficiently high to ensure their $\langle\sigma v\rangle_{\rm eff}$ to be smaller than the observational constraints (cf., Fig. 3). Therefore, the lower bound of the concentration integral $c_{\rm min}(\theta_{\rm s}, M)$ is determined via Eq. (8), choosing the instrument's sensitivity and constraints from Abazajian et al. (2010) and Papucci & Strumia (2010), respectively. To account for the fact that highly extended objects will be hardly detectable (see Appendix B), we conservatively chose $\theta_{\rm s}^{\rm max} = 1°$. For the SHM, Fig. 6 shows the number of detectable subhaloes per mass decade expected in one year of data taking while considering subhaloes at galactic latitudes $|b| \geq 20°$ only (cf., Sect. 5). Given the dependence of $c_{\rm min}$ on the WIMP model, the results for the $b\bar{b}$, $m_\chi = 500$ GeV model are compared to the $\tau^+\tau^-$, $m_\chi = 150$ GeV scenario.

Considering the constraints found by Abazajian et al. (2010) for the $b\bar{b}$ ($\tau^+\tau^-$) model, on average 0.4 (0.2) subhaloes within 10^5 and $10^8\,M_\odot$ are anticipated for detection with *Fermi*-LAT in

---

[7] In comparison with Papucci & Strumia, the work by Abazajian et al. includes a fore- and background subtraction. Note that the MW halo parameters used by Abazajian et al. are similar to those adopted in this work (see Sect. 2.1).

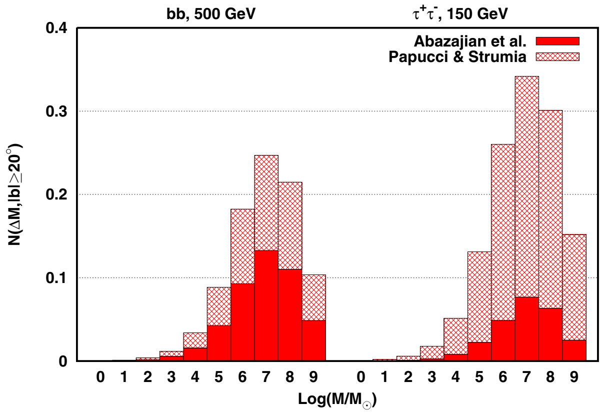

Fig. 6. Expected number of one-year detectable subhaloes per mass decade at $|b| \geq 20°$. The subhaloes' mass and spatial distributions were adopted from Aquarius (Appendix C) while the SHM concentration was used. $M_{\min} = 10^{-6}\,M_\odot$. The number corresponding to the $b\bar{b}$, $m_\chi = 500$ GeV ($\tau^+\tau^-$, $m_\chi = 150$ GeV) WIMP model is shown in the left (right) panel. The mass assigned to each bar denotes the geometric mean of the interval. Red and red-patterned bars show the number considering observational constraints on $\langle\sigma v\rangle_{\rm eff}$ by Abazajian et al. (2010) and Papucci & Strumia (2010), respectively.

one year. Given the Poisson distribution of N, this means that up to *one* massive subhalo is expected in the one-year data set (at 95% confidence). Comparable results have been claimed by other authors, e.g., Baltz et al. (2008), Kuhlen et al. (2008), Pieri et al. (2008, 2011), and Anderson et al. (2010).

In general, note that numerical simulations like Aquarius and Via Lactea II neglect the influences of baryonic matter distributed in galactic disks. A recent study by D'Onghia et al. (2010) indicates that a baryonic disk may reduce the number of (massive) subhaloes in the inner galaxy by a factor of 2 to 3.

4.2.2. Properties

Given a particular γ-ray source (such as the fiducial of Sect. 4.1), massive subhaloes between about 10^5 and $10^8\,M_\odot$ require a minimally enhanced annihilation cross section $\langle\sigma v\rangle_{\rm eff}$, see Fig. 3. Consistently, the probability for these objects to appear in current data sets peaks for high subhalo masses (Fig. 6). Therefore, subhalos with masses of 10^5 up to $10^8\,M_\odot$ in corresponding distances from 0.5 to 10 kpc (Fig. 4) are favoured for detection with *Fermi*-LAT as faint and moderately extended sources. Although for the FHM a DM origin of the fiducial source is excluded, within the scatter of the more realistic SHM cross sections required for sources with $\phi(10{-}100\,{\rm GeV}) \approx 10^{-10}\,{\rm cm}^{-2}\,{\rm s}^{-1}$ and angular extents up to $\sim 1°$ are well consistent with observational constraints. The presence of sub-substructure will even lower $\langle\sigma v\rangle_{\rm eff}$ by a mass-dependent factor of ~ 2 to 3 for massive subhaloes (Kuhlen et al. 2008; Martinez et al. 2009). In case of a cuspier profile ($\gamma = 1.2$), the required cross section is lowered by an additional factor of 1.5. At least for WIMPs of $m_\chi = 150$ GeV annihilating to $\tau^+\tau^-$, this leads to a required enhancement of the order of unity within the scatter. Summarising, in optimistic but realistic scenarios a γ-ray emitter at the (one year) detection level of *Fermi*-LAT with a measured extent θ_{68} of about 0.5° might be consistent with a subhalo driven by self-annihilating DM.

In the next years, *Fermi*-LAT will provide deeper observations with increased observation time $T_{\rm obs}$. This will improve the sensitivity by roughly $\sqrt{T_{\rm obs}}$, leading to a factor of about 2 lower values of the minimum detectable flux for the five-year catalogue. This in turn will allow us to detect fainter subhaloes with a correspondingly reduced minimum $\langle\sigma v\rangle_{\rm eff}$. The average number of detectable subhaloes within five years is about 1.3 (0.8) for the $b\bar{b}$, $m_\chi = 500$ GeV ($\tau^+\tau^-$, $m_\chi = 150$ GeV) scenario.

Via Eq. (8), a comparison with observational constraints on $\langle\sigma v\rangle_{\rm eff}$ allows to estimate the maximum flux subhalo candidates are expected to have. The catalogued flux is $\phi_{\rm p} \propto \theta_{\rm s}^2/h(\theta_{\rm s})$, which is quadratic for $\theta_{\rm s} \ll 0.3°$ and linear in the limit of large $\theta_{\rm s}$. The increase with $\theta_{\rm s}$ originates from decreasing subhalo distance. Because massive subhaloes require minimum $\langle\sigma v\rangle_{\rm eff}$, a subhalo of $10^6\,M_\odot$ is assumed below. Within the concentration scatter, the maximum flux between 10 and 100 GeV expected for a source with $\theta_{\rm s} = 1°$ is

$$\phi_{\rm p}^{\max}(10{-}100\,{\rm GeV}) \simeq 1.2\,(2.8) \times 10^{-11}\,\frac{\langle\sigma v\rangle_{\rm eff}}{\langle\sigma v\rangle_0}\,{\rm cm}^{-2}\,{\rm s}^{-1} \qquad (10)$$

in the $b\bar{b}$, $m_\chi = 500$ GeV and $\tau^+\tau^-$, $m_\chi = 150$ GeV scenario, respectively. Given the observational constraints of Abazajian et al., the high-energy flux of catalogued candidates should not exceed $\phi_{\rm p}^{\max} \lesssim 4.0\,(2.8) \times 10^{-10}\,{\rm cm}^{-2}\,{\rm s}^{-1}$.

5. Searches for DM subhaloes in the 1FGL

In the previous section we demonstrated that DM subhaloes could appear in γ-ray catalogues of sufficient sensitivity as faint, non-variable, and moderately extended objects without astrophysical counterparts. The 11-month[8] point-source catalogue of *Fermi*-LAT (1FGL, Abdo et al. 2010a) lists 1451 sources significantly detected above 100 MeV (test statistic TS $\geq$ 25, corresponding to a significance $S = 4.1\sigma$), together with the flux in five discrete energy bins (up to 100 GeV), position, significance of variability, and spectral curvature. Source spectra have been fitted with power laws. Among the sources, 630 objects[9] are not confidently associated with known sources at other wavelengths.

Although sophisticated methods have been applied to find multi-wavelength associations for unidentified sources, all algorithms suffer from lacking sensitivity or incomplete sky-coverage of current surveys. Therefore, the sample of unassociated high-latitude *Fermi*-LAT sources is expected to be composed of several source classes, among them faint AGN (Active Galactic Nuclei), galaxy clusters, and new exotic sources like DM subhaloes (Stephen et al. 2010; Mirabal et al. 2010, and references therein). Concerning the 1FGL catalogue, improved association methods recently presented by Mirabal et al. (2010) revealed that $\lesssim$20% of all unassociated 1FGL sources with $|b| \geq 15°$ may contain new γ-ray emitters.

To single out possible subhalo candidates within the sample of unassociated sources (cf., Buckley & Hooper 2010), we searched the sample for non-variable[10] sources detected between 10 and 100 GeV. Requiring a detection at high energy provides subhalo candidates driven by heavy WIMPs and avoids confusion with high-energy pulsars[11]. Furthermore, the candidate's

---

[8] August 2008 to July 2009.

[9] Adding sole associations with other γ-ray catalogues, 671 sources are "unassociated".

[10] The cut is passed by sources with a steadiness probability $P_{\rm s} > 1\%$.

[11] The spectral properties of γ-ray pulsars can mimic the spectra of DM subhaloes, see Baltz et al. (2007). However, spectral cut-off energies of γ-ray pulsars are well below 5 GeV (Abdo et al. 2009a), excluding a detection above 10 GeV.

Table 3. Cut efficiencies on the sample of unassociated sources and AGN.

Cut	Unassociated	AGN
–	671	693
$\|b\| \geq 20°$	249 (100%)	539 (100 %)
non-variable	241 (97%)	372 (69%)
detected between 10–100 GeV	12 (5%)	58 (11%)

Notes. The cuts are cumulative, i.e., each number includes all cuts listed by previous rows. See text for details.

location was constrained to galactic latitudes $|b| \geq 20°$ to avoid a general confusion with Galactic sources. Additionally, the lower Galactic foreground improves the detection sensitivity of *Fermi*-LAT at high latitudes (Atwood et al. 2009).

Applying all cuts, *twelve* unassociated sources remain. The twelve sources are listed in Table 4 together with additional information from the catalogue. With the exception of 1FGL J0614.1-3328, the sample consists of sources at the faint end of the entire 1FGL sample. Given the result of Mirabal et al. (2010), the sample should statistically contain two to three subhaloes at most, consistent with the estimate discussed previously (Fig. 6). The expectation of the sample consisting mostly of AGN is met by applying the same cuts to all AGN detected by *Fermi*-LAT. A comparison with the sample of unassociated sources reveals similar cut efficiencies (5% vs. 11%, see Table 3), indicating that the two populations share common properties. Note that for the AGN the variability cut has subdominant influence as well, see Table 3. Except for three, all AGN that passed the cuts have been classified as BL Lac.

Even though the twelve candidate objects are listed in the 1FGL catalogue as unassociated, we extended the counterpart search to a wider choice of astronomical catalogues. Table 4 lists the classifications of counterpart candidates in the 68% confidence regions around the most likely 1FGL positions, retrieved from the NASA/IPAC Extragalactic Database (NED). In particular, possible associatons are provided by radio and X-ray sources, since most of the selected γ-ray sources are expected to be AGN. Given that no detailed association study was conducted, some of the tabulated sources might be by-chance associations.

Governed by lacking association, faintness, and spectral shape, this study focusses on the most promising candidate, 1FGL J0030.7+0724. Within the errors, its high-energy flux and spectral index are well-compatible with a self-annihilating DM scenario. The source has only been detected between 10 and 100 GeV, see Fig. 7.

5.1. Multi-wavelength properties of 1FGL J0030.7+0724

5.1.1. Catalogued data

No counterpart candidate was found within the positional uncertainty of the γ-ray source at a 68% confidence level (Table 4). In the 95% confidence region, the faint radio object NVSS J003030+072132 is located ($f_{1.4\,\mathrm{GHz}} = (3.5 \pm 0.4)$ mJy; Condon et al. 1998). However, no conclusive infrared (2MASS, Skrutskie et al. 2006) or optical (USNO B1.0, Monet et al. 2003) association of the NVSS source is known so far[12]. Note that

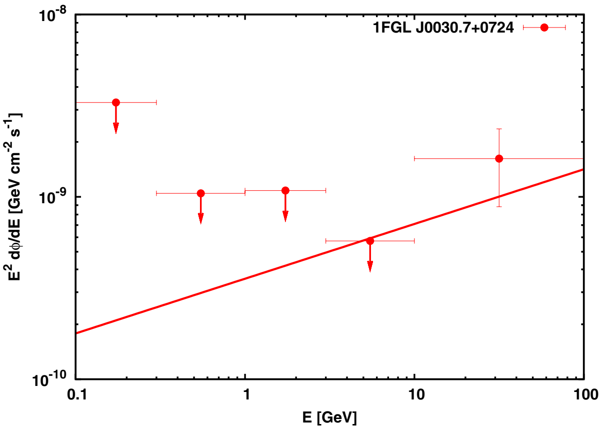

Fig. 7. Energy spectrum of 1FGL J0030.7+0724 as given in the first *Fermi*-LAT catalogue between 100 MeV and 100 GeV (filled circles). The solid red line depicts the (catalogued) power law fitting the data. Only the highest energy bin has been significantly detected, while for the low-energy bins upper limits are shown (95% c.l.).

no dSph galaxy is located in the source region (NED). ROSAT (0.1–2.4 keV; Voges et al. 1999) observations of the region with an exposure of about 170 s revealed no X-ray source down to an energy-flux level of $\sim 10^{-12}$ erg cm^{-2} s^{-1} (Born 2010).

We emphasise that the orphaned faint radio source is likely located in the uncertainty region of 1FGL J0030.7+0724 by chance, because about 0.7 NVSS sources are expected by statistics.

5.1.2. *Fermi*-LAT data

By analysing the 24-month public archival data between 10 and 100 GeV, updated results on 1FGL J0030.7+0724 will be provided. For the same energy range, a reanalysis of the 11-month data is presented for comparison. Particular focus will be drawn on positional properties, the high-energy flux, and the photon distribution, which allows us to investigate possible counterparts, temporal variability, and the angular extent.

The data analysis was performed with the latest public version of the *Fermi* science tools (v9r18p6)[13] along with recommended options and the set of instrument-response functions *P6_V3_DIFFUSE* (Rando 2009). Throughout the analysis, the optimiser MINUIT was used. For reliable results, photons of event class 3 (*Diffuse*) and 4 (*DataClean*) within a radius of 10°, centred on the nominal position of 1FGL J0030.7+0724, were selected. Given that most of the photons are at highest energies (Fig. 7), only events between 10 and 100 GeV were selected to minimise the background and ensure a narrow PSF. The data were processed using *gtselect*, *gtmktime*, *gtltcube*, *gtexpmap*, and unbinned *gtlike*. To compute the most likely position and its corresponding uncertainty on basis of the 10–100 GeV photon sample, we used *gtfindsrc*. For the purpose of detailed counterpart searches, the two-dimensional likelihood function $L(\mathrm{RA}, \mathrm{Dec})$ was computed, which provides the 95% uncertainty contour by $2\,\Delta(\log L) = 6.18$ (2 degrees of freedom).

---

[12] Within the 2σ positional uncertainty of NVSS J003030+072132, a very faint optical SDSS (Sloan Digital Sky Survey) source is located (26.0^{m}) – SDSS J003031.22+072132.2 (SDSS DR7, Abazajian et al. 2009). However, this object was observed with the edge of the plated SDSS camera. Therefore, this detection is probably spurious.

[13] *Fermi* Science Support Center, http://fermi.gsfc.nasa.gov/ssc/

Table 4. Unassociated, non-variable 1FGL sources at high galactic latitudes.

Name 1FGL J	σ_{68}/σ_{95} [arcmin]	S [σ]	$f_\mathrm{p}(0.1{-}100\,\mathrm{GeV})$ [$10^{-11}\,\mathrm{erg\,cm^{-2}\,s^{-1}}$]	Γ	$\phi_\mathrm{p}(10{-}100\,\mathrm{GeV})$ [$10^{-10}\,\mathrm{cm^{-2}\,s^{-1}}$]	Possible associations[a] 68% c.l.	Remarks
0022.2-1850	6.0/9.6	9.4	1.3(4)	1.6(1)	1.6(7)	RadioSs (4, 21, 22), Gs (20–18)	
0030.7+0724	3.0/5.1	5.8	1.0(4)	1.7(4)	1.5(7)	–	
0051.4-6242	2.4/4.2	12.0	1.8(5)	1.7(1)	1.7(8)	Gs (20), XrayS (3.8)	c
0143.9-5845	3.0/4.7	9.0	1.4(4)	2.0(2)	2.0(9)	RadioS (28[§]), Gs (20–13)	
0335.5-4501	2.4/4.0	8.6	1.5(4)	2.1(2)	1.6(8)	Gs (19, 18)	
0614.1-3328	1.2/1.7	54.4	11.2(6)	1.93(3)	3(1)	GrayS	b
0848.6+0504	5.4/8.6	5.4	1.0(5)	1.2(3)	1.6(8)	RadioSs (2, 3, 5), Gs & *s, XrayS (4.4)	c
1323.1+2942	1.8/2.7	11.9	1.5(4)	2.0(1)	2.1(8)	RadioSs (2.8, 263, 724), Gs & *s	
1754.3+3212	2.4/4.1	15.6	2.6(4)	2.09(9)	1.4(7)	RadioS (38[†])	
2134.5-2130	3.0/5.1	6.7	1.1(3)	1.9(2)	1.4(7)	RadioS (22), Gs (20)	
2146.6-1345	3.0/4.4	9.8	1.5(5)	1.8(2)	1.8(8)	RadioS (23), Gs (20), XrayS (1.9)	c
2329.2+3755	1.2/1.9	10.4	1.7(5)	1.6(2)	2.4(9)	G (14)	c

Notes. The columns list the positional uncertainty $\sigma_{68\,(95)}$ [68% (95%) c.l., semimajor axis], detection significance S in Gaussian sigma, integrated energy flux $f_\mathrm{p}(0.1{-}100\,\mathrm{GeV})$, spectral index Γ, and the photon flux $\phi_\mathrm{p}(10{-}100\,\mathrm{GeV})$. Here, parentheses indicate the corresponding error on the last decimal(s). Furthermore, the type classifications of sources found in astronomical catalogues within the 68% uncertainty region of the *Fermi*-LAT position are listed. (a) Classifications referred to are RadioS (radio source), G (galaxy), (*) (star), XrayS (X-ray source), and GrayS (γ-ray source). For radio, optical, and X-ray sources corresponding fluxes are given in mJy (at 1.4 GHz [(§) : 843 MHz. (†) : 4.85 GHz]) , apparent magnitudes, and $10^{-12}\,\mathrm{erg\,cm^{-2}\,s^{-1}}$, respectively. The unabsorbed X-ray flux was derived from the catalogued count-rate, assuming a power law with index 2.0 (with WebPIMMS, `http://heasarc.gsfc.nasa.gov/Tools/w3pimms.html`). The hydrogen column density was obtained from the LAB survey, see Sect. 5.1.3. Sources referred to are listed in the FIRST (Becker et al. 1995), JVAS/CLASS (Jackson et al. 2007), NVSS, SUMSS (Mauch et al. 2003), 2MASS, APMUKS (Maddox et al. 1990), SDSS (Abazajian et al. 2009), ROSAT, or EGRET (Hartman et al. 1999) catalogue, respectively. (b) The spectrum is probably curved. (c) The γ-ray source has been associated by a cross-correlation of unidentified *Fermi*-LAT sources with the ROSAT All Sky Survey Bright Source Catalogue (see Stephen et al. 2010 for details).

Table 5. Positional and spectral properties of 1FGL J0030.7+0724 as given in the catalogue (11 months) and by the (re-)analysis of the first 11 and 24-month data sets.

Data set	E [GeV]	RA (J2000)	Dec (J2000)	$\phi_\mathrm{p}(10{-}100\,\mathrm{GeV})$ [$10^{-10}\,\mathrm{cm^{-2}\,s^{-1}}$]	$S\,(\phi_\mathrm{p})$ [σ]
1FGL	0.1–100	00 30 42.6	+07 24 09	1.5 ± 0.7	6.6
11	10–100	00 30 37.6	+07 24 15	1.4 ± 0.7	6.5
24	10–100	00 30 47.6	+07 24 20	0.9 ± 0.4	6.6

Notes. The second column lists the analysed energy range. The 11 (24)-month analysis focusses on the high-energy flux $\phi_\mathrm{p}(10{-}100\,\mathrm{GeV})$ only. In all cases, the significance S of the high-energy bin is well above 6σ.

Table 6. High-energy photons detected from 1FGL J0030.7+0724 within 0.5°.

E [GeV]	RA [deg]	Dec [deg]	ϑ [deg]	Δt [30 d]	CT	Event class
83.8	7.6330	7.3975	56.26	2.46	B	3
11.8	7.7293	7.3771	36.39	5.19	F	4
39.8	7.7841	7.4962	47.38	7.96	B	4
10.2	7.6426	7.4483	34.21	10.46	F	4
15.0	7.6361	7.1872	38.24	11.12	B	4
43.8	7.8392	7.4151	20.81	18.93	F	4

Notes. The table lists their energy E, celestial position (J2000), inclination ϑ, detection time Δt, and conversion type (CT). By Δt the time between detection and mission start is given. The conversion type is front (F) or back (B). For each event, we list the classification assigned by LAT data reconstruction (Pass 6), where 3 tags the *Diffuse* and 4 the *DataClean* class (see Abdo et al. 2010b).

The source model for the data analysis contains all 1FGL sources within the region of interest (ROI, radius 10°). Their parameters were taken as catalogued and we used the latest Galactic (*gll_iem_v02.fit*) and extragalactic (*isotropic_iem_v02.txt*) diffuse background models. All parameters but those of 1FGL J0030.7+0724 were kept fixed. Furthermore, the catalogued power-law index of 1FGL J0030.7+0724 was used while fitting the flux between 10 and 100 GeV. Although the exposure of the 24-month data has almost doubled with respect to the catalogue, the use of the catalogued properties for sources within the ROI will not affect the analysis between 10 and 100 GeV: The three nearby sources, i.e., 1FGL J0022.5+0607, 1FGL J0030.4+0451, and 1FGL J0023.5+0930, are not only more than 2° away from 1FGL J0030.7+0724, but they are also not significantly detected between 10 and 100 GeV. Furthermore, visual inspection does not reveal any other relevant source within this nearby region.

The analysis of the 11-month data reproduces the catalogued values well (Table 5). After 11 (24) months, five (six) photons between 10 and 100 GeV have been detected within a radius of 0.5° around the nominal position, listed in Table 6. Except one, all photons are classified as class 4 events and are therefore very likely signal events. The Galactic foreground and the extragalactic background at the source position are negligible with respect to the signal, with an expected total number of background photons $N_\mathrm{bg} = 0.6\,(1.2)$ within the considered region of 0.5°. For comparison, the predicted number of signal events is $N_\mathrm{sig} = 4.9\,(5.8)$ after 11 (24) months. According to the 11-month data set, the (10–100 GeV) best-fit position shifts by about 2.5′. The small positional error of the sixth photon also accounts for the increase of the source's positional uncertainty, see Fig. 8.

The average flux over the entire data set has decreased by a factor of roughly 1.5 with respect to the first 11 months (Table 5). To judge on the variability of 1FGL J0030.7+0724, its temporal photon distribution (Table 6) was tested for compatibility with a constant flux, using an unbinned Kolmogorov-Smirnov (KS) test (Press et al. 2007). The KS test is already valid for low photon counts, unlike the binned chi-square method used by the catalogue. The KS test confirms the null-hypothesis

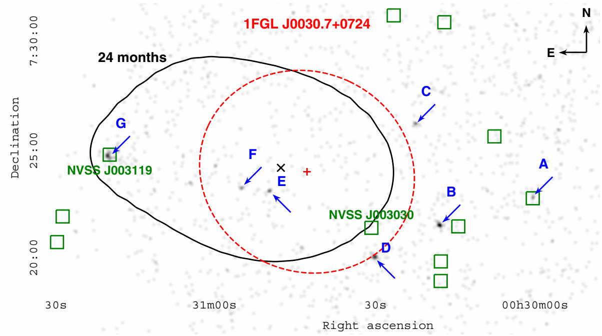

Fig. 8. Celestial region of 1FGL J0030.7+0724, 25′ × 13′. The catalogued position is indicated by the red +, while the dashed red ellipse borders its uncertainty (95% c.l.). The black × marks the 24-month position, the solid black contour its uncertainty at 95% confidence. Photons detected by *Swift*-XRT (10.1 ks) are mapped by the back-image, which is smoothed with a Gaussian (7″). The positions of NVSS radio sources are given by the darkgreen boxes, the two NVSS sources discussed in the text are named. In this region, seven X-ray sources have been discovered, indicated by the blue arrows (see Table 7). Note that the boxes' size is chosen arbitrarily.

of non-variability with a probability of about 0.7 (0.5) for the 11 (24) months data set. The varying exposure on the region was taken into account by examining the photon distribution of the bright pulsar nearby (1FGL J0030.4+0451).

The analysis of the (intrinsic) spatial extent of the source is based upon a likelihood-ratio test, using all photons listed in Table 6. The corresponding statistical measure is given by $L(\theta_s) = -2\sum_{i=1}^{N}\ln[p_{\rm det}(\boldsymbol{x}_i - \overline{\boldsymbol{x}};\theta_s) + b]$, where $p_{\rm det}(\boldsymbol{x};\theta_s)$ is the probability distribution function for a photon detected at $\boldsymbol{x}$, $\overline{\boldsymbol{x}}$ denotes the best-fit position (Table 5), and b incorporates the flat background. For a spatially extended γ-ray emitter $p_{\rm det} = p_{\rm PSF} * p_{\rm int}$, the (two dimensional) convolution of the *Fermi*-LAT PSF (P6_v3, diffuse class) with the intensity profile of the emitter. In the subhalo case, the intensity profile follows the line-of-sight integral of the squared NFW profile (Eq. (1)). The quantity $\Delta L = L - L_{\rm min}$ follows a chi-square distribution with one degree of freedom, with additional terms of the order of $1/N^{1/2}$, which are important for a small number of counts (Wilks 1938; Cash 1979). The likelihood is minimised ($L_{\rm min}$) for the intrinsic extension parameter fitting the photon distribution best. Examining the 11-month data, the test shows the source to be consistent with a point source, implying that the intrinsic extent is smaller than the (average) PSF (about 0.15°). The 24-month data favour a moderate extent $\theta_s = 0.14^{+0.20}_{-0.12}$ deg, which is, however, not significant. Upper limits on the extension parameter are $\theta_s \leq 0.54\,(0.72)$ deg at 95% confidence level, derived from the 11 (24) months data set. Since the low statistics affect the chi-square distribution, note that the confidence level is not precisely defined (Cash 1979; Mattox et al. 1996). Furthermore, we point out that the PSF of *Fermi*-LAT (P6_v3) may be underestimated[14] and changes will have an impact on the fitted extent.

5.1.3. *Swift*-XRT data

The field was successfully proposed for observation with the X-ray telescope (XRT, 0.2–10 keV) onboard the *Swift* satellite (Gehrels et al. 2004, 2005). The observations (Obs. ID 00041265001) were carried out on 10 November, 2010, between 00:23:46 and 19:52:56 UT with a total effective exposure of 10.1 ks. Observations with the XRT were performed in photon-counting (PC) mode. The XRT data were calibrated and selected with standard screening criteria (*xrtpipeline*), using the HEAsoft 6.10 package for data reduction with the current version of calibration files available (release 2010-09-30). For the analysis, events with grades 0–12 (Burrows et al. 2005) were used. The spectral analysis was carried out with *Xspec* (12.6.0, Arnaud 1996), using the PC grade 0–12 response matrix *swxpc0to12s6_20070901v011.rmf* with the ancilliary response function generated by *xrtmkarf* for PSF correction and the position of the source considered. The on-source region was selected to contain about 90% of the PSF (≈47″). For background subtraction, an off-source region with radius of about 4′ was used. To ensure a spectral fit of sufficient quality, the spectra were rebinned to a minimum of 10 events per bin (with *grppha*). Owing to the low statistics accumulated, the C-statistic was used for spectral fitting.

In the field-of-view (FoV) of XRT, seven new X-ray sources were discovered with a probability of being background fluctuations smaller than 10^{-6}. We show them in Fig. 8. Their positional properties, measured flux, and the flux corrected for photoelectric absorption between 0.2 and 2 keV are listed in Table 7. The spectra of the two brightest sources are well-fitted by an absorption corrected power-law model, fixing the hydrogen column density $N_{\rm H}$ to the nominal Galactic value. The power-law index for the faint sources was fixed to 2.0. The Galactic hydrogen column density was obtained from the LAB HI survey (Kalberla et al. 2005) for the corresponding celestial positions.

Associations. The newly discovered X-ray sources were studied for possible associations in other accessible wavelengths. Multi-wavelength surveys covering the region are the NVSS in the radio, the 2MASS in the infrared, and the USNO B1.0 and SDSS DR7 catalogues for the optical band. For every *Swift* source we found at least one SDSS source to be positionally coincident (Table 8), with apparent magnitudes between $21^{\rm m}$ and $17^{\rm m}$. Owing to insufficient sensitivity, the very faint SDSS sources have not been detected by USNO.

6. Discussion

6.1. An AGN origin of 1FGL J0030.7+0724

The γ-ray signal of 1FGL J0030.7+0724 can be explained by a conventional AGN. With respect to the unified scheme for the spectral energy distribution (SED) of AGN (namely Flat Spectrum Radio Quasars (FSRQs) and blazars), see, e.g., Donato et al. (2001), the hard spectral index of 1FGL J0030.7+0724 ($\Gamma \approx 1.7$) is compatible with a high-energy-peaked blazar (HBL). Within the updated positional uncertainty of 1FGL J0030.7+0724 derived from the 24-month data (Fig. 8), the most likely radio counterpart is NVSS J003119+072456 ($f_{1.4\,{\rm GHz}} = (11.6 \pm 0.6)$ mJy), which positionally coincides with the newly discovered hard X-ray source SWIFT J003119.8+072454 ($\Gamma \approx 1.6$). Note that corresponding to the notation of Table 7, the *Swift* source is flagged with a G in Fig. 8. The energy flux observed between 0.2 and 2 keV is $\sim 2 \times 10^{-13}$ erg cm^{-2} s^{-1} (Table 7). Additionally, an optical counterpart of the radio and X-ray source is listed in the SDSS catalogue ($r = 17.4^{\rm m}$), see Table 8. In Fig. 9 we show an empirical model for the average SED of HBLs, which is based on the bolometric luminosity distribution of FSRQs and

---

[14] `http://fermi.gsfc.nasa.gov/ssc/data/analysis/LAT_caveats.html`

Table 7. X-ray sources detected with the *Swift*-XRT.

ID	Name SWIFT J	σ_{90} [arcsec]	S/N	f^{abs}(0.2–2 keV) [10^{-14} erg cm^{-2} s^{-1}]	N_{H} [10^{20} cm^{-2}]	ϕ_0 [10^{-5} keV^{-1} cm^{-2} s^{-1}]	Γ	f^{unabs}(0.2–2 keV) [10^{-14} erg cm^{-2} s^{-1}]
A	003000.3+072301^{a}	6	3.5	$3.5^{+1.1}_{-0.9}$	3.98	1.4 ± 0.4	2.0	5.2 ± 1.5
B	003017.8+072142	5	5.4	$5.0^{+3.0}_{-2.1}$	3.71	$2.2^{+0.6}_{-0.4}$	1.4 ± 0.3	$6.7^{+2.3}_{-1.8}$
C	003022.1+072623^{a}	6	3.1	$1.7^{+0.5}_{-0.4}$	3.10	$0.6^{+0.3}_{-0.2}$	2.0	$2.2^{+1.1}_{-0.7}$
D	003030.0+072013^{a}	5	5.1	$5.2^{+2.8}_{-2.0}$	3.71	$2.0^{+0.6}_{-0.4}$	2.0	$7.4^{+2.2}_{-1.5}$
E	003049.8+072316^{a}	6	3.0	$3.1^{+1.0}_{-1.1}$	3.10	$1.2^{+0.4}_{-0.3}$	2.0	$4.4^{+1.5}_{-1.1}$
F	003054.9+072328^{a}	6	2.8	$2.0^{+0.8}_{-0.6}$	3.10	$0.8^{+0.4}_{-0.3}$	2.0	$3.0^{+1.5}_{-1.1}$
G	003119.8+072454	5	6.5	$15.9^{+4.5}_{-5.0}$	3.10	$6.5^{+1.1}_{-0.9}$	1.6 ± 0.3	$20.7^{+8.8}_{-4.7}$

Notes. The FoV is centred on (RA, Dec) = (7.6315, 7.4211) deg with a radius of 13′. We give an internal ID, the position (SWIFT JHHMMSS.s±DDMMSS) and its corresponding error at 90% confidence level σ_{90} (determined with *xrtcentroid*), and the signal-to-noise ratio S/N (*Ximage*) of the observed flux f^{abs}. If constraining, a power-law model corrected for photoelectric absorption was fitted to the spectrum, $\mathrm{d}\phi/\mathrm{d}E = \phi_0\,(E/\mathrm{keV})^{-\Gamma}$. The hydrogen column density N_{H} was fixed during the fit. The unabsorbed flux f^{unabs} was derived from the power-law fit. (a) Due to a low S/N a two-parameter power-law fit is not constraining. The fluxes were derived assuming the index $\Gamma = 2.0$.

Table 8. Likely counterparts of the X-ray sources listed in Table 7.

ID	NVSS(a)		2MASS		USNO B1.0(b)		SDSS DR7		
	Name	S [mJy]	Name	K	Name	R	Name	g	Type
A	003000+072255	47(2)	–	–	0973-0005315	20.0^{m}	J003000.24+072254.7	20.3^{m}	6
B	–	–	–	–	0973-0005428	20.4^{m}	J003017.75+072140.6	19.6^{m}	6
C	–	–	–	–	–	–	J003022.22+072621.3	21.4^{m}	6
D	–	–	00302977+0720101	15.3^{m}	0973-0005481 0973-0005484	18.9^{m} 19.3^{m}	J003029.77+072010.3	18.5^{m}	3
E	–	–	–	–	–	–	J003049.61+072313.5	21.0^{m}	6
F	–	–	00305500+0723233	15.7^{m}	0973-0005560	18.2^{m}	J003054.80+072323.1 J003055.00+072323.2	20.7^{m} 18.5^{m}	6 6
G	003119+072456	11.6(6)	–	–	0974-0005617	18.6^{m}	J003119.71+072453.5	17.4^{m}	6

Notes. Scans ranging from radio (NVSS) to infrared (2MASS) and optical (USNO and SDSS) wavelength bands are given. The table lists the object's name and the catalogued flux or apparent magnitude. Here, parentheses indicate the corresponding error on the last decimal. Based on photometric morphology, SDSS provides a separation between galaxy-like (3) and star-like objects (6), see Lupton et al. (2001). (a) Frequency $\nu = 1.4$ GHz. (b) The column lists R2. If not available, R1 or B1 is given instead (see Monet et al. 2003, and references therein).

blazars (Fossati et al. 1997, 1998; Donato et al. 2001). The SED is normalised to the radio flux of NVSS J003119+072456 (at 5 GHz). For comparison, the spectral measurements of the optical and X-ray counterparts are presented as well. Within the observational errors and assuming temporal variability, the γ-ray spectrum of 1FGL J0030.7+0724 is consistent with the model prediction. Furthermore, the spectral index of the X-ray source agrees with an HBL, while its flux is fainter than predicted for an (average) HBL. This might be also explainable by temporal variability (the radio, X-ray, and γ-ray observations were not taken simultaneously), and blazars are well known to be variable in all wavelength bands, where the amplitude of variability increases with energy (Ulrich et al. 1997).

The other fainter objects in the uncertainty region (the radio source NVSS J003030+072132 and the two X-ray sources E and F, see Fig. 8) are less likely to be associated with 1FGL J0030.7+0724, but cannot be excluded. For NVSS J003030+072132, no X-ray association was detected with *Swift*-XRT at the level of 2×10^{-14} erg cm^{-2} s^{-1}. No conclusive optical counterpart is catalogued (above $\sim 26^{\mathrm{m}}$, see Sect. 5.1.1). With respect to the comparatively high γ-ray signal (cf., Fig. 9), this source therefore fails to provide a convincing counterpart for 1FGL J0030.7+0724. Similarly, the lacking radio detection as well as energy fluxes ($\sim 4 \times 10^{-14}$ erg cm^{-2} s^{-1}), which are much fainter than the HBL prediction, disfavour a coincidence of the X-ray sources E and F with 1FGL J0030.7+0724.

6.2. A DM subhalo origin of 1FGL J0030.7+0724

Without a clear indication for variability, it remains plausible that the γ-ray emission of 1FGL J0030.7+0724 originates from a DM subhalo. The analysis of the arrival times of the source photons (Sect. 5.1.2) is consistent with a temporally constant source of moderate spatial extent. The reconstructed high-energy flux within the statistical errors is $\phi_{\mathrm{p}}(10{-}100\,\mathrm{GeV}) \gtrsim 5 \times 10^{-11}\,\mathrm{cm}^{-2}\,\mathrm{s}^{-1}$, while the upper limit on the extent is $\theta_{\mathrm{s}} \lesssim 0.7°$, corresponding to $\theta_{68} \lesssim 0.3°$. As shown in Sect. 4, in realistic WIMP scenarios the high effective self-annihilation cross section required to explain the source with DM annihilation in a FHM subhalo is hardly compatible with current observational constraints (see Fig. 3 and Table 1). However, given the more realistic SHM, flux and extent of 1FGL J0030.7+0724 are consistent with a subhalo of mass between 10^6 and $10^8\,M_{\odot}$. Assuming a DM subhalo of $10^6\,M_{\odot}$, the resulting distance would be $2.4^{+1.0}_{-0.7}$ kpc, given the concentration scatter of the SHM model. For a WIMP of 500 GeV annihilating to $b\bar{b}$, the required minimum effective enhancement is 7 for a high-concentrated SHM subhalo with a corresponding distance of 1.7 kpc, while it increases to 31 for an average-concentrated subhalo with a corresponding distance of 2.4 kpc. Note that $h(0.7°) \approx 1.4$. An even lower boost factor is required for a lighter WIMP of 150 GeV which predominantly annihilates to $\tau^+\tau^-$: 3 (13) for a high-concentrated (average-concentrated) SHM subhalo.

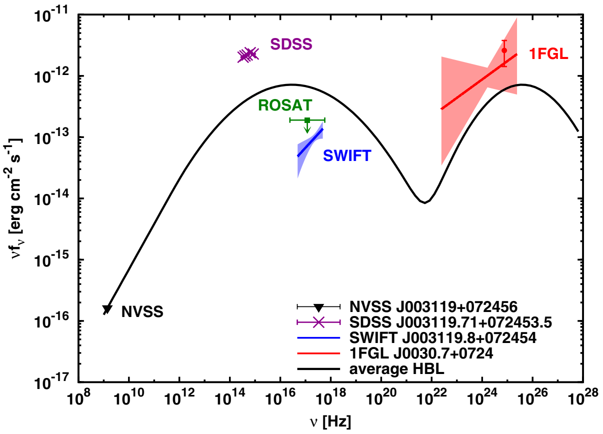

Fig. 9. Energy spectra of 1FGL J0030.7+0724 (solid red line) and the favoured radio (filled black triangle), optical (violet crosses, dereddened *ugriz* magnitudes), and X-ray (solid blue line) counterparts, together with the SED of an average HBL (solid black line). The SED was adapted from Donato et al., assuming the average redshift of known HBLs $z = 0.25$ (Donato et al. 2001), and is normalised to the radio flux of NVSS J003119+072456. The frequency-dependent energy flux νf_ν is given in the observer's frame. Note that the statistical errors of the radio and optical data points are too low to be resolved in the figure. Statistical uncertainties of the X- and γ-ray spectra are indicated by the corresponding shaded areas, which we derived with Eq. (1) in Abdo et al. (2009b). The filled red circle indicates the catalogued high-energy flux from *Fermi*-LAT. Observations with ROSAT provide an upper limit on the X-ray flux at the nominal position of 1FGL J0030.7+0724 between 0.1 and 2.4 keV, which is depicted by the green square (95% c.l., assuming $\Gamma = 2.0$, Borm 2010).

Table 9. Fluxes above the energy thresholds of MAGIC and H.E.S.S., predicted by a DM scenario of 1FGL J0030.7+0724.

Flux prediction for MAGIC/H.E.S.S. [%Crab]			
m_χ	150 GeV	500 GeV	1 TeV
$b\bar{b}$		0.3/10^{-3}	0.6/0.05
W^+W^-		0.5/0.01	0.8/0.2
$\tau^+\tau^-$	0.7/–	3.1/1.1	

Notes. The fluxes are listed in percentages of the Crab Nebula's flux, $\phi_{\rm Crab}(>50\,{\rm GeV}) \approx 1.6 \times 10^{-9}\,{\rm cm}^{-2}\,{\rm s}^{-1}$ (Albert et al. 2008a) and $\phi_{\rm Crab}(>300\,{\rm GeV}) \approx 1.5 \times 10^{-10}\,{\rm cm}^{-2}\,{\rm s}^{-1}$ (Aharonian et al. 2006c), respectively. Effective cross sections required by the individual DM scenarios are discussed in Sect. 6.2, raised by a factor of about 2.3 for $m_\chi = 1$ TeV.

Further decrease of the necessary boost may be provided by subsubstructure and cuspier profiles (Sect. 4).

In addition to theoretical uncertainties on halo properties and their expected scatter (Sect. 2.1), observational uncertainties affect the distance and boost factor estimates. The uncertainties on the flux directly change the boost, while uncertainties on the most crucial measurement, the angular extent θ_s, affect both the required boost and the distance estimate (Sect. 3). The discussed object 1FGL J0030.7+0724 serves as an appropriate benchmark, because the corresponding uncertainties are representative for a typical DM subhalo source. The observational uncertainties are of similar magnitude as the theoretical ones.

6.3. Remarks and prospects for IACTs

The 28-month data of *Fermi*-LAT contains no additional photon detected around the nominal position. This lowers the probability of steadiness to ~25% and may indicate variability, which supports a BL Lac scenario. Vice versa, such a behaviour would also be anticipated by a selection bias: If the true flux is lower than the value found in the discovery data set, the discovery condition would only allow for the detection of sources where the photon number has been fluctuating upwards. Poisson fluctuations of this faint signal could have accounted for a detection with the LAT even if the true flux had remained below the detection sensitivity.

It is instructive to note that with regard to a definite identification of a counterpart (or ruling out a candidate) from observations in other wavelength regimes the limiting factor is the accuracy of the *Fermi*-LAT source position ($O(5')$, cf., Table 4) and PSF. With just six detected photons, probably including one background photon, the source is close to the confusion limit. This situation can only be resolved by future instruments with much larger effective areas, such as the proposed CTA, which will probe deep into the expected population of subhaloes. The much larger number of photons would help to infer significantly improved source positions. Furthermore, for detecting a spectral cut-off and in case of heavy WIMPs ($m_\chi > 1$ TeV), observations in the VHE range with IACTs are favoured. For the particular DM scenarios proposed for 1FGL J0030.7+0724, fluxes anticipated in the energy ranges accessible for MAGIC and H.E.S.S., $\phi(>50\,{\rm GeV})$ and $\phi(>300\,{\rm GeV})$, respectively, are listed in Table 9 (given by $\phi(>E) \propto N_\gamma(>E)/N_\gamma(10{-}100\,{\rm GeV})$, see Eq. (8)). Additionally, flux estimates for WIMPs with $m_\chi = 1$ TeV were derived. Note that the required effective cross sections (see Sect. 6.2) increase by a factor of 2.3, because $\langle\sigma v\rangle_{\rm eff} \propto m_\chi^2\, N_\gamma(10{-}100\,{\rm GeV})^{-1}$. Also note that fluxes expected for VERITAS are comparable to those for H.E.S.S.

The low energy threshold of MAGIC leads to comparatively high integrated VHE fluxes for $m_\chi < 1$ TeV. The flux prediction for MAGIC is of $O(1\%)$ of the Crab Nebula's for the favoured $\tau^+\tau^-, m_\chi = 150$ GeV and $W^+W^-, m_\chi = 1$ TeV model. With MAGIC, 50 h of observation are necessary to detect this source with more than 5σ. For comparison, predicted fluxes for H.E.S.S. are not higher than 0.2% Crab for these models, which requires a few hundred hours of observation (Aharonian et al. 2006c). We remark that advanced analysis methods improve the sensitivity of H.E.S.S. by a factor of 2 (de Naurois & Rolland 2009). In the near future, an additional telescope (H.E.S.S.-II) will lower the energy threshold of H.E.S.S. to about 25–50 GeV. For the corresponding flux level of 1% Crab, the required observation time for H.E.S.S.-II and MAGIC will be similar. Furthermore, the planned CTA observatory will be able to detect such a source in about 50 h (the CTA consortium 2010).

7. Summary and conclusions

Hierarchical structure formation predicts Milky Way-sized galaxies to host numerous DM subhaloes with masses ranging from 10^{10} down to a cut-off scale of 10^{-3}–$10^{-11}\,M_\odot$. Given standard WIMP scenarios, e.g., motivated by supersymmetry, we have demonstrated that DM subhaloes are detectable with the currently operating γ-ray telescope *Fermi*-LAT. Based upon state-of-the-art models, detectable subhaloes would observationally appear as faint high-energy γ-ray sources between 10 and 100 GeV with a flux at the sensitivity level of *Fermi*-LAT (~$10^{-10}\,{\rm cm}^{-2}\,{\rm s}^{-1}$ between 10 and 100 GeV for one year). The observable γ-ray emission exhibits a moderate spatial extent below ~0.5°. Subhaloes favoured for detection are massive (10^5–$10^8\,M_\odot$) at distances of O(kpc), while low-mass subhaloes are not detectable. Within the intrinsic halo-to-halo scatter, only a moderate enhancement of the self-annihilation cross section preferred by standard cosmology, $\langle\sigma v\rangle_0 = 3 \times 10^{-26}\,\mathrm{cm}^3\,\mathrm{s}^{-1}$, between 3 and 12 is necessary (dependent on the WIMP model), which is consistent with current observational constraints. Increasing sensitivity for a data-taking period of five years will allow us to resolve subhaloes requiring a cross section enhanced by a factor between 1.3 and 5. Additional sub-substructure within a subhalo may lower the required enhancement. Within statistics, *one* massive subhalo could be detectable with *Fermi*-LAT in one year and might appear in the first-year catalogue (1FGL), assuming a subhalo population predicted by numerical N-body simulations. Regarding the 1FGL, the high-energy flux (10−100 GeV) of subhalo candidates should be fainter than $\sim 4 \times 10^{-10}\,\mathrm{cm}^{-2}\,\mathrm{s}^{-1}$ (for the WIMP scenarios considered here).

Intensive searches for subhaloes in the 1FGL reveal twelve candidates, which are unassociated, non-variable, high-latitude sources detected above 10 GeV. The physical origin of the most promising object selected by lacking association, faintness, and spectral index, 1FGL J0030.7+0724, was investigated by analysing the 24-month data set of *Fermi*-LAT. With dedicated *Swift*-XRT observations (10.1 ks), seven X-ray sources were discovered around 1FGL J0030.7+0724. Located within the positional uncertainty of the γ-ray source, a radio source positionally coincident with a newly discovered X-ray source hints at a conventional HBL origin of 1FGL J0030.7+0724. However, owing to a large positional uncertainty and the lacking detection of variability, the possibility of a dark nature remains. The measured high-energy flux and spatial extent of the source is compatible with a DM subhalo between 10^6 and $10^8\,M_\odot$ in a distance of about 2 kpc, driven by a 500 (150) GeV WIMP self-annihilating to $b\bar{b}$ ($\tau^+\tau^-$). In this case, the required enhancement of $\langle\sigma v\rangle_0$ is 7 (3) within the intrinsic scatter of the subhalo model, given a subhalo of $10^6\,M_\odot$.

Establishing the – probably more likely – HBL scenario of 1FGL J0030.7+0724 requires a significant detection of γ-ray variability and a confirmation of the radio as well as X-ray counterparts. Vice versa, a steady γ-ray flux with a spectral shape predicted by self-annihilating WIMPs would hint at a DM nature of the object. This validates the necessity of additional intense and long multi-wavelength observations. In particular, IACTs offer a unique capability to reduce the positional uncertainty of faint LAT sources and to detect a spectral cut-off in the VHE range. A detection of the subhalo candidate 1FGL J0030.7+0724 may be possible with telescope systems like H.E.S.S.-II, MAGIC, and CTA within about 50 h of observation.

Our results encourage the search for more subhalo candidates in current and upcoming (very-)high-energy data releases. However, even in optimistic scenarios the expected number of LAT-detectable subhaloes is small. Furthermore, a longer exposure time – while certainly helpful with regard to the single candidate discussed in this work – will not neccessarily remedy the general problem of the γ-ray photon count that limits the positional accuracy and therefore the chance of identifying counterparts. Given $m_\chi < 1$ TeV, acquiring a sufficiently large number of detections which may solve the subhalo problem requires higher sensitivity in the high-energy range.

Acknowledgements. We kindly acknowledge helpful discussions with our colleagues Katharina Borm, Torsten Bringmann, Wilfried Buchmüller, Frederike Jäger, Andrei Lobanov, and Martin Raue. We kindly acknowledge the *Swift* PI Neil Gehrels and his team for the prompt response to our ToO request and the corresponding observations. The help of the Fermi HelpDesk is kindly acknowledged. We kindly thank the anonymous referee for useful comments. This work was supported through the collaborative research center (SFB) 676 "Particles, Strings, and the Early Universe" at the University of Hamburg. This publication makes use of data products from the Two Micron All Sky Survey, which is a joint project of the University of Massachusetts and the Infrared Processing and Analysis Center/California Institute of Technology, funded by the National Aeronautics and Space Administration and the National Science Foundation. This publication makes use of data from the Sloan Digital Sky Survey (SDSS). Funding for the SDSS and SDSS-II has been provided by the Alfred P. Sloan Foundation, the Participating Institutions, the National Science Foundation, the US Department of Energy, the National Aeronautics and Space Administration, the Japanese Monbukagakusho, the Max Planck Society, and the Higher Education Funding Council for England. The SDSS Web Site is `http://www.sdss.org/`. The SDSS is managed by the Astrophysical Research Consortium for the Participating Institutions. The Participating Institutions are the American Museum of Natural History, Astrophysical Institute Potsdam, University of Basel, University of Cambridge, Case Western Reserve University, University of Chicago, Drexel University, Fermilab, the Institute for Advanced Study, the Japan Participation Group, Johns Hopkins University, the Joint Institute for Nuclear Astrophysics, the Kavli Institute for Particle Astrophysics and Cosmology, the Korean Scientist Group, the Chinese Academy of Sciences (LAMOST), Los Alamos National Laboratory, the Max-Planck-Institute for Astronomy (MPIA), the Max-Planck-Institute for Astrophysics (MPA), New Mexico State University, Ohio State University, University of Pittsburgh, University of Portsmouth, Princeton University, the United States Naval Observatory, and the University of Washington. This research has made use of the NASA/IPAC Extragalactic Database (NED) which is operated by the Jet Propulsion Laboratory, California Institute of Technology, under contract with the National Aeronautics and Space Administration.

Appendix A: Concentration of Aquarius subhaloes

The Aquarius simulation provides results on the profile parameters of resolved subhaloes, taking tidal interaction into account (Springel et al. 2008a). These results are used to derive the distance-averaged virial concentration of subhaloes to confront it with the toy-model predictions used here.

Following up on Eq. (1), the *tidal* concentration $c_\mathrm{t} \equiv R_\mathrm{t}/r_\mathrm{s}$ is introduced (cf., Ando 2009), where R_t denotes the tidal and therefore physical radius of a subhalo. For an NFW-type mass density profile, $c_\mathrm{t} = \exp[W(-\mathrm{e}^{-a}) + a] - 1$, $a \equiv 1 + M_\mathrm{t}/(4\pi\rho_\mathrm{s} r_\mathrm{s}^3)$, where $W(x)$ denotes Lambert's W-function and M_t the tidal subhalo mass. In numerical simulations, the directly "observable" quantities of (sub)haloes are related to the dynamics of the halo system, including the maximum velocity V_max and the distance r_max where V_max is reached. To recover the canonical parameters r_s and ρ_s related to the density profile, we use approximate relations $2[V_\mathrm{max}/(H_0 r_\mathrm{max})]^2 \simeq 5.80 \times 10^4\,[M_\mathrm{t}/(10^8\,M_\odot)]^{-0.18}$ and $M_\mathrm{t} \simeq 3.37 \times 10^7\,[V_\mathrm{max}/(10\,\mathrm{km\,s^{-1}})]^{3.49}\,M_\odot$, fitting the results of the simulation (Springel et al. 2008a; Ando 2009). Given analytical relations between $(r_\mathrm{max}, V_\mathrm{max})$ and $(r_\mathrm{s}, \rho_\mathrm{s})$ for the NFW profile (e.g., Eq. (8) in Kuhlen et al. 2008), this yields $r_\mathrm{s}^\mathrm{Aq}(M_\mathrm{t}) \simeq 0.094\,[M_\mathrm{t}/(10^6\,M_\odot)]^{0.38}$ kpc and $\rho_\mathrm{s}^\mathrm{Aq}(M_\mathrm{t}) \simeq 9.6 \times 10^5 \rho_\mathrm{crit}\,[M_\mathrm{t}/(10^6\,M_\odot)]^{-0.18}$. Therefore, the tidal concentration c_t^Aq is determined via $a^\mathrm{Aq} \simeq 1 + 0.66\,[M_\mathrm{t}/(10^6\,M_\odot)]^{0.04}$, which is valid for masses above the resolution limit of the simulation, $M_\mathrm{t} \gtrsim 3.2 \times 10^4\,M_\odot$.

The virial concentration of Aquarius subhaloes is given by $c_\mathrm{vir}^\mathrm{Aq}(M_\mathrm{vir}) = [3M_\mathrm{vir}/(4\pi\Delta_\mathrm{c}\rho_\mathrm{crit})]^{1/3}/r_\mathrm{s}^\mathrm{Aq}(M_\mathrm{vir})$, where the characteristic radius as function of the virial subhalo mass is obtained from an empirical relation mapping M_vir to M_t. Based on c_t^Aq and assuming the FHM virial concentration-to-mass relation (Eq. (2)), the relative tidal mass is $M_\mathrm{t}/M_\mathrm{vir} \approx f[c_\mathrm{t}^\mathrm{Aq}(M_\mathrm{t})]/f[c_\mathrm{vir}^\mathrm{FHM}(M_\mathrm{vir})]$, since $M = 4\pi\rho_\mathrm{s} r_\mathrm{s}^3 f(c)$. Hereby, we have assumed that tidal effects on inner subhalo parts are negligible: $\rho_s(M_{\mathrm{vir}})r_s(M_{\mathrm{vir}})^3 \approx \rho_s(M_t)r_s(M_t)^3$. With $f(c_t^{\mathrm{Aq}}) = a^{\mathrm{Aq}} - 1$, the distance-averaged M_t-M_{vir} relation is

$$M_t(M_{\mathrm{vir}}) \simeq \left(\frac{712.6\,\mathrm{kpc}^{-3}}{4\pi\rho_{\mathrm{crit}}}\right)^{1.04} \left(\frac{M_{\mathrm{vir}}}{f(c_{\mathrm{vir}}^{\mathrm{FHM}})}\right)^{1.04} M_\odot. \tag{A.1}$$

For massive subhaloes ($\gtrsim 10^4\,M_\odot$), $f(c_{\mathrm{vir}}^{\mathrm{FHM}})^{-1.04}$ is well fit by a power law, $f[c_{\mathrm{vir}}^{\mathrm{FHM}}(M_{\mathrm{vir}})]^{-1.04} \approx 0.34\,[M_{\mathrm{vir}}/(10^6\,M_\odot)]^{0.02}$, yielding $M_t/M_{\mathrm{vir}} \approx 0.23[M_{\mathrm{vir}}/(10^6\,M_\odot)]^{0.06}$ for $M_t \gtrsim 3.2 \times 10^4\,M_\odot$. This reveals $r_s^{\mathrm{Aq}}(M_{\mathrm{vir}}) \simeq 0.054\,[M_{\mathrm{vir}}/(10^6\,M_\odot)]^{0.40}$ kpc and, therefore, the distance-averaged virial concentration of subhaloes

$$c_{\mathrm{vir}}^{\mathrm{Aq}}(M_{\mathrm{vir}}) \simeq 46.8 \left(\frac{M_{\mathrm{vir}}}{10^6\,M_\odot}\right)^{-0.07} \tag{A.2}$$

for $M_{\mathrm{vir}} \in [1.5 \times 10^5; \sim 10^{10}]\,M_\odot$.

Appendix B: Moderately extended *Fermi* sources

For γ-ray catalogues such as 1FGL, instrument data have been analysed assuming sources to be point-like. Given that detectable subhaloes would appear as moderately extended according to the PSF of *Fermi*-LAT (see Sect. 4.1.1, $\sigma_{\mathrm{PSF}} \approx 0.15°$ for $E = 10$ GeV), we investigated the effect of the 1FGL point-source-analysis framework on extended sources.

To study the high-energy flux ϕ_p(10−100 GeV) reconstructed by the point-source analysis for a given intrinsic (subhalo) extent θ_s, a Monte-Carlo (MC) simulation dedicated to the particular source 1FGL J0030.7+0724 was used. Based on the 11-month data set (see Sect. 5.1.2 for details), the celestial coordinates of each of the five source photons between 10 and 100 GeV were re-simulated. The intensity profile was assumed to follow the line-of-sight integral over the (squared) NFW profile of a subhalo for the given θ_s (peaking at the nominal source position). Other observational photon parameters, such as energy, inclination, detection time, conversion type, and event class (see Table 6), were kept fixed. Subsequently, detectional influences were accounted for by smoothing with the PSF. For each θ_s, 500 iterations were analysed with the framework described in Sect. 5.1.2 (*gtfindsrc* and *gtlike*) according to flux and significance ($S \approx \sqrt{\mathrm{TS}}$, where TS denotes the test statistic of the analysis). All other sources within the ROI were kept fixed. The study is restricted to the signal-dominated regime chosen to be $\theta_s \lesssim 1°$ given the low background N_{bg}. Since $\theta_{68} \approx 0.46°$, this corresponds to $\sim 3\sigma_{\mathrm{PSF}}$. Justified by the low background, all photons were treated as signal events.

The θ_s dependence of the sample-averaged reconstructed flux ϕ_p(10−100 GeV) and corresponding test statistic TS is shown in the two upper panels of Fig. B.1. For large θ_s, the probability of photons to be located far away from their central position increases. Therefore, both ϕ_p and TS decrease because of a minor contribution of outer photons to the point-source region (defined by the PSF). For $\theta_s \approx 1°$, the average significance drops below the detection criterion (TS ≥ 25). Note that TS ≥ 25 still holds for about 35% of the simulated samples.

In terms of Eq. (8), appropriate investigation of candidates provided by point-source catalogues is therefore admitted by a scaling $h(\theta_s)$, which allows us to map the catalogued flux ϕ_p to the true flux ϕ of the entire source. The angular dependence of h is shown in the lower panel of Fig. B.1. Given $\phi = h(\theta_s)\,\phi_p$, the factor was derived by defining $h(0°) = 1$. Conservatively, the complete MC sample was used to derive $h(\theta_s)$, including realisations with TS < 25 [15]. As expected in the signal-dominated regime, the increase of h with increasing θ_s is comparatively slight, while it is fairly linear in the background-dominated regime. Note again that this result holds for sources similar to 1FGL J0030.7+0724 at high galactic latitudes only, while in general $h = h(l, b, \theta_s)$.

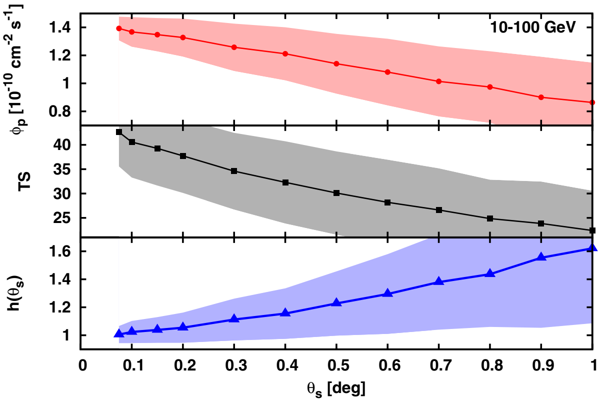

Fig. B.1. Average (solid lines) and rms (shaded areas) of ϕ_p(10−100 GeV) (*upper panel*), TS (*middle panel*), and the scaling $h(\theta_s)$ (*lower panel*) as function of the intrinsic angular extent θ_s. For each θ_s, a sample of 500 simulations of the 1FGL J0030.7+0724 photon distribution between 10 and 100 GeV assuming a DM subhalo intensity profile was analysed with the 1FGL point-source-analysis framework.

Vice versa, Fig. B.1 states a reasonable (but conservative) value of the sensitivity of *Fermi*-LAT for hard sources of similar type: $\phi_p(10{-}100\,\mathrm{GeV}) \approx 10^{-10}\,\mathrm{cm}^{-2}\,\mathrm{s}^{-1}$. Note that this value is similar to the point-source sensitivity stated in Atwood et al. (2009).

Appendix C: Subhalo-induced diffuse flux

In the following, the diffuse flux of the subhalo population is derived using a prescription by Ando (2009), which is extended to include the probability distribution of the concentration parameter c (see Eq. (4)). Numerical N-body simulations have demonstrated that the differential subhalo number density $\mathrm{d}n_{\mathrm{sh}} = \mathcal{N}(r, M)\,\mathrm{d}M$ follows a power-law in subhalo mass M. Following standard assumptions, the number density $\mathcal{N}(r, M)$ factorises such that $\mathcal{N}(r, M) \propto n_{\mathrm{sh}}(r) \cdot M^{-\alpha}$, where $\alpha = 1.9$ and r is the distance to the host's centre. In simulations, the spatial density distribution $n_{\mathrm{sh}}(r)$ is consistently found to be "anti-biased" and, e.g., $n_{\mathrm{sh}}(r) \propto \rho_{\mathrm{Ein}}(r)$ (Springel et al. 2008a), where $\rho_{\mathrm{Ein}}(r)$ denotes the Einasto profile (Einasto 1965)

$$\rho_{\mathrm{Ein}}(r) \propto \exp\left\{-\frac{2}{\alpha_{\mathrm{E}}}\left[\left(\frac{r}{r_{-2}}\right)^{\alpha_{\mathrm{E}}} - 1\right]\right\}. \tag{C.1}$$

For a Milky Way-sized halo, the best-fit parameters for the subhaloes' spatial distribution $\rho_{\mathrm{Ein}}(r)$ have been found to be $\alpha_{\mathrm{E}} = 0.68$ and $r_{-2} = 0.81\,c_{200}^{\mathrm{MW}}\,r_s^{\mathrm{MW}}$ (Springel et al. 2008a), where $c_{200}^{\mathrm{MW}} \approx 15$ (Catena & Ullio 2010). Using $\mathcal{N}(r, M)$ normalised

---

[15] Given the selection bias of the 1FGL catalogue, TS ≥ 25, a more stringent deduction of $h(\theta_s)$ should include realisations with TS ≥ 25 only. This lowers the effective scaling factor $h(\theta_s)$.

to represent a probability density function in M, the differential density is

$$\frac{\mathrm{d}n_{\mathrm{sh}}(r,M)}{\mathrm{d}M} = n_{\mathrm{sh}}(r)\frac{\alpha-1}{M_{\mathrm{min}}}\left(\frac{M}{M_{\mathrm{min}}}\right)^{-\alpha}, \tag{C.2}$$

where $M_{\mathrm{min}} \ll M_{\mathrm{max}}$ are the minimum and maximum mass of Galactic subhaloes, respectively. The normalisation of the subhalo number density $n_{\mathrm{sh}}(r)$ is chosen such that the fraction of the host's mass distributed in subhaloes $f_{\mathrm{sh}} \equiv M_{\mathrm{sh}}/M_{\mathrm{vir}}^{\mathrm{MW}} = 15\%$ for the cut-off scale $M_{\mathrm{min}} = 10^{-6}\,M_{\odot}$, where $M_{\mathrm{vir}}^{\mathrm{MW}} = (1.49 \pm 0.17)\times10^{12}\,M_{\odot}$ (Catena & Ullio 2010). The chosen value of f_{sh} is consistent with recent estimates $f_{\mathrm{sh}} = 10{-}50\%$ (Diemand et al. 2005; Diemand & Moore 2011; Diemand et al. 2008b; Springel et al. 2008b). The total mass contained in subhaloes is given by

$$f_{\mathrm{sh}}M_{\mathrm{vir}}^{\mathrm{MW}} = 4\pi\int_0^{R_{\mathrm{vir}}^{\mathrm{MW}}}\mathrm{d}r\,r^2\int_{M_{\mathrm{min}}}^{M_{\mathrm{max}}}\mathrm{d}M\,M\frac{\mathrm{d}n_{\mathrm{sh}}(r,M)}{\mathrm{d}M}\cdot \tag{C.3}$$

Solving for an Einasto-type profile and $\alpha \neq 2$ yields

$$\begin{aligned} n_{\mathrm{sh}}(r) \quad = \quad & \frac{f_{\mathrm{sh}}M_{\mathrm{vir}}^{\mathrm{MW}}}{2\pi r_{-2}^3 M_{\mathrm{min}}}\left(\frac{2}{\alpha_{\mathrm{E}}}\right)^{3/\alpha_{\mathrm{E}}-1}\Gamma\left[\frac{3}{\alpha_{\mathrm{E}}},\frac{2}{\alpha_{\mathrm{E}}}\left(\frac{R_{\mathrm{vir}}^{\mathrm{MW}}}{r_{-2}}\right)^{\alpha_{\mathrm{E}}}\right]^{-1} \\ & \times\frac{2-\alpha}{(\alpha-1)(\Lambda^{2-\alpha}-1)}\exp\left[-\frac{2}{\alpha_{\mathrm{E}}}\left(\frac{r}{r_{-2}}\right)^{\alpha_{\mathrm{E}}}\right], \end{aligned} \tag{C.4}$$

where $\Gamma(a,x)$ is the lower incomplete gamma function and $\Lambda = M_{\mathrm{max}}/M_{\mathrm{min}}$.

The minimum mass M_{min} of subhaloes is governed by the details of kinetic decoupling of WIMPs in the early Universe (Berezinsky et al. 2003, 2006; Green et al. 2005; Bringmann 2009). Depending upon the mass and composition of, e.g., the neutralino, a wide range of minimal subhalo masses has been considered in the literature, namely $M_{\mathrm{min}} \in [10^{-11}; 10^{-3}]\,M_{\odot}$. Here, two benchmark cases are considered for M_{min}, i.e., 10^{-10} and $10^{-6}\,M_{\odot}$, bracketing the 500 GeV neutralino scenario discussed by Bringmann (2009). The upper mass limit was fixed to $M_{\mathrm{max}} = 10^{-2}\,M_{\mathrm{vir}}^{\mathrm{MW}} \approx 10^{10}\,M_{\odot}$. Results do not depend on the exact value chosen for M_{max}.

Using $\mathcal{L}(M,D)$ (Sects. 2.1 and 2.2), the average specific intensity from a subhalo population with extended, isotropic emissivity profiles is given towards a galactic direction $\hat{\boldsymbol{n}}$ by

$$\langle I_\nu(\hat{\boldsymbol{n}})\rangle = \int\limits_{M_{\mathrm{min}}}^{M_{\mathrm{max}}}\mathrm{d}M\int\limits_{s_*(\mathcal{L}(M,\tilde{s}))}^{s_{\mathrm{max}}(\hat{\boldsymbol{n}})}\mathrm{d}s\frac{\mathrm{d}n_{\mathrm{sh}}(r(s,\hat{\boldsymbol{n}}),M)}{\mathrm{d}M}\int\mathrm{d}c\,P(c,\overline{c})\,\frac{\mathcal{L}_\nu(M,c)}{4\pi}, \tag{C.5}$$

assuming that the spatial extent of each subhalo is much smaller than the scale on which the subhalo distribution changes significantly. The total photon rate $\mathcal{L}_\nu$ is given by Eq. (6) with the substitution $N_\gamma \to E\,\mathrm{d}N_\gamma/\mathrm{d}E$. Furthermore, $\mathcal{L}_\nu(M)$ is required to be one-to-one. The galactocentric radius corresponding to the position $s\hat{\boldsymbol{n}}$ is $r(s,\psi) = (R_0^2 + s^2 - 2R_0 s\cos\psi)^{1/2}$, where ψ denotes the angle between $\hat{\boldsymbol{n}}$ and $\hat{\boldsymbol{R}}_0$ ($\cos(\psi) = \langle\hat{\boldsymbol{n}},\hat{\boldsymbol{R}}_0\rangle$). Subhaloes bright enough to be detected as individual sources are not considered to contribute to the diffuse emission. Therefore, the lower limit of the line-of-sight integral is set by the detection criterion $\mathcal{L} \geq 4\pi s_*^2\phi_{\mathrm{sens}}$, where ϕ_{sens} denotes the flux sensitivity for a detection in one year with *Fermi*-LAT, see Sect. 4. Since $R_0 \ll R_{\mathrm{vir}}$, the upper bound of the s-integral $s_{\mathrm{max}}(\hat{\boldsymbol{n}}) \approx R_{\mathrm{vir}}^{\mathrm{MW}}$. The SHM photon rate is a function of both M and s, and therefore s_* also depends slightly on s. Conservatively, $s_*(M,s) = s_*(M,\tilde{s})$, $\tilde{s} = R_{\mathrm{vir}}^{\mathrm{MW}}$, revealing a lower bound on s_*.

References

Aad, G., Abbott, B., Abdallah, J., et al. 2011, Eur. Phys. J. C, 71, 1682
Abazajian, K. N., Adelman-McCarthy, J. K., Agüeros, M. A., et al. 2009, ApJS, 182, 543
Abazajian, K. N., Agrawal, P., Chacko, Z., & Kilic, C. 2010, J. Cosmology Astropart. Phys., 11, 41
Abdo, A. A., Ackermann, M., Ajello, M., et al. 2009a, Science, 325, 848
Abdo, A. A., Ackermann, M., Ajello, M., et al. 2009b, ApJ, 707, 1310
Abdo, A. A., Ackermann, M., Ajello, M., et al. 2010a, ApJS, 188, 405
Abdo, A. A., Ackermann, M., Ajello, M., et al. 2010b, Phys. Rev. Lett., 104, 101101
Abdo, A. A., Ackermann, M., Ajello, M., et al. 2010c, ApJ, 712, 147
Abramowski, A., Acero, F., Aharonian, F., et al. 2011a, ApJ, 735, 12
Abramowski, A., Acero, F., Aharonian, F., et al. 2011b, Phys. Rev. Lett., 106, 161301, H.E.S.S. Collaboration
Acciari, V. A., Arlen, T., Aune, T., et al. 2010, ApJ, 720, 1174
Ackermann, M., Ajello, M., Allafort, A., et al. 2010, J. Cosmology Astropart. Phys., 5, 25
Aharonian, F., Akhperjanian, A. G., Bazer-Bachi, A. R., et al. 2006a, Phys. Rev. Lett., 97, 221102
Aharonian, F., Akhperjanian, A. G., Bazer-Bachi, A. R., et al. 2006b, Phys. Rev. Lett., 97, 249901
Aharonian, F., Akhperjanian, A. G., Bazer-Bachi, A. R., et al. 2006c, A&A, 457, 899
Aharonian, F., Akhperjanian, A. G., Bazer-Bachi, A. R., et al. 2006d, Nature, 439, 695
Aharonian, F., Akhperjanian, A. G., Bazer-Bachi, A. R., et al. 2008, Astropart. Phys., 29, 55
Aharonian, F., Akhperjanian, A. G., de Almeida, U. B., et al. 2009, ApJ, 691, 175
Aharonian, F., Akhperjanian, A. G., Bazer-Bachi, A. R., et al. 2010, Astropart. Phys., 33, 274
Albert, J., Aliu, E., Anderhub, H., et al. 2008a, ApJ, 674, 1037
Albert, J., Aliu, E., Anderhub, H., et al. 2008b, ApJ, 679, 428
Aleksić, J., Antonelli, L. A., Antoranz, P., et al. 2010, ApJ, 710, 634
Aleksić, J., Alvarez, E. A., Antonelli, L. A., et al. 2011, J. Cosmology Astropart. Phys., 6, 35
Aliu, E., Anderhub, H., Antonelli, L. A., et al. 2009, ApJ, 697, 1299
Anderson, B., Kuhlen, M., Diemand, J., Johnson, R. P., & Madau, P. 2010, ApJ, 718, 899
Ando, S. 2009, Phys. Rev. D, 80, 023520
Arkani-Hamed, N., Finkbeiner, D. P., Slatyer, T. R., & Weiner, N. 2009, Phys. Rev. D, 79, 015014
Arnaud, K. A. 1996, in Astronomical Data Analysis Software and Systems V, ed. G. H. Jacoby, & J. Barnes, ASP Conf. Ser., 101, 17
Atwood, W. B., Abdo, A. A., Ackermann, M., et al. 2009, ApJ, 697, 1071
Baltz, E. A., Taylor, J. E., & Wai, L. L. 2007, ApJ, 659, L125
Baltz, E. A., Berenji, B., Bertone, G., et al. 2008, J. Cosmology Astropart. Phys., 7, 13
Becker, R. H., White, R. L., & Helfand, D. J. 1995, ApJ, 450, 559
Berezinsky, V. S., Gurevich, A. V., & Zybin, K. P. 1992, Phys. Lett. B, 294, 221
Berezinsky, V., Dokuchaev, V., & Eroshenko, Y. 2003, Phys. Rev. D, 68, 103003
Berezinsky, V., Dokuchaev, V., & Eroshenko, Y. 2006, Phys. Rev. D, 73, 063504
Berezinsky, V., Dokuchaev, V., & Eroshenko, Y. 2008, Phys. Rev. D, 77, 083519
Bergström, L., Bringmann, T., Eriksson, M., & Gustafsson, M. 2005a, Phys. Rev. Lett., 95, 241301
Bergström, L., Bringmann, T., Eriksson, M., & Gustafsson, M. 2005b, Phys. Rev. Lett., 94, 131301
Bertone, G. 2010, Nature, 468, 389
Bertone, G., Hooper, D., & Silk, J. 2005, Phys. Rep., 405, 279
Borm, K. 2010, Research on a Possible Dark Matter Substructure within the Galactic Halo, Bachelor thesis, University of Hamburg, Germany
Bringmann, T. 2009, New J. Phys., 11, 105027
Bringmann, T., Bergström, L., & Edsjö, J. 2008, J. High Energy Phys., 1, 49
Brun, P., Moulin, E., Diemand, J., & Glicenstein, J. 2011, Phys. Rev. D, 83, 015003
Bryan, G. L., & Norman, M. L. 1998, ApJ, 495, 80
Buckley, M. R., & Hooper, D. 2010, Phys. Rev. D, 82, 063501
Bullock, J. S., Kolatt, T. S., Sigad, Y., et al. 2001, MNRAS, 321, 559
Burrows, D. N., Hill, J. E., Nousek, J. A., et al. 2005, Space Sci. Rev., 120, 165
Cash, W. 1979, ApJ, 228, 939
Catena, R., & Ullio, P. 2010, J. Cosmology Astropart. Phys., 8, 4
Cirelli, M., Panci, P., & Serpico, P. D. 2010, Nucl. Phys. B, 840, 284
CMS Collaboration 2011, JHEP, 6, 93
Colafrancesco, S., Profumo, S., & Ullio, P. 2006, A&A, 455, 21
Colafrancesco, S., Profumo, S., & Ullio, P. 2007, Phys. Rev. D, 75, 023513
Condon, J. J., Cotton, W. D., Greisen, E. W., et al. 1998, AJ, 115, 1693

D'Amico, G., Kamionkowski, M., & Sigurdson, K. 2009 [arXiv:0907.1912]
de Naurois, M., & Rolland, L. 2009, Astropart. Phys., 32, 231
Diemand, J., & Moore, B. 2011, Adv. Science Lett., 4, 297
Diemand, J., Moore, B., & Stadel, J. 2005, Nature, 433, 389
Diemand, J., Kuhlen, M., & Madau, P. 2007, ApJ, 667, 859
Diemand, J., Kuhlen, M., & Madau, P. 2008a, ApJ, 679, 1680
Diemand, J., Kuhlen, M., Madau, P., et al. 2008b, Nature, 454, 735
Donato, D., Ghisellini, G., Tagliaferri, G., & Fossati, G. 2001, A&A, 375, 739
D'Onghia, E., Springel, V., Hernquist, L., & Keres, D. 2010, ApJ, 709, 1138
Doro, M. 2011, Nuclear Instruments and Methods in Physics Research A, 630, 285, for the CTA Consortium
Einasto, J. 1965, Trudy Inst. Astroz. Alma-Ata, 51, 87
Eke, V. R., Cole, S., & Frenk, C. S. 1996, MNRAS, 282, 263
Fornengo, N., Pieri, L., & Scopel, S. 2004, Phys. Rev. D, 70, 103529
Fossati, G., Celotti, A., Ghisellini, G., & Maraschi, L. 1997, MNRAS, 289, 136
Fossati, G., Maraschi, L., Celotti, A., Comastri, A., & Ghisellini, G. 1998, MNRAS, 299, 433
Gehrels, N., Chincarini, G., Giommi, P., et al. 2004, ApJ, 611, 1005
Gehrels, N., Chincarini, G., Giommi, P., et al. 2005, ApJ, 621, 558
Green, A. M., Hofmann, S., & Schwarz, D. J. 2005, J. Cosmology Astropart. Phys., 8, 3
Hartman, R. C., Bertsch, D. L., Bloom, S. D., et al. 1999, ApJS, 123, 79
Hermann, G. 2010, Nuclear Instruments and Methods in Physics Research A, 623, 408, for the CTA Collaboration
H.E.S.S. Collaboration: Abramowski, A., Acero, F., Aharonian, F., et al. 2011, Astropart. Phys., 34, 608
Hu, W., & Kravtsov, A. V. 2003, ApJ, 584, 702
Jackson, N., Battye, R. A., Browne, I. W. A., et al. 2007, MNRAS, 376, 371
Kalberla, P. M. W., Burton, W. B., Hartmann, D., et al. 2005, A&A, 440, 775
Komatsu, E., Smith, K. M., Dunkley, J., et al. 2011, ApJS, 192, 18
Kuhlen, M., Diemand, J., & Madau, P. 2008, ApJ, 686, 262
Kuhlen, M., Madau, P., & Silk, J. 2009, Science, 325, 970
Lavalle, J., Yuan, Q., Maurin, D., & Bi, X. 2008, A&A, 479, 427
Lupton, R., Gunn, J. E., Ivezić, Z., Knapp, G. R., & Kent, S. 2001, in Astronomical Data Analysis Software and Systems X, ed. F. R. Harnden Jr., F. A. Primini, & H. E. Payne, ASP Conf. Ser., 238, 269
Maddox, S. J., Efstathiou, G., Sutherland, W. J., & Loveday, J. 1990, MNRAS, 243, 692
Martinez, G. D., Bullock, J. S., Kaplinghat, M., Strigari, L. E., & Trotta, R. 2009, J. Cosmology Astropart. Phys., 6, 14
Mattox, J. R., Bertsch, D. L., Chiang, J., et al. 1996, ApJ, 461, 396
Mauch, T., Murphy, T., Buttery, H. J., et al. 2003, MNRAS, 342, 1117
Meade, P., Papucci, M., Strumia, A., & Volansky, T. 2010, Nuclear Physics B, 831, 178
Mirabal, N., Nieto, D., & Pardo, S. 2010 [arXiv:1007.2644]
Monet, D. G., Levine, S. E., Canzian, B., et al. 2003, AJ, 125, 984
Morselli, A., Canadas, B., & V. Vitale on behalf of the Fermi LAT collaboration. 2010, in SciNeGHE 2010, to appear in Il Nuovo Cimento C – Colloquia on physics [arXiv:1012.2292]
Navarro, J. F., Frenk, C. S., & White, S. D. M. 1996, ApJ, 462, 563
Navarro, J. F., Frenk, C. S., & White, S. D. M. 1997, ApJ, 490, 493
Pieri, L., Bertone, G., & Branchini, E. 2008, MNRAS, 384, 1627
Papucci, M., & Strumia, A. 2010, J. Cosmology Astropart. Phys., 3, 14
Pieri, L., Branchini, E., & Hofmann, S. 2005, Phys. Rev. Lett., 95, 211301
Pieri, L., Lavalle, J., Bertone, G., & Branchini, E. 2011, Phys. Rev. D, 83, 023518
Press, W. H., Teukolsky, S. A., Vetterling, W. T., & Flannery, B. P. 2007, Numerical Recipes: The Art of Scientific Computing, 3rd edn. (Cambridge University Press)
Rando, R. 2009, in Proc. 31st ICRC, Łódź, Poland, for the Fermi LAT Collaboration [arXiv:0907.0626]
Salucci, P., Lapi, A., Tonini, C., et al. 2007, MNRAS, 378, 41
Skrutskie, M. F., Cutri, R. M., Stiening, R., et al. 2006, AJ, 131, 1163
Spergel, D. N., Bean, R., Doré, O., et al. 2007, ApJS, 170, 377
Springel, V., Wang, J., Vogelsberger, M., et al. 2008a, MNRAS, 391, 1685
Springel, V., White, S. D. M., Frenk, C. S., et al. 2008b, Nature, 456, 73
Stephen, J. B., Bassani, L., Landi, R., et al. 2010, MNRAS, 408, 422
Strigari, L. E., Koushiappas, S. M., Bullock, J. S., & Kaplinghat, M. 2007, Phys. Rev. D, 75, 083526
The CTA Consortium. 2010 [arXiv:1008.3703]
Tridon, D. B., Schweizer, T., Goebel, F., Mirzoyan, R., & Teshima, M. 2010, Nuclear Instruments and Methods in Physics Research A, 623, 437, for the MAGIC Collaboration
Ulrich, M., Maraschi, L., & Urry, C. M. 1997, ARA&A, 35, 445
Vincent, P. 2005, in International Cosmic Ray Conference, 5, 163
Voges, W., Aschenbach, B., Boller, T., et al. 1999, A&A, 349, 389
Wagner, R. G. 2009, in Proc. 31st ICRC, Łódź, Poland, for the VERITAS Collaboration [arXiv:0910.4563]
Walker, M. G., Combet, C., Hinton, J. A., Maurin, D., & Wilkinson, M. I. 2011, ApJ, 733, L46
Wechsler, R. H., Bullock, J. S., Primack, J. R., Kravtsov, A. V., & Dekel, A. 2002, ApJ, 568, 52
Weekes, T. C., Badran, H., Biller, S. D., et al. 2002, Astropart. Phys., 17, 221
Wilks, S. S. 1938, Ann. Math. Statist., 9, 60
Zaharijas, G., Cuoco, A., Yang, Z., & Conrad, J. 2010, in Proc. IDM 2010 conference, Montpellier, France, published online at http://pos.sissa.it/cgi-bin/reader/conf.cgi?confid=110
Zechlin, H.-S., Fernandes, M. V., Elsaesser, D., & Horns, D. 2011, in 2011 Fermi Symposium proceedings - eConf C110509 [arXiv:1110.6868]
Zemp, M., Diemand, J., Kuhlen, M., et al. 2009, MNRAS, 394, 641

4.2 Publication II

Publication II (Zechlin & Horns 2012) significantly extends the method developed in Publication I for both the gamma-ray and the multi-wavelength investigation. Furthermore, *Fermi*-LAT gamma-ray data spanning a longer time range (3.5 years) were analyzed to search for DM subhalo candidates.

Supplementary material to Publication II is presented in Appendix B.1.

My contributions. The publication was initiated by myself. Almost all parts of Publication II were developed by myself. I wrote most of the manuscript and produced all figures.

Publication II

Unidentified sources in the Fermi-LAT second source catalog:
the case for DM subhalos

Hannes-S. Zechlin and Dieter Horns

Journal of Cosmology and Astroparticle Physics, **11**, 050 (2012)

Journal of Cosmology and Astroparticle Physics
An IOP and SISSA journal

Unidentified sources in the Fermi-LAT second source catalog: the case for DM subhalos

Hannes-S. Zechlin and Dieter Horns

University of Hamburg, Institut für Experimentalphysik,
Luruper Chaussee 149, D-22761 Hamburg, Germany

E-mail: hzechlin@physik.uni-hamburg.de, dieter.horns@physik.uni-hamburg.de

Received October 3, 2012
Accepted October 24, 2012
Published November 23, 2012

JCAP11(2012)050

Abstract. The Large Area Telescope (LAT) aboard the *Fermi* satellite allows us to study the high-energy γ-ray sky with unprecedented sensitivity. However, the origin of 31% of the detected γ-ray sources remains unknown. This population of unassociated γ-ray sources may contain new object classes, among them sources of photons from self-annihilating or decaying non-baryonic dark matter. *Fermi*-LAT might be capable to detect up to a few of these dark matter subhalos as faint and moderately extended γ-ray sources with a temporally steady high-energy emission. After applying corresponding selection cuts to the second year *Fermi* catalog 2FGL, we investigate 13 candidate objects in more detail including their multi-wavelength properties in the radio, infrared, optical, UV, and X-ray bands. For the γ-ray band, we analyze both the 24-month and 42-month *Fermi*-LAT data sets. We probe the γ-ray spectra for indications of a spectral cutoff, which singles out four sources of particular interest. We find all sources to be compatible with a point-source scenario. Multi-wavelength associations and, in particular, their infrared color-color data indicate no source to be compatible with a dark matter origin, and we find the majority of the candidates to probably originate from faint, high-frequency peaked BL Lac type objects. We discuss possibilities to further investigate source candidates and future prospects to search for dark matter subhalos.

Keywords: dark matter experiments, gamma ray experiments, active galactic nuclei

ArXiv ePrint: 1210.3852

doi:10.1088/1475-7516/2012/11/050

Contents

1 Introduction

Current all-sky surveys of the high-energy (HE) γ-ray sky provide unprecedented sensitivity to disseminate the population of high-energy γ-ray emitters. Based upon 24 months of data recorded with the Large Area Telescope (LAT) aboard the *Fermi Gamma-ray Space Telescope* satellite (*Fermi*) [1], the *Fermi* Collaboration recently published the second *Fermi*-LAT point-source catalog (2FGL) [2]. The 2FGL contains 1 873 sources detected between 100 MeV and 100 GeV (with a significance $S \gtrsim 4\sigma$), whereof approximately one third (576 sources) are lacking reliable association with sources detected in other wavelength bands. On the contrary, the majority (∼1 000) of the 1 297 associated sources have been classified to most likely originate from active galactic nuclei (AGN), in particular BL Lacs and flat spectrum radio quasars [3].

While it seems plausible that most of the unassociated (high-latitude) γ-ray sources are expected to originate from faint AGN, this sample may also contain new classes of γ-ray emitting sources [4–9]. In particular, this includes sources potentially driven by self-annihilating (or decaying) dark matter (DM), i.e., DM subhalos (see [10] and references therein). In this context, it is also interesting to note that the intensity of the isotropic diffuse γ-ray background [11] cannot be fully accounted for by the properties of known γ-ray emitters (e.g., blazars) extrapolated below the confusion limit of *Fermi*-LAT [12, 13]. Unravelling the nature of *Fermi* unidentified sources therefore remains a crucial task to tackle searches and constrains on new HE phenomena, e.g., self-annihilating DM.

Significant evidence for the existence of a so far undiscovered form of matter, so-called DM, have been provided by various different astrophysical observations via its gravitational imprint [14–16]. Cold DM manifests itself on both cosmological and galactic scales, i.e., prevailing the formation of large scale structures down to accounting for galactic halos and their DM substructure (DM subhalos) [17, 18]. Observations indicate DM as an unknown non-baryonic type of heavy, electrical neutral, and color neutral particle, which is very weakly interacting with standard model particles. A promising scenario comprises DM to be constituted by weakly interacting massive particles (WIMPs) of Majorana type, with a mass between a few hundred GeV and several TeV. With an interaction strength at the order of weak interactions, thermal production of WIMPs in the early Universe can consistently explain the measured DM relic density [19]. Appropriate WIMP candidates naturally arise in beyond standard model theories, e.g., Supersymmetry [20].

The discovery of WIMPs is then possible via three complementary approaches, i.e., collider, direct, and indirect detection techniques: while WIMPs may be directly produced in colliders with sufficient center-of-mass energy, e.g., the Large Hadron Collider (LHC) [21, 22], underground low-noise experiments [23] are sensitive to their scattering signatures with heavy nuclei. From the astrophysical point of view, WIMPs may be indirectly detected through their self-annihilation (or decay) to standard model final states, eventually producing γ rays, charged light hadrons and leptons, and neutrinos [24].

In this paper, we present a search for DM subhalo candidates in the 2FGL catalog, following up on the 1FGL catalog search we conducted in [10], henceforth called Paper I; for related studies, see e.g. [8, 25–29]. The paper is structured as follows: In section 2, the γ-ray properties of detectable DM subhalos are summarized. The catalog search for candidate γ-ray sources and a study of their spectral and temporal properties are described in section 3, including the investigation of multi-wavelength counterparts and an analysis of archival UV and X-ray data. The results of this study are summarized and discussed in section 4.

JCAP11(2012)050

2 Gamma-ray emission of DM subhalos

In the hierarchical formation of structures, galactic DM halos are anticipated to host a large population of smaller subhalos (up to 10^{16}). Their mass spectrum $\mathrm{d}N/\mathrm{d}M$ follows a power-law distribution over the mass range M between 10^{-11}–$10^{-3}\,M_\odot$ and $\sim 10^{10}\,M_\odot$: $\mathrm{d}N/\mathrm{d}M \propto M^{-\alpha}$, where $\alpha \in [1.9; 2.0]$, see [17, 18, 30]. While some of the massive subhalos are expected to host the Milky Way's luminous dwarf spheroidal satellite galaxies (dSphs), baryonic content of low-mass subhalos and even concentrated massive subhalos can be lacking, see [31, 32] and references therein. In Paper I, we have shown that *up to two* massive DM subhalos between 10^5 and $10^8\,M_\odot$ could be detectable with *Fermi*-LAT within the first two mission years, assuming common models on the self-annihilation of heavy WIMPs, their density distribution in DM subhalos, and the distribution of the subhalos in the Galaxy. These objects at distances of $\mathcal{O}$(kpc) would appear in the γ-ray sky as moderately extended ($\theta_{68} \approx 0.5^\circ$) γ-ray sources above 10 GeV.[1] The faint, temporally constant γ-ray flux at energies E between 10 and 100 GeV is anticipated at the detection level of *Fermi*-LAT, $\phi_\mathrm{p}(10$–$100\,\mathrm{GeV}) \approx 10^{-10}\,\mathrm{cm}^{-2}\,\mathrm{s}^{-1}$, owing to the small self-annihilation cross section of WIMPs, $\langle\sigma v\rangle \sim 3\times10^{-26}\,\mathrm{cm}^3\,\mathrm{s}^{-1}$. The differential γ-ray flux approximately follows a hard power-law (index $\Gamma \lesssim 1.5$) with a distinct cutoff to the WIMP mass m_χ, where we assumed WIMPs of $m_\chi = 500\,(150)$ GeV annihilating to heavy quarks, gauge bosons (e.g., $b\bar{b}$, W^+W^-), or

---

[1] Within the angle θ_{68}, a fraction of 68% of the total γ-ray luminosity is emitted. In comparison with the point spread function of *Fermi*-LAT, $\theta_{68} = 0.5^\circ$ corresponds to about $4\sigma_\mathrm{PSF}$, where $\sigma_\mathrm{PSF} \approx 0.13^\circ$ at 10 GeV (see http://www.slac.stanford.edu/exp/glast/groups/canda/lat_Performance.htm).

to the leptons $\tau^+\tau^-$, see figure 2 in Paper I. We emphasize that the expected γ-ray flux may be even higher when including the possible presence of sub-substructures (enhancement by a factor of 2 to 3) [33, 34] and (rather model-dependent) photon contributions from final state radiation and virtual internal Bremsstrahlung [35–38]. The rather low WIMP velocity in bound subhalos might also lead to resonances in the self-annihilation cross section (Sommerfeld enhancement) [39, 40]. Potential secondary emission from energetic charged leptons eventually produced by WIMP annihilation in Galactic photon and magnetic fields is expected to be rather faint and diffuse, e.g. [41–43], and we therefore anticipate DM subhalos to be γ-ray sources which are not associated to sources detected in other wavelength bands at lower energies.

3 DM subhalo candidates in the 2FGL

3.1 Source selection

The selection of candidate objects in the class of unidentified sources listed in the 2FGL[2] is based upon the properties of γ-ray emitting DM subhalos discussed above:

(i) The sample was reduced to sources at high galactic latitudes $|b| \geq 20°$, to avoid confusion with conventional Galactic sources and to reduce the impact of diffuse Galactic γ-ray emission.

(ii) Sources were selected for a steady γ-ray flux, requiring the cataloged variability parameter $var < 41.64$, which corresponds to a probability of $P_\mathrm{s} > 1\%$ for the source to be steady.

(iii) To select sources potentially driven by massive WIMPs, a detection above 10 GeV was required. In addition, most of the high-energy pulsars located at high Galactic latitude are eliminated by this energy cut. Spectrally, γ-ray pulsars may resemble DM subhalos, given their stable emission of characteristically hard γ-ray spectra ($\Gamma < 2$) with typical cutoff energies E_c between 1 and 10 GeV [44–47].

(iv) Spectrally hard sources were selected constraining the index of the cataloged power-law fit with $\Gamma < 2.0$.

All but the last cut have been already used in Paper I. Applying cuts (i) to (iv) to the unassociated sources listed in the 2FGL, 14 unassociated γ-ray sources remain. With the exception of 2FGL J2339.6−0532, all other sources have a HE flux close to the detection level of *Fermi*-LAT. This is consistent with the expectation for candidate sources as discussed in section 2. We therefore discarded the outstandingly bright object 2FGL J2339.6−0532. Table 1 lists the final sample of 13 candidates sources together with their positional and spectral properties.

The source 2FGL J0031.0+0724 has been extensively studied in Paper I, where also 2FGL J0143.6−5844 has been listed. An updated discussion of 2FGL J0031.0+0724 is presented below. 2FGL J2257.9−3646 has been claimed as a DM subhalo candidate in [29], while very high-energy ($E > 100$ GeV) follow-up observations of 2FGL J2347.2+0707 have been conducted with MAGIC [27]. All remaining sources are new candidates.

---

[2] Version *v06*.

2FGL name	l, b [deg]	σ_{68}/σ_{95} [arcmin]	S [σ]	Γ	$\phi_{\mathrm{p}}(10-100\,\mathrm{GeV})$ [$10^{-10}\,\mathrm{cm}^{-2}\,\mathrm{s}^{-1}$]	S_5 [σ]
J0031.0+0724$^{\mathrm{1st}}$	114.095,−55.108	4.4/7.2	4.4	1.9 ± 0.3	0.7 ± 0.3	4.5
J0116.6−6153	297.749,−54.986	3.7/6.0	5.5	1.6 ± 0.2	0.7 ± 0.3	4.9
J0143.6−5844$^{\mathrm{1st}}$	290.468,−57.102	2.4/3.8	14.2	1.7 ± 0.1	2.2 ± 0.6	9.5
J0305.0−1602$^{\mathrm{1st}}$	200.151,−57.146	4.5/7.3	5.3	1.5 ± 0.2	0.9 ± 0.4	4.4
J0312.8+2013	162.507,−31.569	3.7/6.0	4.4	1.7 ± 0.2	0.7 ± 0.3	4.5
J0338.2+1306	173.471,−32.929	3.9/6.3	5.8	1.5 ± 0.2	1.1 ± 0.5	5.1
J0438.0−7331	286.088,−35.168	4.1/6.6	6.1	1.4 ± 0.2	0.8 ± 0.4	5.0
J0737.5−8246	295.086,−25.467	3.7/6.0	4.4	1.3 ± 0.3	1.0 ± 0.4	5.2
J1223.3+7954	124.470,+37.134	3.6/5.8	4.2	1.4 ± 0.3	0.6 ± 0.3	4.6
J1347.0−2956	317.047,+31.398	4.1/6.6	5.0	1.4 ± 0.3	1.0 ± 0.5	4.2
J1410.4+7411	115.839,+41.825	2.9/4.7	9.1	1.9 ± 0.1	0.7 ± 0.3	4.7
J2257.9−3646$^{\mathrm{1st}}$	3.899,−64.186	5.0/8.2	5.3	1.9 ± 0.2	0.8 ± 0.4	4.1
J2347.2+0707$^{\mathrm{1st}}$	96.214,−52.385	3.7/5.9	7.2	2.0 ± 0.2	0.8 ± 0.4	4.1

Table 1. DM subhalo candidates in the 2FGL catalog. The first column lists the 2FGL name, where the index "1st" flags sources which have already been listed in the 1FGL (i.e., 1FGL J0030.7+0724, 1FGL J0143.9−5845, 1FGL J0305.2−1601, 1FGL J2257.9−3643, and 1FGL J2347.3+0710). For each source, the position is given in galactic coordinates (l, b), together with the positional uncertainty $\sigma_{68(95)}$ [68% (95%) c.l., semi-major axis], detection significance S in Gaussian sigma, the power-law index Γ, and the photon flux in the 10–100 GeV band. The last column S_5 lists the significance of the 10–100 GeV detection (in Gaussian sigma).

3.2 *Fermi*-LAT data

The data analysis of each object in table 1 was based on data recorded with the *Fermi*-LAT in the first 24 as well as 42 months[3] of the mission.[4] We chose the same analysis framework and recommended options that were used for the 2FGL (based upon 24 months of data), with the exception that the considered energy range was extended to cover 100 MeV to 300 GeV. The data analysis was performed with the public version of the Fermi Science Tools (v9r23p1, release date 06 October 2011) using data of Pass-7 event reconstruction along with the P7_V6 instrument response functions.[5] All events passing the SOURCE event class were considered. Events were filtered for a maximum zenith angle of 100° (to eliminate contamination from the Earth's limb), a maximum rocking-angle of 52°, and the recommended quality filters DATA_QUAL == 1 and LAT_CONFIG == 1 were applied. The (quadratic) region-of-interest (RoI) was centered on the nominal 2FGL position of the source-of-interest (SoI) with a size of 20° × 20°. The overall spectral fit was performed using the binned likelihood method (with 10 energy-bins per decade; optimizer NEWMINUIT, requiring an absolute fit tolerance of 10^{-3}), where the source model contained all 2FGL sources within the RoI, along with fixed cataloged positional and spectral parameters. Including the SoI, the normaliza-

---

[3] The 42-month data set covers the time period between the beginning of August 2008 (239557419 MET) up to the beginning of February 2012 (350063020 MET).

[4] The LAT data is publicly available at http://fermi.gsfc.nasa.gov/ssc/data/.

[5] See http://fermi.gsfc.nasa.gov/ssc/data/analysis/.

tions ϕ_0 and indices Γ of the default model of a power-law spectrum $[\mathrm{d}\phi/\mathrm{d}E = \phi_0\,(E/E_0)^{-\Gamma}]$ of the innermost six sources were kept free, while the energy scale E_0 was fixed to the cataloged pivot energy. We used the latest publicly available models for the Galactic foreground (*gal_2yearp7v6_v0.fits*) and isotropic background emission (*iso_p7v6source.txt*). The normalization and corrective power-law index of the Galactic foreground template and the normalization of the isotropic background template were left free. In detail, the analysis was performed with the tools *gtselect*, *gtmktime*, *gtbin*, *gtltcube*, *gtexpcube2*, *gtsrcmaps*, and *gtlike*. For each source, we checked that our overall fit reproduces the cataloged data sufficiently.

The analysis chain for the 42-month data set allowed for a possible change of the positional coordinates of each SoI. We used *gtfindsrc* to refit the position. The refined uncertainty contour (at 95% confidence level) was computed from the two-dimensional likelihood function $\mathcal{L}(\mathrm{RA}, \mathrm{Dec})$, requiring $2\Delta(\log \mathcal{L}) = 6.18$ (2 degrees of freedom).

3.3 Spectral analysis

The energy spectra of the candidate sources have to be consistent with a spectrum generated by self-annihilating WIMPs. For each candidate source, we carried out a statistical hypotheses test based upon a likelihood ratio. The null hypothesis (H_{pl}) of the SoI to follow a conventional power-law spectrum was tested against the hypothesis (H_{exp}) of a spectrum generated by WIMP annihilation. The likelihood ratio defines a test statistic

$$\mathrm{TS}_{\mathrm{exp}} = -2\ln\left(\frac{\mathcal{L}(H_{\mathrm{pl}})}{\mathcal{L}(H_{\mathrm{exp}})}\right), \tag{3.1}$$

where $\mathcal{L}(H)$ denotes the total likelihood for the corresponding RoI, fitted assuming the SoI to follow the spectral hypothesis H (cf. section 3.2).[6]

As benchmark models, we probed for WIMP annihilation to heavy quarks (e.g., $b\bar{b}$), gauge bosons (e.g., W^+W^-), and to the leptons $\tau^+\tau^-$, which lead to a considerably harder γ-ray spectrum. For our purpose, the differential γ-ray spectra resulting from annihilation of supersymmetric neutralinos to the afore mentioned final states, see [48, 49], can be approximated with a power-law spectrum modified by an exponential cutoff [50], $\mathrm{d}N_\gamma/\mathrm{d}x = N_0\,x^{-\Gamma}\exp(-px)$, where $x = E/m_\chi$. This simple parametrization originally introduced for gauge boson final states [50] also provides a reasonable fit to the $\tau^+\tau^-$ final states [49] with different values of N_0, Γ, and p. The used parameters are listed in table 2. This approach simplifies considerably the treatment and interpretation of the fit procedure. Given the small number statistics of the faint sources, more subtle differences in the final state spectrum cannot be resolved.

Therefore, the hypothesis H_{exp} was a power-law spectrum with exponential cutoff, $\mathrm{d}\phi/\mathrm{d}E = \phi_0\,(E/E_0)^{-\Gamma}\exp(-E/E_{\mathrm{c}})$. The WIMP mass is then connected to the cutoff energy via $m_\chi = p\,E_{\mathrm{c}}$, and the normalization is $\phi_0 = N_0\,m_\chi^{\Gamma-1}\,E_0^{-\Gamma}$. The index Γ was fixed to the values given in table 2, while the energy scale was set to $E_0 = 1\,\mathrm{GeV}$. As discussed in section 3.1, we note that this hypothesis also probes for γ-ray pulsars which might contaminate our sample, even though we expect most of them to be eliminated by the energy cut.

Since Γ was kept fixed for H_{exp}, the null and alternative hypotheses are not nested. This implies that the test statistic $\mathrm{TS}_{\mathrm{exp}}$ does not necessarily follow the theorems of Wilks [51] or

---

[6] Note that the spectral models (usually power laws) of all other sources in the RoI are kept fixed. Therefore, another possibility would be to use the test statistic TS assigned by the spectral likelihood fit (*gtlike*) to measure the source's detection significance, $S \propto \sqrt{\mathrm{TS}}$. We checked that both methods give similar results, as expected.

Channel	N_0	Γ	p	Remarks
heavy quarks, gauge bosons	0.73	1.5	7.8	[50]
$\tau^+\tau^-$	5.28	0.35	4.6	

Table 2. Fit parameters to approximate the differential photon spectra originating from final-state fragmentation of self-annihilating neutralinos by power laws with exponential cutoffs. For annihilation to heavy quarks and gauge bosons, we use the spectral parametrization from [50], while the photon yield from annihilation in $\tau^+\tau^-$ is approximated from [49].

Chernoff [52], i.e., $\mathrm{TS}_{\mathrm{exp}}$ is not drawn from a chi-square distribution in the null hypothesis. It also implies that $\mathrm{TS}_{\mathrm{exp}}$ can have both negative as well as positive values: the hypothesis H_{exp} is disfavored if $\mathrm{TS}_{\mathrm{exp}} \ll 0$ and favored if $\mathrm{TS}_{\mathrm{exp}} \gg 0$. Since the distribution of the test statistic is a priori not known, the significance of this test had to be calculated with Monte Carlo simulations. The methods are described in appendix A. Based upon the simulations, we find that for the index $\Gamma = 1.5\,(0.35)$, a significance of 2σ corresponds to $\mathrm{TS}_{\mathrm{exp}} = -6\,(-20)$ and $\mathrm{TS}_{\mathrm{exp}} = 2\,(2)$, respectively, while the 3σ contour is given by $\mathrm{TS}_{\mathrm{exp}} = -25\,(-35)$ and $\mathrm{TS}_{\mathrm{exp}} = 4\,(7)$; table 8 lists further significance and their corresponding $\mathrm{TS}_{\mathrm{exp}}$ values.

The best-fit parameters for a fixed $\Gamma = 1.5$ and $\Gamma = 0.35$ are summarized in table 3 for the 24-month data and in table 4 for the 42-month data. Although the fitted spectrum depends on just two free parameters, the statistical errors of the normalization and cutoff energy remain comparably large, owing to the sample of very faint sources studied.[7] For the 24-month data, we find that a power-law with exponential cutoff spectrum is favored for the sources 2FGL J0305.0−1602 and 2FGL J0338.2+1306, with a significance of 2.4σ and 3.3σ, respectively. After 42 months, for both sources the significance of this initial indication has decreased. However, an exponential cutoff is now favored for the sources 2FGL J0143.6−5844 and 2FGL J1410.4+7411, with significances of $\sim 3\sigma$. Vice versa, note that for no source we find such a spectrum to be disfavored by the data (i.e., by more than 3σ).

The initial indications for an exponential cutoff in the 24-month or 42-month data sets motivate a closer inspection of the sources 2FGL J0305.0−1602, 2FGL J0338.2+1306, 2FGL J0143.6−5844, and 2FGL J1410.4+7411. A comprehensive discussion of each source candidate is given in section 3.6.

3.4 Variability and angular extent

A γ-ray signal from a DM subhalo is expected to be constant in time and may be resolved as an extended source. Therefore, the temporal and spatial distributions of high-energy photons were tested for compatibility with a constant flux and the hypothesis of angular extent. The method used is based upon our previous work in Paper I. Most of the source candidates have been detected exclusively in the upper energy bins with a comparably low background contamination. Therefore, the tests were applied to the high-energy photon distribution between 3–300 GeV and the inclusive interval 10–300 GeV, respectively. As motivated in section 2 (for details see Paper I), high-energy photons within a circular region of radius 0.5° around the nominal 2FGL position were examined. Due to the low background contamination, this sample is dominated by signal events (see below).

---

[7] Note that the errors quoted in tables 3 and 4 are correlated, given that the energy scale E_0 was fixed to 1 GeV. Choosing the decorrelation energy, in principle, reduces the statistical errors.

24 months	$\Gamma = 1.5$			$\Gamma = 0.35$		
2FGL name	$\phi_0/10^{-11}$ $[(\mathrm{cm}^2\,\mathrm{s\,GeV})^{-1}]$	E_c [GeV]	TS_exp	$\phi_0/10^{-11}$ $[(\mathrm{cm}^2\,\mathrm{s\,GeV})^{-1}]$	E_c [GeV]	TS_exp
J0031.0+0724	17.1 ± 8.0	67 ± 84	-2.2	1.3 ± 1.1	21 ± 12	-5.8
J0116.6−6153	20.0 ± 9.0	34 ± 33	0.9	4.7 ± 4.2	9 ± 5	-0.4
J0143.6−5844	70.5 ± 13.2	46 ± 25	1.4	16.8 ± 5.5	10 ± 2	-17.2
J0305.0−1602	21.1 ± 7.5	70 ± 78	1.4	4.8 ± 2.7	12 ± 5	4.1
J0312.8+2013	29.9 ± 11.7	46 ± 40	-0.6	2.8 ± 2.1	16 ± 8	-5.2
J0338.2+1306	48.0 ± 13.5	40 ± 28	4.2	12.6 ± 5.9	9 ± 3	6.7
J0438.0−7331	24.5 ± 9.4	105 ± 134	0.9	3.8 ± 2.5	17 ± 8	1.1
J0737.5−8246	31.6 ± 11.8	66 ± 68	1.3	5.0 ± 2.8	14 ± 6	2.6
J1223.3+7954	8.1 ± 6.0	186 ± 502	0.1	0.3 ± 0.4	41 ± 35	-0.2
J1347.0−2956	26.1 ± 8.6	204 ± 367	0.2	2.0 ± 1.2	31 ± 17	-2.6
J1410.4+7411	40.4 ± 10.7	30 ± 18	1.2	12.4 ± 5.3	7 ± 2	-3.7
J2257.9−3646	33.9 ± 12.6	17 ± 12	1.3	9.4 ± 7.0	6 ± 3	-4.6
J2347.2+0707	36.6 ± 10.8	61 ± 49	-2.5	4.7 ± 2.6	15 ± 6	-12.1

Table 3. Best-fit parameters for a power law with exponential cutoff spectrum, fitting the 24-month data set between 0.1 and 300 GeV. The index was fixed to $\Gamma = 1.5$ or $\Gamma = 0.35$, respectively. The table lists the normalization ϕ_0 and cutoff energy E_c. The column TS_exp gives the likelihood ratio for the comparison with a pure power-law fit. See the text for more details on the interpretation of TS_exp.

42 months	$\Gamma = 1.5$			$\Gamma = 0.35$		
2FGL name	$\phi_0/10^{-11}$ $[(\mathrm{cm}^2\,\mathrm{s\,GeV})^{-1}]$	E_c [GeV]	TS_exp	$\phi_0/10^{-11}$ $[(\mathrm{cm}^2\,\mathrm{s\,GeV})^{-1}]$	E_c [GeV]	TS_exp
J0031.0+0724	17.5 ± 7.7	38 ± 35	-6.9	1.1 ± 1.0	18 ± 11	-13.9
J0116.6−6153	27.1 ± 7.3	44 ± 30	1.2	5.8 ± 3.0	10 ± 4	-7.1
J0143.6−5844	53.6 ± 8.7	53 ± 26	3.9	13.4 ± 3.9	10 ± 2	-17.8
J0305.0−1602		$E_\mathrm{c} \to \infty$		2.9 ± 1.7	12 ± 5	2.3
J0312.8+2013	23.4 ± 8.2	42 ± 32	0.5	3.0 ± 1.8	13 ± 5	-3.0
J0338.2+1306	32.3 ± 7.6	153 ± 177	1.1	5.8 ± 2.5	14 ± 5	-2.7
J0438.0−7331	20.5 ± 7.7	54 ± 48	0.6	2.8 ± 1.9	14 ± 6	-3.6
J0737.5−8246	29.1 ± 9.4	47 ± 38	2.2	6.4 ± 3.5	10 ± 4	2.3
J1223.3+7954	7.8 ± 4.9	103 ± 179	-0.3	0.4 ± 0.4	31 ± 23	-2.1
J1347.0−2956	27.9 ± 6.8	212 ± 285	0.3	2.1 ± 0.9	31 ± 13	-7.5
J1410.4+7411	42.0 ± 8.0	27 ± 12	4.3	15.3 ± 4.7	7 ± 1	-3.3
J2257.9−3646	19.5 ± 7.9	21 ± 15	0.8	3.3 ± 2.4	9 ± 4	-2.8
J2347.2+0707	46.9 ± 9.5	49 ± 27	-0.1	12.0 ± 4.7	8 ± 2	-14.6

Table 4. Best-fit parameters for a power law with exponential cutoff spectrum, fitting the 42-month data set between 0.1 and 300 GeV. The index was fixed to $\Gamma = 1.5$ or $\Gamma = 0.35$, respectively. The table lists the normalization ϕ_0 and cutoff energy E_c. The column TS_exp gives the likelihood ratio for the comparison with a pure power-law fit. See the text for more details on the interpretation of TS_exp.

2FGL name	Number of photons ($r \leq 0.5°$)		$N^{\rm bg}_{\rm pred}$(10 − 300 GeV)	$E_{\rm max}$	Evcl
	3 − 10 GeV	10 − 300 GeV	gal/iso/Σ	[GeV]	
J0031.0+0724		5	0.3/0.6/0.9	44 ± 4	4
J0116.6−6153		5	0.2/0.7/0.9	26^{+1}_{-2}	4
J0143.6−5844	17	15	0.2/0.7/0.9	45 ± 3	4
J0305.0−1602	11	6	0.3/0.6/0.9	39^{+2}_{-1}	4
J0312.8+2013		5	0.9/0.7/1.6	35^{+4}_{-3}	4
J0338.2+1306	27	8	1.3/0.6/1.9	29 ± 2	4
J0438.0−7331	14	6	0.6/0.8/1.4	56 ± 3	4
J0737.5−8246		7	0.9/0.6/1.5	46^{+5}_{-4}	4
J1223.3+7954		6	0.7/0.8/1.5	61^{+6}_{-5}	4
J1347.0−2956		6	0.7/0.7/1.4	55^{+6}_{-4}	2
J1410.4+7411	18	6	0.4/0.9/1.3	35 ± 2	4
J2257.9−3646		6	0.2/0.7/0.9	18^{+2}_{-1}	4
J2347.2+0707	19	5	0.7/0.6/1.3	84^{+10}_{-7}	4
J0143.6−5844	30	23	0.5/1.3/1.8	53 ± 4	4
J0305.0−1602	16	6	0.5/1.0/1.5	39^{+2}_{-1}	4
J0338.2+1306	38	16	2.2/1.0/3.2	152^{+15}_{-13}	4
J1410.4+7411	33	10	0.8/1.6/2.4	36 ± 2	2

Table 5. *Top:* 24-month data: Number of γ-ray photons, listed for detected energy bins between 3–10 GeV and 10–300 GeV, within a radial region of 0.5° around the source's position. Additionally, the expected numbers of background photons from Galactic foreground (gal) and isotropic background (iso) between 10–300 GeV are given. The last columns list the energy of the photon with highest energy, and its corresponding event classification assigned by LAT data reconstruction (2: SOURCE, 4: ULTRACLEAN). *Bottom:* Same as above, for 42-month of data: Number of γ-ray photons in the 42-month data set for spectrally preselected source candidates, see section 3.3.

For the 24-month data, the upper part of table 5 lists the number of photons detected from each source between 3–10 GeV and 10–300 GeV, respectively, together with the energy and event class of the photon with highest energy. The lower part lists the same quantities for the spectrally selected list of candidates after 42 months. Additionally, the number of background photons $N^{\rm bg}_{\rm pred}$ expected within 0.5° around the source is given for the 10–300 GeV interval. These values were derived by fitting a RoI of $1° \times 1°$ centered on the position of the SoI, fixing the normalizations (and power-law correction) of the Galactic foreground and isotropic background templates to the best-fit values obtained from the entire 0.1–300 GeV fit.[8] On average, approximately seven photons above 10 GeV have been detected after 24 months, containing between one to two background photons within a radius of 0.5°. We note that only 2FGL J0338.2+1306 has been detected above 100 GeV.

The potential variability of the source flux was tested with an unbinned Kolmogorov-Smirnov (KS) test [53]. This test is already valid for a small number of photon counts,

---

[8] Owing to the quadratic-shaped RoI, the numbers were multiplied with $\pi\, 0.5^2 \approx 0.785$ to correct for a circular RoI.

2FGL Name	P_{const}		95% upper limit θ_{s}^{95} [deg]	
	3–300 GeV	10–300 GeV	3–300 GeV	10–300 GeV
J0031.0+0724		0.51		0.53
J0116.6−6153		0.17		0.55
J0143.6−5844	0.97	0.83	0.25	0.38
J0305.0−1602	0.006	0.19	0.45	0.73
J0312.8+2013		0.05		0.50
J0338.2+1306	0.15	0.57	0.48	0.60
J0438.0−7331	0.28	0.33	0.30	0.50
J0737.5−8246		1.00		0.35
J1223.3+7954		0.23		0.35
J1347.0−2956		0.40		0.70
J1410.4+7411	0.78	0.66	0.38	0.60
J2257.9−3646		0.08		0.90
J2347.2+0707	0.62	0.65	0.28	0.75

2FGL Name	P_{const}		95% upper limit θ_{s}^{95} [deg]	
	3–300 GeV	10–300 GeV	3–300 GeV	10–300 GeV
J0143.6−5844	0.89	0.46	0.17	0.25
J0305.0−1602	0.004	0.04	0.45	0.70
J0338.2+1306	0.02	0.82	0.23	0.38
J1410.4+7411	0.47	0.97	0.33	0.47

Table 6. Probability for temporally constant γ-ray emission (left columns) and upper limit on the intrinsic angular extent of the signal (95% c.l., right columns). The quantities are listed for the 10–300 GeV band and, in case of a detection between 3–10 GeV, 3–300 GeV band. Quantities derived from the 24 (42)-month data are shown in the *top* (*bottom*) panel.

in distinction to the binned chi-square method used for the 2FGL catalog. The empirical cumulative distribution function of the arrival times of individual photons is compared to a uniform distribution, taking the (possibly varying) exposure into account. The resulting probabilities P_{const} for the temporal photon distribution to be consistent with a constant flux are listed in table 6 for both the 3–300 and inclusive 10–300 GeV interval. In particular, we find 2FGL J0305.0−1602 to show indications for variability ($P_{\mathrm{const}} = 4\,‰$).

We used a likelihood-ratio test to probe for intrinsic spatial extent. The corresponding likelihood function is given by $L(\theta_{\mathrm{s}}) = -2\sum_{i=1}^{N} \ln\left[p_{\mathrm{det}}(\mathbf{x}_i - \overline{\mathbf{x}}; \theta_{\mathrm{s}}) + b\right]$, where $p_{\mathrm{det}}(\mathbf{x}; \theta_{\mathrm{s}})$ follows the probability distribution function (PDF) for a photon to be detected at $\mathbf{x}$, $\overline{\mathbf{x}}$ denotes the best-fit position of the SoI, and b denotes the (flat) PDF of the underlying background $N_{\mathrm{pred}}^{\mathrm{bg}}$ [10]. The PDF of $\mathbf{x} - \overline{\mathbf{x}}$ for an intrinsically extended γ-ray emitter is the convolution of *Fermi*-LAT's point spread function (PSF) p_{PSF} (version P7_V6) with the intensity profile p_{int} of the emitter, $p_{\mathrm{det}} = p_{\mathrm{PSF}} * p_{\mathrm{int}}$. The intensity profile p_{int} of a DM subhalo follows its line-of-sight integrated squared density profile. Similar to the approach followed in Paper I, the DM density profile of a subhalo was assumed to follow the spherically symmetric Navarro-Frenk-White (NFW) profile $\rho(r) \propto \left[r/r_{\mathrm{s}}\,(1 + r/r_{\mathrm{s}})^2\right]^{-1}$ [54], where r denotes the distance to the center of the halo with a characteristic value at r_{s}. Since 87.5% of the total luminosity is produced within r_s, it serves as a convenient proxy for the intrinsic subhalo extent. For a subhalo at distance D, this corresponds to the angle $\theta_s \approx r_s/D$. We remark that 68% of the total luminosity are produced within $\theta_{68} \simeq 0.46\,\theta_s$, which is more convenient for comparison with observational data.

The minimum $L_{\rm min}$ of the likelihood function L arises for the extension parameter θ_s fitting the photon distribution best. Applying the theorem of Wilks [51], the quantity $\Delta L = L - L_{\rm min}$ follows a chi-square distribution with one degree of freedom, with additional terms of the order of $1/N^{1/2}$, which are important for a small number of counts (see also [55]).

We find no source candidate which shows indication for an intrinsic angular extent. Note that this result is in agreement with ref. [28], that also searched for angular extended sources. For each source, we present upper limits on θ_s at 95% confidence level in table 6. For the 24-month data between 10–300 GeV, note hereby that the given confidence level is not precisely defined, owing to the low number statistics which might affect the chi-square distribution. In general, the upper limits range from 0.2° to 0.9°, where the most constraining ones can obviously be derived from the largest data sets (42 months, 3–300 GeV).

3.5 Multi-wavelength counterparts

3.5.1 Catalog data

Although the sources in table 1 are cataloged as unassociated, we carried out a dedicated counterpart search.[9] In particular, radio and X-ray sources positionally located inside the 95 %-confidence-level uncertainty contour (listed in the 2FGL) of the γ-ray source have been searched for, providing counterpart candidates in case of a non-DM origin. The resulting counterpart candidates are listed in table 9 (see appendix B), ordered by increasing angular separation from the 2FGL position. For every radio or X-ray source, the USNO-B1.0 catalog [56] was searched for a matching optical counterpart.

For all but one source (2FGL J1410.4+7411), at least one radio source is located nearby. However, note that owing to the high sensitivity (therefore low confusion limit) of the NVSS [57] and SUMSS [58], which were used for radio associations, the high radio source density ($\sim$0.2 arcmin^{-2}) yields a large number of by-chance associations in the rather large positional uncertainty of the γ-ray sources (see table 1 and figure 2).

3.5.2 WISE data

The sources 2FGL J0312.8+2013, 2FGL J0737.5−8246, and 2FGL J1347.0−2956 have recently been associated with blazar candidates selected from the WISE survey [59] on the basis of their mid-infrared (IR) colors [7]. At least one WISE object located in the positional uncertainty of these γ-ray sources has been found to fulfill the IR properties of (γ-ray) blazars, i.e., lying in the WISE gamma-ray strip. We adopted this approach [7, 60, 61] to classify IR-counterpart candidates of γ-ray sources by their mid-infrared color-color properties. We focus on the IR counterparts of the four spectrally selected 2FGL candidates, together with the candidate selected in Paper I, 2FGL J0031.0+0724. For each of these five 2FGL sources, an infrared counterpart candidate is listed in the WISE catalog [62], which is positionally coincident with the established radio and X-ray associations (see section 3.5.3, table 9, and section 3.6). The associations are listed in table 10 (appendix B), together with their infrared

---

[9] Apart from preselected catalogs, the archives NASA/IPAC Extragalactic Database (NED, http://ned.ipac.caltech.edu/) and HEASARC (http://heasarc.gsfc.nasa.gov/cgi-bin/W3Browse/w3browse.pl) have been queried.

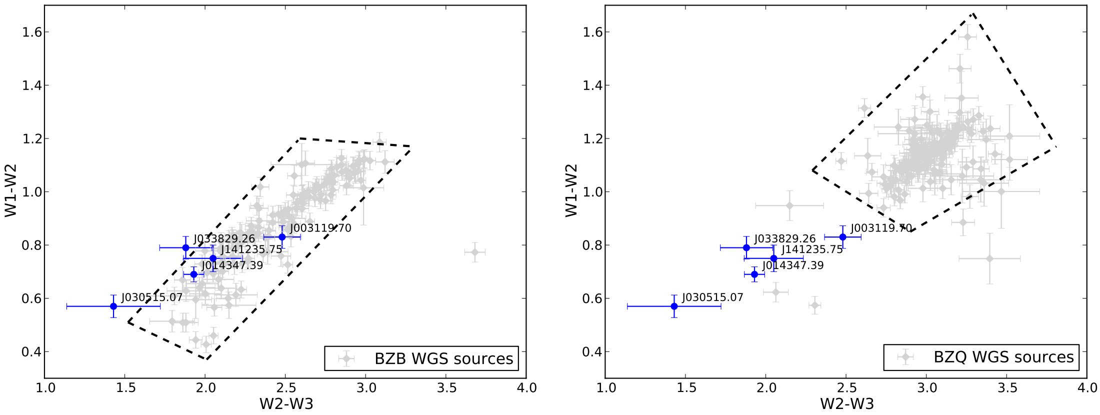

(a) (b)

Figure 1. (a): Infrared color-color diagram of the WISE associations in table 10 (blue circles). The WGS subregion of BZBs is bordered with the dashed line, while the reference sources used in [61] are indicated with the gray diamonds. (b): Same as (a), comparing to the WGS subregion of BZQs.

magnitudes $W1, W2, W3,$ and $W4$. As described in [60, 61] and references therein, the population of blazars spans a distinct region in the infrared color space of WISE objects, the WISE Blazar Strip. In particular, the sample of known γ-ray emitting blazars populates the WISE gamma-ray strip (WGS), which is a subspace of the WISE Blazar Strip. The WGS can be parametrized in two (overlapping) subregions, one which is dominantly populated by γ-ray emitting BL Lacs (BZBs), while the other one is dominated by flat spectrum radio quasars (BZQs). In figure 1, we compare the infrared color-color diagram ($W2 - W3$,$W1 - W2$) of the WISE associations in table 10 with the BZB and BZQ regions of [61].[10] We find that the WISE associations for all five 2FGL sources hint for a BL Lac origin of the γ-ray emission, as being consistent with the BZB region of the WGS.

3.5.3 *Swift*-UVOT/XRT data

Besides the available catalogs of known X-ray sources, we have searched for unpublished archival observations of the remaining four objects. In a dedicated campaign [63], UV and X-ray follow-up observations of unidentified 2FGL sources have been carried out with the UVOT and X-ray telescope (XRT, 0.2 − 10 keV) aboard the *Swift* satellite [64, 65].

The photometric UVOT data have been extracted from the products of the standard pipeline using the HEAsoft 6.12 software package in combination with the calibration files (2012-04-02). The in-orbit calibration procedures are described in detail in [66]. The standard aperture of 5 arcsec has been used for all filters to extract the background subtracted flux with *uvotsource*.

For the corresponding XRT data sets (see table 7 for details), calibration and screening (*xrtpipeline*) of the data acquired in photon-counting (PC) mode was done using standard screening criteria, along with the current release of calibration files (2012-04-02). Data were reduced with the HEAsoft 6.11 software package. We used *Ximage* for source detection and *Xspec* (version 12.7.0) for spectral fitting. The probability limit for a background fluctuation was set to the 5σ-level and we required a signal-to-noise ratio of $S/N \geq 4$. Positions and

---

[10] Since most of the WISE sources tabulated in 10 have not been detected in the $W4$ band, we did not attempt to use the color-color projections including $W4$.

FoV	Obs. ID	Obs. year	Exposure [ks]
2FGL J0143.6−5844	41274	2010	4.4
2FGL J0305.0−1602	41286	2011	3.2
2FGL J0338.2+1306	41292	2010	4.1
2FGL J1410.4+7411	47219	2012	3.5

Table 7. Archival *Swift*-XRT data for the celestial regions of the preselected source candidates. The columns list the observation ID, the observation year, and the total exposure in ks.

corresponding uncertainties were derived with *xrtcentroid*. For each source position, ancillary response functions needed for spectral fitting were derived with *xrtmkarf*, incorporating PSF correction. The circular on-source regions contained about 90% of the PSF (corresponding to a radius of $\sim 47''$), while the background was derived from appropriate off-source regions with radii between $3'$ and $5'$. All X-ray sources were spectrally fit with a power-law model corrected for photoelectric absorption. The hydrogen column density N_{H} was fixed to the nominal Galactic value, calculated from the Leiden/Argentine/Bonn (LAB) HI survey [67]. For faint sources ($S/N < 6$), the power-law index Γ was fixed to 2.0. To achieve sufficient fit quality, the spectral channels were grouped, requiring a minimum of 5 (for $S/N < 15$) or 10 counts per bin, respectively. We used the Cash-statistic for spectral fitting, to properly treat the low count statistic.

In general, we find new X-ray sources in every *Swift* field of view (FoV), detected with comparably hard spectra having (unabsorbed) fluxes at the level of $10^{-13}\,\mathrm{erg\,cm^{-2}\,s^{-1}}$ between 0.2 and 2 keV. For all selected candidates but 2FGL J1410.4+7411, some X-ray sources are positionally consistent with the cataloged γ-ray uncertainty, and additionally with the radio detections mentioned above (see table 9 in appendix B). Therefore, they provide convincing counterpart candidates for the γ-ray sources, cf. Paper I. For reference, positional and spectral parameters of every X-ray detection are listed in table 11 (appendix B).

3.6 Discussion of preselected candidates

Below, we provide a discussion of every preselected source candidate, based upon the results obtained in sections 3.3 to 3.5. Additionally, the updated results on 2FGL J0031.0+0724 are summarized.

Positional and spectral features of the four selected 2FGL candidates and their corresponding multi-wavelength associations (established in section 3.5) are summarized in figures 2 and 3, respectively. In figure 2, the 2FGL as well as 42-month best-fit position and their corresponding uncertainties are overlayed over the photon image measured with *Swift*-XRT, and plotted together with the positions of radio and X-ray sources. For all four 2FGL sources, the updated best-fit position shifts by a few arcmins, where the largest shift was found for 2FGL J0338.2+1306 ($5.2'$). Figure 3 compares the multi-wavelength data with the average spectral energy distribution (SED) of a high-energy peaked blazar (HBL), which has been adapted from [72, 73] for particular redshifts z. Note in this context that the multi-wavelength data have not been taken contemporaneously. The redshift of each source was estimated from the distance modulus $m_{\mathrm{R}} - M_{\mathrm{R}}$, where m_{R} denotes the magnitude in the USNO-B1.0 R-band (table 9), and we assumed the detected optical emission to originate from a standard giant elliptical host galaxy with an absolute magnitude $M_{\mathrm{R}} = -23.1$ [74]. We assumed a vanishing K-correction, i.e., a power-law spectrum with index $\alpha = \Gamma - 1 = 1$.

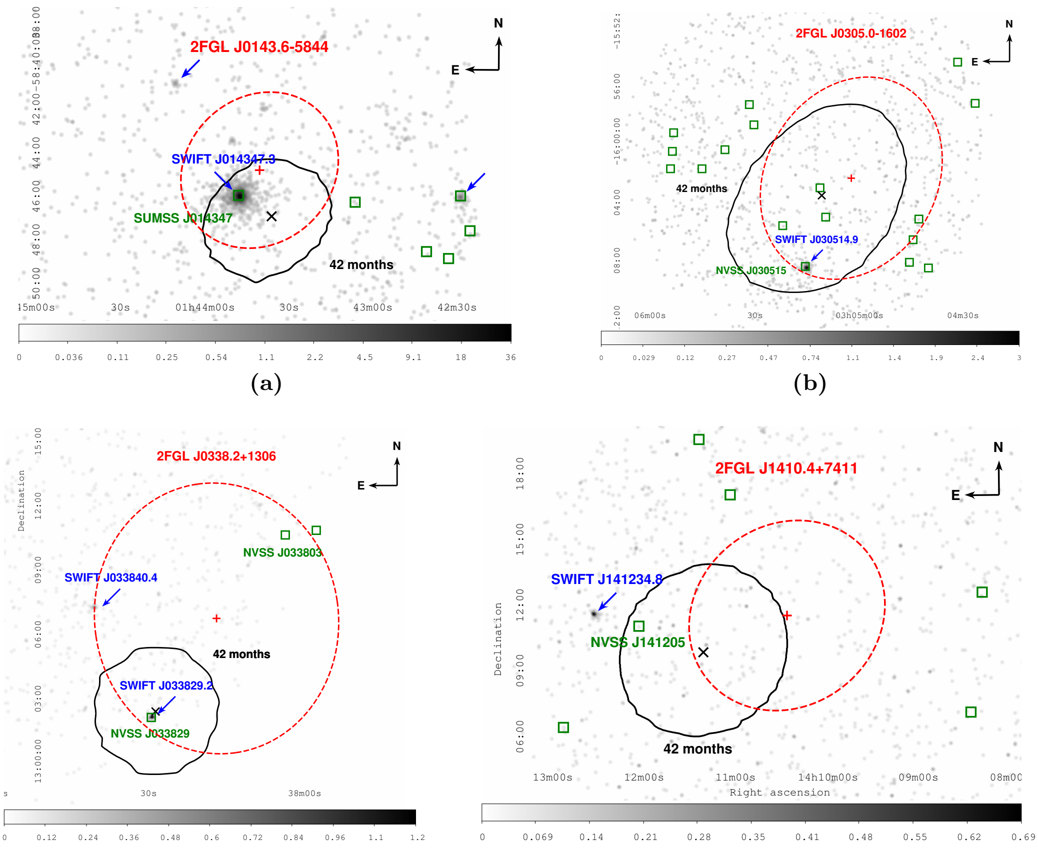

(a)

(b)

(c)

(d)

Figure 2. Best-fit position and uncertainty contour of (a) 2FGL J0143.6−5844, (b) 2FGL J0305.0−1602, (c) 2FGL J0338.2+1306, and (d) 2FGL J1410.4+7411 for 24 and 42 months of *Fermi*-LAT data. The cataloged position is marked with the red "+", while the dashed red line borders its uncertainty ellipse (95% c.l.). The black "×" marks the 42-month position, and the solid black line its uncertainty contour (95% c.l.). An image of X-ray photons (*Swift*-XRT), smoothed with a Gaussian ($7''$), is shown in the background. Note that the region of (c) has not been entirely observed with Swift-XRT, and different z-axis scales are used to improve readability (i.e., (a) log, (b) sqrt, (c) linear, and (d) linear). Positions of radio sources (NVSS) are indicated with dark-green boxes, discovered X-ray sources with blue arrows. Note that the boxes's size does not reflect the positional uncertainty.

We emphasize that this method only provides a rough estimate under the given assumptions, while a precise determination of z requires spectroscopic data in the optical band. In the very high-energy regime, emitted photons are absorbed through γ-γ pair production, which was calculated using the EBL model provided in [75].

2FGL J0031.0+0724. The 24-month *Fermi*-LAT data of this source has been intensively studied in Paper I. The analysis carried out here does not demonstrate a preference for an exponential cutoff in the 42-month data set. With a significance of $\sim 2\sigma$, the lightcurve of high-energy photons (10–300 GeV) is consistent with a temporally variable source, and no indication for angular extended emission was found. In Paper I, we already claimed a

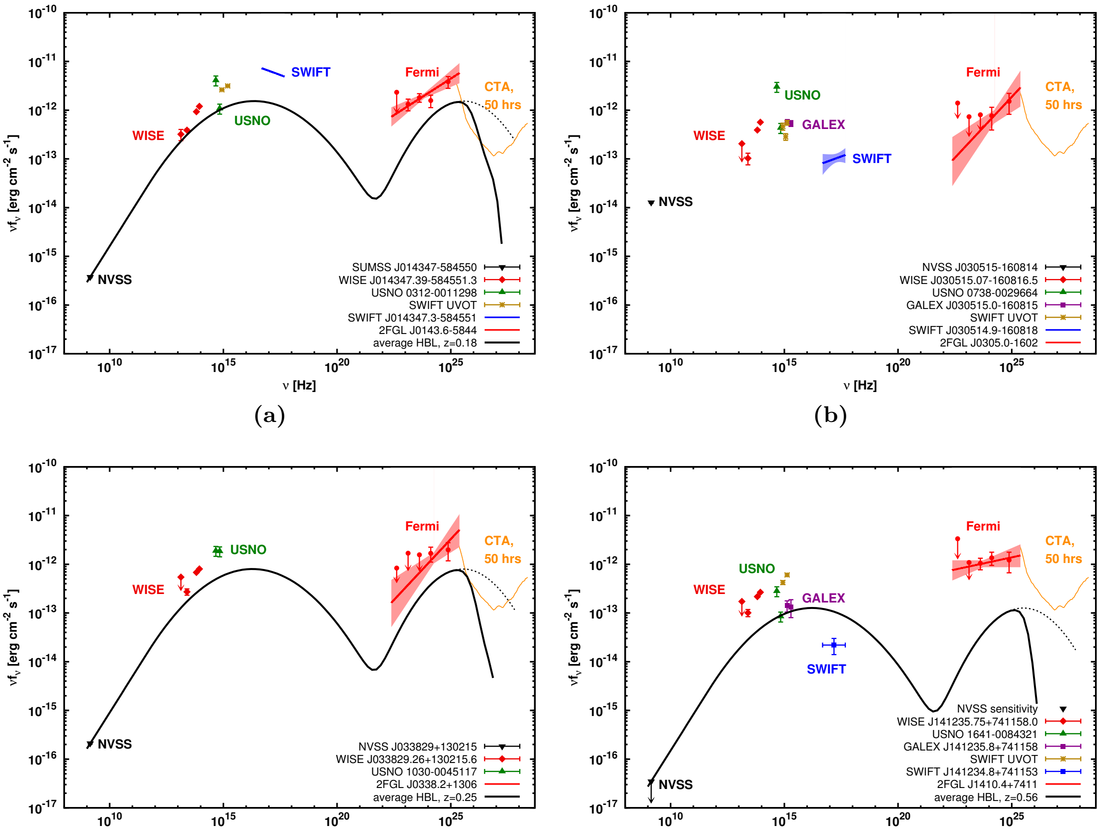

(a) **(b)**

(c) **(d)**

Figure 3. Spectral energy distribution (SED) of (a) 2FGL J0143.6−5844, (b) 2FGL J0305.0−1602, (c) 2FGL J0338.2+1306, and (d) 2FGL J1410.4+7411, assuming the multi-wavelength associations discussed in the text. Included multi-wavelength data, from low to high frequency: radio (NVSS, 1.4 GHz; black triangle), infrared (WISE, $W4, W3, W2, W1$; red diamonds), optical (USNO-B1.0, R, B; green triangles), ultra-violet (GALEX, NUV, FUV; violet boxes; see http://galex.stsci.edu/GR6/; *Swift*-UVOT, U, $UVW1$, $UVM2$, $UVW2$; dark-golden points), X-ray (*Swift*, 0.2–2 keV; blue line), γ-ray (*Fermi*-LAT 2FGL, 0.1–100 GeV; red line and circles). The optical and UV data have been dereddened using $E(B-V)$ from [68] and assuming $R_V = 3.1$ (see [69] for details). Arrows indicate upper limits (95% c.l.). Statistical uncertainties of the X-ray and γ-ray spectra are indicated by the corresponding shaded areas [70]. The orange line shows the sensitivity of the planned CTA observatory for 50 hours of observation [71]. For comparison, the solid black line shows the average SED of a high-frequency peaked blazar (HBL), adapted for the estimated redshifts z. The HBL-SED is normalized to the radio flux, and the energy flux νf_ν is plotted in the frame of a potential observer. The HBL-SED has been corrected for EBL absorption (see text for details), while the dotted black line shows the SED for a vanishing EBL.

possible association of the source with a faint radio source (12 mJy), positionally coincident with a faint X-ray source, $f^{\text{unabs}}(0.2\text{–}2\,\text{keV}) \approx 2.1 \times 10^{-13}\,\text{erg cm}^{-2}\,\text{s}^{-1}$. The spectral energy distribution (SED) is consistent with a BL Lac origin (see Paper I), which is supported by the photometric infrared data of WISE J003119.70+072453.6.

2FGL J0143.6−5844. The 42-month data indicates the γ-ray spectrum to be preferentially fit with an exponential cutoff with $\sim 3\sigma$. Furthermore, the lightcurve is preferred to be steady, but the γ-ray emission is consistent with a point-source. Multi-wavelength observations show the source to be associated with a 27 mJy radio source (SUMSS), positionally coincident with the bright X-ray source SWIFT J014347.3−584551, $f^{\rm unabs}(0.2-2\,{\rm keV}) \approx 1.4 \times 10^{-11}\,{\rm erg\,cm^{-2}\,s^{-1}}$. Together with the simultaneously measured X-ray flux, the UV data seems to indicate variable emission when compared with the optical data. The infrared data supports a BL Lac scenario, which is also consistent with the multi-wavelength SED, see figure 3a.

2FGL J0305.0−1602. While the γ-ray data shows initial indication (at the 2.5σ level) for a spectral cutoff at ~ 10 GeV, the temporal photon distribution of the source excludes a constant flux with $\sim$99% confidence. Multi-wavelength searches indicate the source to be positionally associated with PKS J0305−1608, showing a radio flux at the Jy level (NVSS) and an X-ray flux of $f^{\rm unabs}(0.2-2\,{\rm keV}) \approx 2.3 \times 10^{-13}\,{\rm erg\,cm^{-2}\,s^{-1}}$. The photometric infrared data is sparsely consistent with a BL Lac scenario, while the high radio flux is not in accordance with the expectation from a high-energy peaked BL Lac (see figure 3b).

2FGL J0338.2+1306. The source was initially selected based upon the 24-month data set, preferring a spectral cutoff with a significance of $\sim 3\sigma$. As shown in figure 2c, gaining photon statistics revealed a large positional shift fitting the 42-month data, and the initial indication for a spectral cutoff vanished. The updated data set also indicates a variable γ-ray flux at the 2σ level. The improved positional accuracy allows to associate 2FGL J0338.2+1306 with a radio source (15.1 mJy), which is positionally coincident with SWIFT J033829.2+130217, see figure 2c. Its WISE counterpart suggests a BL Lac origin, in accordance with the entire multi-wavelength emission (see figure 3c).

2FGL J1410.4+7411. The 42-month γ-ray data of this source prefers its spectrum to be fit with a power-law ($\Gamma = 1.5$) with exponential cutoff, with a significance of $\sim 3.3\sigma$. The lightcurve is consistent with steady emission, but no indication for an angular extent was detected. While also being counterpartless after 24 months, the position computed from the larger photon sample seems to shift towards the very faint X-ray source SWIFT J141234.8+741153, see figure 2d, $f^{\rm unabs}(0.2-2\,{\rm keV}) \approx 6.3 \times 10^{-14}\,{\rm erg\,cm^{-2}\,s^{-1}}$.[11] Note that the *Swift* source has no radio counterpart, which might reflect the lacking sensitivity of radio surveys. Assuming the *Swift* source to be the correct X-ray association, its infrared counterpart WISE J141235.75+741158.0 would indicate a BL Lac origin. Additionally, compared to the USNO and GALEX data, the *Swift*-UVOT observations indicate variable emission.

4 Discussion and conclusions

In this work, we investigated the unassociated γ-ray source population of the *Fermi*-LAT second year point-source catalog for sources potentially originating from DM subhalos. Basic catalog selection revealed 13 high-latitude sources, with hard γ-ray spectra detected above 10 GeV, and lacking indication for temporal variability. Using 3.5 years (42 months) of *Fermi*-LAT data, we developed a statistical test to probe the candidates for spectral consistency with self-annihilating DM (a power-law with exponential cutoff). The high-energy spectra of a subset of 4 sources were found to be preferentially fit by power-laws with exponential cutoff (i.e.,

---

[11] Note that the X-ray source XMMSL1 J141002.6+740744 ($f^{\rm unabs}(0.2–2\,{\rm keV}) \approx 2 \times 10^{-12}\,{\rm erg\,cm^{-2}\,s^{-1}}$) [76] is located just outside the 2FGL 95% uncertainty contour, but does not appear in the SWIFT observations.

2FGL J0143.6−5844, 2FGL J0305.0−1602, 2FGL J0338.2+1306, and 2FGL J1410.4+7411), with significances between 2.5σ and 3.3σ. All sources were tested for temporally constant and spatially extended γ-ray emission. The γ-ray emission of 2FGL J0305.0−1602 shows a $\sim 3\sigma$ indication to be temporally variable, while none of the 13 sources shows indications for angular extended emission. Multi-wavelength studies were conducted to search for associations, using refined positional information based upon 3.5 years of *Fermi*-LAT data. For 2FGL J0143.6−5844, 2FGL J0305.0−1602, and 2FGL J0338.2+1306, we established clear associations detected in the radio, infrared, optical, UV, and X-ray bands, while 2FGL J1410.4+7411 is indicated to be associated to a faint X-ray source, which has also been detected in the infrared, optical, and UV band.

With the exception of 2FGL J0305.0−1602, the infrared color-color data of the three other sources is fully consistent with the population of BL Lacs detected with *Fermi*-LAT. In addition, such a scenario would be favored by the multi-wavelength data, in particular by the faint radio, hard X-ray, and hard γ-ray emission, indicating a scenario of a high-frequency peaked BL Lac (see figure 3 and Paper I for details). For all three cases, we note that the γ-ray flux predicted in the average model is below the *Fermi*-LAT measurement. This might indicate a sample bias, meaning that the sources have been detected in a flaring state. Within the errors, the infrared association of 2FGL J0305.0−1602 might also indicate a BL Lac origin, while in particular its bright radio counterpart may point towards a different scenario. Finally, the recent study in [8] has attempted to classify the entire sample of unassociated *Fermi*-LAT sources, distinguishing between AGN-like and pulsar-like sources. Using a Random Forest (RF) classifier trained on cataloged γ-ray properties of associated *Fermi*-LAT sources, the major fraction of the unassociated sources are predicted to be AGN, and no significant outliers have been found. All 13 candidates we selected in table 1 are suggested to be AGN. Consistently, the recent RF classification in [9] assigns all of them to originate from BL Lacs. In particular, this strongly supports the BL Lac origin of the four spectrally selected candidates. Note, however, that since we predict γ-ray sources originating from DM subhalos to be particularly faint, their cataloged spectral and localization parameters suffer from large statistical uncertainties. Therefore, DM subhalos might hide in the sample of sources classified by the RF algorithm, emphasizing the necessity of the in-depth investigations carried out in this paper.

In conclusion, we find no unassociated γ-ray source in the 2FGL catalog which is favored to originate from a subhalo driven by self-annihilating WIMPs at a mass scale above 100 GeV. However, we conclude that, among all candidates, the source 2FGL J1410.4+7411 would be the most interesting, owing to γ-ray properties which might prefer a DM origin and a high uncertainty about its association. From the final source sample, we can exclude 2FGL J0305.0−1602 (owing to variable γ-ray emission). We note that no source can be firmly excluded by spectral properties. We find the remaining candidates to most likely originate from faint BL Lacs.

Albeit our prediction of a BL Lac origin, we investigated all source candidates in the context of the recently claimed evidence for a line-like feature at ∼130 GeV in the Galactic Center region [38, 77–83]. In case of a self-annihilating DM scenario, DM subhalos will also appear with a γ-ray line at ∼130 GeV, and searches have been started in [80, 84–86]. Except for 2FGL J0338.2+1306, having a photon at 152 GeV, we note that none of the other sources has been detected above 100 GeV.

The study presented here has clearly outlined the problems of identifying faint *Fermi* sources. Difficulties are mainly related to the limiting collection area of the LAT at the high energy end, resulting in a small number of photons. This implies the consequently large uncertainty of source locations, which in turn leads to source confusion at the faint end of source populations. Likewise, the small number of photons limits the ability to determine spectral and temporal properties at the high energy end of the *Fermi*-LAT response with sufficient accuracy to distinguish source models. Finally, from the theoretical point of view in the considered DM scenario, the entirely limited number of detectable subhalos prohibits conclusive population studies.

Focussing on high-latitude sources with fluxes at the level of the studied ones, we emphasize that at least some of these issues can be addressed with larger data sets based upon longer observations. The correspondingly large signal-to-background ratios allow us to improve the positional accuracy by a factor of ~2 with 10 years of *Fermi*-LAT data, for instance, and to monitor the temporal photon distribution over longer time periods. The improvement in sensitivity might push the number of detectable subhalos to $\mathcal{O}(5)$.

In particular, the issues can also be addressed with pointed follow-up observations in the very high-energy (VHE) band. The large collection areas provided by imaging air Cherenkov telescopes (IACTs) for energies above $\sim 50\,\mathrm{GeV}$, such as H.E.S.S.-II [87, 88], MAGIC stereo [89, 90], VERITAS [91, 92], and, in particular, the planned Cherenkov telescope array (CTA) [71, 93, 94], allows the detection of a larger photon sample, significantly reducing positional and spectral uncertainties. If detected in the VHE, source candidates therefore can be easily associated or even identified, see [27].

As a final remark, a potential successor of *Fermi*-LAT such as GAMMA-400 [95, 96] will significantly improve the observable energy range ($100\,\mathrm{MeV} - 3\,\mathrm{TeV}$), angular resolution ($\sim 0.01^\circ$ at $100\,\mathrm{GeV}$), and energy resolution ($\sim 1\%$ at $100\,\mathrm{GeV}$). The launch of GAMMA-400 is planned for 2018. For the case of unidentified *Fermi*-LAT sources, such a telescope will constrain their celestial position with enhanced precision.

Acknowledgments

HSZ kindly acknowledges Francesco Massaro for providing data published in [61], Jules P. Halpern, and Christoph Weniger for helpful discussions. We acknowledge the anonymous referee for useful comments. This work was supported through the collaborative research center (SFB) 676 “Particles, Strings, and the Early Universe” at the University of Hamburg. This research has made use of the NASA/IPAC Extragalactic Database (NED) which is operated by the Jet Propulsion Laboratory, California Institute of Technology, under contract with the National Aeronautics and Space Administration.

A Probability distribution of $\mathrm{TS}_{\mathrm{exp}}$

To determine the probability density distribution (pdf) of $\mathrm{TS}_{\mathrm{exp}}$ (eq. (3.1)) in the null-hypothesis H_0, we used bootstrap Monte Carlo simulations [53]. Assuming a pure power-law spectrum (i.e., H_0), we simulated data of the RoI corresponding to 2FGL J0338.2+1306, which was exemplarily selected to check whether an exponential cutoff is preferred by the actual data set (see table 3). The 25 000 simulated data sets were then analyzed with the framework described in section 3.2 and 3.3, therefore calculating $\mathrm{TS}_{\mathrm{exp}}$ in exactly the same way as in the actual data analysis. Each individual analysis procedure was checked for non-converging behavior ($\sim 14\%$), and the final data set of simulations was cleaned accordingly.

The simulations were done in a two-step approach: First, we used *gtobssim* to simulate five individual 24-month data sets of the RoI centered on 2FGL J0338.2+1306 (between 100 MeV and 300 GeV). All sources in the RoI were modeled with the cataloged power-law spectra, since the current version of *gtobssim* does not accept log-parabola spectra (which are sometimes preferred). Background models were implemented as described in section 3.2, and we used the actual spacecraft file of the first 24 months of data-taking. We checked the consistency between the analysis results from the simulated data and the actual data set. As a second step, the five individual simulations were merged to one data set. Applying the bootstrap technique to the merged data, we generated 25 000 individual 24-month data sets to be used in our analysis. Again, we checked that the analysis reproduced the actual data well.

Figure 4a shows the pdf of $\mathrm{TS}_{\mathrm{exp}}$, fixing the index Γ of the alternative hypothesis H_1 (power-law with exponential cutoff) to $\Gamma = 1.5$ and $\Gamma = 0.35$, respectively. The simulation shows that the pdf does indeed not follow a $\chi^2/2$-distribution [52] for both negative as well positive $\mathrm{TS}_{\mathrm{exp}}$ values. Rather, we find asymmetric pdfs with maxima and large tails at negative $\mathrm{TS}_{\mathrm{exp}}$ values.[12] These features are more pronounced for $\Gamma = 0.35$, owing to the sharply peaked γ-ray spectrum. For the positive half-plane, the p-values $p(> \mathrm{TS}_{\mathrm{exp}})$ (the significance of the test statistic) are shown in figure 4b. The p-values are compared to the prediction of Chernoff's theorem [52], where the test statistic in the positive half-plane should follow $0.5\left[\delta(\mathrm{TS}_{\mathrm{exp}}) + \chi^2_1(\mathrm{TS}_{\mathrm{exp}})\right]$, with $\delta(x)$ the delta-function and $\chi^2_1(x)$ the chi-square distribution with one degree of freedom. For $\Gamma = 0.35$, we find that for large, positive $\mathrm{TS}_{\mathrm{exp}}$ the pdf approximately follows Chernoff's theorem, while the pdf of a $\Gamma = 1.5$ spectrum does not. The resulting significances corresponding to selected $\mathrm{TS}_{\mathrm{exp}}$ values are shown in table 8. For the index $\Gamma = 1.5\,(0.35)$, a significance of 2σ corresponds to $\mathrm{TS}_{\mathrm{exp}} = -6\,(-20)$ and $\mathrm{TS}_{\mathrm{exp}} = 2\,(2)$, respectively, while the 3σ contour is given by $\mathrm{TS}_{\mathrm{exp}} = -25\,(-35)$ and $\mathrm{TS}_{\mathrm{exp}} = 4\,(7)$.

---

[12] The maxima are at $\mathrm{TS}_{\mathrm{exp}} = -0.25\,(-2.25)$ for $\Gamma = 1.5\,(0.35)$.

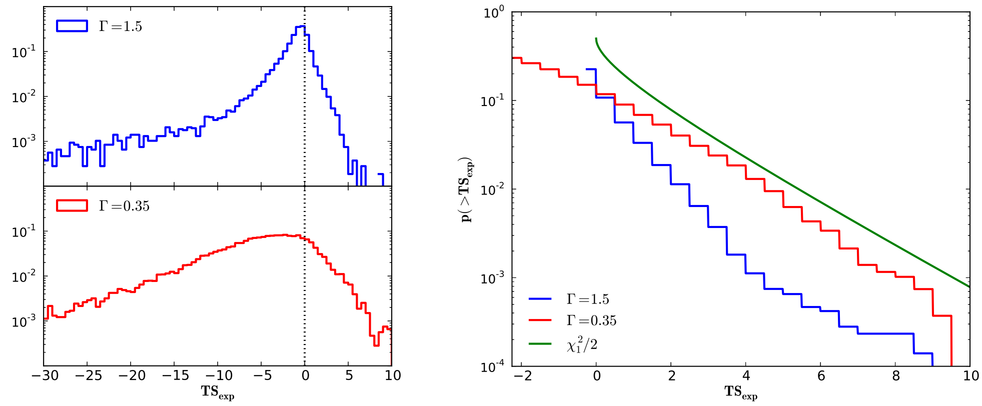

(a) (b)

Figure 4. (a): Probability density distribution of the test statistic $\mathrm{TS}_{\mathrm{exp}}$ in the null hypothesis H_0. The power-law index of the alternative hypothesis H_1 was fixed to $\Gamma = 1.5$ (*top*) and $\Gamma = 0.35$ (*bottom*). The dotted vertical line indicates $\mathrm{TS}_{\mathrm{exp}} = 0$. (b): P-value $p(> \mathrm{TS}_{\mathrm{exp}})$ for the positive half-plane of the distribution, starting from its corresponding maximum. The curves for $\Gamma = 1.5$ (blue line) and $\Gamma = 0.35$ (red line) are compared to a $\chi_1^2/2$ distribution (green line).

$p(< \mathrm{TS}_{\mathrm{exp}})$ $[\sigma]$			$p(> \mathrm{TS}_{\mathrm{exp}})$ $[\sigma]$		
$\mathrm{TS}_{\mathrm{exp}}$	$\Gamma = 1.5$	$\Gamma = 0.35$	$\mathrm{TS}_{\mathrm{exp}}$	$\Gamma = 1.5$	$\Gamma = 0.35$
−40.0		3.9	0.0	1.3	1.5
−35.0		3.0	2.0	2.4	2.0
−30.0	3.8	2.7	4.0	3.2	2.4
−25.0	3.0	2.4	6.0	3.5	2.9
−20.0	2.7	2.1	8.0	3.7	3.3
−15.0	2.5	1.8	10.0	4.0	4.1
−10.0	2.3	1.3			
−5.0	1.8	0.7			
0.0	0.2	0.2			

Table 8. Probability (p-value) to randomly find the test statistic to be less (*left table*) or larger (*right table*) than a certain $\mathrm{TS}_{\mathrm{exp}}$ value, given in Gaussian sigma. The p-value is listed for both assuming the index Γ of the power law with exponential cutoff to be 1.5 and 0.35, respectively.

B Multi-wavelength association

2FGL name	Sep.	Radio	Optical (USNO-B1.0)	X-ray	WGS
J0031.0+0724	3.1′	–	0973-0005560: 19.5$^{\mathrm{m}}$/18.2$^{\mathrm{m}}$	SWIFT J003054.9+072328: 0.03(1)	✓
	3.4′	NVSS J003119+072456: 12(1) mJy	0974-0005617: 19.8$^{\mathrm{m}}$/18.6$^{\mathrm{m}}$	SWIFT J003119.8+072454: 0.21(7)	
	4.5′	–	[HB2010a] J007.70635+07.38744: 20.9$^{\mathrm{m}\,\star}$	SWIFT J003049.8+072316: 0.04(1)	
	6.2′	NVSS J003128+072204: 12(1) mJy	–	–	
J0116.6−6153	2.7′	SUMSS J011619−615343: 24(1) mJy/beam§	0281-0014602: 18.2$^{\mathrm{m}}$/17.8$^{\mathrm{m}}$ QORG J011619.6−615344, $p_{\mathrm{QSO}} = 0.98$	–	
	3.4′	SUMSS J011656−615013: 43(2) mJy/beam§	–	–	
	3.7′	SUMSS J011643−615653: 33(1) mJy/beam§	0280-0013875: 20.0$^{\mathrm{m}}$/15.1$^{\mathrm{m}}$ 0280-0013876: 18.0$^{\mathrm{m}}$/15.0$^{\mathrm{m}}$	–	
J0143.6−5844	1.6′	SUMSS J014347−584550: 27(1) mJy/beam§	0312-0011298: 18.5$^{\mathrm{m}}$/16.6$^{\mathrm{m}}$	SWIFT J014347.3−584551:13.9(4)	✓
J0305.0−1602	2.3′	NVSS J030511−160249: 7(1) mJy	–	–	
	3.2′	NVSS J030509−160450: 3(1) mJy	0739-0030568: 21.6$^{\mathrm{m}}$/18.9$^{\mathrm{m}}$ 0739-0030569: 20.6$^{\mathrm{m}}$/18.8$^{\mathrm{m}\,\dagger}$	–	
	5.4′	NVSS J030442−160458: 8(2) mJy	–	–	
	5.8′	NVSS J030521−160525: 47(2) mJy	–	–	
	6.9′	NVSS J030515−160814: 917(35) mJy	0738-0029664: 19.6$^{\mathrm{m}}$/17.0$^{\mathrm{m}}$	2RXP J030515.3−160811: 1.26 SWIFT J030514.9−160818: 0.23(6)	
J0312.8+2013	2.4′	NVSS J031247+201606: 5.1(4) mJy	–	–	✓ [7]
	2.8′	NVSS J031240+201141: 18(1) mJy	1101-0034847: 21.2$^{\mathrm{m}}$/19.4$^{\mathrm{m}}$	–	
	4.7′	NVSS J031307+201229: 2.7(4) mJy	–	–	
	5.6′	NVSS J031245+201913: 4(1) mJy	1103-0035146: –/19.4$^{\mathrm{m}}$	–	
J0338.2+1306	5.1′	NVSS J033803+131045: 28(1) mJy	–	–	
	5.5′	NVSS J033829+130215: 15.1(6) mJy	1030-0045117: 19.3$^{\mathrm{m}}$/18.3$^{\mathrm{m}}$	SWIFT J033829.2+130217	✓
J0438.0−7331	3.3′	SUMSS J043836−732921: 20(1) mJy/beam§	0165-0071403: 15.6$^{\mathrm{m}}$/14.1$^{\mathrm{m}}$	–	
	6.3′	SUMSS J043900−732648: 63(2) mJy/beam§	0165-0071476: 17.8$^{\mathrm{m}}$/17.0$^{\mathrm{m}}$	–	
J0737.5−8246	2.3′	SUMSS J073706−824836: 14(1) mJy/beam§	0071-0020954: 17.8$^{\mathrm{m}}$/17.5$^{\mathrm{m}}$	–	✓ [7]
J1223.3+7954	1.9′	NVSS J122358+795329: 31(1) mJy	1698-0045483: 20.2$^{\mathrm{m}}$/18.5$^{\mathrm{m}}$	–	
J1347.0−2956	2.2′	NVSS J134706−295840: 27(1) mJy	0600-0304193: 18.8$^{\mathrm{m}}$/17.1$^{\mathrm{m}}$	1WGA J1347.1−2958: 0.23(4)	✓ [7]
	3.5′	NVSS J134653−295346: 12(1) mJy	0601-0302620: 19.8$^{\mathrm{m}}$/18.4$^{\mathrm{m}}$	–	
	4.7′	–		1WGA J1347.0−2952: 0.28(5)	
J1410.4+7411	–	–	–	–	✓
J2257.9−3646	0.2′	–	0532-0895676: 19.9$^{\mathrm{m}}$/18.4$^{\mathrm{m}}$	1WGA J2257.9−3645: 0.08(1)	
	3.7′	NVSS J225741−364833: 6.9(5) mJy	0531-0930900: 19.8$^{\mathrm{m}}$/18.9$^{\mathrm{m}}$	–	
	4.3′	NVSS J225815−364433: 10.6(6) mJy	0532-0895730: 19.2$^{\mathrm{m}}$/18.1$^{\mathrm{m}}$	1WGA J2258.2−3644: 0.21(2)	
	4.5′	NVSS J225817−364520: 7.4(5) mJy	0532-0895735: 20.7$^{\mathrm{m}}$/18.5$^{\mathrm{m}}$	–	
	5.2′	–	multiple	1WGA J2258.3−3647: 0.05(1)	
	7.0′	–	0533-0862976: 19.7$^{\mathrm{m}}$/19.8$^{\mathrm{m}}$	1WGA J2258.0−3638: 0.027(5)	
J2347.2+0707	3.9′	NVSS J234706+070351: 40(2) mJy	0970-0695942: 21.2$^{\mathrm{m}}$/20.5$^{\mathrm{m}}$	–	

Table 9. Counterpart candidates, sorted by increasing angular separation from the nominal 2FGL position. Radio and X-ray sources are located within the 95% positional uncertainty of the 2FGL source. The radio flux is given in mJy at 1.4 GHz (§: 843 MHz), while the unabsorbed X-ray flux between 0.2–2 keV is listed in $10^{-12}\,\mathrm{erg\,cm^{-2}\,s^{-1}}$. Apart from the *Swift* sources, the X-ray flux was derived from the cataloged count rates (2RXP [97], 1WGA [98]), assuming a power-law with index $\Gamma = 2.0$ and a hydrogen column density N_H as obtained from the LAB survey, see section 3.5.3 (with WebPIMMS, http://heasarc.gsfc.nasa.gov/Tools/w3pimms.html). For every radio or X-ray source, the table lists corresponding optical counterpart candidates along with optical flux in USNO B2/R2 [†: B1/R2, *: SDSS r] magnitudes (HB2012a [99], QORG [100]). Parentheses indicate the error on the last decimal. The last column indicates sources associated with infrared (WISE) blazar candidates, see section 3.5.2 in this paper and [7].

2FGL name	WISE name	$W1$ [mag]	$W2$ [mag]	$W3$ [mag]	$W4$ [mag]
J0031.0+0724	J003119.70+072453.6	13.89(3)	13.06(3)	10.58(11)	8.47(39)
J0143.6−5844	J014347.39−584551.3	13.39(2)	12.70(2)	10.77(6)	8.88(28)
J0305.0−1602	J030515.07−160816.5	14.21(3)	13.64(3)	12.21(29)	9.36
J0338.2+1306	J033829.26+130215.6	13.83(3)	13.04(3)	11.16(16)	8.30
J1410.4+7411	J141235.75+741158.0	15.03(3)	14.28(4)	12.23(18)	9.55

Table 10. Infrared sources detected with WISE [62], positionally coinciding with the radio and X-ray associations established for the preselected 2FGL candidate sample. We list the WISE magnitudes $W1, W2, W3$, and $W4$, corresponding to the $3.4, 4.6, 12$, and $22\,\mu\text{m}$ bands. The error on the last decimals is written in parentheses. If no error is given, the value represents an upper limit (95 % confidence level).

Obs. ID	Name SWIFT	σ_{90} [arcsec]	S/N	$N_{\rm H}$ [$10^{20}\,\text{cm}^{-2}$]	$f^{\rm abs}(0.2-2\,\text{keV})$ [$10^{-13}\,\text{erg}\,\text{cm}^{-2}\,\text{s}^{-1}$]	ϕ_0 [$10^{-4}\,\text{keV}^{-1}\,\text{cm}^{-2}\,\text{s}^{-1}$]	Γ	$C_{\rm stat}$/dof	$f^{\rm unabs}(0.2-2\,\text{keV})$ [$10^{-13}\,\text{erg}\,\text{cm}^{-2}\,\text{s}^{-1}$]
	J014229.0–584553	5	7.4	2.13	$2.92^{+0.49}_{-0.44}$	$1.12^{+0.18}_{-0.17}$	$1.44^{+0.21}_{-0.22}$	8.2/10	$3.43^{+0.63}_{-0.59}$
41274	J014347.3–584551	4	47.4	2.04	$106.50^{+2.90}_{-2.80}$	$34.50^{+0.78}_{-0.77}$	$2.17^{+0.03}_{-0.03}$	133.0/146	$138.81^{+4.22}_{-4.18}$
	J014410.1–584042	6	4.1	2.03	$0.77^{+0.21}_{-0.21}$	$0.26^{+0.08}_{-0.07}$	2.00	3.4/3	$0.97^{+0.29}_{-0.25}$
41286	J030514.9–160818	4	13.1	3.62	$1.67^{+0.22}_{-0.22}$	$0.67^{+0.17}_{-0.13}$	$1.83^{+0.34}_{-0.28}$	10.5/4	$2.29^{+0.60}_{-0.41}$
41292	J033829.2+130217*	5	6.5	15.30					
	J033840.4+130722	5	4.4	15.20	$0.34^{+0.11}_{-0.10}$	$0.23^{+0.12}_{-0.10}$	2.00	0.4/1	$0.83^{+0.44}_{-0.37}$
47219	J141234.8+741153	5	5.4	2.35	$0.49^{+0.10}_{-0.10}$	$0.17^{+0.11}_{-0.06}$	2.00	0.3/1	$0.63^{+0.40}_{-0.24}$

Table 11. List of X-ray sources detected with *Swift*-XRT, sorted by right ascension. Apart from positional information (SWIFT JHHMMSS.s±DDMMSS, where σ_{90} denotes the uncertainty at 90% confidence), the table lists the signal-to-noise ratio of the absorbed flux $f^{\rm abs}$ between 0.2 and 2 keV for each observation (Obs. ID). The spectra were fit with a power-law model corrected for photoelectric absorption (normalization ϕ_0, power-law index Γ), fixing the hydrogen column density $N_{\rm H}$ to the nominal Galactic value. The C-statistic as implemented in *Xspec* was used for spectral fitting ($C_{\rm stat}$, dof denotes the number on degrees of freedom). The unabsorbed flux $f^{\rm unabs}$ between 0.2 and 2 keV was derived from the power-law fit. *: The source was excluded from spectral fitting, due to its location right to the edge of *Swift*-XRT's field of view.

References

[1] LAT collaboration, W. Atwood et al., *The Large Area Telescope on the Fermi Gamma-ray Space Telescope Mission*, *Astrophys. J.* **697** (2009) 1071 [arXiv:0902.1089] [INSPIRE].

[2] FERMI-LAT collaboration, *Fermi Large Area Telescope Second Source Catalog*, *Astrophys. J. Suppl.* **199** (2012) 31 [arXiv:1108.1435] [INSPIRE].

[3] FERMI-LAT collaboration, M. Ackermann et al., *The Second Catalog of Active Galactic Nuclei Detected by the Fermi Large Area Telescope*, *Astrophys. J.* **743** (2011) 171 [arXiv:1108.1420] [INSPIRE].

[4] N. Mirabal, D. Nieto and S. Pardo, *The exotic fraction among unassociated Fermi sources*, arXiv:1007.2644 [INSPIRE].

[5] J. Stephen et al., *Using the Rosat Catalogue to find Counterparts for Unidentified Objects in the 1st Fermi/LAT Catalogue*, *Mon. Not. Roy. Astron. Soc.* **408** (2010) 422 [arXiv:1004.5232] [INSPIRE].

[6] FERMI-LAT collaboration, M. Ackermann et al., *A Statistical Approach to Recognizing Source Classes for Unassociated Sources in the First Fermi-LAT Catalog*, *Astrophys. J.* **753** (2012) 83 [arXiv:1108.1202] [INSPIRE].

[7] F. Massaro, R. D'Abrusco, G. Tosti, M. Ajello and A.P. Gasparrini, *Unidentifed gamma-ray sources: hunting gamma-ray blazars*, *Astrophys. J.* **752** (2012) 61 [arXiv:1203.3801] [INSPIRE].

[8] N. Mirabal, V. Frias-Martinez, T. Hassan and E. Frias-Martinez, *Fermi's Sibyl: Mining the gamma-ray sky for dark matter subhaloes*, *Mon. Not. Roy. Astron. Soc.* **424** (2012) L64 [arXiv:1205.4825] [INSPIRE].

[9] T. Hassan, N. Mirabal, J. Contreras and I. Oya, *Gamma-Ray Active Galactic Nucleus Type through Machine-Learning Algorithms*, arXiv:1209.4359 [INSPIRE].

[10] H. Zechlin, M. Fernandes, D. Elsaesser and D. Horns, *Dark matter subhaloes as gamma-ray sources and candidates in the first Fermi-LAT catalogue*, *Astron. Astrophys.* **538** (2012) A93 [arXiv:1111.3514] [INSPIRE].

[11] FERMI-LAT collaboration, A. Abdo et al., *The Spectrum of the Isotropic Diffuse Gamma-Ray Emission Derived From First-Year Fermi Large Area Telescope Data*, *Phys. Rev. Lett.* **104** (2010) 101101 [arXiv:1002.3603] [INSPIRE].

[12] FERMI-LAT collaboration, A.A. Abdo et al., *The Fermi-LAT high-latitude Survey: Source Count Distributions and the Origin of the Extragalactic Diffuse Background*, *Astrophys. J.* **720** (2010) 435 [arXiv:1003.0895] [INSPIRE].

[13] A. Cuoco, E. Komatsu and J. Siegal-Gaskins, *Joint anisotropy and source count constraints on the contribution of blazars to the diffuse gamma-ray background*, *Phys. Rev.* **D 86** (2012) 063004 [arXiv:1202.5309] [INSPIRE].

[14] G. Jungman, M. Kamionkowski and K. Griest, *Supersymmetric dark matter*, *Phys. Rept.* **267** (1996) 195 [hep-ph/9506380] [INSPIRE].

[15] G. Bertone, D. Hooper and J. Silk, *Particle dark matter: Evidence, candidates and constraints*, *Phys. Rept.* **405** (2005) 279 [hep-ph/0404175] [INSPIRE].

[16] G. Bertone, *The moment of truth for WIMP Dark Matter*, *Nature* **468** (2010) 389 [arXiv:1011.3532] [INSPIRE].

[17] J. Diemand et al., *Clumps and streams in the local dark matter distribution*, *Nature* **454** (2008) 735 [arXiv:0805.1244] [INSPIRE].

[18] V. Springel et al., *A blueprint for detecting supersymmetric dark matter in the Galactic halo*, *Nature* **456** (2008) 73 [arXiv:0809.0894] [INSPIRE].

[19] WMAP collaboration, E. Komatsu et al., *Seven-Year Wilkinson Microwave Anisotropy Probe (WMAP) Observations: Cosmological Interpretation*, *Astrophys. J. Suppl.* **192** (2011) 18 [arXiv:1001.4538] [INSPIRE].

[20] S.P. Martin, *A Supersymmetry primer*, in *Perspectives on Supersymmetry* G.L. Kane ed., World Scientific (1998), pg. 1 [`hep-ph/9709356`] [INSPIRE].

[21] ATLAS collaboration, G. Aad et al., *Search for supersymmetry in events with three leptons and missing transverse momentum in $\sqrt{s} = 7$ TeV pp collisions with the ATLAS detector*, Phys. Rev. Lett. **108** (2012) 261804 [`arXiv:1204.5638`] [INSPIRE].

[22] CMS collaboration, S. Chatrchyan et al., *Search for anomalous production of multilepton events in pp collisions at $\sqrt{s} = 7$ TeV*, JHEP **06** (2012) 169 [`arXiv:1204.5341`] [INSPIRE].

[23] T. Saab, *An Introduction to Dark Matter Direct Detection Searches & Techniques*, `arXiv:1203.2566` [INSPIRE].

[24] M. Cirelli et al., *PPPC 4 DM ID: A Poor Particle Physicist Cookbook for Dark Matter Indirect Detection*, JCAP **03** (2011) 051 [*Erratum ibid.* **1210** (2012) E01] [`arXiv:1012.4515`] [INSPIRE].

[25] M.R. Buckley and D. Hooper, *Dark Matter Subhalos In the Fermi First Source Catalog*, Phys. Rev. **D 82** (2010) 063501 [`arXiv:1004.1644`] [INSPIRE].

[26] P. Brun, E. Moulin, J. Diemand and J.-F. Glicenstein, *Searches for dark matter subhaloes with wide-field Cherenkov telescope surveys*, Phys. Rev. **D 83** (2011) 015003 [`arXiv:1012.4766`] [INSPIRE].

[27] MAGIC collaboration, D. Nieto et al., *The search for galactic dark matter clump candidates with Fermi and MAGIC*, proceedings of the *32nd International Cosmic Ray Conference (ICRC)*, Beijing China, 2011, `arXiv:1109.5935` [INSPIRE].

[28] FERMI LAT collaboration, M. Ackermann et al., *Search for Dark Matter Satellites using the FERMI-LAT*, Astrophys. J. **747** (2012) 121 [`arXiv:1201.2691`] [INSPIRE].

[29] A.V. Belikov, D. Hooper and M.R. Buckley, *Searching For Dark Matter Subhalos In the Fermi-LAT Second Source Catalog*, Phys. Rev. **D 86** (2012) 043504 [`arXiv:1111.2613`] [INSPIRE].

[30] T. Bringmann, *Particle Models and the Small-Scale Structure of Dark Matter*, New J. Phys. **11** (2009) 105027 [`arXiv:0903.0189`] [INSPIRE].

[31] M. Boylan-Kolchin, J.S. Bullock and M. Kaplinghat, *Too big to fail? The puzzling darkness of massive Milky Way subhaloes*, *Mon. Not. Roy. Astron. Soc.* **415** (2011) L40 [`arXiv:1103.0007`] [INSPIRE].

[32] T.M. Brown et al., *The Primeval Populations of the Ultra-Faint Dwarf Galaxies*, *Astrophys. J.* **753** (2012) L21 `arXiv:1206.0941` [INSPIRE].

[33] M. Kuhlen, J. Diemand and P. Madau, *The Dark Matter Annihilation Signal from Galactic Substructure: Predictions for GLAST*, *Astrophys. J.* **686** (2008) 262 [`arXiv:0805.4416`] [INSPIRE].

[34] G.D. Martinez, J.S. Bullock, M. Kaplinghat, L.E. Strigari and R. Trotta, *Indirect Dark Matter Detection from Dwarf Satellites: Joint Expectations from Astrophysics and Supersymmetry*, JCAP **06** (2009) 014 [`arXiv:0902.4715`] [INSPIRE].

[35] L. Bergstrom, T. Bringmann, M. Eriksson and M. Gustafsson, *Gamma rays from Kaluza-Klein dark matter*, Phys. Rev. Lett. **94** (2005) 131301 [`astro-ph/0410359`] [INSPIRE].

[36] L. Bergström, T. Bringmann, M. Eriksson and M. Gustafsson, *Gamma rays from heavy neutralino dark matter*, Phys. Rev. Lett. **95** (2005) 241301 [`hep-ph/0507229`] [INSPIRE].

[37] T. Bringmann, L. Bergström and J. Edsjö, *New Gamma-Ray Contributions to Supersymmetric Dark Matter Annihilation*, JHEP **01** (2008) 049 [`arXiv:0710.3169`] [INSPIRE].

[38] T. Bringmann, X. Huang, A. Ibarra, S. Vogl and C. Weniger, *Fermi LAT Search for Internal Bremsstrahlung Signatures from Dark Matter Annihilation*, JCAP **07** (2012) 054 [`arXiv:1203.1312`] [INSPIRE].

[39] N. Arkani-Hamed, D.P. Finkbeiner, T.R. Slatyer and N. Weiner, *A Theory of Dark Matter*, Phys. Rev. **D 79** (2009) 015014 [`arXiv:0810.0713`] [INSPIRE].

[40] M. Kuhlen, P. Madau and J. Silk, *Exploring Dark Matter with Milky Way substructure*, *Science* **325** (2009) 970 [arXiv:0907.0005] [INSPIRE].

[41] E.A. Baltz and L. Wai, *Diffuse inverse Compton and synchrotron emission from dark matter annihilations in galactic satellites*, *Phys. Rev.* **D 70** (2004) 023512 [astro-ph/0403528] [INSPIRE].

[42] S. Colafrancesco, S. Profumo and P. Ullio, *Detecting dark matter WIMPs in the Draco dwarf: A multi-wavelength perspective*, *Phys. Rev.* **D 75** (2007) 023513 [astro-ph/0607073] [INSPIRE].

[43] T.E. Jeltema and S. Profumo, *Searching for Dark Matter with X-ray Observations of Local Dwarf Galaxies*, *Astrophys. J.* **686** (2008) 1045 [arXiv:0805.1054] [INSPIRE].

[44] E.A. Baltz, J.E. Taylor and L.L. Wai, *Can Astrophysical Gamma Ray Sources Mimic Dark Matter Annihilation in Galactic Satellites?*, *Astrophys. J.* **659** (2007) L125 [astro-ph/0610731] [INSPIRE].

[45] FERMI LAT collaboration, A. Abdo et al., *The First Fermi Large Area Telescope Catalog of Gamma-ray Pulsars*, *Astrophys. J. Suppl.* **187** (2010) 460 [*Erratum ibid.* **193** (2011) 22] [arXiv:0910.1608] [INSPIRE].

[46] M. Kerr et al., *Five New Millisecond Pulsars From a Radio Survey of 14 Unidentified Fermi-LAT Gamma-ray Sources*, *Astrophys. J.* **748** (2012) L2 [arXiv:1201.5160] [INSPIRE].

[47] P. Ray et al., *Radio Searches of Fermi LAT Sources and Blind Search Pulsars: The Fermi Pulsar Search Consortium*, arXiv:1205.3089 [INSPIRE].

[48] N. Fornengo, L. Pieri and S. Scopel, *Neutralino annihilation into gamma-rays in the Milky Way and in external galaxies*, *Phys. Rev.* **D 70** (2004) 103529 [hep-ph/0407342] [INSPIRE].

[49] J. Cembranos, A. de la Cruz-Dombriz, A. Dobado, R. Lineros and A. Maroto, *Photon spectra from WIMP annihilation*, *Phys. Rev.* **D 83** (2011) 083507 [arXiv:1009.4936] [INSPIRE].

[50] L. Bergström, P. Ullio and J.H. Buckley, *Observability of gamma-rays from dark matter neutralino annihilations in the Milky Way halo*, *Astropart. Phys.* **9** (1998) 137 [astro-ph/9712318] [INSPIRE].

[51] S.S. Wilks, *The Large-Sample Distribution of the Likelihood Ratio for Testing Composite Hypotheses*, *Ann. Math. Statist.* **9** (1938) 60.

[52] H. Chernoff, *On the Distribution of the Likelihood Ratio*, *Ann. Math. Statist.* **25** (1954) 573.

[53] W.H. Press, S.A. Teukolsky, W.T. Vetterling and B.P. Flannery, *Numerical Recipes: The Art of Scientific Computing*, third edition, Cambridge University Press, (2007).

[54] J.F. Navarro, C.S. Frenk and S.D. White, *A universal density profile from hierarchical clustering*, *Astrophys. J.* **490** (1997) 493 [astro-ph/9611107] [INSPIRE].

[55] W. Cash, *Parameter estimation in astronomy through application of the likelihood ratio*, *Astrophys. J.* **228** (1979) 939 [INSPIRE].

[56] D.G. Monet et al., *The USNO-B catalog*, *Astron. J.* **125** (2003) 984 [astro-ph/0210694] [INSPIRE].

[57] J.J. Condon et al., *The NRAO VLA Sky survey*, *Astron. J.* **115** (1998) 1693 [INSPIRE].

[58] T. Mauch et al., *SUMSS: A wide-field radio imaging survey of the southern sky. 2. The Source catalogue*, *Mon. Not. Roy. Astron. Soc.* **342** (2003) 1117 [astro-ph/0303188] [INSPIRE].

[59] E.L. Wright et al., *The wide-field Infrared Survey Explorer (WISE): Mission Description and Initial On-orbit Performance*, *Astron. J.* **140** (2010) 1868 [arXiv:1008.0031] [INSPIRE].

[60] R. D'Abrusco, F.M. Ajello, J. Grindlay, H. Smith and G. Tosti, *Infrared Colors of the gamma-ray detected blazars*, arXiv:1203.0568 [INSPIRE].

[61] F. Massaro et al., *The WISE gamma-ray strip parametrization: the nature of the gamma-ray Active Galactic Nuclei of Uncertain type*, *Astrophys. J.* **750** (2012) 138 [arXiv:1203.1330] [INSPIRE].

[62] R.M. Cutri et al., *WISE All-Sky Data Release (Cutri+ 2012)*, *VizieR Online Data Catalog* **2311** (2012).

[63] A. Falcone et al., *Systematic Search for X-ray Counterparts of Fermi-LAT Unassociated Sources Using Swift Observations*, volume. 12 of *AAS/High Energy Astrophysics Division*, (2011) pg. 04.03.

[64] Swift Science collaboration, N. Gehrels et al., *The Swift Gamma-Ray Burst Mission*, *AIP Conf. Proc.* **727** (2004) 637 [astro-ph/0405233] [inSPIRE].

[65] N. Gehrels et al., *Erratum: "The Swift Gamma-Ray Burst Mission"*, *Astrophys. J.* **621** (2005) 558.

[66] T. Poole et al., *Photometric Calibration of the Swift Ultraviolet/Optical Telescope*, *Mon. Not. Roy. Astron. Soc.* **383** (2008) 627 [arXiv:0708.2259] [inSPIRE].

[67] P.M. Kalberla et al., *The Leiden/Argentine/Bonn (LAB) survey of Galactic HI: Final data release of the combined LDS and IAR surveys with improved stray-radiation corrections*, *Astron. Astrophys.* **440** (2005) 775 [astro-ph/0504140] [inSPIRE].

[68] D.J. Schlegel, D.P. Finkbeiner and M. Davis, *Maps of dust IR emission for use in estimation of reddening and CMBR foregrounds*, *Astrophys. J.* **500** (1998) 525 [astro-ph/9710327] [inSPIRE].

[69] J.A. Cardelli, G.C. Clayton and J.S. Mathis, *The relationship between infrared, optical and ultraviolet extinction*, *Astrophys. J.* **345** (1989) 245 [inSPIRE].

[70] Fermi LAT collaboration, A. Abdo et al., *Fermi observations of TeV-selected AGN*, *Astrophys. J.* **707** (2009) 1310 [arXiv:0910.4881] [inSPIRE].

[71] CTA Consortium collaboration, M. Actis et al., *Design concepts for the Cherenkov Telescope Array CTA: An advanced facility for ground-based high-energy gamma-ray astronomy*, *Exper. Astron.* **32** (2011) 193 [arXiv:1008.3703] [inSPIRE].

[72] G. Fossati, A. Celotti, G. Ghisellini and L. Maraschi, *Unifying models for x-ray selected and radio selected bl lac objects*, *Mon. Not. Roy. Astron. Soc.* **289** (1997) 136 [astro-ph/9704113] [inSPIRE].

[73] D. Donato, G. Ghisellini, G. Tagliaferri and G. Fossati, *Hard x-ray properties of blazars*, *Astron. Astrophys* **375** (2001) 739 [astro-ph/0105203] [inSPIRE].

[74] K. Nilsson et al., *Host galaxy subtraction of TeV candidate BL Lacertae objects*, *Astron. Astrophys.* (2007) [arXiv:0709.2533] [inSPIRE].

[75] A. Franceschini, G. Rodighiero and M. Vaccari, *The extragalactic optical-infrared background radiations, their time evolution and the cosmic photon-photon opacity*, *Astron. Astrophys.* **487** (2008) 837 [arXiv:0805.1841] [inSPIRE].

[76] R. Saxton et al., *The first XMM-Newton slew survey catalogue: XMMSL1*, *Astron. Astrophys.* **480** (2008) 611 [arXiv:0801.3732] [inSPIRE].

[77] C. Weniger, *A Tentative Gamma-Ray Line from Dark Matter Annihilation at the Fermi Large Area Telescope*, *JCAP* **08** (2012) 007 [arXiv:1204.2797] [inSPIRE].

[78] M. Su and D.P. Finkbeiner, *Strong Evidence for Gamma-ray Line Emission from the Inner Galaxy*, arXiv:1206.1616 [inSPIRE].

[79] D.P. Finkbeiner, M. Su and C. Weniger, *Is the 130 GeV Line Real? A Search for Systematics in the Fermi-LAT Data*, arXiv:1209.4562 [inSPIRE].

[80] A. Hektor, M. Raidal and E. Tempel, *Fermi-LAT gamma-ray signal from Earth Limb, systematic detector effects and their implications for the 130 GeV gamma-ray excess*, arXiv:1209.4548 [inSPIRE].

[81] L. Bergstrom, G. Bertone, J. Conrad, C. Farnier and C. Weniger, *Investigating Gamma-Ray Lines from Dark Matter with Future Observatories*, arXiv:1207.6773 [inSPIRE].

[82] E. Tempel, A. Hektor and M. Raidal, *Fermi 130 GeV gamma-ray excess and dark matter annihilation in sub-haloes and in the Galactic centre*, *JCAP* **09** (2012) 032 [arXiv:1205.1045] [inSPIRE].

[83] A. Hektor, M. Raidal and E. Tempel, *An evidence for indirect detection of dark matter from galaxy clusters in Fermi-LAT data*, `arXiv:1207.4466` [INSPIRE].

[84] M. Su and D.P. Finkbeiner, *Double Gamma-ray Lines from Unassociated Fermi-LAT Sources*, `arXiv:1207.7060` [INSPIRE].

[85] D. Hooper and T. Linden, *Are Lines From Unassociated Gamma-Ray Sources Evidence For Dark Matter Annihilation?*, *Phys. Rev.* **D 86** (2012) 083532 [`arXiv:1208.0828`] [INSPIRE].

[86] N. Mirabal, *The Dark Knight Falters*, `arXiv:1208.1693` [INSPIRE].

[87] P. Vincent, *H.E.S.S. Phase II*, in *International Cosmic Ray Conference*, volume 5, (2055), pg. 163.

[88] H.E.S.S. collaboration, F. Aharonian et al., *Observations of the Crab Nebula with H.E.S.S*, *Astron. Astrophys.* **457** (2006) 899 [`astro-ph/0607333`] [INSPIRE].

[89] MAGIC collaboration, J. Albert et al., *VHE Gamma-Ray Observation of the Crab Nebula and Pulsar with MAGIC*, *Astrophys. J.* **674** (2008) 1037 [`arXiv:0705.3244`] [INSPIRE].

[90] MAGIC collaboration, D. Borla Tridon, T. Schweizer, F. Goebel, R. Mirzoyan and M. Teshima, *The MAGIC-II gamma-ray stereoscopic telescope system*, *Nucl. Instrum. Meth.* **A 623** (2010) 437 [INSPIRE].

[91] T. Weekes et al., *VERITAS: The Very energetic radiation imaging telescope array system*, *Astropart. Phys.* **17** (2002) 221 [`astro-ph/0108478`] [INSPIRE].

[92] J. Holder et al., *VERITAS: Status and Highlights*, proceedings of the *32nd International Cosmic Ray Conference (ICRC)*, Beijing China, (2011), [`arXiv:1111.1225`] [INSPIRE].

[93] CTA collaboration, M. Doro, *CTA – A Project for a New Generation of Cherenkov Telescopes*, *Nucl. Instrum. Meth.* **A 630** (2011) 285 [`arXiv:0908.1410`] [INSPIRE].

[94] CTA collaboration, M. Doro et al., *Dark Matter and Fundamental Physics with the Cherenkov Telescope Array*, `arXiv:1208.5356` [INSPIRE].

[95] A. Galper et al., *Status of the GAMMA-400 Project*, `arXiv:1201.2490` [INSPIRE].

[96] A. Galper, O. Adriani, R. Aptekar, I. Arkhangelskaja, A. Arkhangelskiy, et al., *Design and Performance of the GAMMA-400 Gamma-Ray Telescope for the Dark Matter Searches*, `arXiv:1210.1457` [INSPIRE].

[97] ROSAT Consortium, *ROSAT News No. 74*, ROSAT News (2001).

[98] N.E. White, P. Giommi and L. Angelini, *The WGACAT version of ROSAT sources (White+ 2000)*, *VizieR Online Data Catalog* **9031** (2000) 0.

[99] J.B. Hutchings and L. Bianchi, *A Catalog of 19,100 Quasi-stellar Object Candidates with Redshift 0.5-1.5*, *Astron. J.* **140** (2010) 1987.

[100] E. Flesch and M.J. Hardcastle, *An all-sky optical catalogue of radio/x-ray sources*, *Astron. Astrophys.* **427** (2004) 387 [`astro-ph/0407310`] [INSPIRE].

4.3 Further investigation of the selected candidate sources

Further investigations on the candidate sources selected in Publication I and Publication II were carried out within the framework of this thesis. In Section 4.3.1, the origin of their infrared and optical emission is investigated by confronting the SEDs with the thermal emission spectrum of a standard BL-Lac host galaxy. Temporal variability is addressed with data from an optical monitoring campaign in Section 4.3.2. Updated X-ray data taken with *Swift*-XRT are presented in Section 4.3.3, while UV data contemporaneously taken with *Swift*-UVOT are analyzed in Section 4.3.4. In addition, studies of 2FGL J0031.0+0724 were carried out with optical and VHE follow-up observations, reported in Section 4.3.5 and Section 4.3.6. Possible physical origins of 2FGL J0031.0+0724 are discussed in Section 4.3.7.

4.3.1 Thermal emission of the host galaxy

The next two paragraphs are based on the conclusions of Publication I and II, i.e., a BL-Lac-type nature of the selected gamma-ray sources is assumed. Precise redshift determinations are required to further investigate this scenario with the interpretation of multiwavelength SEDs. While flat spectrum radio quasars (FSRQs) generically show strong optical emission lines for spectroscopic redshift measurements, a defining property of BL Lacs are weak or absent emission lines (with rest-frame equivalent widths of less than 5 Å). The optical spectra of BL Lacs are dominated by a continuum of polarized non-thermal emission. Therefore, a spectroscopic determination of BL-Lac redshifts is heavily hampered.

BL Lacs are however known to be embedded in luminous giant elliptical galaxies. Yet another temporally steady component of AGN spectra can manifest in a big blue bump (BBB; e.g., Peterson 1997; Calderone *et al.* 2013), which arises from the thermal emission of the accretion disk surrounding the central supermassive black hole. A BBB would contribute to the optical and UV emission of a BL Lac. Once a thermal component can be photometrically and spatially separated from the underlying continuum emission, photometric measurements of the redshift would be feasible.

Redshift lower limits. Extensive survey campaigns of BL-Lac host galaxies with the Hubble Space Telescope (HST) have established giant elliptical galaxies as well-defined photometric standard candles (see Sbarufatti *et al.* 2005 and references therein). In Publication II, lower limits on the redshift of the selected *Fermi*-LAT objects have been determined by assuming the integral optical R-band emission to originate from a standard giant elliptical host galaxy. The redshift lower limits have been calculated from the corresponding distance moduli. In the following, the method is improved by a modified calibration and an expanded set of USNO data from temporally separated observational epochs.

From HST observations of 106 BL Lacs, Sbarufatti *et al.* (2005) have deduced an average value of $M_R = -22.9^{\mathrm{m}} \pm 0.5^{\mathrm{m}}$ for the distribution of absolute R-band magnitudes of giant elliptical BL-Lac host galaxies. The alignment of all studied objects ($z \lesssim 0.7$) in a Hubble diagram provides a well-defined relation between the apparent magnitude of the thermal emission $\hat{m}_R$ and the corresponding redshift,

$$\log_{10}(1+z) = 10^{-2}\left(0.293\hat{m}_R^2 - 7.19\hat{m}_R + 45.1\right), \tag{4.1}$$

which can be used to estimate the redshift of a BL Lac for a given measurement of $\hat{m}_R$.

Name	Optical counterpart	m_{R1}	m_{R2}	A_R	z_ℓ	$z_\ell^{95\%}$
2FGL J0031.0+0724	USNO 0974-0005617	18.2^{m}	18.6^{m}	0.096^{m}	0.33	0.27
2FGL J0143.6–5844	USNO 0312-0011298	16.7^{m}	16.6^{m}	0.056^{m}	0.16	0.13
2FGL J0305.0–1602	USNO 0738-0029664	17.2^{m}	17.0^{m}	0.123^{m}	0.19	0.16
2FGL J0338.2+1306	USNO 1030-0045117	19.4^{m}	18.3^{m}	0.914^{m}	0.33	0.27
2FGL J1410.4+7411	USNO 1641-0084321	19.5^{m}	19.5^{m}	0.068^{m}	0.45	0.38

Table 4.1: Lower limits z_ℓ on the photometric redshifts z for *Fermi*-LAT sources selected in Publication I and II. Besides the 2FGL name, the table lists the established optical counterpart (USNO-B1.0) together with the R-band apparent magnitudes observed in the first and second catalog epochs (USNO $R1$ and $R2$). Interstellar reddening (coefficient A_R) was subtracted as obtained from Schlegel *et al.* (1998). Strict lower limits $z_\ell^{95\%}$ (95% CL) incorporate the uncertainty of $\sigma_{m_R} \approx 0.25^{\mathrm{m}}$ (Monet *et al.* 2003) on the $R1$ and $R2$ magnitudes.

In the case considered here, the integral R-band magnitude m_R of the thermal and continuum emission therefore provides a lower limit on the redshift of the source. Table 4.1 lists lower limits on the redshift of the studied sources, derived with Eq. (4.1) from magnitudes listed in the USNO catalog. The values imply the assumption of constant thermal emission, i.e., the faintest apparent magnitudes m_R were selected among the corresponding catalog entries for separate observational epochs. Strict lower redshift limits are given incorporating the uncertainties of the measurements.

Thermal emission spectrum of a giant elliptical host galaxy. With the redshift lower limits, the near-infrared and optical spectrum of the candidate sources can be investigated for a thermal component of a standard BL-Lac host galaxy. The standard spectrum of a giant elliptical host galaxy as obtained by Yee & Oke (1978) was confronted with the SEDs of the candidate sources shown in Fig. 4.2. The infrared extrapolation of the galaxy spectrum was adopted from Falomo *et al.* (1993), and the R-band emission of the template galaxy was normalized to $M_R = -22.9^{\mathrm{m}}$. Its apparent magnitude can be calculated from the distance modulus $m_R - M_R$ by

$$m_R = M_R + K_R(z) + E_R(z) + 5\log_{10}(d_{\mathrm{L}}(z)/\mathrm{pc}) - 5\,, \tag{4.2}$$

where the redshift-dependent K-correction $K_R(z)$ and evolutionary correction $E_R(z)$ were obtained from Poggianti (1997). The luminosity distance d_{L} is given by the cosmological model,

$$d_{\mathrm{L}}(z) = (1+z)\frac{c}{H_0}\int_0^z \frac{\mathrm{d}z'}{\sqrt{\Omega_{\mathrm{m}}(1+z')^3 + \Omega_\Lambda}}\,, \tag{4.3}$$

where a flat Universe with $\Omega_{\mathrm{m}} + \Omega_\Lambda = 1$ is assumed, and c denotes the speed of light. The absolute magnitude M_R corresponds to the apparent magnitude of the galaxy if it were 10 pc away, at rest, and compact (e.g., Hogg *et al.* 2002), in accordance to the sign convention chosen in Eq. 4.2 (Poggianti 1997). For redshifts $z \lesssim 0.5$, the correction for chemical evolution does not significantly change the form of the thermal spectrum for red and infrared bands. The band-dependent K-correction can however result in changing galaxy colors in blue bands. Given comparably small redshifts and the effective template approach used here, these changes have been neglected.

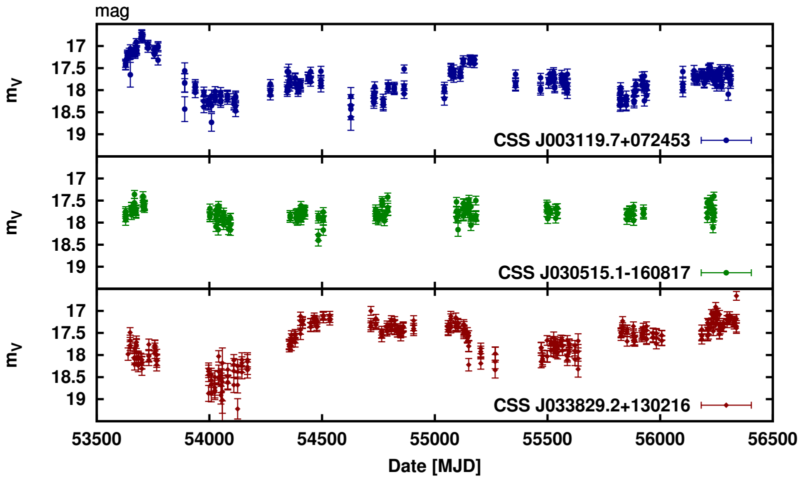

Figure 4.1: V-band light curves of CSS J003119.7+072453 (USNO 0974-0005617), CSS J030515.1-160817 (USNO 0738-0029664), CSS J033829.2+130216 (USNO 1030-0045117), taken with the Catalina Sky Survey 0.7 m Schmidt telescope. The data were retrieved from `http://crts.caltech.edu/`. The Modified Julian Dates of 53 500, 55 000, and 56 500 correspond to the dates 2005-05-10, 2009-06-18, and 2013-07-27, respectively.

For the candidate sources selected in Publication I and II, the SEDs including the thermal emission spectra of a standard BL-Lac host galaxy are shown in Appendix B.2, Fig. B.4, assuming the corresponding redshift lower limits z_ℓ given in Table 4.1. In the cases for 2FGL J0143.6–5844 and 2FGL J0305.0–1602, the galaxy spectrum fits the optical (USNO) B-band and R-band emission well within the uncertainties. However, its near-infrared flux outshines the 2MASS data by approximately 1 and 1.5 magnitudes, respectively. This discrepancy can be resolved by assuming an intrinsically fainter host galaxy, a higher source redshift, or both effects in combination. For the case of a BL-Lac scenario, this indicates that the measured R-band fluxes are dominated by the non-thermal continuum. For 2FGL J0338.2+1306, the standard galaxy spectrum matches the 2MASS data and the R-band ($R1$) emission detected in the first catalog epoch, indicating the flux level of thermal emission. The optical emission of 2FGL J0338.2+1306 is however indicated to be temporally variable by comparing the two observational epochs of the USNO catalog. Again, this implies a significant contribution of a non-thermal continuum, although the UV flux, increasing with frequency, might hint for an additional contribution of a BBB (see Section 4.3.4). For 2FGL J1410.4+7411, no near-infrared data is reported in the 2MASS catalog.

For 2FGL J0031.0+0724, the thermal host galaxy emission is shown in Fig. 4.6 on page 106 for a redshift lower limit of $z > 0.33$ as obtained in this section, and for a spectroscopically determined redshift lower limit of $z > 0.87$ (see Section 4.3.5). In the case of a BL-Lac scenario, the fact that the expected thermal flux is considerably below the USNO and SDSS data, as well as the temporal variation of the USNO magnitudes, hint for a dominating non-thermal emission in the optical R-band.

4.3.2 Optical monitoring

Optical monitoring campaigns such as the Catalina Real-Time Transient Survey (CRTS; Drake *et al.* 2009) provide the opportunity of obtaining optical light curves for a variety of sources over time periods of several years. The optical associations established for

FoV	Target ID	Observational epoch	Epoch length [d]	Exposure [ks]
2FGL J0031.0+0724	41265	2010-11-10	1	10.1
	47130	2012-01-24 – 2012-02-11	19	8.2
2FGL J0143.6—5844	41274	2010-10-12 – 2010-11-05	25	4.4
2FGL J0305.0—1602	41286	2011-01-07 – 2011-03-02	55	3.2
	49995	2013-03-12	1	1.1
2FGL J0338.2+1306	41292	2010-10-07 – 2010-12-22	77	4.1
	47147	2012-07-04	1	3.4
2FGL J1410.4+7411	41402	2011-03-08 – 2011-03-11	4	3.7
	47219	2012-03-08 – 2012-04-05	29	3.5

Table 4.2: Target IDs, observational epochs, epoch lengths, and total exposures of the analyzed archival *Swift*-XRT data sets of the celestial regions around the targeted *Fermi*-LAT sources.

2FGL J0031.0+0724, 2FGL J0305.0—1602, and 2FGL J0338.2+1306 have been monitored by the CRTS for more than seven years. The V-band light curves of the three sources taken with the Catalina Sky Survey 0.7 m Schmidt telescope are shown in Fig. 4.1. The optical fluxes associated to 2FGL J0031.0+0724 and 2FGL J0338.2+1306 vary with time by up to two magnitudes, supporting the previous conclusion of a dominant contribution of non-thermally produced optical emission. The optical variability of 2FGL J0305.0—1602 is less pronounced and within approximately one magnitude.

4.3.3 *Swift*-XRT data

New data sets were added to the *Swift*-XRT data analyzed in Publication I and Publication II. The new data were taken in correspondingly different observational epochs, separated by one to two years. Table 4.2 gives an overview of the archival *Swift*-XRT data analyzed in the publications and the new data sets from additional observations of the studied *Fermi*-LAT candidate sources. The new data sets were calibrated and analyzed with the analysis framework discussed in Publication II.[1]

In general, each observational epoch of *Swift* data (i.e., a data set flagged by a single target ID) splits in a number of different day-wise observations (flagged by a single observation ID). As shown in Table 4.2, single observations combined in one epoch have been taken within a period of ~2.5 months at most, while the average epoch length is ~24 days.

---

[1] The *Swift*-XRT analysis reported in Publication II accidentally resulted in flux values which are systematically below the actual ones. The combination of events from different XRT pointings by *xselect* leaded to a lack of events in the final PHA files. The effect occurred due to inconsistent handling of physical sky coordinates by the event selection algorithm of *xselect* and is not documented in the analysis manual (Capalbi *et al.* 2005). Imaging and source detection (Publication II, Fig. 2) are not affected. Also, the corrections neither affect the overall conclusions nor anything else of the analysis presented in Publication II. The XRT analysis in Publication I is also not affected by this effect.
The analysis routine was improved accordingly. While the spectrum of 2FGL J0143.6–5844 remains nearly unchanged (the reason why thorough cross-checks did not reveal the effect in earlier stages of this work), the X-ray fluxes of 2FGL J0305.0–1602 and 2FGL J1410.4+7411 change to higher values (see below). The corrections to Publication II will be published as Erratum (in preparation).

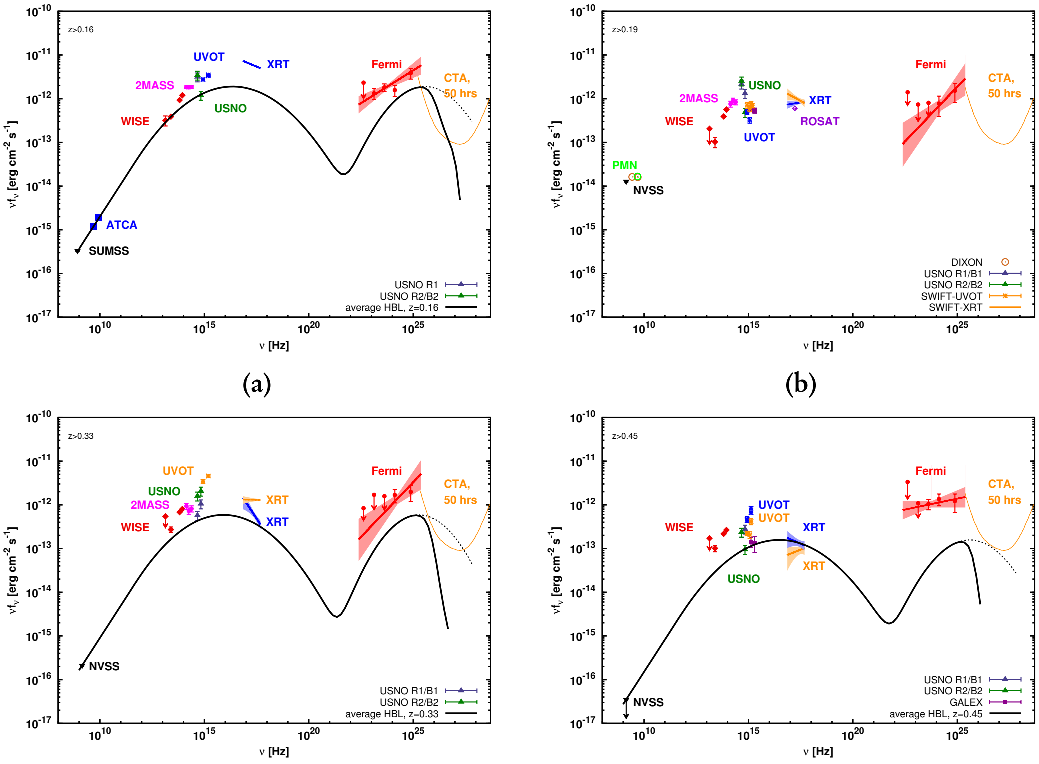

(a) (b)

(c) (d)

Figure 4.2: SEDs of **(a)** 2FGL J0143.6–5844, **(b)** 2FGL J0305.0–1602, **(c)** 2FGL J0338.2+1306, and **(d)** 2FGL J1410.4+7411, plotted as in Fig. 3 in Publication II. The averaged HBL SED is normalized to 5GHz ATCA data (Petrov *et al.* 2013), and otherwise to NVSS or SUMSS radio data, assuming the redshift lower limits z_ℓ given in Table 4.1. For 2FGL J0305.0–1602, radio data from the DIXON catalog (43rd version, Nov. 1981; Dixon 1970) and the Parkes-MIT-NRAO survey (PMN J0305–1608; Griffith *et al.* 1994) are included. The near-infrared counterparts 2MASS 01434742–5845514, 2MASS 03051508–1608168, and 2MASS 03382926+1302151 are added, together with the optical R-band and B-band magnitudes from the first observational epoch listed in the USNO-B1.0 catalog ($R1$ and $B1$). The SEDs include the updated X-ray spectra in the 0.3 keV to 2 keV band (see Section 4.3.3) in blue and orange, where the different colors correspond to separate observational epochs. Contemporaneously taken UV data (see Section 4.3.4) is plotted in the correspondingly same colors. Additionally, the ROSAT source 1WGA J0305.2–1607 is included.

Following Publication II, the data taken in one epoch have been combined for the analysis, in order to gain sufficient exposure. It should be remarked, however, that this analysis approach results in averaged flux values and averaged spectral photon indices in the case for variable sources. In comparison to a day-wise binning with correspondingly reduced exposures and thus increased statistical uncertainties, the considered temporal average implies a conservative choice in the light of the search for X-ray variability.

All X-ray spectra of the studied candidate sources are presented in the multi-wavelength SEDs shown in Fig. 4.2. The case for 2FGL J0031.0+0724 is discussed in Fig. 4.6 later in this section. Table B.1 (in Appendix B.3) lists the spectral fit parameters for the entire list of X-ray sources detected in the analyzed XRT fields. In the analysis, the standard energy threshold of 0.3 keV (Godet *et al.* 2009) was adopted for spectral fitting.[2] For the X-ray associations of the studied *Fermi*-LAT sources, the binned count spectra fitted with a power law corrected for Galactic photoelectric absorption are presented in Appendix B.5.

The X-ray analysis in Publication II has been optimized for analyzing faint X-ray sources. With regard to the interpretation of the spectra listed in Table B.1, it should be emphasized that a spectral fitting of faint sources suffers systematic uncertainties, in particular on the spectral photon index. While for bright sources a channel-wise data binning turns out to be most appropriate when using the Cash statistic for spectral fitting[3], the grouping of detector channels to at least 5 counts per bin turned out to be more reliable for faint sources. Given the sample of X-ray sources analyzed here, the systematics between the different analyses were investigated. The systematic uncertainty on the index of the fitted power-law spectra was estimated with $|\Delta\Gamma_{\mathrm{syst}}| \lesssim 0.2$.

In conclusion, the X-ray fluxes of all candidate sources are compatible with the blazar hypothesis (see Fig. 4.2). Comparing the X-ray spectra of the respective observational epochs indicates variable X-ray emission from the sources 2FGL J0338.2+1306 and 2FGL J1410.4+7411. This supports a BL-Lac origin of these sources.

In particular for the case of 2FGL J1410.4+7411 the X-ray flux is compatible with the flux of the average HBL SED. A similar comparison in the gamma-ray band however indicates that the measured gamma-ray flux is a factor of ~10 higher than the average flux expectation. In combination with the rather hard index of the gamma-ray spectrum, this result might point to a specific class of objects predicted with a separate emission component at GeV to TeV energies. The emission would arise in addition to the conventional synchrotron self-Compton (SSC; Band & Grindlay 1985; Katarzyński *et al.* 2001) emission, and could originate in CMB photons Compton-upscattered by the accelerated electron population of an extended jet (see Böttcher *et al.* 2008). Given an energy density of the CMB $u_{\mathrm{cmb}} \propto (1+z)^4$, such a component would be most pronounced in comparably high-redshifted BL Lacs, to which 2FGL J1410.4+7411 with $z > 0.45$ seems to belong to (the median spectroscopic redshift of the known BL-Lac population is 0.33, see Shaw *et al.* 2013). Such a scenario can be addressed with TeV follow-up observations.

4.3.4 *Swift*-UVOT data

All X-ray sources previously associated to the candidate *Fermi*-LAT sources have been detected in the UV band by simultaneous observations with the Ultraviolet/Optical Telescope aboard the *Swift* satellite (*Swift*-UVOT; Roming *et al.* 2005). The photometric UVOT data were extracted using the HEAsoft 6.13 package following the standard pipeline outlined in Immler *et al.* (2008) for calibration. The *Swift* calibration files as of 2013-05-07 were used. Aspect correction was applied with *uvotskycorr*, calibrating with the USNO-B1.0 catalog. Source detection was performed with *uvotdetect*. The background-subtracted flux in all available UVOT filters (see Poole *et al.* 2008 for details) was extracted with *uvotsource*, using the standard aperture of 5″. A radius of 50″ was used for background regions. A signal-to-noise ratio of 5 was required for source detection. For each target (i.e., a single target ID as listed in Table B.1 in the appendix), UVOT exposures within a single observation (i.e., a single observation ID) were stacked for each available filter. The stacked images were corrected for the large-scale detector sensitivity, computed

---

[2] See `http://www.swift.ac.uk/analysis/xrt/index.php` for details. [3] See `http://www.swift.ac.uk/analysis/xrt/index.php` and Humphrey *et al.* (2009).

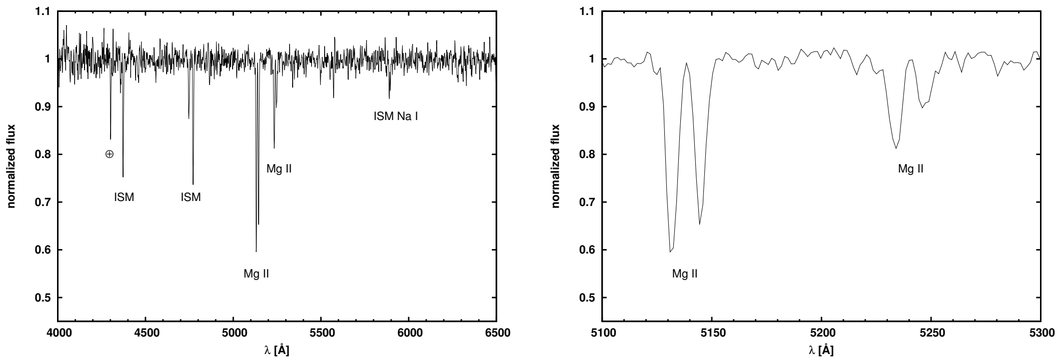

(a) (b)

Figure 4.3: Normalized optical spectrum of USNO 0974-0005617 obtained with the NOT 2.5 m telescope. **(a)**: Full spectral range covered with the ALFOSC with the line identification discussed in the text and in Table 4.3. The ⊕ symbol denotes a telluric line. **(b)**: Mg II doublets detected from two intervening systems.

with *uvotskylss*. The magnitudes of the analyzed UVOT sources are listed in Table B.2 in Appendix B.5 and are shown in the SEDs in Fig. 4.2.

In particular for the case of 2FGL J1410.4+7411 the indication for X-ray variability is supported by the variability observed in the UV band. The data might indicate a BBB on top of a variable continuum.

4.3.5 Observations of 2FGL J0031.0+0724 with the Nordic Optical Telescope

Spectroscopic observations in the optical band are required to determine the redshift of the sources. We observed the USNO counterpart of 2FGL J0031.0+0724 with the Nordic Optical Telescope (NOT; 2.5 m mirror diameter), which is located at the Spanish Observatorio del Roque de los Muchachos, La Palma, Canaries, Spain[4]. The initial observational proposal is presented in Appendix C.2. The observations were carried out in Service Mode in two time segments on 2012-09-06 and 2012-09-20, each composed of three exposures with 2 050 s (total exposure 12.3 ks). The Andalucia Faint Object Spectrograph and Camera (ALFOSC) was used. The spectrograph was configured with grism #7, with a slit of 1″, covering the spectral range between 4 000 Å and 6 500 Å with a dispersion of ∼1.5Å per pixel. Calibration was done with a helium-neon lamp. Data reduction was performed with the Image Reduction and Analysis Facility (IRAF)[5] with standard procedures.[6] Bias subtraction, flat fielding, and cosmic-ray rejection were applied, and both combined images and a combined one-dimensional spectrum were extracted. The flux was normalized, but no absolute flux calibration with standard stars was performed.

The optical spectrum of USNO 0974-0005617 is shown in Fig. 4.3 in the range between 4 000 Å and 6 500 Å. The spectrum is dominated by continuum emission. No emission lines have been detected. Most of the detected absorption lines are due to foreground, i.e., a telluric line at 4 300 Å, absorption by the interstellar medium (ISM) at 4 372 Å (Fe III; Thompson *et al.* 2008), 4 745 Å (C II; Parrent *et al.* 2011), 4 771 Å (C I; Jaschek & Jaschek

---

[4] See `http://www.not.iac.es/` [5] See `http://iraf.noao.edu/` [6] The data reduction was carried out in collaboration with Dr. J. Becerra (Universität Hamburg, Institut für Experimentalphysik, Hamburg, Germany).

Line	Observed wavelength [Å]	EW [Å]	Redshift z
Mg II	5131	2.7	0.84
	5144	1.9	
Mg II	5233	1.2	0.87
	5246	0.5	

Table 4.3: Observed wavelengths of absorption lines from intervening Mg II absorption systems. EW denotes the line equivalent width. The redshift z is calculated from the observed line wavelengths.

1995), and the ISM Na I doublet at 5 889 Å and 5 895 Å (Osterbrock *et al.* 1996). However, the two remaining line doublets can be interpreted as Mg II doublets (rest-frame wavelengths 2 796 Å and 2 803 Å), based upon the intensity ratio and the wavelength separation. The lines would be associated with two intervening systems (e.g., Evans *et al.* 2013; Nielsen *et al.* 2013). Details of the Mg II line-doublets are listed in Table 4.3.

The dominating continuum emission and the absence of strong emission lines exclude the scenario of a FSRQ and support a BL-Lac origin, which is consistent with the conclusions of Publication I. Although the absence of emission lines hampers a clear determination of the source's redshift, the redshifts of the two intervening Mg II absorption systems set a lower limit on the redshift of the USNO source and therefore of 2FGL J0031.0+0724. The redshifts of the Mg II systems are calculated in Table 4.3, revealing a lower limit of $z > 0.87$ for the redshift of 2FGL J0031.0+0724. It should be emphasized that Mg II absorption systems are quite common in the redshift range between 0.1 and 2.6 (Evans *et al.* 2013; Landoni *et al.* 2013).

4.3.6 VHE observations of 2FGL J0031.0+0724 with H.E.S.S.

As mentioned above, VHE observations of unassociated *Fermi*-LAT sources incorporate various opportunities of pinpointing their origin. A detection in the VHE band would significantly reduce the positional uncertainty, improving association prospects, and would also permit the investigation of the source spectrum in the TeV range. Eventually, this would enable discrimination of WIMP-powered sources from conventional sources driven by accelerated charged particles. Even the case for a non-detection can imply constraints on a WIMP scenario or blazar origin.

The investigations carried out in Publication I (Section 4.1) have triggered VHE follow-up observations of 1FGL J0030.7+0724 (2FGL J0031.0+0724) with H.E.S.S. Based upon the data published in the 1FGL catalog, I proposed H.E.S.S. observations of this source in 2010, see Appendix C.3 and C.4 for the corresponding proposal texts. The total flux from 1FGL J0030.7+0724 in the energy range of H.E.S.S. was estimated to be between $\sim 1\%$ and 35% of the flux from the Crab Nebula. The flux estimate was derived from a simple extrapolation of the cataloged power-law spectrum to energies above 300 GeV (see Appendix C.3 and C.4 for details)[7].

H.E.S.S. observations have been taken in the observing periods *P2010-10* (2 runs), *P2011-06* (26 runs), *P2011-07* (16 runs), *P2011-08* (14 runs), resulting in a total of 58 runs with an observing time of ~ 28 min per run (Aharonian *et al.* 2006c). Apart from five

---

[7] Since type and distance of the source were unknown, the impact of EBL absorption was neglected in this approach.

Model++ analysis	
Cuts	Std. (60 p.e.)
Background	reflected
Data (live time)	46 runs (18.7 h)
Mean zenith angle	$(33.8 \pm 2.4)\,\mathrm{deg}$
Mean off-axis angle	$(0.50 \pm 0.07)\,\mathrm{deg}$
ON region	$\theta^2 = 0.01\,\mathrm{deg}^2$
E_{min}	0.32 TeV
N_{ON}	205
N_{OFF}	2123
α	0.0877
N_{XS}	18.8
$N_{\mathrm{ON}}(> E_{\mathrm{min}})$	104
$N_{\mathrm{OFF}}(> E_{\mathrm{min}})$	975
$N_{\mathrm{XS}}(> E_{\mathrm{min}})$	18.8 ± 10.0
Significance	1.89σ
$\phi^{\mathrm{UL,95\%}}(> E_{\mathrm{min}}, \Gamma = 1.5)$	$5.5 \times 10^{-13}\,\mathrm{cm}^{-2}\,\mathrm{s}^{-1} = 0.4\%$ Crab
$\phi^{\mathrm{UL,95\%}}(> E_{\mathrm{min}}, \Gamma = 1.9)$	$5.7 \times 10^{-13}\,\mathrm{cm}^{-2}\,\mathrm{s}^{-1} = 0.4\%$ Crab
$\phi^{\mathrm{UL,95\%}}(> E_{\mathrm{min}}, \Gamma = 2.5)$	$7.2 \times 10^{-13}\,\mathrm{cm}^{-2}\,\mathrm{s}^{-1} = 0.5\%$ Crab
$\phi^{\mathrm{UL,95\%}}(> E_{\mathrm{min}}, \Gamma = 3.0)$	$8.8 \times 10^{-13}\,\mathrm{cm}^{-2}\,\mathrm{s}^{-1} = 0.7\%$ Crab

Table 4.4: VHE analysis (*Model++*), assuming a point source at the position of 2FGL J0031.0+0724. The table lists the cuts applied on the image amplitude (in photo-electrons), the method used for background estimation, the number of runs after quality selection, the live time (the given value corresponds to an acceptance-corrected live time of 17.1 h), the mean zenith angle, the mean wobble angle, the radius of the on-source region θ, the energy threshold E_{min} (defined at a value of 20% of the nominal acceptance), the number of events within the on-source region N_{ON}, and the number of events in the background region N_{OFF}; the excess is given by $N_{\mathrm{XS}} = N_{\mathrm{ON}} - \alpha N_{\mathrm{OFF}}$, where α denotes the geometrical factor between on-source region and background region. Event numbers are listed before and after applying the energy cut E_{min}. The significance is given in Gaussian sigma. The last four rows list upper limits on the integrated gamma-ray flux ϕ at 95% CL, assuming a power-law spectrum with different indices Γ. The case of $\Gamma = 1.9$ corresponds to the power-law listed in the 2FGL catalog. The upper limits were derived using the method of Feldman & Cousins (1998). For convenience, the upper limits are given in fractional Crab units as well, where $\phi_{\mathrm{Crab}}(> 320\,\mathrm{GeV}) = 1.35 \times 10^{-10}\,\mathrm{cm}^{-2}\,\mathrm{s}^{-1}$ (Aharonian *et al.* 2006c power-law fit).

runs with only two or fewer telescopes passing standard data-quality selection (HAP 12-03 selection, see below), the remaining sample of runs consists of 25 three-telescope runs (mostly CT1,CT2, and CT3) and 28 four-telescope runs (CT1, CT2, CT3, and CT4)[8].

---

[8] Note that the mirrors of CT1, CT2, and CT3 have already been re-coated by the time of the observations. The re-coating periods were *P2011-04* for CT1, *P2010-11* for CT2, *P2010-05* for CT3, and *P2011-11* for CT4.

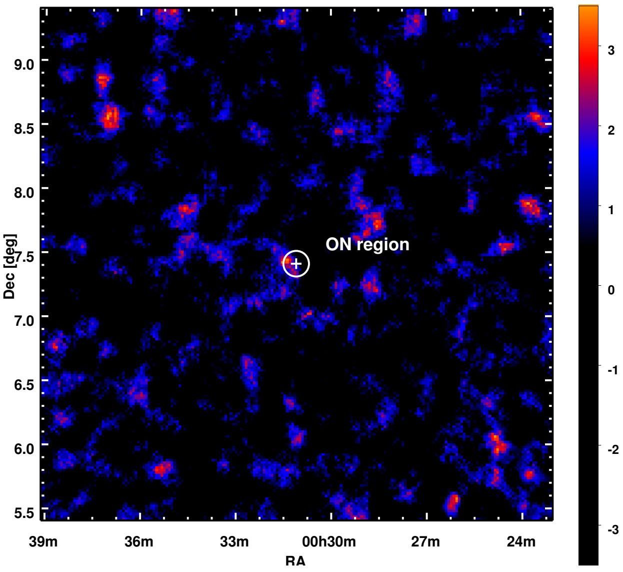

Figure 4.4: Pixeled significance sky map (oversampled) of a 4° × 4° region around 2FGL J0031.0+0724 as observed with H.E.S.S. in the VHE band. The data were analyzed with the *Model++* framework. The white circle marks the on-source region, centered on the position of 2FGL J0031.0+0724 (white cross). The pixel significance represented by the color scale is gauged in Gaussian sigma.

The data were analyzed with two independent methods: (i) a standard Hillas analysis (Aharonian *et al.* 2006c) using the *Heidelberg Analysis Package* (HAP 12-03-pl01) and (ii) *Model++* (Paris Analysis PA0820), a more sensitive gamma-ray likelihood technique based on comparison with predictions from semi-analytical modeling (de Naurois & Rolland 2009). The standard data-quality selection criteria corresponding to the respective analysis frameworks were used. Both analyses were cross-checked, giving consistent results.[9] In both analyses, a gamma-ray point-source at the cataloged position of 2FGL J0031.0+0724 (Nolan *et al.* 2012) and a circular on-source region with a radius of 0.1° were assumed. Note that the on-source region includes the nominal position of the radio association NVSS J003119+072456, which is located 3.4′ east to the position of the *Fermi* source. Table 4.4 lists the results of the *Model++* analysis. Details on the parameters are given in the caption of the table. With an acceptance-corrected live time of 17.1 h, no significant excess has been found at the position of the *Fermi* source (or anywhere else in the sky map) above the energy threshold of 320 GeV. The null result can be verified considering the distribution of pixel significances in the sky map (see Figs. 4.4 and 4.5a), which is compatible with a Gaussian centered on zero and with a width of one.[10] Likewise, the θ^2-plot in Fig. 4.5b does not show any signal excess in the on-source region $\theta^2 < 0.01\,\mathrm{deg}^2$, where θ^2 denotes the squared angular distance from the nominal position of 2FGL J0031.0+0724. Assuming a power-law spectrum with an index $\Gamma = 1.9$ (in accordance with the power-law fitting the GeV data) results in an upper limit on the integrated gamma-ray flux of $\phi^{\mathrm{UL},95\%}(> 320\,\mathrm{GeV}) = 5.7 \times 10^{-13}\,\mathrm{cm}^{-2}\,\mathrm{s}^{-1}$ (95% CL). The upper limit corresponds to 0.4% of the flux detected from the position of the Crab Nebula. It should be remarked that no indication for a constantly rising significance has been found in the on-source region.

---

[9] The HAP analysis was carried out together with M. V. Fernandes (Universität Hamburg, Institut für Experimentalphysik, Hamburg, Germany) and cross-checked by Dr. L. Oakes (Humboldt-Universität zu Berlin, Institut für Physik, Berlin, Germany), while the *Model++* analysis was carried out together with Dr. J. Biteau (Laboratoire Leprince-Ringuet, École polytechnique, CNRS/IN2P3, Palaiseau, France) and cross-checked by Dr. A. Jacholkowska (Université Paris 6 et 7, LPNHE, IN2P3, Paris, France).

[10] The deviations of the fitted mean and width of the Gaussian distribution from zero and one, respectively, represent a small bias of the pixel significance distribution. For the given interpretation of the data, this bias is negligible.

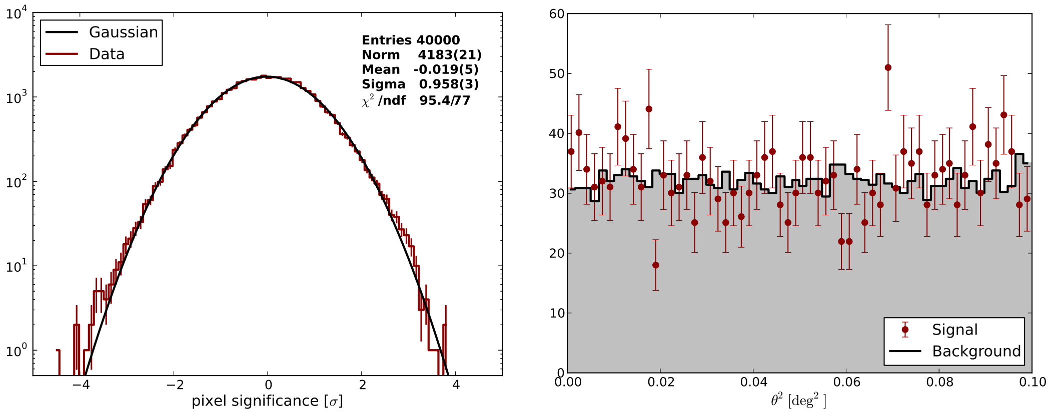

(a)

(b)

Figure 4.5: **(a)**: Significance distribution of the sky map shown in Fig. 4.4. The histogram (in dark red) is fit with a Gaussian (black solid line). The error on the last decimal is given in parentheses. **(b)**: Distribution of photon-like on-source events as function of the squared angular distance θ^2 from 2FGL J0031.0+0724 (dark red data points). The black filled bars mark the corresponding (normalized) distribution of off-source background events.

4.3.7 Interpretation of 2FGL J0031.0+0724

Figure 4.6 shows a state-of-the-art compilation of multi-wavelength data on 2FGL J0031.0+0724, confronted with an empirically determined average spectral energy distribution of a high-frequency peaked blazar (HBL) in a redshift of (a) $z = 0.33$ (see Section 4.3.1) and (b) $z = 0.87$ (see Section 4.3.5). The figure is based upon the findings reported in Publication I, II, and the previous sections, and additionally includes radio observations with ATCA (Petrov *et al.* 2013) and the upper bound derived in Section 4.3.6 from VHE observations with H.E.S.S. In the following, two different scenarios on the origin of the gamma-ray emission from 2FGL J0031.0+0724 are discussed.

Conventional astrophysical origin. The non-detection at TeV energies is consistent with a blazar origin of 2FGL J0031.0+0724, as illustrated by the empirical blazar SEDs included in Fig. 4.6. The photometric optical data and, in particular, the spectroscopic observations with NOT constrain the redshift of the source to $z > 0.87$. As a result from the discussions in Publication I, II, and in the previous sections, an HBL origin of the gamma-ray emission is favored, given

(a) the point-like gamma-ray emission,

(b) associated radio, infrared, optical, UV, and X-ray sources,

(c) the consistency of the infrared color-color data with the BL-Lac span of the WISE gamma-ray strip,

(d) an optical spectrum dominated by continuous non-thermal emission, shown by optical spectroscopy (see Section 4.3.5) and the comparably low emission of a standard giant elliptical BL-Lac host galaxy at $z = 0.87$ (see Fig. 4.6),

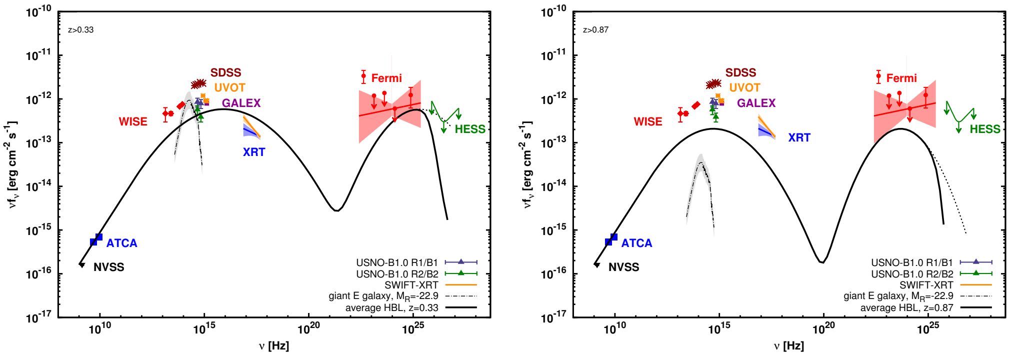

(a) (b)

Figure 4.6: Spectral energy distribution of 2FGL J0031.0+0724, following the conventions and assumptions of Fig. 3 in Publication II. Included multi-wavelength associations are NVSS J003119+072456, WISE J003119.70+072453.6, USNO 0974-0005617, SDSS J003119.71+072453.5, GALEX J003119.6+072454, and SWIFT J003119.8+072454. The blue solid line denotes the X-ray spectrum from the 2010 epoch[12], while the orange solid line and the orange data points mark the X-ray flux and corresponding UV flux obtained from more recent observations in 2012 (cf. Table 4.2 and Table B.1). In addition, the radio flux measured with ATCA (at 5 GHz and 9 GHz; blue boxes; Petrov *et al.* 2013) and the upper limit (95% CL) derived from H.E.S.S. observations are included. The dark-green solid line shows the most conservative upper limit from the H.E.S.S. data, enclosing bounds derived assuming power-law spectra with indices between 1.5 and 3.0. Redshifts of **(a)** $z = 0.33$ and **(b)** $z = 0.87$ are assumed in the Figure, in consistency with the lower limits established from the optical observations. The average HBL SED is normalized to the ATCA 5 GHz data. The thermal emission expected from a standard giant elliptical BL-Lac host galaxy is denoted with a black dot-dashed line, peaking at $\sim 10^{14}$ Hz. The gray-shaded area corresponds to a scatter of 0.5^{m}.

(e) the absence of resolved emission lines,

(f) variable optical emission, indicated by flux variations between the USNO, CRTS (see Section 4.3.2), and SDSS data[11],

(g) an X-ray spectrum which is consistent with the average HBL expectation,

(h) indication of gamma-ray variability in the 42-month *Fermi*-LAT data (with a significance of $\sim 2\sigma$),

(i) the hard gamma-ray spectral index,

(j) and the rough consistency of the measured SED with the average empirical SED of HBLs, in particular with a HE emission at the same flux level as the optical/UV emission.

---

[11] Compared to the USNO data, the SDSS data were taken in a different observational epoch.

[12] The X-ray spectrum obtained from a re-analysis of the 2010 data with the improved analysis routine of Section 4.3.3 differs from the one obtained in Publication I. The small difference in the flux normalization originates in improved exposure corrections. The difference in the photon index is dominantly owed to systematics between the threshold energy of 0.3 keV and the inclusion of events with lower energies. While the former energy threshold usually reduces systematical uncertainties (Godet *et al.* 2009) and is thus used here, it should be emphasized that a physical origin of this effect (e.g., by intrinsic absorption) remains possible.

With a redshift larger than 0.87, this source would belong to the most redshifted BL-Lac candidates known. Up to date, only 13 BL Lacs are known to reside in redshifts larger than 1 (as large as $z = 2.471$), while lower limits from intervening absorption systems indicate another 26 objects to belong to this category (see Shaw *et al.* 2013). So far, just one object with a redshift above 1 has been classified as an HBL.

Dark matter origin. The upper limit on the VHE flux of 2FGL J0031.0+0724 partly constrains the dark matter scenarios discussed in Publication I. According to Publication II, the high-energy flux from 2FGL J0031.0+0724 reconstructed from a point-source analysis is $\phi_{\mathrm{p}}(10-100\,\mathrm{GeV}) = (7 \pm 3) \times 10^{-11}\,\mathrm{cm}^{-2}\,\mathrm{s}^{-1}$, with an upper limit on the spatial extent of $\theta_{\mathrm{s}} \lesssim 0.5^{\circ}$ (95% CL). The boost factors required to explain the origin of the gamma-ray emission with dark matter self-annihilation in a DM subhalo thus increase by a factor of $\sim$2.5 compared to the values derived from the 11-month *Fermi*-LAT data (see Publication I, Section 6.2). To avoid loss in sensitivity, a point-like on-source region was assumed in the H.E.S.S. analysis. In combination with the modified source parameters, the eventual expectations for the dark matter annihilation flux from 2FGL J0031.0+0724 in the VHE band are approximately similar to the flux expectations reported in Publication I, Table 9. The observational upper limit of 0.7% Crab[13] on the VHE emission at the nominal position of 2FGL J0031.0+0724 thus excludes a subhalo of dark matter with a particle mass of 500 GeV, totally annihilating to $\tau^{+}\tau^{-}$ final states, as the origin of the GeV emission detected with *Fermi*-LAT.[14] However, the VHE upper limit does not constrain the other dark matter scenarios discussed in Publication I.

---

[13] The number refers to the most conservative upper limit, assuming a power-law with a photon index of 3.0.

[14] In this case, the flux anticipated in the energy range observable with H.E.S.S. is 1.1% Crab, see Publication I.

Chapter 5

The Imprint of Dark Matter in the Diffuse Gamma-ray Background

As outlined in Publication I (Section 4.1), both a Galactic and an extragalactic distribution of annihilating or decaying dark matter would imprint in the overall diffuse gamma-ray background (DGB). The DGB thus serves as a promising observable in terms of indirect dark matter searches. Yet, a breakdown of the total background emission into individual components requires precise knowledge of the gamma-ray spectra and population properties of all astrophysical constituents. Discrimination of dark matter signatures from conventional sources is however facilitated by considering their spatial distributions. The overall density distribution of dark matter gives rise to a unique signature in the angular anisotropy spectrum of the DGB, which might already be resolvable with current instruments. In addition, the search for angular anisotropies in the DGB will provide new insights with regard to the population properties of high energy and very-high energy gamma-ray emitters. Within the framework of this thesis, I participated in a study to investigate the sensitivity of current and planned ground-based Cherenkov telescope systems for detecting small-scale angular anisotropies in the DGB.

5.1 Publication III

The results of the study have been summarized in the following publication (Ripken *et al.* 2012). Parts of this publication have also been published in the framework of a collaborative study on the sensitivity of CTA for the astrophysical imprint of dark matter and fundamental physics, see Section 1.4 in Doro *et al.* (2013), including Zechlin, H.-S., *Dark matter and fundamental physics with the Cherenkov Telescope Array*, Astroparticle Physics, Special Issue on physics with the Cherenkov Telescope Array, Volume 43, Pages 189–214.

My contributions. I contributed to the initial idea, the setup, and the development of the study. In addition, I contributed to the investigation of the different instrumental setups, the study of their backgrounds, the discussion of the results, the writing of the manuscript, and the finalization of the figures.

Publication III

The sensitivity of Cherenkov telescopes to dark matter and astrophysical anisotropies in the diffuse gamma-ray background

Joachim Ripken, Alessandro Cuoco, Hannes-S. Zechlin,
Jan Conrad, Dieter Horns

Submitted to Journal of Cosmology and Astroparticle Physics,
in revision

Prepared for submission to JCAP

The sensitivity of Cherenkov telescopes to dark matter and astrophysical anisotropies in the diffuse gamma-ray background

Joachim Ripken,[a,b] **Alessandro Cuoco,**[a,c,d] **Hannes-S. Zechlin,**[e] **Jan Conrad,**[a,f] **Dieter Horns**[e]
[a]The Oskar Klein Centre for Cosmo Particle Physics, AlbaNova,
SE-106 91 Stockholm, Sweden
[b]Max-Planck-Institute for solar system research,
Max-Planck-Straße 2, D-37191 Katlenburg-Lindau, Germany
[c]Department of Physics, University of Torino, via P. Giuria 1, 10125 Torino, Italy
[d]Istituto Nazionale di Fisica Nucleare, via P. Giuria 1, 10125 Torino, Italy
[e]University of Hamburg, Institut für Experimentalphysik,
Luruper Chaussee 149, D-22761 Hamburg, Germany
[f]Wallenberg Academy Fellow
E-mail: ripken@mps.mpg.de, cuoco@fysik.su.se,
hzechlin@physik.uni-hamburg.de, conrad@fysik.su.se,
dieter.horns@physik.uni-hamburg.de

Abstract. In this article, the capability of present (H.E.S.S., MAGIC, VERITAS) and planned (CTA) ground-based Cherenkov telescope systems for detecting angular anisotropies in the diffuse gamma-ray background is investigated. Following up on a study of the impact of instrumental characteristics (effective area, field of view, angular resolution, and background rejection efficiency), the first part examines the influence of different observational strategies, i.e. whether a single deep observation or a splitting over multiple shallow fields is preferred. In the second part, the sensitivity to anisotropies generated by self-annihilating dark matter is studied for different common dark matter models. We find that a relative contribution of $\sim 10\%$ from dark matter annihilation to the diffuse gamma-ray background can be detected with planned configurations of CTA. In terms of the thermally-averaged self-annihilation cross section, the sensitivity of CTA corresponds to values below the thermal freeze-out expectation $\langle \sigma v \rangle = 3 \times 10^{-26}\,\mathrm{cm^3 s^{-1}}$ for dark matter particles lighter than $\sim$200 GeV. We stress the importance of constraining anisotropies from unresolved astrophysical sources with currently operating instruments already, as a novel and complementary method for investigating the properties of TeV sources.

Contents

1 Introduction

The study of gamma-ray anisotropies [1, 2] has recently provided new and complementary insights into the nature of gamma-ray sources and the extra-galactic diffuse gamma-ray background (EDGB) [3, 4]. Experimentally, EDGB means the residual large-scale isotropic emission measured at high galactic latitudes after subtracting the *galactic* diffuse emission. This emission arises mostly from the integrated contribution of unresolved extra-galactic sources and, possibly, from the annihilation or decay of dark matter (DM). A contribution from galactic sources is however also possible if their emission extends to sufficiently high galactic latitudes to produce an almost isotropic contribution. It has been argued, for example, that millisecond pulsars can give a contribution to the EDGB [5]. Similarly, also galactic DM could contribute to the EDGB, besides the extra-galactic one. The measured energy spectrum of the EDGB is, however, compatible with a simple featureless power law [3] so that complementary information, for example from anisotropy, can help isolating different contributions to this emission. The pattern of anisotropies has been studied with different techniques, mainly through its angular power spectrum (APS), as in [1, 2]. Likewise, the study of the 1-point probability distribution function (PDF) [6] and the cross-correlation with galaxy catalogues [7] provide complementary information.

It has been argued that dark matter self-annihilation or decay could leave a specific imprint on the anisotropy pattern and spectrum of the EDGB [8–19]. In fact, while the emissivity of ordinary astrophysical sources scales with the inner source densities $\sim \varrho$ (modulo a source-class dependent bias factor), the emissivity of self-annihilating DM scales with its density squared $\sim \varrho^2$. Owing to this difference, self-annihilating DM could leave its signature in the angular power spectrum of the EDGB. This simple picture can be further complicated by the presence of unresolved point sources that produce a Poissonian-like APS, more closely resembling the DM one. Nonetheless, even if the astrophysical Poissonian term dominates the intrinsic clustering APS, revealing the astrophysical and dark matter APS to be similar, it is still possible to separate the two contributions by measuring their energy dependence, i.e. the *anisotropy energy spectrum* [14]. The different hypotheses about the origin of the EDGB can thus be tested by measuring both the angular power spectrum and its energy dependence.

In addition, theoretical predictions for the anisotropies generated by different gamma-ray source populations (e.g., blazars and galaxy clusters [20], millisecond pulsars [21], star-forming galaxies [22]) become available, extending our knowledge of this approach and its potential.

Gamma-rays are currently detected mainly with two techniques. Observatories in space, such as the Fermi Large Area Telescope (Fermi-LAT) [23], enable the detection of gamma-rays through pair conversion in the detector itself. With the Fermi-LAT, gamma-ray photons can be observed in the energy range from a few ten MeV up to a few hundred GeV, with an effective area close to $1\,\mathrm{m}^2$ and a field of view (fov) of $\sim$1 sr. Fermi-LAT routinely operates in sky surveying mode, continuously mapping the entire sky within $\sim$3 h. Complementary, Cherenkov light emitted from air showers initiated by gamma-rays penetrating the upper atmosphere can be observed with ground-based telescopes, such as H.E.S.S. [24], MAGIC [25], and VERITAS [26], or the planned Cherenkov telescope array (CTA) [27, 28]. The effective collection area of ground-based instruments is typically of the order of $10^5\,\mathrm{m}^2$ to $10^6\,\mathrm{m}^2$. The energy range of current experiments lies between 60 GeV and 100 TeV, but future realizations of this concept will lower the threshold to 10 GeV or even 5 GeV [29]. Contrary to Fermi-LAT, ground-based instruments only offer a relatively small fov of typically a few msr, so that all-sky scans are not feasible. Observations can only be pursued during darkness under the condition of a clear sky, reducing the duty-cycle to $\sim$1 000 h per year. Furthermore, the trigger rate is dominated by a large background of hadronic showers. Specific techniques are employed to reduce this background substantially. However, even after sufficient gamma-hadron separation, air showers induced by cosmic-ray electrons can still contribute significantly to the background at a few hundred GeV [30–33], hardly separable from photon-induced air showers. Despite the difficulties mentioned above, interesting scales for the investigation of anisotropies are typically very small (less than 1°), so that a small fov does not pose a serious limit for their study. The angular resolution of Cherenkov telescopes is typically better than 0.1°, i.e. multipoles in the range between 100 and 1 000 can be easily resolved. At the same time, the background is expected to be isotropic at small scales and therefore no fundamental obstacle either.

In this paper, we investigate the capabilities of ground-based Cherenkov telescopes for measuring gamma-ray angular anisotropies. In section 2, we introduce a simplified

Monte-Carlo approach that is used to study the impact of instrumental characteristics (fov, angular resolution, and background rejection power) to the detection sensitivity for anisotropies. Given that a combined analysis of data collected from observations of several different targets would be most effective, we investigate the influence of the *observational strategy*, i.e. whether it would be advantageous or disadvantageous to split the data into several fov. In section 3, we list the instrumental setups that are used as benchmarks, and we provide estimates of the CR background rates expected for these configurations. Section 4 introduces a more realistic simulation setup and a sensitivity study to anisotropies from DM self-annihilation for different DM models. Final comments and discussion are provided in section 5.

2 Optimizing the observational strategy

2.1 Simplified setup

As a measure of anisotropy we use the angular power spectrum (APS) of fluctuations throughout this paper. Given a map $I(\vartheta, \varphi)$ on the sphere, the fluctuation map is defined as $\delta(\vartheta, \varphi) = I(\vartheta, \varphi)/\bar{I} - 1$, where $\bar{I}$ denotes the mean value of I. Thus, by definition, the mean value of $\delta(\vartheta, \varphi)$ is 0. The fluctuation map $\delta(\vartheta, \varphi)$ is decomposed into spherical harmonics $Y_m^\ell(\vartheta, \varphi)$ as $\delta(\vartheta, \varphi) = \sum_{\ell m} a_{\ell m} Y_m^\ell(\vartheta, \varphi)$, where $a_{\ell m}$ denote the coefficients of the spherical harmonic decomposition, $\ell = 0, \ldots, \infty$, and $m = -l, \ldots, l$. The coefficients $a_{\ell m}$ define the APS by

$$C_\ell \equiv \langle |a_{\ell m}|^2 \rangle, \tag{2.1}$$

where $\langle \ldots \rangle$ indicates the statistical ensemble average. Then, the quantity

$$\hat{C}_\ell = \sum_m \frac{|a_{\ell m}|^2}{2l+1} \tag{2.2}$$

provides an unbiased estimator of the true power spectrum C_ℓ, i.e. $\langle \hat{C}_\ell \rangle = C_\ell$.

Note that apart from the dimensionless fluctuation APS the dimension-full APS of the map $I(\vartheta, \varphi)$ itself can be used. This is particularly useful for the analysis of real data sets (see [1]), but we refrain from further consideration.

In order to simulate event lists containing anisotropies, we generate sky maps with a given C_ℓ spectrum. C_ℓ can be interpreted as the width of the $a_{\ell m}$ distribution over m for a fixed ℓ. Assuming Gaussian fluctuations, the $a_{\ell m}$ coefficients for a fixed ℓ can be randomly chosen from a Gaussian distribution centered on 0 with a width $\sqrt{C_\ell}$. The phase is chosen equally distributed between 0 an 2π with the condition $a_{\ell m} = a^\star_{-\ell m}$, to ensure fluctuation maps with real values. Twelve realizations of the $a_{\ell m}$ are generated for a given spectrum, and thus twelve independent fluctuation maps $\delta(\vartheta, \varphi)$. Moreover, we simulate maps with five different benchmark APS following a power law with slopes $s = 0.5$, 1.0, 1.5, 2.0, 2.5, i.e. $\ell(\ell+1)C_\ell \sim \ell^s$. The angular resolution of the simulated sky maps is chosen to be $0.002°$, corresponding to a maximum resolvable multipole $\ell = 9 \times 10^4$. The maps are normalized as $\delta'(\vartheta, \varphi) = (\delta(\vartheta, \varphi) - \delta_{\min})/(\delta_{\max} - \delta_{\min})$, in order to obtain a distribution between 0 and 1 to simulate events. Hence, the map δ' acts as effective intensity map $I'(\vartheta,\varphi) \equiv \delta'(\vartheta,\varphi)$. We emphasize that the anisotropies of this effective intensity map are independent of the original $\delta(\vartheta,\varphi)$ normalization and always in the range $-1 < \delta I'/\bar{I}' < 1$ by definition, thus implying large fluctuations of the order of 100%. The setup has been optimized for the purpose of investigating instrumental effects on the APS. However, the setup is extended to a more realistic approach in section 4, allowing the choice of an arbitrary anisotropy level.

Based upon the template intensity maps $I'(\vartheta,\varphi)$, the simulation of events requires the definition of the following three parameters: σ_{fov}, the half-width of the camera acceptance, σ_{psf}, the width of the point-spread function (PSF), and the signal fraction f_{sig}, the ratio of signal events with respect to the sum of signal and background events. Event lists contain an anisotropic *signal* component and a *background* component. The latter is isotropic by definition. Both the camera acceptance and the PSF are assumed to follow Gaussian distributions.

Each event of a list is handled in three subsequent steps: The celestial position is chosen randomly according to the camera acceptance. Comparing a uniform deviate with f_{sig}, it is then decided whether the event is treated as a *signal* or a *background* event. If the event belongs to the background, the event is just retained. In the signal case, instead, a variate z is generated, following a normalized uniform distribution. If z is smaller than $I'(\vartheta,\varphi)$ at the event's position, the event is kept, otherwise it is rejected. Eventually, each event is randomly displaced from its original direction according to the PSF, in order to realize the convolution of the map with the PSF. If not particularly specified, an event list contains $N_{\mathrm{ev}} = 10^7$ entries. We point out that this number is unrealistically high, even for CTA, and is used to isolate and emphasize instrumental effects only. Simulations with a more realistic number of signal and background events are provided in section 4.

We use the HEALPix software and pixelization scheme [35] to create and analyze count maps (with N_{pix} pixels) as well as to extract the APS. Before the analysis, a count map is cast into a fluctuation map

$$\delta''(\vartheta,\varphi) = \frac{N_{\mathrm{pix}}}{N_{\mathrm{ev}}}\left[\sum_{i=1}^{N_{\mathrm{pix}}} x_i\, b_i(\vartheta,\varphi)\right] - 1, \tag{2.3}$$

where x_i denotes the number of events in pixel i, and $b_i(\vartheta,\varphi)$ equals 1 inside pixel i and 0 otherwise. In this way, $\delta''(\vartheta,\varphi)$ is normalized such that $\int \mathrm{d}\Omega\ [1+\delta''(\vartheta,\varphi)] = 4\pi$, where $\mathrm{d}\Omega$ is the differential solid angle element in spherical coordinates. It should be noted that, strictly speaking, $\delta''(\vartheta,\varphi)$ represents a fluctuation map (i.e. $\langle\delta''(\vartheta,\varphi)\rangle = 0$) only in the case that the average is performed over the whole sky rather than over the region of interest where the counts are located. The normalization has been chosen to keep a simple form of the noise term in the recovered APS (see next section), i.e. $C_N = 4\pi/N_{\mathrm{ev}}$, where no factors of $f_{\mathrm{sky}} = \Omega_{\mathrm{fov}}/4\pi$ are involved (Ω_{fov} denotes the solid angle of the fov). We remark that a direct analysis of a fluctuation map built from a raw count map is pursued, while in principle the fluctuation map built from the reconstructed flux map (the count map divided by the exposure of the experiment or the fov in our case) can be

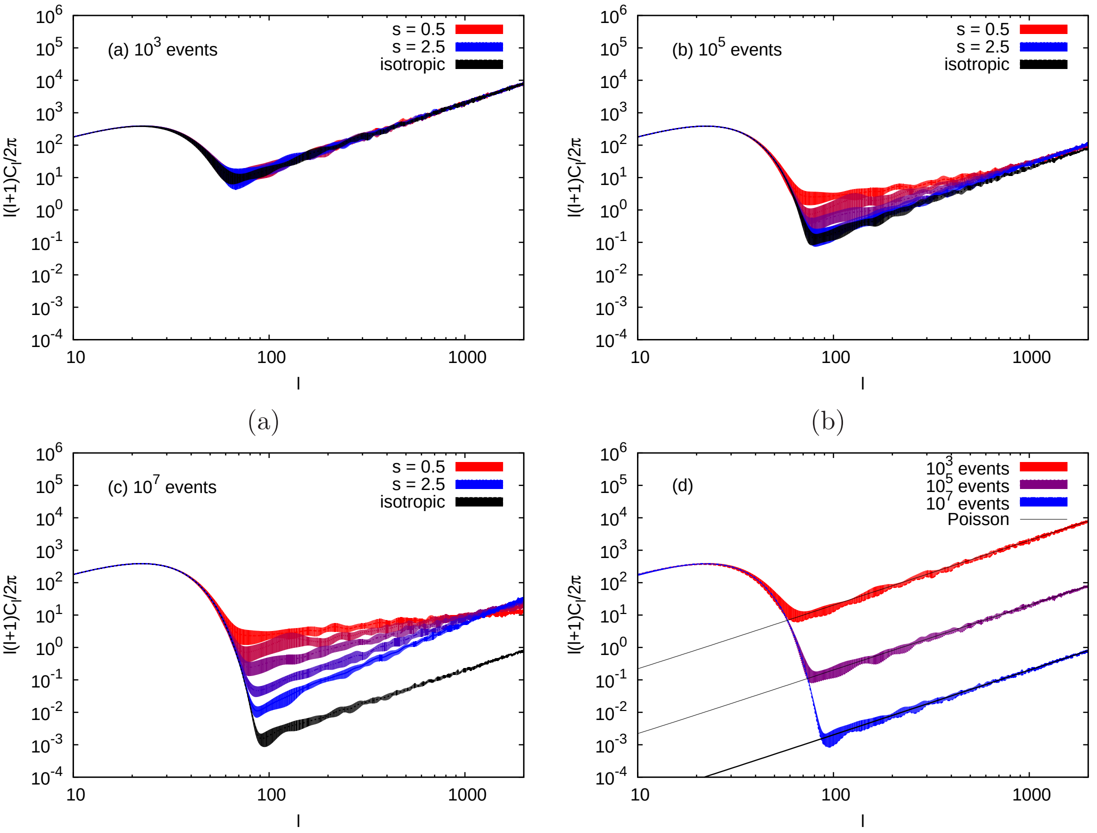

(a) (b) (c) (d)

Figure 1: Angular power spectra measured from simulated event maps with different input APS slopes s between 0.5 and 2.5 in steps of $\Delta s = 0.5$ (from red to blue). The simulations contain signal-only events. The lower, black APS, labeled "isotropic", refers to a background-only simulation with the same number of events. In this figure, PSF effects are neglected and $\sigma_{\text{fov}} = 2.5°$. Sub-figures represent the cases of (a) 10^3 events, (b) 10^5 events, and (c) 10^7 events. The effect of an increasing event number on the Poissonian noise is depicted in (d), which shows together the APS of the background-only simulations from the panels (a), (b), and (c).

analyzed. While the latter is preferred for real data analyses, the former is sufficiently accurate for a sensitivity study. It implies the extracted APS to be a convolution of the experiment's windowing function (the APS of the camera acceptance) with the true signal. For the large ℓ considered below, the windowing effect is marginal.

The statistical uncertainty of the APS is derived from the twelve simulations that have been performed for each case. In the following plots, the RMS as estimates of the standard deviation are shown as uncertainty bands.

2.2 Influence of the detector configuration

In figure 1, examples of APS measured from the simulated maps with given input-APS slopes are shown for a varying total number of events. No background events have been included and all events are of signal type, except the lowest, black APS, which is measured from a simulation containing background events only (an isotropic simulation). For small ℓ, the windowing function dominates the spectrum, which is distorted accordingly. For larger ℓ we see that the measured APS is the sum of the Poissonian noise and of the intrinsic APS. If the number of events is large enough, the different signal slopes can be easily discriminated. If the number of events is small, however, the random noise from the finite number of events prevails the measured APS. The Poissonian noise is given by $C_N = 4\pi/N_{\mathrm{ev}}$ for full sky coverage (see appendix B in [10] and section IV.A in [8]), where $N_{\mathrm{ev}} = N_{\mathrm{sig}}{+}N_{\mathrm{bg}}$ is the total number of events. This is in good agreement with the noise estimates from the background-only simulations (and partial sky-coverage corrected APS, see previous section), as shown in the lower right panel of figure 1. Since the Poissonian noise term is known, it is customary to remove it from the estimated APS so that to better show the intrinsic APS. We will discuss noise-subtracted APS for the realistic simulations in section 4. The same considerations apply to the PSF effect and the background fraction discussed in the following, which can all be modeled, and thus corrected to give a final, unfolded APS. In the forward-folding approach used in section 4, these corrections are in principle not required, since the model is directly convolved with the PSF before comparison with the simulated data.

The effect of the instrument's PSF on the measured APS is illustrated in the top-left panel of figure 2: The PSF suppresses the signal at large ℓ and drives it toward the level of the Poissonian noise. The characteristic multipole of the downturn is related to the PSF width σ_{psf} by $\ell_s \approx 180^\circ/\sigma_{\mathrm{psf}}$. This effect can be corrected if σ_{psf} (or the full PSF shape in a non-Gaussian case) is known [1], however at the expense of an increasing uncertainty on the measured APS.

Anisotropies at an angular scale larger than the fov are suppressed. This effect is illustrated in the top-right panel of figure 2, where the APS of an isotropic (background-only) event list is shown for different fov. A larger fov allows exploring larger scales and thus lower multipoles. The minimum resolvable multipole is approximately given by $\ell_{\mathrm{min}} \approx 180^\circ/\sigma_{\mathrm{fov}}$.

The bottom panel of figure 2 illustrates the effect of different signal fractions f_{sig}. The background component mainly originates from two different processes:

(i) Events caused by mostly isotropic cosmic rays (protons and electrons), which have been misclassified as photons. Anisotropies in the hadronic cosmic-ray background are indeed present at the level of 10^{-4} [38–42]. However, they extend to a multipole of $\sim$20 only [38] and are thus negligible in our analysis. Anisotropies in the electron background have not been detected so far [36, 37]. For Cherenkov telescope systems the hadronic cosmic-ray background component dominantes the gamma-ray signal. Therefore, a sufficiently good gamma-hadron separation is a crucial characteristic of the instrument. To reduce the residual background of cosmic-ray electrons, which becomes important at energies below a few hundred GeV, a sufficiently good gamma-electron separation would be favorable as well. However, gamma-electron separation capabilities are limited due to the similarity of electron and photon initiated showers. With current instruments a rejection of $\sim 50\%$ of the electrons seems possible [32, 33], while the expected performance of CTA on this aspect has not been studied in detail yet.

(ii) An intrinsically isotropic component of the diffuse photon background, which does not act as signal according to our definition. For instance, cosmological photons produced by truly diffuse processes may account for this component.

Note that we do not consider the effect of the local variations of the *night-sky background* and its effect on the camera acceptance [34]. Rather, we assume that prominent features in the fov such as bright stars can be eventually masked and excluded from the analysis. A more realistic MC simulation would be required to study this effect in detail. This is left for future work.

The bottom panel of figure 2 shows the measured APS for different signal factions. A slope of $s = 0.5$ has been assumed for the input spectrum used to simulate the signal part of the maps and event lists. Dotted lines show the measured APS in the ideal case of vanishing PSF effects, vanishing fov distortion, and vanishing noise (but with background still included). As expected, the background fraction has a large impact and considerably reduces the signal height with respect to the intrinsic Poissonian noise, i.e. the signal-to-noise ratio. For the shown case of 10^7 events a signal fraction of 20% is still easily detectable. However, the signal-to-noise ratio decreases rapidly with decreasing $f_{\rm sig}$, and for realistic cases $f_{\rm sig}$ can be as low as 0.1% while reaching a value of 2% in optimistic scenarios (see table 2 in section 4). We thus conclude that a good *background rejection* is crucial.

Finally, we investigate the effect of the observational strategy. In general, the detection of anisotropies requires a large amount of observation time. Thus, dedicated observations could eventually not be feasible, given different targets competing for the limited observation time available. The use of combined observations obtained on different targets would thus be preferable. This approach is investigated in figure 3. Here, a number of 10^3, 10^5, and 10^7 signal-only events are distributed within one fov as well as ten different ones. Qualitatively, when the same number of events is distributed in a single or multiple fov two competing effects arise: On the one hand, the density of signal events decreases since they are spread over a larger area, and thus the signal-to-noise ratio decreases (with our definition of the normalization of the maps, the Poissonian noise depends only on the number of events and it is the same in the single or multiple fov cases). On the other hand, multiple fov result in an increased number of modes available for the APS calculation, reducing the statistical error on the measured APS (on the sphere this effect is known as *cosmic variance*) and thus improving the sensitivity. The overall number of events eventually determines the dominating error and thus the dominating effect.

As illustrated in figure 3, multiple fov indeed decrease the error on the measured APS and reduce the signal-to-noise ratio. The 10^7-events case shows that a highly

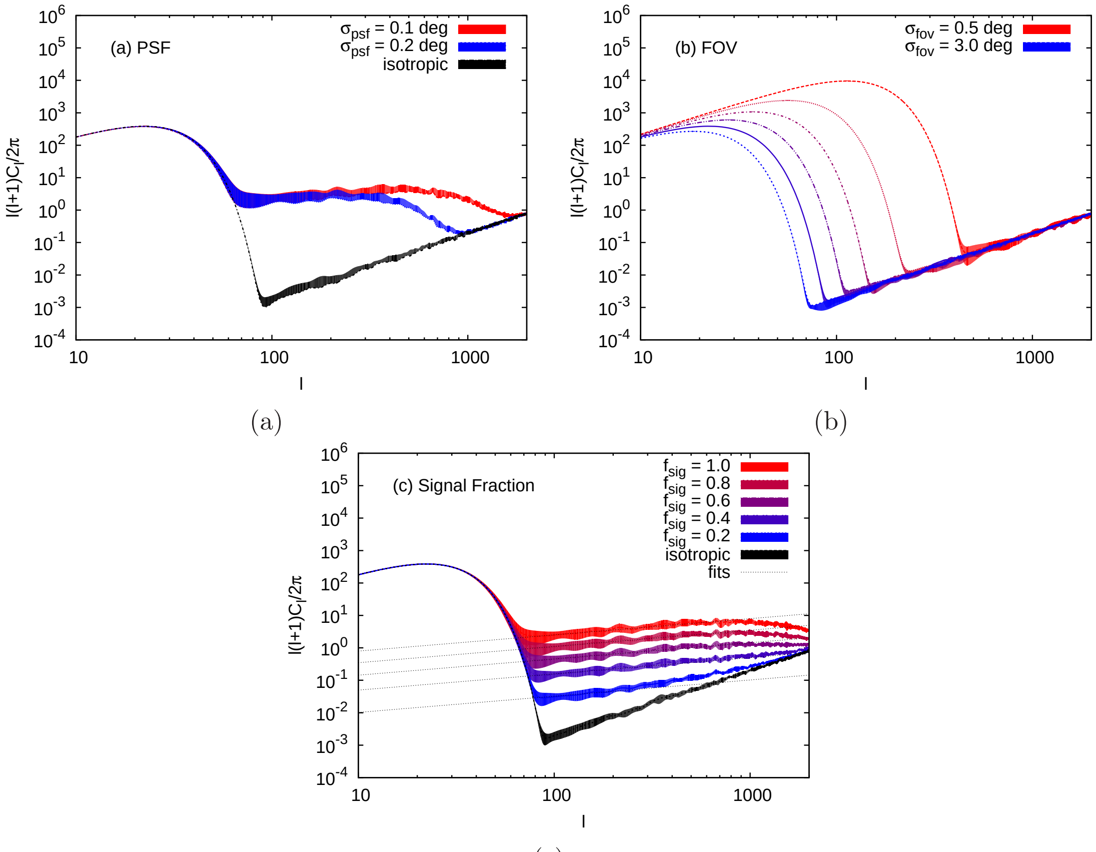

(a) (b)

(c)

Figure 2: (a): Influence of the PSF on the measured APS. The slope of the input spectrum is $s = 0.5$. The chosen PSF widths are $\sigma_{\text{psf}} = 0.1°$ (red band) and $\sigma_{\text{psf}} = 0.2°$ (blue band). (b): Influence of the fov on the APS for a pure background (isotropic) event list, with $\sigma_{\text{psf}} = 0.05°$. The width σ_{fov} is increased in steps of 0.5, in the range from $\sigma_{\text{fov}} = 0.5°$ (red) to $\sigma_{\text{fov}} = 3.0°$ (blue). (c): Influence of the signal fraction f_{sig} on the measured APS for an input slope of $s = 0.5$; background events are distributed isotropically. Dotted lines show the APS in case of vanishing PSF, vanishing fov distortions, and vanishing noise.

significant detection over all multipoles is achieved both in the single and multiple fov cases. On the other hand, the 10^5-events case shows that while with the single fov observation a non zero APS can be detected up to a multipole of ∼1000, with the multiple fov case it is possible to significantly detect the anisotropy only up to a multipole of ∼ 400. In fact, while the error is decreased, the signal-to-noise ratio becomes too low to get a significant detection. Finally, in the 10^3-events case there is no significant detection both in the single or multiple fov. A quantitative numerical study of this effect in a realistic scenario including background is presented in the section 4. Analytical formulae are derived in appendix A.

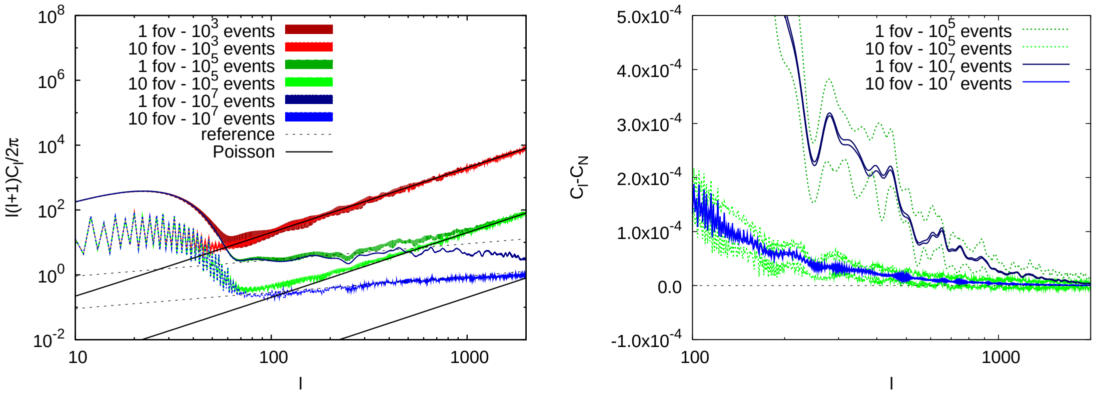

(a) (b)

Figure 3: Impact of the observational strategy. (a): The measured APS for an input spectrum with a slope $s = 0.5$ is shown for 10^3 (red), 10^5 (green), and 10^7 (blue) signal-only events, distributed in a single fov (dark colors) or in ten different fov (light colors), respectively. Note that with our definition of the normalization of the maps, the Poissonian noise (depicted by the solid black lines) depends only on the number of events and it is the same in the single or multiple fov cases. For comparison, the thin dotted lines show the input APS for the two 10^7-event cases. A Gaussian PSF with a width of 0.05° is assumed. (b): Same as above, but showing the noise-subtracted power $C_\ell - C_N$ on the y-axis instead of $\ell(\ell+1)C_\ell/2\pi$. The green (blue) lines enclose the 1σ error regions on the measured APS for 10^5 (10^7) events, distributed in a single (dark colors) or in ten different fov (light colors).

It should be stressed that the use of multiple fov requires the systematic error in the absolute calibration of each fov to be kept reasonably under control. In the following, we assume that this systematic error can be neglected compared to the statistical ones. A better assessment of this uncertainty will likely be available from future performance studies of CTA.

3 Benchmark instrumental setups and cosmic-ray backgrounds

Simulations of two instrument classes are presented in the following. The used instrumental setups are motivated by the characteristics of currently operating instruments such as H.E.S.S., MAGIC, and VERITAS, and the expected properties of CTA. Two different threshold energies (100 GeV and 300 GeV) have been adopted, revealing different signal-to-background ratios.

For currently operating instruments, the performance below 1 TeV typically degrades rapidly in energy. Hence, a threshold energy of 300 GeV is considered only. Above 300 GeV, an effective area of 10^5 m^2 (after selection cuts which improve the fraction of gamma rays with respect to hadrons) is assumed. So is a fov of 1.7° and an angular resolution of 0.1° [24–26, 43].

IACT	$E_\mathrm{thr} = 100\,\mathrm{GeV}$			$E_\mathrm{thr} = 300\,\mathrm{GeV}$		
	A_eff [m^2]	σ_fov [deg]	σ_psf [deg]	A_eff [m^2]	σ_fov [deg]	σ_psf [deg]
current		—		10^5	1.7	0.1
CTA	10^5	3, 4, 5	0.05	3×10^5	3, 4, 5	0.05

Table 1: Characteristics (effective area A_eff, field of view σ_fov, and PSF σ_psf) of the benchmark instrumental setups used in the simulations. The setups have been chosen in accordance with characteristics of current-generation IACTs and the planned CTA observatory. Predictions are made for two different threshold energies E_thr, 100 GeV and 300 GeV, respectively.

For CTA, recent Monte-Carlo studies of the performance [27, 44, 45] indicate an effective area of $3 \times 10^5\,\mathrm{m}^2$ above 300 GeV and $10^5\,\mathrm{m}^2$ above 100 GeV (see figure 15 in [44]). In both cases, we assume an angular resolution of 0.05° (see figures 10 and 17 in [44]). The effective area as well as the angular resolution improve with energy, but the simulations have been considerably simplified choosing constant values close to the threshold energies, representing a conservative choice. For the fov, values between between 3° and 5° are considered (see table 3 in [44]). We emphasize that a rather large fov of $\mathcal{O}(5^\circ)$ might be provided by the types C, D, and J of the suggested CTA arrays [44]. In addition, an effectively larger fov can be achieved with dedicated pointing patterns, adjusting the pointings of individual telescopes to correspondingly different offsets from a targeted position (see figure 3c in [27]). Table 1 summarizes the characteristics of the instruments used in this study. The performance of the recently built H.E.S.S.-II array is expected to lie in between the two setups considered here [43].

The intensity of the isotropic hadronic background component depends on analysis cuts and the quality of the gamma-hadron separation. With respect to present instruments, CTA will provide improvement in the performance of the hadron rejection process. However, a substantial part of the low-energy background is made by cosmic-ray electrons, which are more difficult to separate from gamma rays. The study in [44] provides a simulation of the total expected background from hadronic and leptonic components, which are used to estimate the background corresponding to our setups. In particular, we refer to their figure 16 of the integrated background rate per beam above a given energy threshold (and for the assumed effective area).

For a threshold energy of 100 GeV, a background rate of 0.01 Hz to 0.03 Hz per beam yields a total background rate of 50 Hz to 150 Hz for an angular resolution of $\sim 0.1^\circ$ and a fov of 5°. Thus, benchmark background rates of 10 Hz and 100 Hz are assumed in this study, the first being slightly optimistic (but still possible depending on eventual improvements of the background rejection), and the second represents a more conservative choice. Rates for different fov scale with the factor $(\sigma_{\mathrm{fov},1}/\sigma_{\mathrm{fov},2})^2$. For simplicity, we use 10 Hz and 100 Hz as benchmark background rates for all considered fov, although these rates are over-estimated for smaller fov of 3° and 4°. The background for a threshold of 300 GeV covers a range between 3×10^{-4} Hz and 3×10^{-3} Hz per beam, and the angular resolution covers values between 0.06° and 0.1°. For a fov of 5°, this corresponds to a total background rate of 1.5 Hz up to 42 Hz. Again, an optimistic and a more conservative background rate are chosen, i.e., 1 Hz and 10 Hz, respectively.

Assuming the same characteristics as for CTA for threshold energies above 300 GeV for current IACTs, the scaling to the correspondingly smaller fov reduces the background rate by a factor of 10. A further reduction in the rate is given by the smaller effective area. However, the background rejection capabilities are inferior with respect to the expectation for CTA, thus increasing the background rate. We use the same benchmark background rates as for CTA with threshold energies above 300 GeV, i.e. 1 Hz and 10 Hz. These values match typically observed background rates.

4 Dark matter sensitivity

A more realistic setup can now be employed to simulate maps with a given level of anisotropy. Here, we consider an anisotropy spectrum with a slope of $s = 2$ only, i.e. the same slope as of Poissonian noise. With the conventions given in section 2, $s = 2$ corresponds to an APS constant in multipole and can therefore be characterized by a single number, i.e. $C_\ell = C_P$ for all ℓ. This kind of anisotropy spectrum, known as Poisson anisotropy, is typically expected from unresolved point sources and provides a good approximation for most of the common DM scenarios [8, 9, 11–19]. The similarity to the Poissonian noise also suggests a straightforward way to simulate this kind of anisotropy: For N identical sources distributed all over the sky, the Poisson anisotropy of the fluctuation map will be $C_P = 4\pi/N$. Inverting the process, a map with an anisotropy equal to C_P can be simulated distributing $N = 4\pi/C_P$ equal sources on the sphere. This method is adopted in the following. In general, unresolved sources are not identical but have a certain flux distribution $\mathrm{d}N/\mathrm{d}S$, which typically follows a power law or broken power-law distribution. Anisotropy measurements can be used to recover the underlying $\mathrm{d}N/\mathrm{d}S$ [2, 6]. To check our approximation of using an effective delta-like $\mathrm{d}N/\mathrm{d}S$, simulations for a realistic $\mathrm{d}N/\mathrm{d}S$ have been performed, and are described later in this section. We follow the algorithm described in section 2 to produce a sequence of background or signal events from the simulated source maps. Different to section 2, the source maps are not rescaled, since they possess an intrinsic anisotropy normalization that we want to retain.

The total number of background events is given by the integrated background rates estimated in the previous section. The gamma-ray flux is normalized to the EDGB measured with Fermi-LAT: $\phi(E) = \phi_0\,(E/100\,\mathrm{MeV})^{-2.41}$, with $\phi_0 = 1.45 \times 10^{-7}\,\mathrm{cm}^{-2}\,\mathrm{s}^{-1}\,\mathrm{sr}^{-1}\,\mathrm{MeV}^{-1}$ [3]. Extrapolating the power-law spectrum above the considered threshold energies of 100 GeV and 300 GeV gives the integral fluxes $\phi(E > 100\,\mathrm{GeV}) \approx 6\times10^{-10}\,\mathrm{cm}^{-2}\,\mathrm{s}^{-1}\,\mathrm{sr}^{-1}$ and $\phi(E > 300\,\mathrm{GeV}) \approx 1.3\times10^{-10}\,\mathrm{cm}^{-2}\,\mathrm{s}^{-1}\,\mathrm{sr}^{-1}$. The effect of the EDGB attenuation expected from pair production on the extragalactic background light is neglected here. The expected softening is mild in most of the attenuation models [46–52], and taking it into account would only slightly reduce the total flux above 100 GeV, while the attenuation could be more pronounced above 300 GeV. For a CTA observation of 100 h, this results in 10 448 and 6 659 signal events in total, assuming a fov of 5° and a threshold energy of 100 GeV and 300 GeV, respectively (setups as discussed in table 1). The events are distributed between DM and astrophysical sources according to the relative contribution to the EDGB as considered in the following. Changing the threshold energy from 100 GeV to 300 GeV, the number of gamma-ray events is reduced by less than a factor of 2, while the number of background events is reduced by a factor of 10 (due to their steeper energy spectrum and improved background rejection at higher energies). The signal-to-noise ratio of a given data set can thus be improved considering a threshold energy of 300 GeV. The numbers of gamma rays and background events for all the setups are reported in table 2.

The intrinsic anisotropy of astrophysical sources is modeled in accordance to the recent measurement of anisotropy performed with Fermi-LAT in the range of 1 GeV to 50 GeV [1]. The fluctuation energy spectrum of the measured anisotropy is compatible with a constant value of $\sim 10^{-5}$, while the *intensity* energy spectrum of anisotropy is compatible with a power law with slope ~ 2.4. In combination, these results indicate that the measured anisotropy originates from unresolved blazars. This is further supported by the analysis performed in [2]. We assume that the result holds above 100 GeV. Thus, a value of $C_P^A = 10^{-5}$ is used for the intrinsic astrophysical source anisotropies. However, also other values of C_P^A will be explored to assess the robustness of the results with respect to the choice of this parameter.

The theoretical predictions for the intrinsic DM anisotropy are uncertain and span over a few orders of magnitude ranging from 10^{-4} to 10^{-1}. We assume a benchmark value $C_P^{DM} = 10^{-3}$ and will comment on other values in the following. A simplified analytic calculation is reported in the appendices A, B and C, illustrating the expected dependence of the sensitivity on the choice of C_P^{DM} and C_P^A.

To estimate the sensitivity to the DM component, we vary the relative contribution of DM to the total EDGB flux, assigning the remaining flux to the astrophysical component. In particular, we simulate 20 values of the DM contribution p from 0% to 100% in steps of 5%. The average astrophysical spectrum C_ℓ^{A}, its error σ_{C_ℓ}, and the average spectrum $C_\ell^{\mathrm{A+DM},p\%}$ composed of both the astrophysical and a fractional DM contribution of p are estimated from 20 realizations each. Note that C_ℓ^{A} indicates the *measured* average APS as function of the multipole ℓ. Ideally, assuming that no biases are present in the simulation pipeline, and after correcting for the instrumental effects, the CR background, and the Poisson noise, we should observe that $\langle C_\ell^{\mathrm{A}} \rangle = C_P^A$ for all ℓ, where $\langle \dots \rangle$ indicates the average over many simulations. The same consideration applies to $C_\ell^{\mathrm{A+DM},p\%}$.

To quantify the sensitivity to the relative DM contribution, we use a simple chi-square approach, comparing two different definitions:

$$\chi_i^2(p) = \sum_{\ell=100}^{1000} \left(\frac{C_\ell^{\mathrm{A+DM},p\%} - C_\ell^{\mathrm{A},i}}{\sigma_{C_\ell}} \right)^2 , \tag{4.1}$$

$$\chi_j^2(p) = \sum_{\ell=100}^{1000} \left(\frac{C_\ell^{\mathrm{A+DM},p\%,j} - C_\ell^{\mathrm{A}}}{\sigma_{C_\ell}} \right)^2 , \tag{4.2}$$

where $C_\ell^{\mathrm{A+DM},p\%,j}$ and $C_\ell^{\mathrm{A},i}$ are the spectra from the single realizations as opposed to the average ones, $C_\ell^{\mathrm{A+DM},p\%}$ and C_ℓ^{A}, respectively. Only multipoles above 100 are used, discarding lower multipoles affected by the fov of the instrument. The quantity $\chi^2(p)$ follows a chi-square distribution with 901 degrees of freedom, so that we can quote sensitivities at 95% confidence level (CL) for the value of p corresponding to a $\chi^2(p)$ larger than 972. Given that $\chi^2(p)$ scatters among different realizations, an additional criterion must be specified. For example, the average value of $\chi_i^2(p)$ over i can be used. Here, we adopt the more conservative requirement that at least 19 out of the 20 different $\chi_i^2(p)$ values (for a given p) are larger than the sensitivity threshold of 972, in order to set the value of p corresponding to the 95% CL. The two different ways to define $\chi^2(p)$, see Eqs. (4.1) and (4.2), correspond to two different definitions of the sensitivity. In the first approach, we assume and simulate a "true" case without a DM component and search for the minimum (at 95% CL) DM fraction required to exclude the null hypothesis. In the second approach, we assume and simulate "true" cases including a DM contribution of p and search for the minimum contribution for which the null hypothesis becomes incompatible with the simulated data. Both cases are found to give consistent results. We point out that the definition of sensitivity used here is in short a "95% CL incompatibility with the null hypothesis", which implies a comparison of two χ^2-distributions. Another commonly employed definition of a sensitivity as "95% upper limit in the case of a null detection outcome of the experiment" (which requires interval estimation through a profile likelihood or test statistic procedure) can give more stringent sensitivities, but is not considered in this work.

Finally, it should be noted that the sensitivity estimation described above assumes previous knowledge of the intrinsic astrophysical and DM anisotropies. In realistic cases, a measurement of these quantities from the analysis itself would be preferable in order to perform a comparison with the model predictions. This can be done, in practice, analyzing the data in multiple energy bands. The presence of more components at different energies and the intrinsic anisotropies of the components can then be inferred from a study of the anisotropy energy spectrum in intensity and fluctuation [14, 18]. We do not pursue such detailed analysis here, while for the sensitivity estimate to the DM contribution the above approach is sufficiently accurate.

The results are shown in table 2. Clearly, current instruments have limited prospects of constraining DM through small-scale angular anisotropies. It is worth stressing, nonetheless, that anisotropy searches also constrain population properties of astrophysical sources (as discussed in more detail below), so that this particular result should not hamper a dedicated search for anisotropies with current observatories. However, prospects for DM searches improve for CTA, especially if the background rate can be kept reasonably low. Sensitivities of ∼ 20% and ∼ 10% at 100 GeV and 300 GeV, respectively, can be achieved with single-target observations of 1 000 h. Even in the most conservative case of a fov of 3°, a sensitivity of ∼ 30% above 300 GeV can still be reached with CTA (not shown in the table), while a fov of 4° would result in a sensitivity of ∼ 15%.

Facing realistic data sets, the change in sensitivity for different observational strate-

H.E.S.S./MAGIC/VERITAS $\mathbf{E_{th}}$=300 GeV $\sigma_{\mathbf{fov}} = \mathbf{1.7^\circ}$

Observation time [h]	Bg. rate [Hz]	Sens.	N_{sig}	N_{bg}
100	1	$\gtrsim 100\%$	257	3.6×10^5
	10	$\gtrsim 100\%$		3.6×10^6
300	1	$\gtrsim 100\%$	770	1.08×10^6
	10	$\gtrsim 100\%$		1.08×10^7
1000	1	$\gtrsim 100\%$	2567	3.6×10^6
	10	$\gtrsim 100\%$		3.6×10^7
10 × 100	1	$\gtrsim 100\%$	2567	3.6×10^6
	10	$\gtrsim 100\%$		3.6×10^7

CTA $\mathbf{E_{th}}$=100 GeV

Observation time [h]	Bg. rate [Hz]	$\sigma_{\mathrm{fov}} = 4^\circ$		$\sigma_{\mathrm{fov}} = 5^\circ$		N_{bg}
		Sens.	N_{sig}	Sens.	N_{sig}	
100	10	90%	6687	70%	10448	3.6×10^6
	100	$\gtrsim 100\%$		$\gtrsim 100\%$		3.6×10^7
300	10	45%	20059	35%	31343	1.08×10^7
	100	$\gtrsim 100\%$		$\gtrsim 100\%$		1.08×10^8
1000	10	30%	66867	20%	104476	3.6×10^7
	100	95%		75%		3.6×10^8
10 × 100	10	55 %	66867	40%	104476	3.6×10^7
	100	$\gtrsim 100\%$		$\gtrsim 100\%$		3.6×10^8

CTA $\mathbf{E_{th}}$=300 GeV

Observation time [h]	Bg. rate [Hz]	$\sigma_{\mathrm{fov}} = 4^\circ$		$\sigma_{\mathrm{fov}} = 5^\circ$		N_{bg}
		Sens.	N_{sig}	Sens.	N_{sig}	
100	1	55%	4262	30%	6659	3.6×10^5
	10	$\gtrsim 100\%$		95%		3.6×10^6
300	1	30%	12785	20%	19976	1.08×10^6
	10	80%		60%		1.08×10^7
1000	1	15%	42617	10%	66587	3.6×10^6
	10	45%		30%		3.6×10^7
10 × 100	1	30%	42617	20%	66587	3.6×10^6
	10	85%		65%		3.6×10^7

Table 2: Sensitivity for detecting a self-annihilating DM contribution to the EDGB, utilizing anisotropy measurements in terms of the angular power spectrum. The sensitivity is given in terms of the minimum detectable DM gamma-ray flux, expressed in percentages of the EDGB. The three tables list the sensitivities for instrumental setups resembling current IACTs and the planned CTA, respectively, for several observation times, background rates, fov, and observational strategies. For reference, the number of simulated signal (N_{sig}) and background (N_{bg}) events is listed. A value of $\gtrsim 100\%$ refers to a sensitivity outside our tested range.

gies is worth mentioning. As shown in table 2, the sensitivity for a combination of ten different observations of 100 h each is just a factor of 2 worse compared to a continuous 1 000 h single target observation. In addition, the sensitivity of the combined data set

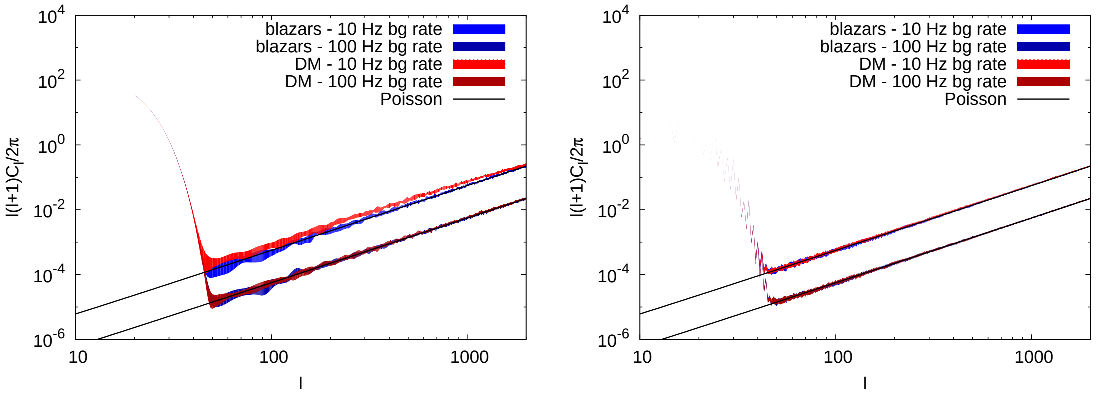

(a) Single fov, 1 000 h, $E_{\rm thr} = 100\,{\rm GeV}$ (b) Multiple fov, 10×100 h, $E_{\rm thr} = 100\,{\rm GeV}$

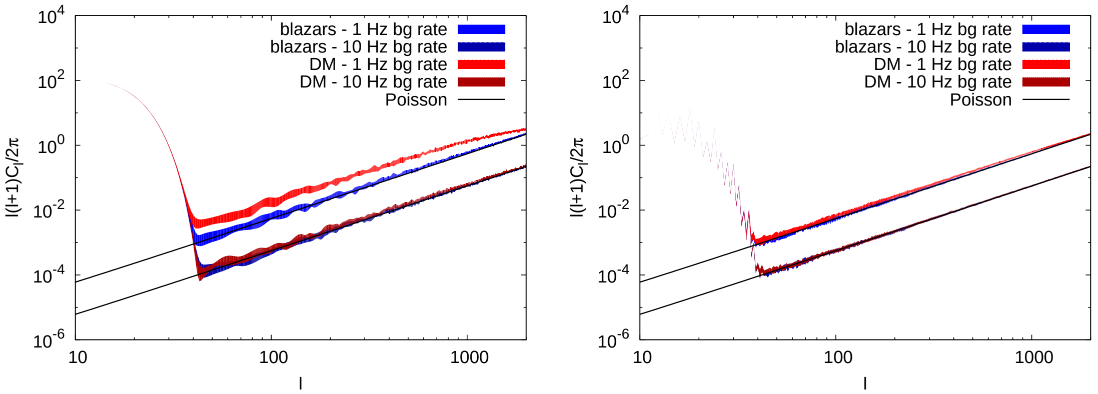

(c) Single fov, 1 000 h, $E_{\rm thr} = 300\,{\rm GeV}$ (d) Multiple fov, 10×100 h, $E_{\rm thr} = 300\,{\rm GeV}$

Figure 4: Comparison between the measured APS for a pure astrophysical case with $C_\ell = C_P^A = 10^{-5}$ (blue bands) and a case with 40% of the total radiation originating from self-annihilating DM with $C_\ell = C_P^{DM} = 10^{-3}$ (red bands). An observation with a CTA-like telescope system of 1 000 h on a single target (left column) and of 10×100 h splitted on ten different targets (right column) is considered. The upper plots refer to an energy threshold of 100 GeV and the lower ones refer to a threshold of 300 GeV. The two cases in each panel refer to background rates of 10 Hz and 100 Hz for 100 GeV, and 1 Hz and 10 Hz for 300 GeV. The size of the fov is $\sigma_{\rm fov} = 5°$. The lines show the estimated noise levels.

is approximately equivalent to a full 300 h observation of a single target. Following the discussion at the end of section 2.2 we see that, even with CTA, the statistical regime where a multiple-fov strategy results in a reduction of the errors cannot be reached. Rather, the combination of multiple fov results in errors comparable or slightly larger than the single fov observation. Nonetheless, observations of single targets for 1 000 h each are practically not feasible (perhaps apart from the Galactic Center over several

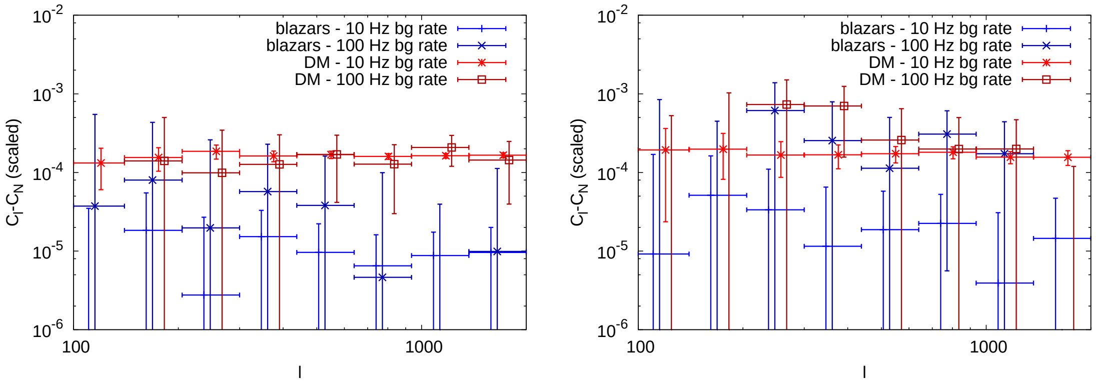

(a) Single fov, 1 000 h, $E_{\mathrm{thr}} = 100\,\mathrm{GeV}$ (b) Multiple fov, 10 × 100 h, $E_{\mathrm{thr}} = 100\,\mathrm{GeV}$

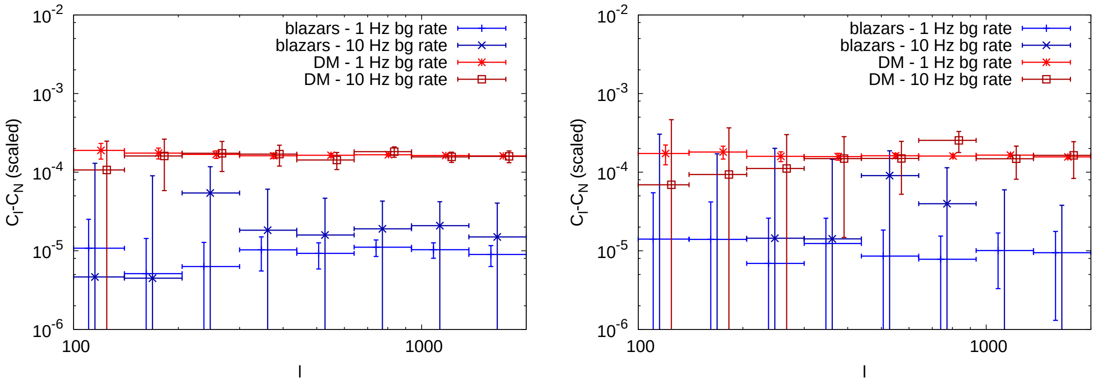

(c) Single fov, 1 000 h, $E_{\mathrm{thr}} = 300\,\mathrm{GeV}$ (d) Multiple fov, 10 × 100 h, $E_{\mathrm{thr}} = 300\,\mathrm{GeV}$

Figure 5: Same as figure 4, but showing the noise-subtracted and instrumental effects unfolded APS. Note that, in difference to figure 4, the y-axis shows $C_\ell - C_N$ instead of $\ell(\ell+1)C_\ell/2\pi$. Also, the APS are binned into 8 logarithmically spaced bins in ℓ. See text for more details. For readability, the bins for each sub-case in each plot are slightly shifted.

years), and the observation of ten different targets for 100 h each is more likely to be realized. We emphasize that these observations do not need to specifically target anisotropy searches, but observations taken for different purposes can be analyzed instead. In this manner, the loss in sensitivity by a factor of ∼2 is compensated by the availability of a significantly larger data set.

As a specific example of our analysis, figures 4 and 5 show the APS for the cases of 1 000 h and 10×100 h of observation time with CTA for the threshold energies of 100 GeV and 300 GeV, and a fov of 5°. The pure astrophysical case ($C_P^A = 10^{-5}$) and a case of a 40% DM ($C_P^{DM} = 10^{-3}$) contribution are shown, as well as the two different choices of background rates. Figure 4 shows the raw measured APS and illustrates the fact that the variance of the APS decreases when the observation time is splitted over several fov, but, at the same time, the signal over noise ratio also decreases. Further informations are difficult to infer from figure 4. For this reason unfolded and binned APS are shown in figure 5. Unfolding involves subtraction of the Poissonian noise and correction for the PSF attenuation. In the simple case of a Gaussian beam, which we adopted, the PSF correction is simply given by the factor $w_\ell^2 = \exp(\sigma_{\rm psf}^2\,\ell(\ell+1))$, see [1, 8] and appendix A. The presence of the background also alters the normalization of the APS. This effect can be corrected by rescaling the noise-subtracted APS by the factor $N_{\rm ev}^2/N_{\rm sig}^2$. Clearly, this correction requires a perfect, and thus unrealistic, knowledge of the fraction of signal and background in the collected data, while this information will likely be available with a large error only. However, this will not pose a problem in the analysis of real data, where the *intensity* APS is used instead of the dimensionless APS and no a priori knowledge of the gamma-ray flux is required. Finally, the limited fov also introduces a renormalization of the APS by a factor $f_{\rm sky}$ which we corrected in the unfolding. A binning of data is implemented given the large error for a single multipole. Since C_ℓ coefficients of neighboring multipoles are correlated, the knowledge of the full covariance matrix is in principle necessary to calculate the error after binning. Here, we use a simple analytical estimate of the error, which is given by $\delta C_{\bar\ell} = (C_{\bar\ell} + C_N\, w_{\bar\ell}^2)\sqrt{2/(2\bar\ell+1)/\Delta\ell/f_{\rm sky}}$, where $\Delta\ell$ is the width of the bin, $\bar\ell$ is the average ℓ of the bin, and $w_\ell = \exp(\sigma_{\rm psf}^2\,\ell(\ell+1)/2)$. This approach is accurate for all but very low ($\ell < 10$) multipoles. The unfolded APS of figure 5 show that we recover within the errors the input anisotropy $C_P^A = 10^{-5}$ for the astrophysical case and the anisotropy $C_P^{\rm A+DM,40\%} = 0.4^2 \cdot C_P^{DM} + 0.6^2 \cdot C_P^A \simeq 1.6 \times 10^{-4}$ for the case of 40% DM. It can be also seen from the plot that, when the background rate increases, the input signal can still be recovered although, as expected, with a larger error. The case of ten fov observations explicitly shows that the errors worsen by approximately a factor of 2 in agreement with the results of table 2. The sensitivity to DM inferred from figure 5 is in line with the values reported in table 2.

The other crucial parameters determining the sensitivity are C_P^{DM} and C_P^A. To test the dependence on these parameters, we performed a further simulation with $C_P^A = 10^{-4}$ (instead of $C_P^A = 10^{-5}$), keeping the value $C_P^{DM} = 10^{-3}$, and we found the sensitivities to decrease by a factor ~ 3. This seems to be in good agreement with the analytic scaling relation $(C_P^A/C_P^{DM})^{1/2}$ found in the appendix. Given the strong dependence on these two parameters, a firmer prediction of the sensitivity requires pinning down their uncertainties. More accurate calculations of C_P^{DM} have been recently reported in [19], indicating that C_P^{DM} can be as high as 10^{-1}, dominated by the contribution of the galactic substructures over extragalactic ones (see in particular their figure 7). Although such a large DM anisotropy would push the sensitivity to values better than 1%, the intrinsic emission from these very anisotropic structures is expected to be very low, as witnessed by the fact that the *intensity* anisotropies are instead dominated by the extragalactic component (see [19]). The results presented in [19] also indicate that the DM APS is not exactly flat in multipole, but shows a slight attenuation to higher multipoles. Given the good angular resolution of CTA, this effect can in principle be used to disentangle the DM contribution from the astrophysical one. However, the detection of a non-zero anisotropy will likely be at a low signal-to-noise ratio, therefore it will be difficult to explore large ℓ since they will be noise-dominated. The effect is also somewhat degenerated with the PSF attenuation and will thus require a good calibration of the instrumental performance. A more accurate estimate of C_P^A, instead, awaits a direct measurement with Cherenkov telescopes or further work on the modeling of blazar populations at TeV energies. In this respect, the examples depicted in figures 4 and 5 show that the observation of an anisotropy $C_P^A = 10^{-5}$ is close to the sensitivity attainable with 1 000 h of observation time with CTA (for the optimistic background estimate), while it would be more challenging for the splitted observation strategy. However, C_P^A is not precisely known, and the possibility of a larger power such as 10^{-4} would obviously improve its detection capabilities, albeit implying a lower DM sensitivity. We thus propose explicit observations of these kind of anisotropies even with the current generation of instruments. Beside the possibility to constrain a DM contribution, an observation of anisotropy would provide a complementary and powerful tool to investigate astrophysical TeV sources.

We checked that the results are robust with respect to the approximation of a delta-like source flux distribution $\mathrm{d}N/\mathrm{d}S$, as opposed to a more realistic distribution, which typically shows a power law or a broken power-law behavior (see for example [53]). We simulated the case of a power-law distribution $\propto S^{-2.4}$ for both DM and astrophysical sources, spanning two orders of magnitude in flux and normalized to give the same level of anisotropy as in the delta case, i.e. $C_P^A = 10^{-5}$ and $C_P^{DM} = 10^{-3}$. The resulting sensitivities are identical to the delta-like case. This result is perhaps not surprising, since the anisotropy C_P is given by an integral over $\mathrm{d}N/\mathrm{d}S$ below the point-source detection threshold S_{lim}, more precisely $C_P = \int_0^{S_{\mathrm{lim}}} \mathrm{d}S\, S^2 \mathrm{d}N/\mathrm{d}S$, so that different $\mathrm{d}N/\mathrm{d}S$ distributions can still result in the same C_P.

The sensitivities given in table 2 as fraction of the EDGB flux can be expressed in terms of the more common quantity of the velocity-averaged DM self-annihilation cross section $\langle\sigma v\rangle$, although this introduces further model dependence. To normalize the DM signal, we use the cosmological DM model of [54] in its optimistic version, where DM halos are modeled with NFW profiles and include the presence of DM subhalos, boosting the annihilation signal further (see, e.g., [55, 56] for gamma-ray implications of galactic DM subhalos). In addition, the less optimistic version neglecting DM subhalos is considered, resulting in a factor of ~ 10 less DM annihilation flux and thus a correspondingly worse sensitivity. It should be noted that considering the results of [16] from the Millennium-II simulation, an order of magnitude enhancement with respect to the above "optimistic" case is predicted with a correspondingly improved sensitivity (see also [57], in particular figure 1). The results are shown in figure 6 for various annihilation channels as function of the DM particle mass m_χ. In conclusion, the self-annihilation cross section $\langle\sigma v\rangle = 3 \times 10^{-26}\,\mathrm{cm}^3\mathrm{s}^{-1}$ expected from thermal dark matter freeze-out can be probed with CTA for DM particle masses up to a few hundred GeV. Interestingly, even using the conservative version of the EDGB DM model above, sensitivities better than the ones achievable with dwarf spheroidal galaxies observed with CTA and comparable with achievable limits using cluster observations can be reached [28].

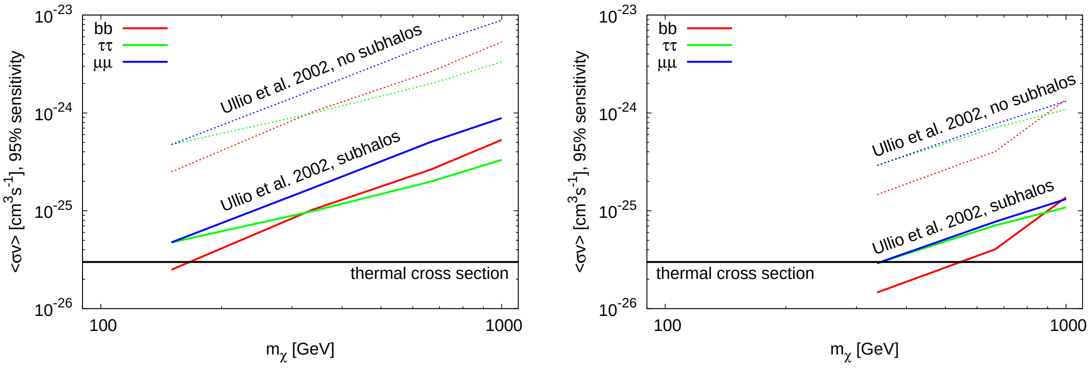

(a) (b)

Figure 6: (a): Sensitivity of CTA on the velocity-averaged DM self-annihilation cross section $\langle \sigma v \rangle$ as a function of the DM particle mass m_χ, for an energy threshold of 100 GeV, 300 h (or 10 × 100 h) of observation time, $\sigma_{\text{fov}} = 5^\circ$, and a background rate of 10 Hz (corresponding to a contribution from self-annihilating DM of ∼35% to the total EDGB, see table 2). Solid lines correspond to the model of [54], i.e. incorporating DM annihilation in subhalos, while dotted lines refer to the more conservative case of absent DM subhalos, giving a sensitivity by approximately a factor of 10 worse. We consider DM annihilation in $b\bar{b}$ (red), $\tau^+\tau^-$ (green), and $\mu^+\mu^-$ (blue) final states. Assumed instrumental characteristics are discussed in the text. (b): Same as above for an energy threshold of 300 GeV, 300 h (or 10 × 100 h) of observation time, and a background rate of 1 Hz (corresponding to a contribution from self-annihilating DM of ∼20% to the total EDGB, see table 2).

5 Conclusions

We have investigated the key aspects of the capability of ground-based gamma-ray telescopes with small fields of view (i.e. imaging atmospheric Cherenkov telescopes) for observing anisotropies in the diffuse gamma-ray background. In particular, the effects of the effective area, the field of view, the angular resolution (PSF), and of the hadron-background rejection efficiency have been studied. These properties have been identified as crucial instrumental characteristics, determining the sensitivity for detecting small-scale angular anisotropies.

The sensitivity for detecting a contribution of self-annihilating dark matter to the diffuse gamma-ray background has been investigated, focussing on the analysis of angular anisotropies. Benchmark instrumental setups of currently operating imaging atmospheric Cherenkov telescopes such as H.E.S.S., MAGIC, and VERITAS, as well as the forthcoming CTA have been considered. We have used realistic expectations for the anisotropy power spectra from self-annihilating dark matter and from astrophysical sources. We find that the sensitivity of CTA will be sufficient to resolve a relative contribution of ∼10% from self-annihilating dark matter to the total isotropic gamma-ray background flux, given an observation time of 1 000 h and a background rate of 1 Hz above 300 GeV. More important, we find that with a multiple field-of-view strategy of 1 000 h of observation time splitted over ten separate targets of 100 h each yields a slight reduction in sensitivity (to ∼20%, a factor of 2) only. In practice, this means that it will be possible to obtain interesting constrains on dark matter without dedicated deep observations, but combining existing observations of different primary astrophysics targets. The sensitivity achievable can be already sufficient to probe the thermal annihilation cross section for WIMP masses $\lesssim 200\,\mathrm{GeV}$ (for common models of dark matter annihilation in galactic and extragalactic environments). We also find that CTA will have sufficient sensitivity for detecting small-scale anisotropies from astrophysical sources with a Poissonian anisotropy level of 10^{-5}, while the sensitivity of current-generation instruments is approximately an order of magnitude lower. Given the uncertainty on the exact expected anisotropy level, we propose that available deep exposures, preferably at high galactic latitudes, should be analyzed in order to search for anisotropies. An observation of anisotropy would provide a complementary and invaluable tool for investigating the nature of TeV sources.

Acknowledgments

We wish to thank Mattia Fornasa and Jesus Zavala for providing suggestions on the manuscript and for useful discussions. We kindly thank the anonymous referee for useful and important suggestions on improving the manuscript. DH acknowledges support through the collaborative research center (SFB) 676 “Particles, Strings, and the Early Universe” at the University of Hamburg. JC is Royal Academy of Science Fellow financed by a grant of the Knut and Alice Wallenberg foundation.

A Error on the Poisson Anisotropy

The error on the *fluctuation* angular power spectrum is given by

$$\delta C_\ell \equiv \sigma_\ell = (C_\ell + C_N w_\ell^2)\sqrt{\frac{2}{f_{\mathrm{sky}}(2\ell+1)}}\,, \tag{A.1}$$

where $C_N = \Omega_{\mathrm{fov}}(1/N_\gamma + N_b/N_\gamma^2)$ is the (Poissonian) noise, N_γ the number of gamma-ray events, N_b the number of background events, and Ω_{fov} the total fov in steradians [8]; $w_\ell = \exp(\sigma_{\mathrm{psf}}^2\ \ell(\ell+1)/2)$ describes the correction for a Gaussian PSF of width σ_{psf} (in radians). In the following derivation of the sensitivity, we assume a Poisson-like power spectrum, i.e. $C_\ell = C_P$. In practice, C_P is estimated by calculating the weighted average of the measured angular power spectrum, so that $C_P = \sum_\ell p_\ell C_\ell$, where $p_\ell = (1/\sigma_\ell^2)/(\sum_\ell 1/\sigma_\ell^2)$ (the weight of higher multipoles is larger, owing to smaller errors until the PSF error starts to dominate). The corresponding error on C_P is the given by $(\delta C_P)^2 = \sum_\ell p_\ell^2(\delta C_\ell)^2 = 1/(\sum_\ell 1/\sigma_\ell^2)$.

A.1 Simple calculation

In the following, we consider both a sufficiently narrow PSF, resulting in a sufficiently small PSF correction for the multipole range of interest, and the high statistics limit, so that C_N is negligible with respect to C_P. In this limit, we have (implicitly, $\ell \gg 1$ is assumed)

$$\sigma_\ell = C_\ell \sqrt{\frac{1}{f_{\rm sky}\ \ell}}\,. \tag{A.2}$$

Evaluating the sum in $(\delta C_P)^2 = 1/(\sum_\ell 1/\sigma_\ell^2)$ (this can be done analytically or approximating the sum as an integral) yields

$$\delta C_P \approx C_P \sqrt{\frac{2}{f_{\rm sky}(\ell_{\rm max}^2 - \ell_{\rm min}^2)}} \approx \frac{C_P}{\ell_{\rm max}} \sqrt{\frac{2}{f_{\rm sky}}}\,. \tag{A.3}$$

A.2 More accurate calculation

Assuming $\ell \gg 1$,

$$\sigma_\ell = (C_\ell + C_N w_\ell^2) \sqrt{\frac{1}{f_{\rm sky}\ \ell}}\,. \tag{A.4}$$

Evaluating the sum $(\delta C_P)^2 = 1/(\sum_\ell 1/\sigma_\ell^2)$ by approximating it as an integral we find

$$\delta C_P \approx \sqrt{\frac{1}{f_{\rm sky}}} \left(-\frac{\ell_{\rm min}^2}{C_P^2} - \frac{\ln\left(C_P/C_N + w_{\ell_{\rm min}}^2\right)}{C_P^2\ \sigma_{\rm psf}^2} - \frac{1}{2\, C_P\, \sigma_{\rm psf}^2 \left(C_P + C_N w_{\ell_{\rm min}}^2\right)} \right)^{-\frac{1}{2}}\,. \tag{A.5}$$

With $\ell_{\rm min} \approx 100$, $\sigma_{\rm psf} = 0.05^\circ \ll 1/\ell_{\rm min} \approx 0.6^\circ$, and in the limit of high statistics $(C_P \gg C_N)$, the expression can be simplified as

$$\delta C_P \approx C_P\, \sigma_{\rm psf} \sqrt{\frac{2}{f_{\rm sky}\ \ln\left(\frac{C_P}{e\, C_N}\right)}} \equiv \frac{C_P}{\ell_{\rm max}} \sqrt{\frac{2}{f_{\rm sky}}}\,, \tag{A.6}$$

which is equivalent to the previous simplified calculation with the definition $\ell_{\rm max} = \sigma_{\rm psf}^{-1} \sqrt{\ln\left(\frac{C_P}{e\, C_N}\right)}$. Note that the quantity $\ln\left(\frac{C_P}{e\, C_N}\right)$ is of order ~ 1 in the high statistics limit. In the case discussed in the paper, $\sigma_{\rm psf} = 0.05^\circ$ is assumed, so that the first condition is satisfied. Further, a fov of 5° corresponds to $\Omega_{\rm fov} \approx 10^{-2}$ sr and $f_{\rm sky} \approx 10^{-3}$. Given a 1 000 h observation and a background rate of 10 Hz above 100 GeV, $C_N \approx 3 \times 10^{-5}$, referring to the number of events in table 2, while the case for 1 Hz above 300 GeV corresponds to $C_N \approx 8 \times 10^{-6}$, both to be compared with $C_P = 10^{-5}$. Therefore, we face the condition $C_P \sim C_N$ even for the most optimistic cases. Nonetheless, for illustration purposes, the following derivation focusses on the regime $C_P \gg C_N$, estimating the sensitivity achievable under optimal conditions.

B Sensitivity using the intensity APS

More convenient calculations can be carried out in terms of the intensity APS, since power spectra are linearly additive in case of uncorrelated summands. This is indeed the case for Poisson-like anisotropies.

The intensity APS is simply related to the fluctuation APS as

$$C_P^I = I^2\, C_P, \tag{B.1}$$

where I is the intensity of the considered component. We consider the same scenario as above, i.e. an astrophysical component with Poissonian anisotropy C_A and intensity I_A, and a DM component with anisotropy C_{DM} and intensity I_{DM}. The corresponding intensity anisotropies are given by $C_A^I = I_A^2\, C_A$ and $C_{DM}^I = I_{DM}^2\, C_{DM}$. Assuming that the intensity anisotropy $C_P^{I,\mathrm{data}} \pm \delta C_P^{I,\mathrm{data}}$ has been measured in a given energy band, we can set a conservative upper limit on the DM contribution as

$$C_{DM}^I \lesssim C_P^{I,\mathrm{data}}, \tag{B.2}$$

which implies

$$\frac{I_{DM}}{I} \lesssim \sqrt{\frac{C_P^{\mathrm{data}}}{C_{DM}}}\,. \tag{B.3}$$

If the DM component is subdominant, we have $C_P^{\mathrm{data}} \sim C_A$ and $I_{DM}/I \lesssim \sqrt{C_A/C_{DM}}$. For the benchmark case with $C_A = 10^{-5}$ and $C_{DM} = 10^{-3}$, this yields a maximum sensitivity of $I_{DM}/I \lesssim 10\%$.

A case more accurately approximating the case discussed with the previous simulations is given when the quantity $C_P^{I,\mathrm{data}} = C_A^I$ is known within a certain error in advance, either because we have measured this quantity in a different energy band, or because it matches our theoretical expectations. In this case, a more interesting upper limit can be derived from

$$C_{DM}^I \lesssim \delta C_P^{I,\mathrm{data}}, \tag{B.4}$$

which implies

$$\frac{I_{DM}}{I} \lesssim \sqrt{\frac{C_P^{\mathrm{data}}}{C_{DM}}} \times \sqrt[4]{\frac{2}{f_{\mathrm{sky}}\ \ell_{\mathrm{max}}^2}}\,. \tag{B.5}$$

Again, with $C_P^{\mathrm{data}} = C_A$ and for our benchmark case $C_A = 10^{-5}$, $C_{DM} = 10^{-3}$, $\ell_{\mathrm{max}} \approx 1000$, and $f_{\mathrm{sky}} \approx 10^{-3}$, we have a maximum sensitivity of $I_{DM}/I \lesssim 2\%$. Note that the sensitivity improves with a larger fov, although only with the fourth root. However, the sensitivity improves faster with the angular resolution (ℓ_{max}).

We emphasize that the above results are clearly back-of-the-envelope calculations, with the purpose of estimating the sensitivity and its dependence on the relevant quantities. Dealing with real data, more appropriate derivations can be conducted, for example, with a likelihood analysis.

C Sensitivity using the fluctuation APS

In the paper, fluctuation anisotropies are used to calculate the sensitivities. In this case, the relation effectively imposed to derive the sensitivity is

$$C_P^{\rm data} - \delta C_P^{\rm data} \lesssim C_{\rm tot} \lesssim C_P^{\rm data} + \delta C_P^{\rm data}\,, \tag{C.1}$$

where

$$C_{\rm tot} = \frac{C_{DM} I_{DM}^2 + C_A I_A^2}{(I_{DM} + I_A)^2}\,. \tag{C.2}$$

Rewriting $C_P^{\rm data} \pm \delta C_P^{\rm data}$ as $C_P^{\rm data}\,(1 \pm \Delta)$, where $\Delta \equiv \sqrt{2/(f_{\rm sky}\ell_{\rm max}^2)}$, we find that the sensitivity is given by a second order equation, solved by

$$\frac{I_{DM}}{I_A} = \frac{C_P^{\rm data}\,(1 \pm \Delta) \pm \sqrt{C_P^{\rm data}\,(1 \pm \Delta)\,(C_A + C_{DM}) - C_A C_{DM}}}{C_P^{\rm data}\,(1 \pm \Delta) - C_{DM}}\,. \tag{C.3}$$

The equation can be simplified in a few relevant cases. For example, if $C_{DM} \gg C_A$ (as in the benchmark case), and again assuming $C_P^{\rm data} \approx C_A$, the positive (physical) solution is

$$\frac{I_{DM}}{I} \lesssim \frac{C_P^{\rm data}}{C_{DM}} + \sqrt{\frac{C_P^{\rm data}}{C_{DM}}}\,\sqrt[4]{\frac{2}{f_{\rm sky}\ell_{\rm max}^2}}\,. \tag{C.4}$$

For the benchmark numbers, we get a sensitivity of $I_{DM}/I \lesssim 3\%$, only slightly worse than in the intensity case. Therefore, the actual value of 10% for the sensitivity quoted in the paper for the most favorable scenario is not very far from the analytical estimate.

For $C_A = 10^{-4}$ and $C_{DM} = 10^{-3}$ the above sensitivity degrades quite rapidly, worsening by a factor of 10, in agreement with the simulations performed. In the intensity case, instead, the dependence only goes with the square root, and the sensitivity should worsen by a factor of ∼3 only.

Finally, unlike in the intensity case, we get an upper limit on I_{DM}, even in the case $C_{DM} \ll C_A$. This scenario is quite unphysical, although it can be practically taken as case study for a further (non-DM) component with negligible anisotropy. This is expected, for example, from normal galaxies or truly diffuse processes like photons from UHECRs cascades on the CMB. In this case, after a few simplifications we get

$$\frac{I_{DM}}{I} \lesssim \sqrt{\frac{2}{f_{\rm sky}\ell_{\rm max}^2}}\,, \tag{C.5}$$

which is independent of C_A. The benchmark numbers for $f_{\rm sky}$ and $\ell_{\rm max}$ yield a limit of $I_{DM}/I \lesssim 5\%$.

The case $C_A \sim C_{DM}$ seems to give the worst limit. For this regime, a simple formula cannot be derived and the full expression Eq. C.3 needs to be used.

References

[1] M. Ackermann *et al.* [Fermi LAT Collaboration], Phys. Rev. D **85** (2012) 083007 [arXiv:1202.2856 [astro-ph.HE]].

[2] A. Cuoco, E. Komatsu and J. M. Siegal-Gaskins, Phys. Rev. D **86** (2012) 063004 [arXiv:1202.5309 [astro-ph.CO]].

[3] A. A. Abdo et al. [Fermi LAT Collaboration], Phys. Rev. Lett. **104** (2010) 101101.

[4] C. D. Dermer, AIP Conf. Proc. **921** (2007) 122-126 [arXiv:0704.2888 [astro-ph]].

[5] C. -A. Faucher-Giguere and A. Loeb, JCAP **1001** (2010) 005 [arXiv:0904.3102 [astro-ph.HE]].

[6] D. Malyshev and D. W. Hogg, Astrophys. J. **738** (2011) 181 [arXiv:1104.0010 [astro-ph.CO]].

[7] J. -Q. Xia, A. Cuoco, E. Branchini, M. Fornasa and M. Viel, Mon. Not. Roy. Astron. Soc. **416** (2011) 2247 [arXiv:1103.4861 [astro-ph.CO]].

[8] S. Ando and E. Komatsu, Phys. Rev. D **73** (2006) 023521;

[9] S. Ando, E. Komatsu, T. Narumoto and T. Totani, Phys. Rev. D **75** (2007) 063519;

[10] A. Cuoco, S. Hannestad, T. Haugbolle, G. Miele, P. D. Serpico and H. Tu, JCAP **0704** (2007) 013 [astro-ph/0612559].

[11] A. Cuoco, J. Brandbyge, S. Hannestad, T. Haugboelle and G. Miele, Phys. Rev. D **77** (2008) 123518;

[12] J. M. Siegal-Gaskins, JCAP **0810** (2008) 040;

[13] M. Fornasa, L. Pieri, G. Bertone, E. Branchini, Phys. Rev. **D80** (2009) 023518;

[14] J. M. Siegal-Gaskins, V. Pavlidou, Phys. Rev. Lett. **102** (2009) 241301;

[15] S. 'i. Ando, Phys. Rev. D **80** (2009) 023520 [arXiv:0903.4685 [astro-ph.CO]].

[16] J. Zavala, V. Springel, M. Boylan-Kolchin, Mon. Not. Roy. Astron. Soc. **405** (2010) 593;

[17] B. S. Hensley, J. M. Siegal-Gaskins, V. Pavlidou, Astrophys. J. **723** (2010) 277;

[18] A. Cuoco, A. Sellerholm, J. Conrad and S. Hannestad, Mon. Not. Roy. Astron. Soc. **414** (2011) 2040;

[19] M. Fornasa, J. Zavala, M. A. Sanchez-Conde, J. M. Siegal-Gaskins, T. Delahaye, F. Prada, M. Vogelsberger and F. Zandanel *et al.*, arXiv:1207.0502 [astro-ph.HE].

[20] S. Ando, E. Komatsu, T. Narumoto and T. Totani, Mon. Not. Roy. Astron. Soc. **376** (2007) 1635; F. Miniati, S. M. Koushiappas and T. Di Matteo, Astrophys. J. **667** (2007) L1

[21] J. M. Siegal-Gaskins, R. Reesman, V. Pavlidou, S. Profumo, T. P. Walker, Mon. Not. Roy. Astron. Soc. **415** (2011) 1074S.

[22] S. Ando and V. Pavlidou, Mon. Not. Roy. Astron. Soc. **400** (2009) 2122

[23] W. B. Atwood *et al.* [LAT Collaboration], Astrophys. J. **697**, 1071 (2009)

[24] F. Aharonian *et al.* [H.E.S.S. Collaboration], Astron. Astrophys. **457** (2006) 899 [astro-ph/0607333].

[25] J. Albert *et al.* [MAGIC Collaboration], Astrophys. J. **674** (2008) 1037 [arXiv:0705.3244 [astro-ph]].

[26] E. Aliu *et al.* [VERITAS Collaboration], Science **334** (2011) 69 [arXiv:1108.3797 [astro-ph.HE]].

[27] The CTA Consortium, arXiv:1008.3703 (2010).

[28] M. Doro *et al.* [CTA Collaboration], Astropart. Phys. **43**, 189 (2013) [arXiv:1208.5356 [astro-ph.IM]].

[29] F. A. Aharonian, A. K. Konopelko, H. J. Volk and H. Quintana, Astropart. Phys. **15** (2001) 335 [astro-ph/0006163].

[30] A. A. Abdo *et al.* [Fermi LAT Collaboration], Phys. Rev. Lett. **102** (2009) 181101 [arXiv:0905.0025 [astro-ph.HE]].

[31] M. Ackermann *et al.* [Fermi LAT Collaboration], Phys. Rev. D **82** (2010) 092004 [arXiv:1008.3999 [astro-ph.HE]].

[32] F. Aharonian *et al.* [H.E.S.S. Collaboration], Phys. Rev. Lett. **101** (2008) 261104 [arXiv:0811.3894 [astro-ph]].

[33] F. Aharonian *et al.* [H.E.S.S. Collaboration], Astron. Astrophys. **508** (2009) 561 [arXiv:0905.0105 [astro-ph.HE]].

[34] G. P. Rowell, Astron. Astrophys. **410** (2003) 389 [astro-ph/0310025].

[35] K. M. Gorski, E. Hivon, A. J. Banday, B. D. Wandelt, F. K. Hansen, M. Reinecke and M. Bartelman, Astrophys. J. **622** (2005) 759 [arXiv:astro-ph/0409513].

[36] M. Ackermann *et al.* [Fermi-LAT Collaboration], Phys. Rev. D **82** (2010) 092003 [arXiv:1008.5119 [astro-ph.HE]].

[37] M. Aguilar *et al.* [AMS Collaboration], Phys. Rev. Lett. **110**, no. 14, 141102 (2013).

[38] R. Abbasi *et al.* [IceCube Collaboration], Astrophys. J. **740** (2011) 16 [arXiv:1105.2326 [astro-ph.HE]].

[39] R. Abbasi *et al.* [IceCube Collaboration], Astrophys. J. **746** (2012) 33 [arXiv:1109.1017 [hep-ex]].

[40] A. A. Abdo, B. Allen, T. Aune, D. Berley, E. Blaufuss, S. Casanova, C. Chen and B. L. Dingus *et al.*, Phys. Rev. Lett. **101** (2008) 221101 [arXiv:0801.3827 [astro-ph]].

[41] A. A. Abdo, B. T. Allen, T. Aune, D. Berley, S. Casanova, C. Chen, B. L. Dingus and R. W. Ellsworth *et al.*, Astrophys. J. **698** (2009) 2121 [arXiv:0806.2293 [astro-ph]].

[42] S. Vernetto *et al.* [ARGO-YBJ Collaboration], arXiv:0907.4615 [astro-ph.HE].

[43] J. Masbou, G. Lamanna and S. Rosier-Lees for the H.E.S.S. Collaboration [Proceeding of the 31 ICRC Conference, Lodz, Poland 2009], http://icrc2009.uni.lodz.pl/proc/pdf/icrc1059.pdf

[44] K. Bernlohr, A. Barnacka, Y. Becherini, O. B. Bigas, E. Carmona, P. Colin, G. Decerprit and F. Di Pierro *et al.*, Astropart. Phys. **43**, 171 (2013) [arXiv:1210.3503 [astro-ph.IM]].

[45] M. Martinez *et al.* [CTA Consortium Collaboration], arXiv:1111.2183 [astro-ph.IM].

[46] A. Dominguez, J. R. Primack, D. J. Rosario, F. Prada, R. C. Gilmore, S. M. Faber, D. C. Koo and R. S. Somerville *et al.*, arXiv:1007.1459 [astro-ph.CO].

[47] J. D. Finke, S. Razzaque and C. D. Dermer, Astrophys. J. **712** (2010) 238 [arXiv:0905.1115 [astro-ph.HE]].

[48] A. Franceschini, G. Rodighiero and M. Vaccari, Astron. Astrophys. **487** (2008) 837 [arXiv:0805.1841 [astro-ph]].

[49] R. C. Gilmore, R. S. Somerville, J. R. Primack and A. Dominguez, arXiv:1104.0671 [astro-ph.CO].

[50] T. M. Kneiske and H. Dole, arXiv:1001.2132 [astro-ph.CO].

[51] F. W. Stecker, M. A. Malkan and S. T. Scully, arXiv:1205.5168 [astro-ph.HE].

[52] M. Meyer, M. Raue, D. Mazin and D. Horns, Astron. Astrophys. **542** (2012) A59 [arXiv:1202.2867 [astro-ph.CO]].

[53] A. A. Abdo *et al.* [Fermi-LAT Collaboration], Astrophys. J. **720** (2010) 435 [arXiv:1003.0895 [astro-ph.CO]].

[54] P. Ullio, L. Bergstrom, J. Edsjo and C. G. Lacey, Phys. Rev. D **66**, 123502 (2002) [arXiv:astro-ph/0207125].

[55] H.-S. Zechlin, M. V. Fernandes, D. Elsaesser and D. Horns, Astron. Astrophys. **538** (2012) A93 [arXiv:1111.3514 [astro-ph.HE]].

[56] H.-S. Zechlin and D. Horns, JCAP **1211** (2012) 050 [arXiv:1210.3852 [astro-ph.HE]].

[57] A. A. Abdo *et al.* [Fermi-LAT Collaboration], arXiv:1002.4415 (2010a).

Chapter 6

The Case for WISPs – Hidden U(1) Gauge Bosons

Beyond-SM physics results in the prediction of new light particles as well. Recent theoretical results have shown that weakly interacting slim particles (WISPs) can constitute cold dark matter, once they are produced by non-thermal mechanisms. An introduction to WISPs is given in Section 6.1, while a new study of the astrophysical signatures of ultra-light hidden sector photons and the corresponding sensitivity of radio observations is presented in Section 6.2, as developed in the framework of this thesis.

6.1 The theoretical framework of WISPs

WISPs are naturally predicted by higher-level SM extensions. One of the prime examples are QCD axions (Peccei & Quinn 1977), whose existence would solve the strong-CP problem of quantum chromodynamics (QCD). Generalizations of this framework provide axion-like particles (ALPs), which interact similar to axions. Likewise, string compactifications and grand unified theories mostly predict additional $U(1)$ gauge symmetries in a hidden sector, resulting in the prediction of hidden sector photons (Okun 1982). For recent reviews on this subject see, e.g., Jaeckel & Ringwald (2010), Ringwald (2012), and Jaeckel (2013).

Axions and axion-like particles. The generic Lagrangian of QCD allows for a CP-violating term, which would lead to an electric dipole moment of the neutron. However, accelerator experiments have significantly demonstrated that strong interactions conserve CP-symmetry. In addition, upper bounds on the dipole moment of the neutron directly imply a strong suppression of the effective CP-violating parameter $|\overline{\theta}| \lesssim 10^{-10}$. Peccei & Quinn (1977) first proposed that the strong-CP problem, posed by the lack of a theoretical explanation for the suppression of $|\overline{\theta}|$, can be solved by introducing a dynamical field a, whose global shift symmetry is spontaneously broken. Axions arise as pseudo-Nambu-Goldstone bosons of this field with a parametrically small mass m_a, which is related to the coupling strength of the axion with SM particles. In particular, axions couple to photons via the Lagrangian

$$\mathscr{L}_{a\gamma} = -\frac{1}{4} g_{a\gamma} a F_{\mu\nu} \tilde{F}^{\mu\nu} = g_{a\gamma} a \mathbf{E} \cdot \mathbf{B}, \tag{6.1}$$

where $F_{\mu\nu}$ denotes the electromagnetic field-strength tensor, $\tilde{F}_{\mu\nu}$ its dual, **E** and **B** the electric and magnetic field vectors, respectively, and $g_{a\gamma}$ the coupling strength of axions to photons. Therefore, photon-axion mixing results in observable effects of the conversion of photons to axions in the presence of ambient magnetic fields, and vice versa.

ALPs are provided by a generalization of this concept and may arise from breaking scenarios of other global symmetries. In contrast to the QCD axion, the ALP mass is not related to its coupling strength. Axions and ALPs generally appear as Kaluza-Klein modes in compactified extra-dimensions of string theory, which connects their coupling strength with the string scale.

For a sufficiently weak coupling strength, axion production in the very early Universe is accomplished by a non-thermal mechanism. Once the Hubble expansion rate falls below the axion mass, coherent and spatially uniform oscillations of the axion field around its expectation value $\langle a \rangle = 0$ form a coherent state of non-relativistic matter. It can be shown that axions with masses between $\sim 10\,\mu$eV and $\sim 1\,$meV can contribute the total relic density of cold dark matter, corresponding to reasonable values of the coupling strength $g_{a\gamma}$ between $\sim 10^{-15}\,\mathrm{GeV}^{-1}$ and $\sim 10^{-12}\,\mathrm{GeV}^{-1}$, see Fig. 6.1a. The parameter space for ALP dark matter is even larger. See, e.g., Jaeckel & Ringwald (2010), Sikivie (2010), Arias *et al.* (2012), and Ringwald (2012) for details.

A number of laboratory experiments, astrophysical observations, and cosmological data sets have been utilized to search for imprints of axions and ALPs. Strong bounds on the mass and coupling strength of axions have been placed from photon-regeneration experiments such as light-shining-through-walls setups (e.g., the ALPS experiment, Ehret *et al.* 2010), helioscopes (e.g., CAST, Arik *et al.* 2011), haloscopes (e.g., ADMX, Asztalos *et al.* 2010; van Bibber & Carosi 2013), stellar evolution (e.g., Raffelt 1996), and cosmology (Mirizzi *et al.* 2009a; Horns *et al.* 2012b; Cadamuro & Redondo 2012), for instance, see Fig. 6.1a and corresponding references in Ringwald (2012). Tantalizing hints for ALPs are provided by astrophysics and cosmology, e.g., non-standard energy loss in white dwarfs (Isern *et al.* 2008) and the gamma-ray transparency of the Universe (Horns & Meyer 2012; Horns *et al.* 2012a; Meyer *et al.* 2013). A variety of experimental setups and astrophysical observations have been proposed, which will be sensitive to probing deep into the remaining parameter space for axions and ALPs, e.g., ALPS-II (Bähre *et al.* 2013) or IAXO (Vogel *et al.* 2013).

Hidden sector photons. Hidden sector photons have been initially suggested by Okun (1982) to parameterize possible deviations from electrodynamics. From a more theoretical point of view, a generic feature of standard string compactifications is the appearance of additional $U(1)$ gauge symmetries in a hidden sector, which only gravitationally interacts with the SM gauge group. For instance, gauge symmetry in standard orbifold compactifications of the heterotic string in $\mathrm{E}_8 \times \mathrm{E}_8$ supergravity is broken to the product of the SM gauge group and a non-Abelian and $U(1)$ gauge symmetry in a hidden sector (Lebedev & Ramos-Sánchez 2010),

$$\mathrm{E}_8 \times \mathrm{E}_8 \rightarrow \underbrace{SU(3) \times SU(2) \times U(1)}_{\mathrm{SM}} \times [SU(6) \times U(1)]\,. \tag{6.2}$$

An unbroken $U(1)$ at low energies would give rise to a new hidden sector gauge boson (hidden photon), which kinetically mixes with the ordinary SM photon. The amplitude of

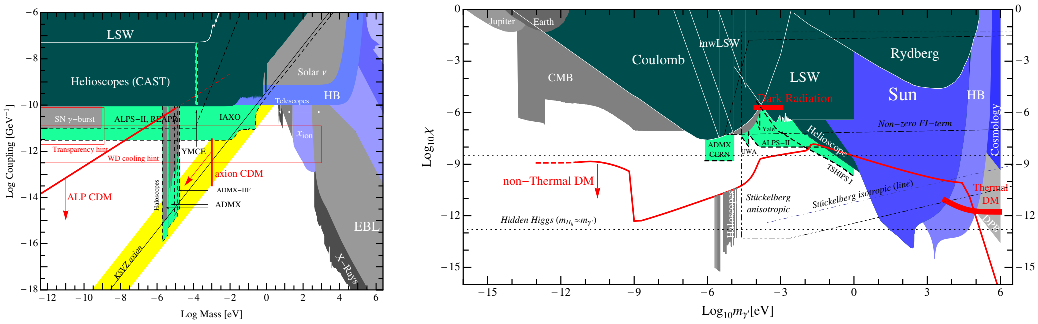

(a) **(b)**

Figure 6.1: **(a)**: Mass – coupling (m_a – $g_{a\gamma}$) parameter space for QCD axions and ALPs, including bounds from various laboratory experiments, astrophysical observations, and cosmological arguments shown in dark green, gray, and blue (see text and Ringwald 2012 for details). In addition, the sensitivity of future experiments is shown in light green. The parameter space for axion and ALP cold dark matter is indicated with the bold red lines, while thin red lines mark parameter regions of possible ALP hints. The yellow region shows the parameter space of the QCD axion. From Ringwald (2012). **(b)**: Mass – mixing ($m_{\gamma'}$ – χ) parameter space for hidden photons. Current bounds from laboratory experiments, astrophysical observations, and cosmological arguments are shown in dark green, gray, and blue, while the sensitivity of future experiments is indicated in light green. The red line marks the parameter space for hidden-photon cold dark matter. Dashed and dot-dashed black lines show the parameter space allowed for Higgs and Stückelberg mass generation. See Ringwald (2012) for details.

the kinetic mixing term is governed by the mixing angle χ, while the hidden-photon mass $m_{\gamma'}$ can either arise from Higgs or Stückelberg mechanisms. Details on the low-energy phenomenology of the mixing mechanism are discussed in the next section. As a result, the existence of massive hidden photons would introduce a new force, and can additionally lead to oscillations of ordinary photons in hidden photons (and vice versa). Photon–hidden-photon oscillations are in close analogy to the flavor oscillations of neutrinos. The strongly suppressed coupling of hidden photons to SM matter facilitates observability of these imprints, given that hidden photons are almost invisible for detectors.

The existence of hidden photons has been investigated in a variety of laboratory experiments, astrophysical observations, and cosmology, already giving strong bounds in the mass – mixing plane of hidden photons. Hidden photons can lead to deviations in the Coulomb law, and (in relation to axion and ALPs searches) have been searched with particle accelerators such as the LHC, light-shining-through-walls experiments (e.g., ALPS, Ehret *et al.* 2010), changes in the lifetime of the Sun and in the energy loss of stars (Redondo 2008; An *et al.* 2013), helioscopes (e.g., SHIPS, Schwarz 2012), haloscopes (e.g., ADMX, Wagner *et al.* 2010), and via possible distortions in the CMB spectrum (Mirizzi *et al.* 2009b). Photon oscillations can result in energy-dependent modulations of astrophysical spectra (Zechlin *et al.* 2008; Zechlin 2009). For a state-of-the-art summary of existing bounds, see Fig. 6.1b. Besides sensitivity improvements of existing methods (e.g., ALPS-II, Bähre *et al.* 2013), new concepts might allow us to probe deep into the remaining parameter space of hidden photons in the near future (e.g., Horns *et al.* 2013).

For masses in the range between 10^{-13} eV and 10^{6} eV and mixing angles up to $\sim 10^{-8}$, hidden photons can constitute cold dark matter (see Fig. 6.1b). Production mechanisms involved are analogous to the ones for axions, where coherent field oscillations around the field minimum behave as non-relativistic matter (Arias *et al.* 2012).

6.2 Publication IV

The large remaining parameter space of hidden photons shown in Fig. 6.1b clearly demonstrates the necessity of future searches for a hidden-photon signal. The development of new methods and laboratory experiments with significantly improved sensitivity is required to constrain favorable regions. In the framework of this thesis, a new method of searching for the astrophysical signature of ultra-light hidden photons in radio data has been developed. Our study on the sensitivity of radio observations has been published as Lobanov *et al.* (2013) and is presented in the following.

My contributions. The study was initiated by myself, based upon investigations carried out in my diploma thesis (Zechlin *et al.* 2008; Zechlin 2009). I significantly contributed to the development of the method, the discussions of oscillation and coherence length, the derivation of propagation effects, and the estimates of the measurable mass range. I contributed to the sensitivity study, and the discussion and interpretation of the results. Furthermore, I was considerably involved in the writing of the manuscript.

Publication IV

Astrophysical searches for a hidden-photon signal in the radio regime

Andrei P. Lobanov, Hannes-S. Zechlin and Dieter Horns

Physical Review D **87**, 065004 (2013)

PHYSICAL REVIEW D **87,** 065004 (2013)

Astrophysical searches for a hidden-photon signal in the radio regime

Andrei P. Lobanov[*]
Max-Planck-Institut für Radioastronomie, Auf dem Hügel 69, 53121 Bonn, Germany

Hannes-S. Zechlin[†] and Dieter Horns[‡]
University of Hamburg, Institut für Experimentalphysik, Luruper Chaussee 149, D-22761 Hamburg, Germany

(Received 26 November 2012; published 5 March 2013)

Common extensions of the Standard Model of particle physics predict the existence of a "hidden" sector that comprises particles with a vanishing or very weak coupling to particles of the Standard Model (visible sector). For very light ($m < 10^{-14}$ eV) hidden U(1) gauge bosons (hidden photons), broadband radio spectra of compact radio sources could be modified due to weak kinetic mixing with radio photons. Here, search methods are developed and their sensitivity discussed, with specific emphasis on the effect of the coherence length of the signal, instrumental bandwidth, and spectral resolution. We conclude that radio observations in the frequency range of 0.03–1400 GHz probe kinetic mixing of $\sim 10^{-3}$ of hidden photons with masses down to $\sim 10^{-17}$ eV. Prospects for improving the sensitivity with future radio astronomical facilities as well as by stacking data from multiple objects are discussed.

DOI: 10.1103/PhysRevD.87.065004 PACS numbers: 14.80.−j, 95.30.Cq, 98.38.−j

I. INTRODUCTION

Finding experimental evidence for physics beyond the Standard Model (SM) of particle physics is one of the pinnacles of present-day physical research, embracing both extensive laboratory studies and indirect (primarily) astrophysical measurements made across a very broad range of energies. Most of the present-day SM extensions into a more generic, unified scenario predict existence of a class of particles only weakly interacting with the normal matter. These particles are typically divided into two broad classes defined by the particle mass, with weakly interacting massive particles (WIMP) acting at a mass scale of $\mathcal{O}(100)$ GeV [1–3] and ultralight weakly interacting sub-eV particles (WISP) whose masses can be $\ll 1$ eV [4–9].

The existence of ultralight particles has been argued to be at least theoretically plausible in a number of different scenarios, including additional pseudoscalar (axions and axionlike particles (ALP), ϕ, [10–12]) as well as vector fields (U(1) hidden photons, γ_s, [4,5,7,8,13]). In either scenario, the prevailing nonbaryonic matter could be explained by these ultralight fields [14,15].

Hidden photons arise in low-energy extensions of the SM which leave all the SM fields uncharged under the additional U(1) gauge group. Interaction between hidden photons and massive SM particles is expected to be suppressed by the particle masses. However, it can be manifested by kinetic mixing with normal photons [4,13,16]. In low-energy SM extensions with hidden photons, the kinetic mixing is expressed by the effective Lagrangian describing two-photon interactions $\mathcal{L} = \mathcal{L}_{\mathrm{SM}} + \mathcal{L}_{\mathrm{h}} + \mathcal{L}_{\chi}$ [cf. [14,17,18]], with $\mathcal{L}_{\mathrm{SM}}$ denoting the Maxwell-Lagrangian for the SM photon field, the $\mathcal{L}_{\mathrm{h}}$ term describing the Proca-Lagrangian for the massive hidden-photon field, and $\mathcal{L}_{\chi}$ representing a gauge-invariant kinetic mixing term. The kinetic mixing term induces photon oscillations between the massless "normal" state (γ) and a nonzero mass "hidden" state (γ_s). In this hidden state, photons acquire a nonvanishing mass and propagate on timelike geodesics, without any interaction with normal matter. The physical properties of a hidden photon can be completely described by its mass m_{γ_s} and the kinetic mixing with a SM photon (expressed by the mixing angle χ). Theoretical predictions for χ fall in the broad range between 10^{-16} and 10^{-2} [16,19–23].

Accelerator experiments are generally optimized to search for new heavy particles such as WIMPs and are therefore of limited sensitivity and mass reach for WISPs. Hence, the potential discovery of ultralight particles requires high-precision experiments for which nonaccelerator setups often appear more promising [24–26].

Pioneering work on the phenomenology of hidden photons has already focussed on astrophysical implications of low-mass hidden photons [4,5]. Subsequently, evidence for the $\gamma - \gamma_s$ oscillations has been searched for in a number of laboratory [27–32] and astrophysical experiments [8,18,29,33–36], focusing in particular on "light shining through the wall" (LSW, [37]) experiments such as ALPS [28] and searches for hidden photons from the Sun (SHIPS; [29,38]). The nondetection of hidden-photon signals has so far yielded strong bounds on the kinetic mixing parameter χ for a broad range of hidden-photon masses [[7,8,15] and references therein]. The mass range which has been currently probed extends

---

[*] Visiting scientist (University of Hamburg and Deutsches Elektronen Synchrotron (DESY) Forschungszentrum, D-22607 Hamburg, Germany).
alobanov@mpifr-bonn.mpg.de
[†] hzechlin@physik.uni-hamburg.de
[‡] dieter.horns@physik.uni-hamburg.de

down to $m_{\gamma_s} = 2 \times 10^{-14}$ eV, with the lowest hidden-photon masses probed by the WMAP CMB measurements in the radio domain at frequencies above 22 GHz [34]. Below 10^{-14} eV, only weak limits of $\chi \approx 10^{-2}$ [7] have been obtained from analysis of early measurements of magnetic fields around Earth and Jupiter [39], and no limits are reported for $m_{\gamma_s} \lesssim 5 \times 10^{-16}$ eV.

Radio observations at frequencies below 22 GHz offer an excellent (if not unique) tool for placing bounds on the mixing angle χ for $m_{\gamma_s} < 10^{-14}$ eV. Initial bounds on χ can be obtained from existing radio data on compact, weakly variable objects with well-known radio spectra (such as young supernova remnants (SNR), planetary nebula, and steep spectrum radio sources typically used for the absolute flux density calibration of radio telescopes). With this approach, one can reasonably expect to reach $\chi \lesssim 0.01$. Propagation through a refractive medium (in which an SM photon also acquires an effective mass m_γ) can strongly affect this limit, improving it substantially near the resonance condition $m_{\gamma_s} = m_\gamma$, and suppressing the hidden photon conversion at $m_\gamma \gg m_{\gamma_s}$ [34]. The latter effect can become important at $m_{\gamma_s} \lesssim 10^{-15}$ eV.

Placing better bounds on χ can now be achieved by using the expanded capabilities of existing radio telescopes (utilizing the upgraded broadband coverage and spectral resolution of the Effelsberg 100-meter antenna and the Karl Jansky Very Large Array (JVLA) in the 0.3–40 GHz frequency range), by extending the measurements both to lower frequencies (0.03–0.3 GHz) covered by the low frequency array (LOFAR) and to submillimeter wavelengths probed by Atacama Large Millimeter Array (ALMA), and by employing the superb brightness sensitivity (~1 μJy [40]) of the SKA [41] and its precursors, MeerKAT [42] and ASKAP [43].

The existing data for the primary absolute flux density calibrators in the radio regime (such as Cas A, Tau A, and Cyg A) [44] feature a few dozen absolute flux density measurements made in the 0.01–30 GHz spectral range and reaching a ~3–5% accuracy. These data should enable placing a bound of $\chi \approx 0.02$, from measurements of the rms of deviations from a canonical source spectrum. If the spectral resolution is sufficiently high to assess the periodicity in the oscillation signal (particularly at the lower end of the spectrum), both the limits on χ and the range of photon mass studied can be improved. Further improvements of the bounds on χ can be achieved by stacking the signal from a number of objects, under the condition that the observations of different objects are sensitive to the same range of the hidden-photon mass.

In this paper, a methodology and prospects for detection of the hidden photon signal in the radio regime are considered. The basic physics of the $\gamma - \gamma_s$ oscillation and the propagation of the hidden-photon signal are described in Sec. II. Methods for the detection of the oscillation signal with different instruments and targets are discussed in Sec. III and potentials of these studies are discussed in Sec. IV.

II. PHOTON OSCILLATIONS IN THE RADIO REGIME

For a photon field, A_μ, and a hidden photon field, B_μ, the kinetic mixing term is given by [17]

$$\mathcal{L}_\chi = \frac{\sin\chi}{2} A_{\mu\nu} B^{\mu\nu} + \frac{\cos^2\chi}{2} m_{\gamma_s}^2 B_\mu B^\mu, \tag{1}$$

where $A_{\mu\nu}$ and $B_{\mu\nu}$ are the respective field-strength tensors. The nonzero kinetic mixing angle χ implies a mismatch between the interaction and propagation eigenstates, which induces oscillation between the two states (with a close analogy to the neutrino oscillation effect [45]). The last term accounts for massive hidden photons via Higgs or Stückelberg mechanisms, where the former case suffers from additional constraints [7]. The probability of the $\gamma \to \gamma_s$ conversion after propagating a distance L in vacuum is then given by

$$P_{\gamma\to\gamma_s}(L) = a_\chi \sin^2\left(\frac{m_{\gamma_s}^2}{4E} L\right) = a_\chi \sin^2\left(\frac{m_{\gamma_s}^2}{8\pi\nu} L\right), \tag{2}$$

where all quantities are expressed in natural units, and E and ν are the energy and frequency of the normal photon [13,17,33]. It should be noted that the validity of Eq. (2) is restricted to the case of $m_{\gamma_s} \ll 2\pi\nu$, which is fulfilled for all considerations in this paper.

The first term of Eq. (2) describes the amplitude of the oscillation, $a_\chi = \sin^2(2\chi) \approx 4\chi^2$ (for $\chi \ll 1$), that can be identified as a periodic signal over a range of distances L or wavelengths $\lambda = 1/\nu$. The second term,

$$\varphi_{\gamma_s}(\nu) = \frac{m_{\gamma_s}^2 L}{8\pi\nu} = 9.45 \left(\frac{m_{\gamma_s}}{10^{-15}\ \mathrm{eV}}\right)^2 \left(\frac{L}{\mathrm{pc}}\right) \left(\frac{\nu}{\mathrm{MHz}}\right)^{-1}, \tag{3}$$

gives the periodic signature of the oscillation. The oscillation signal affects the broadband spectrum, $F(\nu)$, of an astrophysical source, which results in a received spectrum $F_{\gamma_s}(\nu) = F(\nu)(1 - P_{\gamma\to\gamma_s})$.

The resulting spectrum $F_{\gamma_s}(\nu)$ will have local minima and maxima at the frequencies $\nu_{\min,i} = \nu_\star/(2i - 1)$ and $\nu_{\max,i} = \nu_\star/(2i)$, $i \in \mathbb{N}$, where

$$\nu_\star = \frac{m_{\gamma_s}^2 L}{4\pi^2} = 6.02 \left(\frac{m_{\gamma_s}}{10^{-15}\ \mathrm{eV}}\right)^2 \left(\frac{L}{\mathrm{pc}}\right)\ \mathrm{MHz} \tag{4}$$

is the frequency of the first (highest frequency) minimum obtained with $i = 1$. The frequency, $\nu_{\max,1}$, of the first maximum defines the characteristic wavelength,

$$\lambda_\star = \frac{8\pi^2}{m_{\gamma_s}^2 L} = 99.64 \left(\frac{m_{\gamma_s}}{10^{-15}\ \mathrm{eV}}\right)^{-2} \left(\frac{L}{\mathrm{pc}}\right)^{-1}\ \mathrm{m}, \tag{5}$$

of the periodic modulation induced by the hidden-photon signal on a broadband spectrum $F(\lambda)$ in the wavelength domain.

A. Oscillation and coherence lengths

The oscillation length of the hidden-photon signal is set by the condition $\varphi_{\gamma_s}(L, \nu) = \pi$,

$$L_{\mathrm{osc}} = 0.33\left(\frac{\nu}{\mathrm{MHz}}\right)\left(\frac{m_{\gamma_s}}{10^{-15}\ \mathrm{eV}}\right)^{-2}\ \mathrm{pc}. \qquad (6)$$

However, decoherence effects in the photon and hidden-photon mass eigenstates may arise during propagation, owing to the finite mass, m_{γ_s}, of the latter. An accurate quantum mechanical treatment of the oscillation probability $P_{\gamma\to\gamma_s}$ using wave packets [Eq. (2) has been derived assuming plane waves] yields an upper bound on the accessible distance range [33,46,47], $L_{\mathrm{coh}} = 4\sqrt{2}\sigma_x E^2/m_{\gamma_s}^2$, where $\sigma_x^2 = \sigma_{x,\mathrm{P}}^2 + \sigma_{x,\mathrm{D}}^2$ denote the quantum mechanical uncertainties of the production and detection processes, respectively. The nonthermal radio emission of compact radio sources is produced by synchrotron radiation, with the mean energy loss path of synchrotron emitting electrons $\sigma_{x,\mathrm{P}} = \Delta\tau$. Note that the mean energy loss path is of the same order of magnitude as the gyro radius of the relativistic electrons under consideration. A reasonable estimate of the cooling time $\Delta\tau = 2\pi\nu_c/(-\mathrm{d}E/\mathrm{d}t)$ can be obtained at the critical frequency ν_c of synchrotron radiation (averaging over the pitch angle) [48], eventually yielding

$$L_{\mathrm{coh}} = 19.84\left(\frac{\nu}{\mathrm{MHz}}\right)^{2}\left(\frac{m_{\gamma_s}}{10^{-15}\ \mathrm{eV}}\right)^{-2}\left(\frac{B}{\mathrm{mG}}\right)^{-1}\ \mathrm{kpc}, \qquad (7)$$

where B denotes the magnetic field inside the considered source. The $\gamma - \gamma_s$ oscillations can therefore be probed in vacuum at any distance L fulfilling the condition $L_{\mathrm{osc}} \leq L \leq L_{\mathrm{coh}}$.

Together with this condition, Eqs. (6) and (7) imply effective lower and upper bounds on the hidden-photon mass that can be probed with radio data of a compact synchrotron emitting source at distance L_0 and above a given frequency ν_0. Table I lists corresponding bounds considering three distinct types of radio sources, namely nearby Galactic supernova remnants (SNR), distant radio-emitting lobes of active galactic nuclei (AGN), and AGN cores at cosmological distances. It demonstrates that the oscillation length and decoherence effects should enable effective radio measurements for a range of hidden-photon masses between $\sim 10^{-19}$ eV and $\sim 10^{-11}$ eV.

B. Propagation through refractive media

Photon propagation through a medium with refractive index n can be described by introducing an effective photon mass m_γ to the Lagrangian $\mathcal{L}$. This operation affects the kinetic mixing term, and the resulting effective mixing angle χ_{r} depends on the mass ratio $\xi = m_\gamma^2/m_{\gamma_s}^2$ so that [17,18,34]

$$\sin 2\chi_{\mathrm{r}} = \frac{\sin 2\chi}{\sqrt{\sin^2 2\chi + (\cos 2\chi - \xi)^2}}. \qquad (8)$$

For small effective photon masses, $\xi \ll 1$, the $\gamma - \gamma_s$ oscillations approach the vacuum regime, with $\chi_{\mathrm{r}} \to \chi$. A resonance with the maximum amplitude $\chi_{\mathrm{r}} = \pi/4$ of the oscillations is reached at the resonant mass ratio $\xi = \cos 2\chi$. For higher effective photon masses, the oscillations are rapidly damped (medium suppression), with $\chi_{\mathrm{r}} \to \pi/2$ for $\xi \gg 1$. The condition $\sin 2\chi_{\mathrm{r}} \geq \sin 2\chi$ implies that hidden photons with a given m_{γ_s} and χ can be detected in a medium with the effective photon mass $m_\gamma^2 \leq 2m_{\gamma_s}^2\cos 2\chi$, which can be approximated with $m_\gamma \lesssim \sqrt{2}m_{\gamma_s}$ for $\chi \ll 1$.

For photon propagation in the interstellar (ISM) and intergalactic (IGM) medium, the dominant factor is scattering off free electrons and neutral atoms (with the medium described by the electron and proton number densities, n_{e} and n_{p}). In this case, the effective photon mass, $m_\gamma^2 \approx \omega_{\mathrm{P}}^2 - 2\omega^2(n-1)_{\mathrm{medium}}$ [34], depends on the photon frequency ω, the plasma frequency $\omega_{\mathrm{P}}^2 = 4\pi\alpha n_{\mathrm{e}}/m_{\mathrm{e}}$, and the refraction index $(n-1)_{\mathrm{medium}}$ of the medium.

For Galactic objects and extragalactic objects at small redshifts ($z < 1$), the medium can be assumed strongly ionized (with the ionized fraction of hydrogen $X_{\mathrm{e}} = n_{\mathrm{e}}/n_{\mathrm{p}} \to 1$). Contributions from helium and heavier elements can be neglected. This yields [34]

$$\begin{aligned} m_\gamma^2 &\approx \omega_{\mathrm{P}}^2 - 2\omega^2(n-1)_{\mathrm{medium}} \\ &\simeq 1.4\times 10^{-21}\left(\frac{n_{\mathrm{p}}}{\mathrm{cm}^{-3}}\right)\left[X_{\mathrm{e}} - 1.2\times 10^{-19}\right. \\ &\quad \left.\times\left(\frac{\nu}{\mathrm{MHz}}\right)^{2}(1 - X_{\mathrm{e}})\right]\ \mathrm{eV}^2. \qquad (9)\end{aligned}$$

TABLE I. Lower and upper bounds on the mass range of hidden photons, $m_{\gamma_s}^{\ell}$ and $m_{\gamma_s}^{\mathrm{u}}$, respectively, detectable with radio data ($\nu > 1$ GHz) of SNR and AGN. For $m_{\gamma_s} < m_{\gamma_s}^{\ell}$, no $\gamma - \gamma_s$ oscillations will arise; for $m_{\gamma_s} > m_{\gamma_s}^{\mathrm{u}}$, decoherence effects yield a freeze out of the oscillation signal. The columns B and ΔL list the assumed magnetic fields and distance ranges.

Source class	B [mG]	ΔL	$m_{\gamma_s}^{\ell}$ [eV]	$m_{\gamma_s}^{\mathrm{u}}$ [eV]
SNR	0.1	1–10 kpc	2×10^{-16}–6×10^{-16}	4×10^{-12}–1×10^{-11}
AGN: radio lobes	1	0.02–3 Gpc	3×10^{-19}–4×10^{-18}	3×10^{-15}–3×10^{-14}
AGN: nuclear regions	10^3	0.02–3 Gpc	3×10^{-19}–4×10^{-18}	10^{-16}–10^{-15}

For observations in the radio band, $m_\gamma \approx \omega_\mathrm{P} \simeq 3.7\times 10^{-11}(n_\mathrm{e}/\mathrm{cm}^{-3})^{1/2}$ eV provides a good estimate of the effective photon mass under the assumption of $X_e \approx 1$. This limits, formally, the hidden-photon mass that can be probed in Galactic and extragalactic objects to $\sim 10^{-13}$ eV and $\sim 10^{-14}$ eV, respectively (for generic assumptions for the average densities of $\tilde{n}_\mathrm{ISM} \approx 10^{-4}\ \mathrm{cm}^{-3}$ and $\tilde{n}_\mathrm{IGM} \approx 10^{-6}\ \mathrm{cm}^{-3}$ [49]). However, both the ISM and the IGM are inhomogeneous, with variations of the density exceeding two to three orders of magnitude [50,51]. Hence, generation and propagation of the hidden-photon signal depend on the line-of-sight (LOS) properties of the medium and its inhomogeneities.

C. Effects of inhomogeneous media

In an inhomogeneous medium, the minimum value of m_{γ_s} without medium damping is limited by the electron density of underdense regions with $n_\mathrm{e} \ll \tilde{n}_\mathrm{e}$. The traversed underdense region needs to be sufficiently extended to affect the propagation, such that the LOS path length, l_los, in these regions is $l_\mathrm{los} \gg L_\mathrm{osc}$ (for observations in the radio domain at $\nu \gtrsim 100$ MHz, this effectively limits $m_{\gamma_\mathrm{s}} \gtrsim 10^{-16}$ eV for Galactic objects, while permitting probing hidden photons with $m_{\gamma_\mathrm{s}} \gtrsim 10^{-19}$ eV with extragalactic targets, see Table I). Given steep density gradients typically found at the edges of voids [cf. Ref. [52]], one can reasonably assume that propagation through voids would not significantly distort the oscillation pattern. The resulting spectral pattern after propagating through underdense regions remains "frozen" during subsequent propagation through denser regions (where $m_{\gamma_\mathrm{s}} \gtrsim 2.6\times 10^{-11}(n_\mathrm{e}/\mathrm{cm}^{-3})^{1/2}$), as both direct and reverse photon conversions are suppressed there. Therefore, for Galactic objects, the lowest detectable hidden-photon mass would be achieved for photon beams propagating between the Galactic arms, while propagation through cosmic voids would set the lower limit on the hidden-photon mass that can be detected in the broadband spectra of extragalactic targets.

A density of free electrons $n_\mathrm{e,loc} \approx 0.005$–$0.01\ \mathrm{cm}^{-3}$ is measured in the local ISM [53,54], and there is ample evidence for n_e to vary strongly across the Galaxy [53,54], with $n_\mathrm{e} \gtrsim 10\ \mathrm{cm}^{-3}$ near the Galactic center, $n_\mathrm{e} \sim 10^{-2}\ \mathrm{cm}^{-3}$ in the spiral arms, and $n_\mathrm{e} \ll 10^{-4}\ \mathrm{cm}^{-3}$ above the Galactic disk. In mini "void" regions of ~ 1 kpc in extent and located between the spiral arms [54], $n_\mathrm{e} \lesssim 10^{-6}\ \mathrm{cm}^{-3}$ can be found [51], which is similar to the values typically measured in the IGM. Hence, detectability of hidden-photon oscillation in Galactic sources should depend strongly on the LOS to a specific target, with likely $m_{\gamma_\mathrm{s}} \gtrsim 10^{-12}$ eV detectable for LOS not crossing the spiral arms, while $m_{\gamma_\mathrm{s}} \gtrsim 10^{-14}$ eV may still be detectable for objects at high galactic latitudes, and the LOS crossing interarm plasma and the local "voids."

The electron and proton densities in different structural components of the IGM can be estimated from observations, i.e., IRAS data [55] and SDSS data [52], as well as detailed numerical simulations of large-scale structures [50,56,57]. The SDSS data indicates that the voids have a volume filling factor of 0.62 and a median size of $17h^{-1}$ Mpc, and Ref. [50] finds the baryonic matter density, $\Omega_\mathrm{b,void} \approx (0.045 \pm 0.015)\Omega_\mathrm{b}$, where $h = H/(100\ \mathrm{km\,s^{-1}\,Mpc^{-1}})$ is the dimensionless Hubble constant and $\Omega_\mathrm{b} = 0.046 \pm 0.002$ is the average baryon density in the Universe [58]. Table II summarizes the mass fraction, m/m_b, the volume fraction, V/V_c, and the relative density, ρ/ρ_b, of different IGM components (the warm, warm-hot ionized (WHIM), hot, and void components, measured with respect to the total baryon mass m_b, density ρ_b, and the comoving volume V_c). Based on these values, one can estimate the electron density in the individual IGM components,

$$n_\mathrm{e,medium} = X_\mathrm{e}\frac{\rho_\mathrm{c}\Omega_\mathrm{b}}{m_\mathrm{p} + X_\mathrm{e}m_\mathrm{e}}\frac{\rho_\mathrm{medium}}{\rho_\mathrm{b}}, \tag{10}$$

where $\rho_\mathrm{c} = 3H^2/(8\pi G)$ is the critical density of the Universe, m_p and m_e are the proton and electron masses, and G denotes the gravitational constant. This yields $n_\mathrm{e}(\rho_\mathrm{b}) = 2.5\times 10^{-7}\ \mathrm{cm}^{-3}$ and enables calculating n_e and respective limits on m_{γ_s} for different baryonic matter components as listed in Table II (compiled from the results reported in Refs. [50,52,55–57]).

TABLE II. Baryonic matter components and hidden-photon propagation. Each IGM component is described by the temperature T, mass fraction m/m_b, comoving volume fraction V/V_c, local density relative to the average baryon density ρ/ρ_b, estimated average electron density n_e, and resulting minimum detectable hidden-photon mass m_{γ_s} as estimated from the average electron density.

Baryonic component	T [K]	m/m_b	V/V_c	ρ/ρ_b	n_e [cm^{-3}]	m_{γ_s} [eV]
Galaxies	$<10^3$	0.054	0.002	27.0	6.7×10^{-6}	6.7×10^{-14}
Warm IGM	$<10^5$	0.350	0.342	1.02	2.6×10^{-7}	1.3×10^{-14}
WHIM IGM	$<10^6$	0.471	0.030	15.7	3.9×10^{-6}	5.1×10^{-14}
Hot IGM	$>10^6$	0.097	0.006	16.2	4.0×10^{-6}	5.2×10^{-14}
Voids	$\sim 10^6$(?)	0.028	0.620	0.05	1.1×10^{-8}	2.7×10^{-15}

TABLE III. Minimum detectable hidden-photon mass m_{γ_s} in eV, assuming photon propagation through cosmic voids.

Void	Observing frequency		
$2r_{\rm void}$ [Mpc]	30 MHz	100 MHz	1 GHz
10	1.7×10^{-17}	2.3×10^{-17}	4.1×10^{-17}
30	1.3×10^{-17}	1.7×10^{-17}	3.1×10^{-17}
100	9.6×10^{-18}	1.3×10^{-17}	2.3×10^{-17}

In cosmic voids, strong density gradients are observed [[52,59] and references therein], with densities at the void center being at least 2–3 orders of magnitude lower than at the edge of the void. Given the galaxy density as a tracer of the gas density, the density profile of electrons, $n_e(r')$, can be calculated from the average radial density profile obtained from the galaxy counts (see Figs. 4–6 in Ref. [52]), where $r' = r/r_{\rm void}$, with $r_{\rm void}$ denoting the void radius. The profile was normalized to reproduce the void average density reported in Ref. [50], see Table II. For such a profile, the minimum m_{γ_s} can then be calculated by evaluating $n_e(r)$ at $L_{\rm osc}/2$ (to account propagation on both sides from the center of the void). The resulting values are given in Table III for several typical values of the void size and observing frequencies.

This calculation demonstrates that for the assumptions used here, hidden photons with masses as low as $\sim 10^{-17}$ eV can in principle be probed with astrophysical measurements of targets located behind sufficiently large voids. A more detailed account of ISM/IGM inhomogeneities on generation and propagation of the hidden photon signal would rely on extensive numerical simulations of large scale structures, which is beyond the scope of this paper. In the following discussion, the generic m_{γ_s} limits obtained for Galactic ($\gtrsim 10^{-14}$ eV) and extragalactic ($\gtrsim 10^{-17}$ eV) objects will be assumed, while performing calculations for the $m_\gamma \leq \sqrt{2} m_{\gamma_s}$ regime.

It is interesting to note that the signal from hidden photons with a sufficiently low mass, $m_{\gamma_s}^{\rm free}$, should be unaffected by propagation through a high-density structure with a characteristic size l_s, for which $l_s < L_{\rm osc}$. This implies $m_{\gamma_s}^{\rm free} = 2\pi\sqrt{2}(\nu/l_s)^{1/2}$ and yields, at $\nu = 1$ GHz, $m_{\gamma_s}^{\rm free} \approx 1.3 \times 10^{-16}$ eV for propagation through galaxies ($l_s \approx 20$ kpc).

III. DETECTION OF THE OSCILLATION SIGNAL

For measurements in the $m_\gamma \leq \sqrt{2} m_{\gamma_s}$ regime, the two main factors limiting the sensitivity for a hidden-photon signal are the spectral energy distribution of the (typically, multicomponent) astrophysical signal and spectral range covered by the resolution of astronomical instruments. As the hidden-photon signal modulates the astrophysical signal, the latter has to be well understood before attempting to detect the oscillation signal in a broadband spectrum. The astrophysical signal can be modeled with $\mathcal{M}(\nu)$, such that a condition

$$F'_{\gamma_s}(\nu) = F_{\gamma_s}(\nu)/\mathcal{M}(\nu) = C_{\mathcal{M}}(1 - P_{\gamma\to\gamma_s}) + \mathcal{F}_{\rm noise} \quad (11)$$

is achieved (or approached), where $C_{\mathcal{M}}$ is a constant (expecting $C_{\mathcal{M}} \to 1$) and $\mathcal{F}_{\rm noise}$ is the residual fractional noise due to measurement errors and systematic uncertainties of the fit by $\mathcal{M}(\nu)$ (with $|\mathcal{F}_{\rm noise}| \ll C_{\mathcal{M}}$). In the radio regime, measurement errors will be dominated by the system noise and atmospheric/ionospheric fluctuations, while the effect of scattering in interstellar and intergalactic plasma would be orders of magnitude smaller and could be safely neglected. If necessary, the condition $C_{\mathcal{M}} = 1$ can be achieved by normalizing $F'_{\gamma_s}(\nu)$ over the observed frequency range (this measure would increase the noise and potentially introduce a bias, but it may be necessary to facilitate subsequent searches for a periodic signal).

The conversion probability $P_{\gamma\to\gamma_s}$ is periodic in the wavelength domain, which requires that the model description $\mathcal{M}(\nu)$ must not contain harmonic terms within a certain frequency range. This range is determined by several specific factors, including the distance to the object and the specific value of m_{γ_s} to be probed. This range is calculated and discussed below.

In the following, it is assumed that the observational setup for a broadband spectrum measurement can be simplified and characterized by a range $[\nu_1; \nu_2]$ of frequencies probed with a spectral resolution $\Delta\nu$ (implying that the flux density measurements are made at average intervals $\Delta\nu$). In general, $\Delta\nu$ may vary across the frequency range, hence it is used here only in the sense of defining the total number of independent flux density measurements $N_{\rm mes} = (\nu_2 - \nu_1)/\Delta\nu$.

A. Effective ranges of frequency and hidden-photon mass

The sensitivity to detect the imprint of the amplitude a_χ with a significance of n_σ on an observed radio spectrum with a Gaussian noise described by $\sigma_{\rm rms}$ is given by $a_\chi = n_\sigma \sigma_{\rm rms}$ (neglecting for the moment systematic errors resulting from an imperfect model representation, $\mathcal{M}(\nu)$, of the astrophysical signal and systematic uncertainties of the measurement process). The highest radio frequency, ν_h, useful for recovering the oscillation signal can be estimated from $P_{\gamma\to\gamma_s} = \sigma_{\rm rms}$, yielding [for $n_\sigma \geq 1$, using Eq. (2)]

$$\nu_h = \frac{\pi}{2} \frac{\nu_\star}{\arcsin(1/\sqrt{n_\sigma})}, \quad (12)$$

with $\nu_h = \nu_\star$ at $n_\sigma = 1$. At $n_\sigma \geq 2$, $\nu_h \approx (\pi/2) n_\sigma^{1/2} \nu_\star$ gives an estimate of ν_h to within a 10% accuracy.

The lowest frequency, ν_ℓ, containing a usable response from the oscillation is determined by the spectral spacing, $\Delta\nu$. In this case, a conservative estimate of ν_ℓ is provided

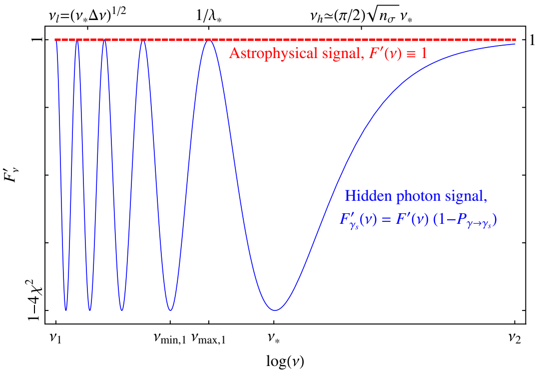

FIG. 1 (color online). Modulation of an ideally modeled astrophysical signal, $F'(\nu)\equiv 1$, by the hidden photon oscillations. Measurements cover the $[\nu_1;\nu_2]$ frequency range and are made with a spectral resolution of $\Delta\nu$. Oscillations occur at a constant wavelength $\lambda_\star$. Detection of the hidden-photon signal can be made if $\nu_1 \le \nu_{\min,2}$ and $\nu_2 \ge \nu_\star$. Effective measurements (using the full sensitivity of the data) can be performed if $\nu_1 \le \nu_\ell$ and $\nu_2 \ge \nu_{\rm h}$. The spectral resolution must be better than $\nu_\star/4$.

by the double of the Nyquist sampling rate, $f_{\rm s}$, of the oscillation signal (this is required to take into account that measurements are made at a fixed set of frequencies and hence no "phase tuning" is feasible). The requirement corresponds to $\varphi_{\gamma_{\rm s}}(L,\nu_\ell-\Delta\nu/2)-\varphi_{\gamma_{\rm s}}(L,\nu_\ell+\Delta\nu/2)=\pi/2$ and yields $\nu_\ell=\sqrt{\nu_\star\Delta\nu+(\Delta\nu/2)^2}\approx\sqrt{\nu_\star\Delta\nu}$.

Generic properties of a possible measurement are illustrated in Fig. 1, showing a modulation of an astrophysical signal in the observed frequency range $[\nu_1;\nu_2]$, together with the limiting frequencies ν_ℓ and $\nu_{\rm h}$.

The characteristic frequencies translate into an accessible mass range extending from $m^\ell_{\gamma_{\rm s}}$ to $m^u_{\gamma_{\rm s}}$. The lower limit on the detectable hidden-photon mass $m^\ell_{\gamma_{\rm s}}$ is determined by $L=L_{\rm osc}(\nu_1)$ (see Sec. II A), corresponding to ν_1 set to the frequency of the first local maximum $\nu_{\max,1}$. This yields

$$m^\ell_{\gamma_{\rm s}} = 2\sqrt{2}\pi\left(\frac{\nu_1}{L}\right)^{1/2}$$
$$= 5.77\times10^{-16}\left(\frac{\nu_1}{\rm MHz}\right)^{1/2}\left(\frac{L}{\rm pc}\right)^{-1/2}\ {\rm eV}. \tag{13}$$

The largest accessible hidden-photon mass $m^{\rm u}_{\gamma_{\rm s}}$ is obtained by requiring $\nu_\ell=\nu_2$, which gives

$$m^{\rm u}_{\gamma_{\rm s}} = \frac{2\pi\nu_2}{(L\Delta\nu)^{1/2}} = \frac{1}{\sqrt{2}}\frac{\nu_2}{\nu_1}\left(\frac{\Delta\nu}{\nu_1}\right)^{-1/2} m^\ell_{\gamma_{\rm s}}. \tag{14}$$

These limits are analyzed and presented in Fig. 2 for several existing and planned radioastronomical facilities, and for different types of astrophysical targets. In real experiments, the accessible mass ranges may be further limited by coherence effects and medium propagation as discussed in Secs. II A and III. This is illustrated in Fig. 2

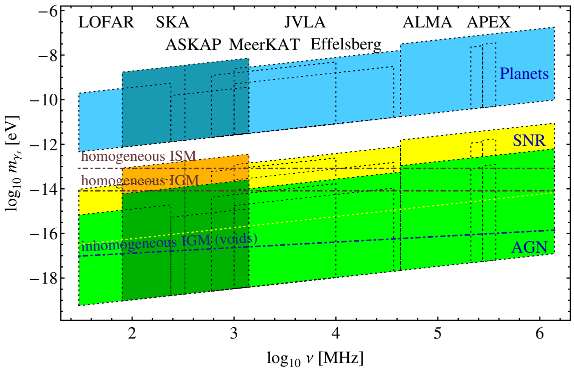

FIG. 2 (color online). Ranges of hidden-photon mass, $m_{\gamma_{\rm s}}$, that can be probed with various radio astronomical instruments at different observing frequencies. The mass ranges are calculated for measurements done with planets (blue shades; top), supernovae remnants (yellow shades; middle) and active galactic nuclei (green shades; bottom). For each individual color, darker shades mark the mass ranges accessible to measurements with the first and second phases of Square Kilometer Array (SKA). The calculations are made assuming typical instrumental setups and generic ranges of distances to planets (0.5–10 au), supernova remnants (1–10 kpc) and active galaxies (0.02–3 Gpc). Brown dot-dashed lines mark the lower limits on detectable mass imposed by homogeneous ISM and IGM suppression. The dashed blue line illustrates the lower limit on detectable mass arising from propagation through an inhomgeneous IGM containing large-scale voids (for the assumed void diameter of 100 Mpc).

by comparing the accessible ranges of hidden-photon masses to the limits imposed by the homogeneous ISM and IGM suppression. The impact of the medium suppression can be alleviated at lower photon masses by free propagation through a homogeneous medium (also illustrated in Fig. 2), in addition to the favorable conditions that may exist for propagation through an inhomogeneous medium.

The sensitivity to χ varies within the mass ranges described by Eqs. (13) and (14). The lowest hidden-photon mass $m^{\ell,\rm full}_{\gamma_{\rm s}}$ for which a set of measurements made in the $[\nu_1;\nu_2]$ frequency range is fully sensitive to χ is set by the condition $\nu_\ell=\nu_1$, which corresponds to

$$m^{\ell,\rm full}_{\gamma_{\rm s}} = \frac{2\pi\nu_1}{(L\Delta\nu)^{1/2}} = \frac{1}{\sqrt{2}}\left(\frac{\Delta\nu}{\nu_1}\right)^{-1/2} m^\ell_{\gamma_{\rm s}}. \tag{15}$$

The largest mass that can be detected at the full sensitivity is then given by the condition $\nu_{\rm h}=\nu_2$, resulting in

$$m^{\rm u,full}_{\gamma_{\rm s}} = 2\sqrt{2\pi}\left[\frac{\nu_2}{L}\arcsin\left(\frac{1}{\sqrt{n_\sigma}}\right)\right]^{1/2}, \tag{16}$$

with $m^{\rm u,full}_{\gamma_{\rm s}}=2\pi(\nu_2/L)^{1/2}$ for $n_\sigma=1$ and $m^{\rm u,full}_{\gamma_{\rm s}}\approx 2\sqrt{2}\pi(\nu_2/L)^{1/2}n_\sigma^{-1/4}$ for $n_\sigma\ge 2$. With this approximation, $m^{\rm u,full}_{\gamma_{\rm s}}$ can be expressed through $m^\ell_{\gamma_{\rm s}}$

$$m_{\gamma_s}^{\mathrm{u,full}} \approx \frac{1}{\sqrt{\pi} n_\sigma^{1/4}} \left(\frac{\nu_2}{\nu_1}\right)^{1/2} m_{\gamma_s}^{\ell}. \tag{17}$$

The mass limits described by Eqs. (13)–(16) can be used to estimate the frequency dependence (or, conversely, the hidden-photon mass dependence) of the sensitivity provided by a given set of measurements for detecting the hidden-photon signal.

Equations (15) and (16), in particular, can be used for experiment optimization by requiring that $m_{\gamma_s}^{\mathrm{u,full}} > m_{\gamma_s}^{\ell,\mathrm{full}}$, which corresponds to the inequality

$$\sqrt{\frac{2}{\pi}} \frac{1}{n_\sigma^{1/4}} \left(\frac{\nu_2}{\nu_1}\right)^{1/2} \left(\frac{\Delta\nu}{\nu_1}\right)^{1/2} > 1$$

and connects the main parameters of the observational setup. For the goal of extending hidden photon studies to progressively lower hidden-photon masses, the most efficient strategy would therefore be to reduce ν_1. Improving the frequency spacing can result in producing a progressively larger number of data points that could not be used for probing higher hidden-photon masses. Hence, the overall range of full sensitivity of a given experimental setup would be reduced in this case.

B. Sensitivity for the mixing angle χ

The amplitude term a_χ of $P_{\gamma\to\gamma_s}$ implies that an n_σ bound on $\chi \approx \sqrt{n_\sigma \sigma_{\mathrm{rms}}}/2$ can be obtained from multifrequency flux density measurements. For N individual flux density measurements with fractional errors σ_i, $\sigma_{\mathrm{rms}} = (\sum_{i=1}^{N} \sigma_i^2)^{1/2}/N \approx \sigma/N^{1/2}$ (if $\sigma_i \approx \sigma$ for all $i = 1, \ldots, N$). One can assume, as an example, that the astrophysical signal from a target object can be described by a simple power-law spectrum $F(\nu) = F_{\mathrm{r}}(\nu/\nu_{\mathrm{r}})^\alpha$ and that the frequency dependence of the errors on flux density measurements changes can also be described by a power-law dependence $\sigma(\nu) = \sigma_{\mathrm{r}}(\nu/\nu_{\mathrm{r}})^\beta$ (here, F_{r} and σ_{r} refer to a flux density and its associated error, measured at a reference frequency ν_{r} chosen inside the relevant frequency range).

With these assumptions, measurements over the entire relevant frequency range $[\nu_{\ell'}; \nu_{\mathrm{h'}}]$ can be described by a characteristic signal-to-noise ratio,

$$\hat{S} = \frac{1}{\nu_{\mathrm{h'}} - \nu_{\ell'}} \int_{\nu_{\ell'}}^{\nu_{\mathrm{h'}}} \frac{F(\nu)}{\sigma(\nu)} \mathrm{d}\nu = \frac{F_{\mathrm{r}}}{\sigma_{\mathrm{r}} \nu_{\mathrm{r}}^{\xi}} \frac{\nu_{\mathrm{h'}}^{\xi+1} - \nu_{\ell'}^{\xi+1}}{(\xi + 1)(\nu_{\mathrm{h'}} - \nu_{\ell'})}, \tag{18}$$

where $\xi = \alpha - \beta$ and the integration limits are given by $\nu_{\ell'} = \max(\nu_1, \nu_\ell)$ and $\nu_{\mathrm{h'}} = \min(\nu_2, \nu_{\mathrm{h}})$. At a frequency spacing $\Delta\nu$, the number of measurements contributing to the detection is $N_{\mathrm{mes}} = (\nu_{\mathrm{h'}} - \nu_{\ell'})/\Delta\nu$, hence the effective cumulative signal-to-noise ratio of the data set is $\tilde{S} = N_{\mathrm{mes}}^{1/2} \hat{S}$. Recalling that, after accounting for the astrophysical signal, $\tilde{S} \approx 1/\sigma_{\mathrm{rms}}$ gives an estimate of the lowest achievable bound on the hidden-photon coupling

$$\chi_{\mathrm{low}} = \left(\frac{\sigma_{\mathrm{r}} \nu_{\mathrm{r}}^{\xi}}{4F_{\mathrm{r}}} \frac{(\xi + 1)(\nu_{\mathrm{h'}} - \nu_{\ell'})^{1/2} (\Delta\nu)^{1/2}}{\nu_{\mathrm{h'}}^{\xi+1} - \nu_{\ell'}^{\xi+1}}\right)^{1/2}. \tag{19}$$

The bound χ_{low} remains constant for hidden-photon masses $m_{\gamma_s}^{\ell,\mathrm{full}} \le m_{\gamma_s} \le m_{\gamma_s}^{\mathrm{u,full}}$ and decreases rapidly outside this mass range as a progressively larger fraction of the measured data points are rendered outside the useful ranges of frequencies.

Figure 3(a) presents limits χ_{low} calculated for several existing and planned radio astronomical facilities and for measurements made with Mars (with $F_{\mathrm{r}} = 30$ Jy and

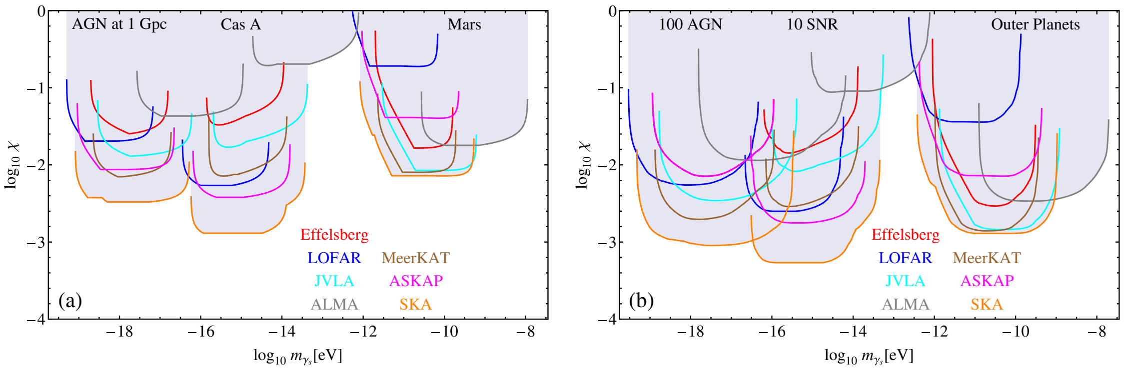

FIG. 3 (color online). Expected limits on χ that can be obtained with different radio astronomical facilities and different astrophysical objects under the assumption that the measurements are not affected by the plasma propagation effects (vacuum oscillations). The limits are calculated assuming generic instrumental parameters, (a) single-target sources at distances of 1 Gpc, 3.4 kpc [75], and 2 au for the AGN, Cas A, and Mars, respectively, and (b) stacked data limits obtained from simulated populations of 100 AGN ($L = 0.02$–3 Gpc, $F = 1$–30 Jy), 10 SNR ($L = 1$–10 kpc, $F = 10$–100 Jy), and 100 measurements made for the outer planets ($L = 0.5$–10 au, $F = 10$–200 Jy), with $\gamma = -2$ used for all three populations.

$\alpha = 0.7$ at $\nu_{\rm r} = 86$ GHz; see Ref. [60]), the supernova remnant Cassiopeia A ($F_{\rm r} = 3000$ Jy, $\sigma_{\rm rms} = 100$ Jy, $\nu_{\rm r} = 1$ GHz, $\alpha = -0.8$; see Ref. [61]), and a fiducial compact AGN ($F_{\rm r} = 10$ Jy, $\alpha = -0.1$, $\nu_{\rm r} = 5$ GHz) at a distance of 1 Gpc. These limits are obtained for the vacuum oscillation regime, without taking into account the potential medium suppression at lower hidden photon masses. For each of the instruments included in the plot, conservative assumptions for generic technical parameters (summarized in Appendix B) have been made, hence the actual limits could be further improved by optimizing observations with a given telescope, for instance by increasing the spectral resolution of the measurements or applying accurate in-band (bandpass) calibration [62]. The figure clearly reflects the effect of improvements of $\sigma_{\rm rms}$ (factor of ~ 10) and $\Delta\nu/\nu$ (factor of ~ 100) that will be provided by the JVLA and SKA precursors, as well as the extension (factor of ~ 10) to lower frequencies provided by LOFAR.

C. Source stacking

Since the frequency behavior of the hidden-photon signal is determined solely by the hidden-photon mass and the distance to the target object, signals from any number of objects with known distances can be stacked together to improve the resulting bound on the coupling constant. For the stacking, a suitable reference distance L' can be chosen, yielding for each object located at a distance L a modification of observed frequency $\nu' = \nu(L'/L)$.

If all of the stacked sources have the same spectra and distances, stacking of $N_{\rm obj}$ objects will lead to a $N_{\rm obj}^{1/4}$ improvement of $\chi_{\rm low}$. Let the stacked objects be drawn from a population with a uniform spatial density over distances $[L_{\rm min}; L_{\rm max}]$, similar spectral indices, and an observed source count, $N(F) = n(F_{\rm r})(F/F_{\rm r})^{\gamma}$ over a range of flux densities $[F_{\rm min}; F_{\rm max}]$.

In this case, stacking of $N_{\rm obj}$ spectra (each obtained with the same observational apparatus as described above) would yield a bound,

$$\chi_{\rm stack} = \chi_{\rm low} N(\hat{F})^{-1/4}, \qquad (20)$$

where $\hat{F}$ is estimated at a frequency $\hat{\nu}$ at which the signal-to-noise ratio $\hat{S}$ is achieved. Calculation of $\hat{S}$ may now involve different integration limits, as the frequencies ν_ℓ and $\nu_{\rm h}$ must be calculated for a characteristic distance $\hat{L}$. This distance is given by $[(L_{\rm max}^2 + L_{\rm min}^2)/2]^{1/2}$ for planets and Galactic objects and by $[(L_{\rm max}^3 + L_{\rm min}^3)/2]^{1/3}$ for extragalactic objects.

For the source and observation properties specified by $F(\nu)$ and $\sigma(\nu)$ (see Sec. III B), $\hat{\nu} = \nu_{\rm r}(\hat{S}\sigma_{\rm r}/F_{\rm r})^{1/\xi}$, giving $\hat{F} = F_{\rm r}^{1-\alpha/\xi}(\hat{S}\sigma_{\rm r})^{\alpha/\xi}$. Consequently, $N(\hat{F}) = n(F_{\rm r}) \times (\hat{F}/F_{\rm r})^{\gamma}$, where $n(F_{\rm r}) = N_{\rm obj} F_{\rm r}^{\gamma}(1+\gamma)(F_{\rm max}^{1+\gamma} - F_{\rm min}^{1+\gamma})^{-1}$.

Potential improvements of source stacking are illustrated in Fig. 3(b), which shows the limits on χ that can be achieved by stacking together measurements made for 100 AGN, 10 SNR, and 100 measurements obtained for different outer planets of the Solar System. Improvements in both χ and the range of accessible hidden-photon mass are visible, compared to the single object limits in Fig 3(a). The predictions for best cumulative limits from radio measurements in the entire 30 MHz to 1400 GHz range are compared in Fig. 4 to the bounds derived from other experiments and observations. Figure 4 demonstrates that radio measurements would be unique for detecting hidden

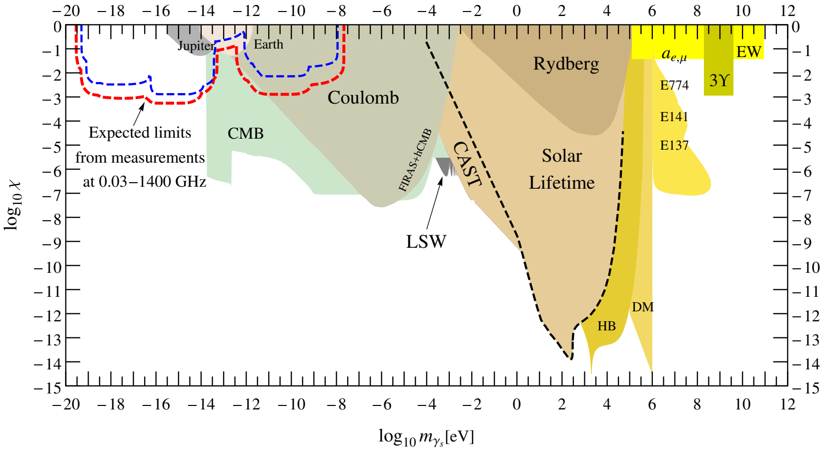

FIG. 4 (color online). Compound limits on χ expected to be achievable from observations at 0.03–1400 GHz compared with the limits obtained presently with other facilities and experiments [Ref. [8] and references therein]. The limits from single object (blue; thin dashed) and multiple object stacking (red; thick dashed) are shown. Radio observations (particularly at frequencies below 40 GHz) will provide a unique probe for the hidden photon with masses below 10^{-14} eV and extending down to $\sim 10^{-17}$ eV, where the measurements are likely to be limited by the medium suppression of the hidden-photon signal in the IGM plasma as described in Secs. II B and II C.

photons with $m_{\gamma_s} \lesssim 3 \times 10^{-16}$ eV and would substantially improve the existing limits for hidden photon masses below 2×10^{-14} eV which is the lowest mass for which the resonant conversion can be assessed from the FIRAS CMB measurements [34]. The limits based on the FIRAS data can in principle be extended to photon masses as low as $\approx 7 \times 10^{-17}$ eV, if nonresonant conversion is considered. However, even in this case, the radio measurements would provide stronger constrains on χ for $m_{\gamma_s} \lesssim 10^{-15}$ eV.

The potential effect of propagation through refractive media on the hidden-photon limits is illustrated in Fig. 5 for three different cases describing the minimum values of the plasma density, $n_{\mathrm{e,min}}(l)$, as a function of distance, l, along the propagation path. The three scenarios for $n_{\mathrm{e,min}}(l)$ are adopted here solely to assess the potential range of possible outcomes of the propagation of the hidden-photon signal through refractive media.

In all three scenarios, $n_{\mathrm{e,min}}(1\ \mathrm{kpc}) = 10^{-5}\ \mathrm{cm}^{-3}$ is adopted, implying effectively that the LOS paths for Galactic objects cross at least one of the Galactic "mini void" regions. The worst case scenario assumes that the photon signal from extragalactic objects propagates mostly through Galactic ISM, i.e., not crossing large patches of IGM. In this case, $n_{\mathrm{e,min}}$ decreases from $10^{-5}\ \mathrm{cm}^{-3}$ at $l = 1$ kpc to $10^{-7}\ \mathrm{cm}^{-3}$ at $l = 3$ Gpc, implying that for more distant objects, the LOS path has a progressively larger probability to cross lower density IGM regions. The average case corresponds to propagation through typical IGM resulting in a $n_{\mathrm{e,min}} \sim 10^{-5}$–$10^{-8}\ \mathrm{cm}^{-3}$ range of densities. The best case allows for propagation through cosmic voids, with the corresponding $n_{\mathrm{e,min}} \sim 10^{-5}$–$10^{-10}\ \mathrm{cm}^{-3}$. For the planets, the densities of 50, 30, and 10 cm^{-3} (measured at 1 au and scaling as $\propto (l/1\ \mathrm{au})^{-2}$) have been adopted for the respective scenarios, based on measurements from Ref. [63].

The effects of resonant enhancement and medium suppression are clearly visible in the modified limits shown in Fig. 5. Assuming that the best case scenarios would apply for the majority of the lines of sight (since it is likely that a photon beam from a distant galaxy crosses one or more rarefied IGM or void regions), it is reasonable to conclude that the medium suppression would reduce the detectable χ to ≥ 0.01 only for estimates made for $m_{\gamma_s} \lesssim 10^{-17}$ eV. Above this mass, the propagation effects should not pose severe problems for constraining χ (and they indeed may even play a constructive role at least for some fraction of the photon mass range).

D. Detection of periodic modulations

The modulations induced by the hidden-photon signal on the broadband spectrum of an astrophysical object can be best detected in the wavelength domain, where the modulation is sinusoidal, with the period given by $\lambda_\star$. A fast Fourier transform (FFT) can be applied for searches in the data with dense and uniform coverage of wavelength space. For sparsely sampled data, epoch folding [64] or generic uniformity tests such as the Rayleigh test [65] or Z_m^2 test [66] can be applied.

These searches employ Eq. (11) with the $C_{\mathcal{M}} = 1$ normalization of the residual flux density, which yields a functional form,

$$f_\lambda = f_\star[1 + a_\star \sin(\omega_\star \lambda + \phi_0)], \tag{21}$$

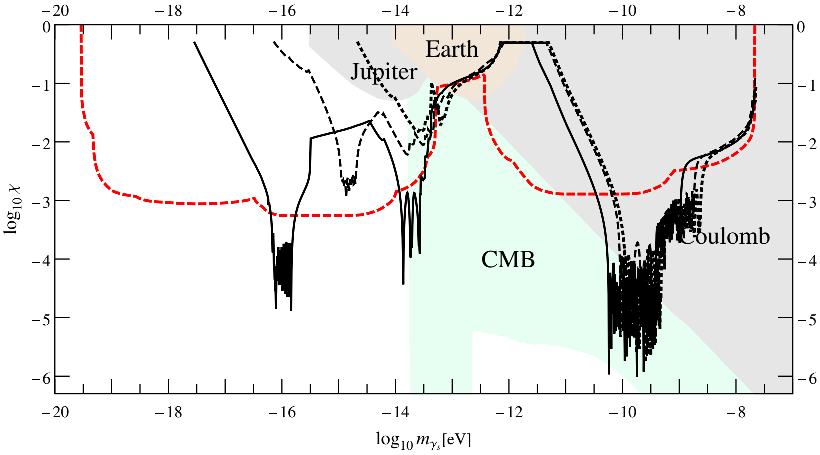

FIG. 5 (color online). Modifications of the combined limits on χ due to propagation through refractive media. The dashed red line shows the limits predicted for object stacking observations under the vacuum condition (the same as the dashed red line in Fig. 4). The best (solid black), average (dashed black), and worst (dotted black) propagation scenarios illustrate potential effects of the ISM and IGM plasma for constraining the hidden-photon signal. For the best-case scenario, the effect of resonant enhancement is visible. The medium suppression affects strongly the limits on χ for hidden-photon masses below $\sim 10^{-17}$ eV.

of the periodic signal to be searched for. Assuming that the residual errors after the normalization are $\delta_\lambda = \sigma_{\rm rms}/C_{\mathcal{M}}$, the parameters of the functional form are related to the properties of the hidden-photon signal as follows: $f_\star = 1 - a_\chi/2 + \delta_\lambda$, $a_\star = a_\chi/(2f_\star)$, $\omega_\star = \pi\nu_\star$, $\phi_0 = \pi/2$. Appendix A provides specific details of application of three different methods (FFT, epoch folding, and generic uniformity tests) to searches for periodic signals due to hidden photon oscillations.

IV. DISCUSSION

The analysis described above demonstrates principal feasibility of searching for a hidden-photon signal in broadband radio spectra of cosmic radio sources, with Galactic supernova remnants and radio-loud AGN presenting the best opportunity for extending the measurements below the hidden-photon mass of 10^{-14} eV, where essentially no measurements have been previously made.

The mass ranges and kinetic mixing limits accessible for these potential searches are determined by several factors, including the oscillation and coherence lengths of the hidden-photon signal, the instrumental bandwidth and resolution, as well as the plasma density changes along the line-of-sight path to the source of the photons. The combined effect of the signal coherence and oscillation length is expected to limit the searches to hidden-photon masses $\gtrsim 10^{-19}$ eV, while the limits imposed by the propagation through the cosmic plasma may increase this limit up to $\sim 10^{-17}$ eV.

Bandwidth and spectral resolution of the existing and planned radio astronomical facilities can support searches for hidden photons with masses well below 10^{-20} eV. The limiting instrumental aspect is the accuracy of amplitude calibration of radio receiver, which may limit plausible constraints on kinetic mixing to $\chi \approx 10^{-3}$. This problem may be alleviated by the advent of ultra broadband receivers supporting in-band measurements across bandwidths in excess of 1 GHz. For this type of measurements, accurate bandpass calibration could deliver in-band amplitude accuracy of $\geq 0.01\%$, thus potentially further lovering the limits on the kinetic mixing by at least an order of magnitude.

For hidden-photon searches based on such in-band measurements, a combination of targets located at significantly different distances can be employed, profiting from the distance scaling of the hidden-photon signal. This ensures that any oscillatory pattern associated with a specific photon mass will be detectable only in one of the two measurements. This is realized for two objects at a distance ratio of $L_2/L_1 (L_2 > L_1) \geq (\pi^2/4)(n_\sigma/\delta_\nu)$, where δ_ν is the fractional spectral resolution of the measurements. With such arrangements, the upper limit for an amplitude of a periodic oscillation in the bandpass obtained by dividing one of the two measured signals by the other would enable constraining χ for the ranges of photon mass probed with either of the two targets.

The effect of propagation on the sensitivity introduces a dependence on the assumed electron density $n_{\rm e}$ of the intervening medium and therefore on the line of sight. For Galactic sources, estimates of $n_{\rm e}$ at a specific line of sight can be obtained from pulsar dispersion measurements [53,54]. Optical hydrogen absorption lines can be used for assessing the line-of-sight structure of the IGM [67], which can be applied for measurements in individual extragalactic targets. The situation may improve substantially after the large-scale HI surveys planned at the LOFAR, MeerKAT, ASKAP, and the SKA [68–71] would deliver a very detailed picture of the IGM up to very high redshifts.

In the absence of information about the plasma properties on individual lines of sight, a potential remedy for the object stacking would be to make generic assumptions on the minimum plasma density as a function of distances to individual targets (similarly to the approach employed in Sec. III C). Despite being inherently imprecise, this approach should still enable improving the constraints obtained on χ from object stacking.

Data from the next generation of large-scale continuum and spectral line surveys at radio wavelengths will provide sufficiently accurate information about the broadband continuum, line-of-sight distribution of the IGM, and distances to many thousands of extragalactic radio sources. This will make object stacking the tool of choice for the hidden-photon searches in the radio regime and will certainly lead to strong improvements of the limits obtained from radio data on the kinetic mixing of hidden photons in the 10^{-14}–10^{-17} eV mass range.

ACKNOWLEDGMENTS

We kindly acknowledge helpful discussions with Alessandro Mirizzi, Andreas Ringwald, and Günter Sigl. We thank the referee for useful suggestions for improving the manuscript. A. P. L. acknowledges support from the Collaborative Research Center (Sonderforschungsbereich) SFB 676 "Particles, Strings, and the Early Universe," funded by the German Research Society (Deutsche Forschungsgemeinschaft, DFG).

APPENDIX A: ANALYSIS TECHNIQUES FOR PERIODIC SIGNALS

1. FFT searches

An FFT search can be employed effectively for recovering the hidden-photon signal, if measurements are made in a frequency range $[\nu_1; \nu_2]$, corresponding to a wavelength range $\Lambda = \lambda_1 - \lambda_2$. The measurements are assumed to be sampled densely enough to be binned into $n_{\rm b} = 2^m$ bins, with each bin described by the bin flux density f_i and its associated error δ_i. This situation can be realized, for instance, for observations with high spectral resolution (e.g., with LOFAR, JVLA, or ALMA) applied to search for hidden photons with $m_{\gamma_s} > 2\pi\sqrt{\nu_2/L}$, for which $\nu_\star > \nu_2$. The resulting $2m - 1$ Fourier coefficients are given by

$$|a_i|^2 = \sum_{j=1}^{n_b} f_j \exp(i\omega_i \lambda_j), \tag{A1}$$

where $\lambda_j = (j - 1/2)\Lambda/n_b$ is the arithmetic mean wavelength of the j^{th} bin and f_j is the respective bin-averaged flux density. The corresponding power spectrum w_i is given by

$$w_i = 2|a_i|^2/F_{\mathrm{tot}}, \tag{A2}$$

where $F_{\mathrm{tot}} = \sum_{j=1}^{n_b} f_j$ is the total flux density in the bins. The average power spectrum contribution from the measurement noise is accounted for by the term

$$\tilde{\delta} = \frac{1}{n_b}\sum_{i=1}^{n_b}\delta_i^2. \tag{A3}$$

Adding the noise contribution and taking into account frequency dependence of $|a_i|^2$ [64], the average power in the ith bin can be written as

$$\langle w_i \rangle = \frac{\xi_\omega F_{\mathrm{tot}}}{2}\left(\frac{a_\star \sin\varphi_i}{\varphi_i}\right)^2 + \tilde{\delta}, \tag{A4}$$

where $\varphi_i = \pi i/(2n_b)$ and $\xi_\omega = 0.773$ [64] is a correction factor taking into account the finite bin width. Reaching, in a given bin, a desired confidence level, c (in percent), of detection of the oscillations, implies $\langle w_i \rangle \geq w_0$, where w_0 is derived from the χ^2 probability distribution, $p_2(\chi^2)$, with two degrees of freedom, requiring that

$$1 - c/100 = (\Lambda/\lambda_\star)\int_{w_0}^{\infty} p_2(\chi^2)\mathrm{d}\chi^2. \tag{A5}$$

If a signal is detected, the amplitude $a_\star$ (and consequently, the kinetic mixing parameter a_χ) can be obtained by requiring that

$$c/100 = \int_{w_a}^{\infty} p_2(\chi^2)\mathrm{d}\chi^2, \tag{A6}$$

with $w_a = w_0 - \langle w_i \rangle + \tilde{\delta}/2$.

2. Epoch folding

If the data are not homogeneously sampled across the measured wavelength domain Λ but still can be divided into phase bins of size $\leq \Delta\nu/\nu_2$ (thus giving $n_\phi \geq 2\nu_2(\nu_2 - \nu_1)/(\nu_1\Delta\nu)$ phase bins), epoch folding [cf. Refs. [64,72]] can be effectively performed in order to search for all hidden-photon masses in the $[m_{\gamma_s}^{\ell}; m_{\gamma_s}^{\mathrm{u}}]$ range. After epoch folding with a given trial wavelength λ', each bin is characterized by the bin flux density f_i and its associated error δ_i. The significance of the signal can be assessed using the statistics $s = \sum_{i=1}^{n_\phi - 1}(f_i - \tilde{f})^2/\delta_i^2$, where $\tilde{f} = F_{\mathrm{tot}}/n_\phi$. For the same assumptions as used above for the FFT searches, the mean value of the statistics is given by

$$\langle s \rangle = \frac{\xi_\phi F_{\mathrm{tot}}}{2}\left(\frac{a_\star \sin\varphi}{\varphi}\right)^2 + \frac{\tilde{\delta}}{2}, \tag{A7}$$

with $\varphi = \pi/n_\phi$ and $\xi_\phi = 0.935$ [64]. The sensitivity to oscillations is established at a confidence level c by requiring $\langle s \rangle \geq s_0$ where s_0 is obtained from the condition

$$1 - c/100 = (\Lambda/\lambda')\int_{s_0}^{\infty} p_{n_\phi - 1}(\chi^2)\mathrm{d}\chi^2. \tag{A8}$$

Similarly, the amplitude of the detected signal can be estimated from

$$c/100 = \int_{s_a}^{\infty} p_{n_\phi - 1}(\chi^2)\mathrm{d}\chi^2, \tag{A9}$$

where $s_a = s_0 - \langle s \rangle + \tilde{\delta}/2$.

3. Generic uniformity tests

For poorly and unevenly sampled data, generic uniformity tests such as the Rayleigh test [65,72,73], the Z_m^2 test [66] or the H-test [74] can be applied, relieving also the requirement to bin the data before searching for a periodic signal.

Similar to the case of epoch folding, the data consisting of n flux density measurements have to be first normalized by a factor of $f_{\mathrm{min}} = \min(f_i)$ and folded with a trial wavelength λ', yielding a set of amplitudes $f_i' = f_i/f_{\mathrm{min}}$ and phases ϕ_i, with $i = 1, \ldots, n$. Calculation of the respective trigonometric moments is done using the terms $f_i' \cos\phi_i$ and $f_i' \sin\phi_i$, so that the resulting Rayleigh power becomes

$$nR^2 = \frac{1}{n}\left[\left(\sum_{i=1}^{n} f_i' \cos\phi_i\right)^2 + \left(\sum_{i=1}^{n} f_i' \sin\phi_i\right)^2\right]. \tag{A10}$$

Similar modification should be done to the trigonometric moments entering the Z_m^2 statistics,

$$Z_m^2 = \frac{2}{n}\sum_{j=1}^{m}\left\{\left[\sum_{i=1}^{n} f_i' \cos(j\phi_i)\right]^2 + \left[\sum_{i=1}^{n} f_i' \sin(j\phi_i)\right]^2\right\}. \tag{A11}$$

The resulting calculated powers $2nR^2$ and Z_m^2 should be tested against χ^2 distributions $p_2(\chi^2)$ and $p_{2m}(\chi^2)$, respectively. Adopting the same approach as for the epoch folding, these values will yield confidence limits for detecting a periodic signal with the wavelength λ'.

APPENDIX B: BASIC TECHNICAL CHARACTERISTICS OF SIMULATED RADIO OBSERVATIONS

Table IV describes general technical parameters adopted for simulating observations with the radio telescopes used for the predictions of the hidden-photon mass ranges and the limits on χ from measurements in the radio regime at frequencies of 0.03–1400 GHz. The parameters presented in the table are the lowest, ν_1, and highest, ν_2, observing frequencies; the number of measurements, $N_{\rm ch}$, available within the observing range; the rms noise, $\sigma_{\rm r}$, of a single measurement at the reference frequency $\nu_{\rm r}$; and the power index, β, describing the frequency dependence of the rms noise. The parameter values given in Table IV provide only basic benchmark description of technical capabilities of the individual telescopes. Conservative estimates have been adopted for the number of spectral channels and the rms noise (assuming typical "shallow" survey observations), and these values can be improved by one or more orders of magnitude by employing full correlator capabilities and dedicated targeted observations.

TABLE IV. Generic technical parameters of radio telescopes used in the calculations of sensitivity for χ in the radio regime.

Telescope	ν_1 [GHz]	ν_2 [GHz]	$N_{\rm ch}$	$\sigma_{\rm r}$ [Jy]	β
LOFAR	0.03	0.24	1000	0.3	-0.25
SKA$_1$	0.08	0.33	5000	0.04	-0.1
ASKAP	0.1	1.4	2000	0.1	-0.25
SKA$_2$	0.3	3.0	5000	0.04	0.1
MeerKAT	0.6	10	200	0.03	0.25
Effelsberg	0.3	37	40	0.1	0.25
JVLA	0.3	43	500	0.1	0.25
APEX	170	410	4000	10	0.25
ALMA	86	1389	5000	1	0.25

---

[1] G. Jungman, M. Kamionkowski, and K. Griest, Phys. Rep. **267**, 195 (1996).
[2] G. Bertone, D. Hooper, and J. Silk, Phys. Rep. **405**, 279 (2005).
[3] G. Bertone, Nature (London) **468**, 389 (2010).
[4] L. B. Okun, Sov. Phys. JETP **56**, 502 (1982).
[5] H. Georgi, P. Ginsparg, and S. L. Glashow, Nature (London) **306**, 765 (1983).
[6] L. Bergström, Rep. Prog. Phys. **63**, 793 (2000).
[7] M. Ahlers, J. Jaeckel, J. Redondo, and A. Ringwald, Phys. Rev. D **78**, 075005 (2008).
[8] J. Jaeckel and A. Ringwald, Annu. Rev. Nucl. Part. Sci. **60**, 405 (2010).
[9] A. Ringwald, Phys. Dark Univ. **1**, 116 (2012).
[10] J. Jaeckel, E. Massó, J. Redondo, A. Ringwald, and F. Takahashi, Phys. Rev. D **75**, 013004 (2007).
[11] G. Raffelt and L. Stodolsky, Phys. Rev. D **37**, 1237 (1988).
[12] E. Zavattini, G. Zavattini, G. Ruoso, E. Polacco, E. Milotti, M. Karuza, U. Gastaldi, G. di Domenico, F. Della Valle, R. Cimino, S. Carusotto, G. Cantatore, and M. Bregant, Phys. Rev. Lett. **96**, 110406 (2006).
[13] M. Ahlers, H. Gies, J. Jaeckel, J. Redondo, and A. Ringwald, Phys. Rev. D **76**, 115005 (2007).
[14] J. Redondo and M. Postma, J. Cosmol. Astropart. Phys. 2 (2009) 005.
[15] P. Arias, D. Cadamuro, M. Goodsell, J. Jaeckel, J. Redondo, and A. Ringwald, J. Cosmol. Astropart. Phys. 6 (2012) 013.
[16] B. Holdom, Phys. Lett. **B166**, 196 (1986).
[17] J. Jaeckel, J. Redondo, and A. Ringwald, Phys. Rev. Lett. **101**, 131801 (2008).
[18] J. Redondo, J. Cosmol. Astropart. Phys. 7 (2008) 008.
[19] K. R. Dienes, C. Kolda, and J. March-Russell, Nucl. Phys. **B492**, 104 (1997).
[20] S. A. Abel, M. D. Goodsell, J. Jaeckel, V. V. Khoze, and A. Ringwald, J. High Energy Phys. 7 (2008) 124.
[21] S. A. Abel, J. Jaeckel, V. V. Khoze, and A. Ringwald, Phys. Lett. B **666**, 66 (2008).
[22] M. Goodsell, J. Jaeckel, J. Redondo, and A. Ringwald, J. High Energy Phys. 11 (2009) 027.
[23] M. Cicoli, M. Goodsell, J. Jaeckel, and A. Ringwald, J. High Energy Phys. 7 (2011) 114.
[24] S. J. Asztalos, G. Carosi, C. Hagmann, D. Kinion, K. van Bibber, M. Hotz, L. J. Rosenberg, G. Rybka, J. Hoskins, J. Hwang, P. Sikivie, D. B. Tanner, R. Bradley, J. Clarke, and ADMX Collaboration, Phys. Rev. Lett. **104**, 041301 (2010).
[25] P. Sikivie, arXiv:1009.0762.
[26] O. K. Baker, M. Betz, F. Caspers, J. Jaeckel, A. Lindner, A. Ringwald, Y. Semertzidis, P. Sikivie, and K. Zioutas, Phys. Rev. D **85**, 035018 (2012).
[27] A. Afanasev, O. K. Baker, K. B. Beard, G. Biallas, J. Boyce, M. Minarni, R. Ramdon, M. Shinn, and P. Slocum, AIP Conf. Proc. **1200**, 1081 (2010).
[28] K. Ehret, M. Frede, S. Ghazaryan, M. Hildebrandt, E.-A. Knabbe, D. Kracht, A. Lindner, J. List, T. Meier, N. Meyer, D. Notz, J. Redondo, A. Ringwald, G. Wiedemann, and B. Willke, Phys. Lett. B **689**, 149 (2010).
[29] D. Cadamuro and J. Redondo, arXiv:1010.4689.
[30] A. Wagner, G. Rybka, M. Hotz, L. J. Rosenberg, S. J. Asztalos, G. Carosi, C. Hagmann, D. Kinion, K. van Bibber, J. Hoskins, C. Martin, P. Sikivie, D. B. Tanner, R. Bradley, and J. Clarke, Phys. Rev. Lett. **105**, 171801 (2010).
[31] S. Andreas, C. Niebuhr, and A. Ringwald, Phys. Rev. D **86**, 095019 (2012).
[32] M. Betz and F. Caspers, arXiv:1207.3275.
[33] H.-S. Zechlin, D. Horns, and J. Redondo, AIP Conf. Proc. **1085**, 727 (2009).

[34] A. Mirizzi, J. Redondo, and G. Sigl, J. Cosmol. Astropart. Phys. 3 (2009) 026.

[35] P. Arias, J. Jaeckel, J. Redondo, and A. Ringwald, Phys. Rev. D **82**, 115018 (2010).

[36] J. Redondo, arXiv:1002.0447.

[37] J. Redondo and A. Ringwald, Contemp. Phys. **52**, 211 (2011).

[38] M. Schwarz, A. Lindner, J. Redondo, A. Ringwald, and G. Wiedemann, arXiv:1111.5797.

[39] A. S. Goldhaber and M. M. Nieto, Rev. Mod. Phys. **43**, 277 (1971).

[40] 1 Jy = 10^{-26} J $\mathrm{m}^{-2}\,\mathrm{s}^{-1}\,\mathrm{Hz}^{-1}$.

[41] Square Kilometer Array, a next generation radio telescope that will provide about a two orders of magnitude improvement in imaging sensitivity and surveying speed for radio observations in the 0.3–20 GHz frequency range, http://www.skatelescope.org.

[42] MeerKAT, an SKA prototype located in South Africa, http://www.ska.ac.za/meerkat.

[43] ASKAP, an SKA prototype located in Australia, http://www.atnf.csiro.au/SKA.

[44] J. W. M. Baars, R. Genzel, I. I. K. Pauliny-Toth, and A. Witzel, Astron. Astrophys. **61**, 99 (1977).

[45] T. K. Kuo and J. Pantaleone, Phys. Rev. D **39**, 1930 (1989).

[46] S. Nussinov, Phys. Lett. B **63**, 201 (1976).

[47] C. Giunti and C. W. Kim, Phys. Rev. D **58**, 017301 (1998).

[48] M. Meyer, Diploma thesis, University of Hamburg.

[49] G. Hinshaw, J.L. Weiland, R.S. Hill, N. Odegard, D. Larson, C.L. Bennett, J. Dunkley, B. Gold, M.R. Greason, N. Jarosik, E. Komatsu, M.R. Nolta, L. Page, D.N. Spergel, E. Wollack, M. Halpern, A. Kogut, M. Limon, S.S. Meyer, G.S. Tucker, and E.L. Wright, Astrophys. J. Suppl. Ser. **180**, 225 (2009).

[50] S. Gottlöber, E.L. Łokas, A. Klypin, and Y. Hoffman, Mon. Not. R. Astron. Soc. **344**, 715 (2003).

[51] A.V. Pynzar' and V.I. Shishov, Astronomy Reports **52**, 623 (2008).

[52] D.C. Pan, M.S. Vogeley, F. Hoyle, Y.-Y. Choi, and C. Park, Mon. Not. R. Astron. Soc. **421**, 926 (2012).

[53] J.H. Taylor and J.M. Cordes, Astrophys. J. **411**, 674 (1993).

[54] J.M. Cordes and T.J.W. Lazio, arXiv:astro-ph/0207156.

[55] M. Plionis and S. Basilakos, Mon. Not. R. Astron. Soc. **330**, 399 (2002).

[56] A.V. Kravtsov, A. Klypin, and Y. Hoffman, Astrophys. J. **571**, 563 (2002).

[57] R. Cen, K. Nagamine, and J. P. Ostriker, Astrophys. J. **635**, 86 (2005).

[58] E. Komatsu, K.M. Smith, J. Dunkley, C.L. Bennett, B. Gold, G. Hinshaw, N. Jarosik, D. Larson, M.R. Nolta, L. Page, D.N. Spergel, M. Halpern, R.S. Hill, A. Kogut, M. Limon, S.S. Meyer, N. Odegard, G.S. Tucker, J.L. Weiland, E. Wollack, and E.L. Wright, Astrophys. J. Suppl. Ser. **192**, 18 (2011).

[59] R. K. Sheth and R. van de Weygaert, Mon. Not. R. Astron. Soc. **350**, 517 (2004).

[60] J.L. Weiland, N. Odegard, R.S. Hill, E. Wollack, G. Hinshaw, M.R. Greason, N. Jarosik, L. Page, C.L. Bennett, J. Dunkley, B. Gold, M. Halpern, A. Kogut, E. Komatsu, D. Larson, M. Limon, S.S. Meyer, M.R. Nolta, K.M. Smith, D.N. Spergel, G.S. Tucker, and E.L. Wright, Astrophys. J. Suppl. Ser. **192**, 19 (2011).

[61] J.W.M. Baars, Astron. Astrophys. **17**, 172 (1972).

[62] B. Winkel, A. Kraus, and U. Bach, Astron. Astrophys. **540**, A140 (2012).

[63] S.J. Tappin, Planet. Space Sci. **34**, 93 (1986).

[64] D.A. Leahy, W. Darbro, R.F. Elsner, M.C. Weisskopf, S. Kahn, P.G. Sutherland, and J.E. Grindlay, Astrophys. J. **266**, 160 (1983).

[65] K.T.S. Brazier, Mon. Not. R. Astron. Soc. **268**, 709 (1994).

[66] R. Buccheri, K. Bennett, G.F. Bignami, J.B.G.M. Bloemen, V. Boriakoff, P.A. Caraveo, W. Hermsen, G. Kanbach, R.N. Manchester, J.L. Masnou, H.A. Mayer-Hasselwander, M.E. Ozel, J.A. Paul, B. Sacco, L. Scarsi, and A.W. Strong, Astron. Astrophys. **128**, 245 (1983).

[67] S. Caucci, S. Colombi, C. Pichon, E. Rollinde, P. Petitjean, and T. Sousbie, Mon. Not. R. Astron. Soc. **386**, 211 (2008).

[68] F.B. Abdalla and S. Rawlings, Mon. Not. R. Astron. Soc. **360**, 27 (2005).

[69] A.R. Duffy, R.A. Battye, R.D. Davies, A. Moss, and P.N. Wilkinson, Mon. Not. R. Astron. Soc. **383**, 150 (2008).

[70] H. Röttgering, J. Afonso, P. Barthel, F. Batejat, P. Best, A. Bonafede, M. Brüggen, G. Brunetti, K. Chyży, J. Conway, F.D. Gasperin, C. Ferrari, M. Haverkorn, G. Heald, M. Hoeft, N. Jackson, M. Jarvis, L. Ker, M. Lehnert, G. Macario, J. McKean, G. Miley, R. Morganti, T. Oosterloo, E. Orrù, R. Pizzo, D. Rafferty, A. Shulevski, C. Tasse, I.V. Bemmel, B. van der Tol, R. van Weeren, M. Verheijen, G. White, and M. Wise, J. Astrophys. Astron. **32**, 557 (2011).

[71] A.R. Duffy, M.J. Meyer, L. Staveley-Smith, M. Bernyk, D.J. Croton, B.S. Koribalski, D. Gerstmann, and S. Westerlund, Mon. Not. R. Astron. Soc. **426**, 3385 (2012).

[72] D.A. Leahy, R.F. Elsner, and M.C. Weisskopf, Astrophys. J. **272**, 256 (1983).

[73] K.V. Mardia and P.E. Jupp, *Directional Statistics* (Wiley, New York, 2000).

[74] O.C. de Jager, B.C. Raubenheimer, and J.W.H. Swanepoel, Astron. Astrophys. **221**, 180 (1989).

[75] R.A. Fesen, M.C. Hammell, J. Morse, R.A. Chevalier, K.J. Borkowski, M.A. Dopita, C.L. Gerardy, S.S. Lawrence, J.C. Raymond, and S. van den Bergh, Astrophys. J. **645**, 283 (2006).

Chapter 7

Summary and Conclusions

A plethora of fundamental discoveries in particle physics, astrophysics, and cosmology established a modern physical world model, which can consistently describe the evolution of the Universe from very early times to the present and beyond. According to concordance ΛCDM cosmology, cold dark matter constitutes the scaffold which gravitationally ties the cosmic web of luminous structures. However, the physical origin of dark matter is not known. This thesis has been dedicated to searching in observables of high-energy astroparticle physics for imprints of this elusive cosmic glue, most likely formed by undiscovered elementary particles. A synopsis of the investigated topics is given below, followed by more detailed summaries.

In the first part of this thesis, a consistent multi-wavelength approach to search for Galactic DM subhalos powered by WIMPs has been applied for the first time. The method aims at probing the small-scale predictions of ΛCDM cosmology and opens a new way of WIMP dark matter searches. WIMP-powered subhalos are expected to be recognizable by steady high-energy gamma-ray emission above $\sim$10 GeV. The samples of unassociated gamma-ray sources cataloged in the *Fermi*-LAT all-sky catalogs have been searched for candidates. The investigation of gamma-ray properties of selected candidates and subsequent multi-wavelength association resulted in evidence for all promising candidates to originate from conventional AGN-like sources. Except for one object, the multi-wavelength SEDs of all promising sources are consistent with high-energy peaked BL-Lac-type objects, revealing new insights in the unexplored population of unassociated gamma-ray sources at the faint end of the cataloged source sample.

The second part of this thesis widens the hunt for gamma-ray signatures of annihilating WIMPs to the very-high energy band of the diffuse gamma-ray background. The sensitivity of ground-based Cherenkov telescope systems to small-scale angular anisotropies in the extragalactic diffuse gamma-ray background has been investigated, with a particular focus on the sensitivity of the planned CTA observatory. Proposed configurations for CTA will enable us to resolve a gamma-ray contribution from annihilating WIMPs to the diffuse gamma-ray background of fractions as low as 10%.

Extensions of the Standard Model commonly predict light particles such as WISPs. String compactifications and grand unified theories naturally motivate the existence of WISPs like axions, axion-like particles, and hidden photons. Recent theoretical progress demonstrated that non-thermally produced WISPs can also provide a promising class of dark matter candidates. In the third part of this work, the sensitivity of current and future radio astronomical facilities to astrophysical signatures of ultra-light hidden photons has been investigated.

7.1 The indirect search for dark matter subhalos

Summary. In Publication I, it has been demonstrated that *Fermi*-LAT provides sufficient sensitivity for detecting Galactic subhalos, powered by self-annihilating thermal WIMP dark matter, with total masses in the range between $10^5\,M_\odot$ and $10^8\,M_\odot$. WIMP-powered subhalos can be discovered as very faint gamma-ray sources at a flux level of $\sim 10^{-10}\,\mathrm{cm}^{-2}\,\mathrm{s}^{-1}$ above 10 GeV, with a moderate angular extent of $\lesssim 0.5$ deg in radius. The spectrum of the temporally steady gamma-ray flux follows a universal hard power-law spectrum with a distinct cutoff, where the cutoff energy depends on the WIMP mass. The faint annihilation flux confines detectable subhalos to solar distances below ∼10 kpc. Under conservative assumptions with regard to the WIMP model and the subhalo distribution, less than two of these objects are predicted to appear in the second year *Fermi*-LAT catalog 2FGL. Missing gaseous content presumably suppresses star formation in subhalos of the considered mass range, making them essentially dark in other wavelength bands.

The origin of the unexplored population of ∼600 high-energy gamma-ray sources listed in the 1FGL and 2FGL catalogs each has been investigated accordingly in Publication I and II, with the purpose of finding subhalo candidate sources. From the 1FGL catalog, twelve candidate sources, revealed by selection for unassociated sources at high galactic latitudes ($|b| \geq 20^\circ$) with a temporally steady gamma-ray emission detected above 10 GeV, have been studied. Source selection in the 2FGL catalog additionally included a cut for hard gamma-ray spectra ($\Gamma < 2.0$), revealing thirteen 2FGL candidates. Of the 1FGL candidates, one source has been preselected by lacking multi-wavelength counterparts. In the study of 2FGL candidates in Publication II, a preselection of four sources has been made based upon indications for a spectral cutoff in the 24-month data (2 years) or 42-month data (3.5 years). The total sample of candidate sources has been investigated for angular extent, temporally constant emission, and a gamma-ray spectrum following a power law with a distinct cutoff, using 3.5 years of *Fermi*-LAT data between 100 MeV and 300 GeV.

Refined localization has enabled subsequent multi-wavelength association. With a collection of archival multi-wavelength data in the radio, infrared, optical, UV, and X-ray band, as well as dedicated follow-up X-ray observations (with *Swift*-XRT), it has been demonstrated that the SEDs of all five promising objects show consistency with AGN spectra, in particular with high-energy peaked BL-Lac objects in the most cases. Indications supporting the BL-Lac nature of the objects also emerged from infrared color-color data (WISE). Lower limits on the redshift of each object have been determined from R-band photometry by comparison with a standard giant elliptical BL-Lac host galaxy, resulting in redshift lower limits in the range between 0.2 and 0.5. Temporal variability of the optical and UV fluxes shows that the emission in these energy bands is considerably influenced by a non-thermal continuum, thus further substantiating a BL-Lac origin. The SED of one object (2FGL J0338.2+1306) indicates a thermal contribution of a standard giant elliptical BL-Lac host galaxy. Optical spectroscopic observations of one particular object (2FGL J0031.0+0724) have supported the hypothesis of dominant continuum emission. The absence of emission lines excludes an FSRQ nature for this object. Absorption lines from detected intervening Mg II absorption systems have allowed setting a lower limit of $z > 0.87$ on the redshift. For two of the five candidate sources, indications for X-ray variability have been found, using data from observational epochs separated by one to two years. The high-energy gamma-ray data is consistent with a point-source scenario for all studied objects. For one source (2FGL J0305.0–1602) indications for gamma-ray variability have been found at ∼99% CL. All five candidate sources share the common property of a comparably hard gamma-ray index. In addition, the gamma-ray flux at ∼30 GeV is larger between a factor of 2 and 10 than expected from an averaged empirical HBL hypothesis, as shown in Figs. 4.2 and 4.6. VHE follow-up observations of 2FGL J0031.0+0724 with H.E.S.S. are sufficiently sensitive to exclude some possible dark matter scenarios for the considered DM subhalo origin of this object.

Conclusions. For no unassociated *Fermi*-LAT source compelling evidence has been found for the gamma-ray emission to originate from a subhalo of self-annihilating WIMP dark matter. Five promising candidate sources, selected from the 1FGL and 2FGL catalogs, have been classified to likely originate from high-energy peaked BL-Lac-type objects (four sources) or similar AGN-like objects (one source) in comparably high redshifts.

Within the underlying conservative theoretical assumptions, the prediction of less than two DM subhalos detected in the 2FGL arises within the Poissonian scatter (95% CL) around the mean. A non-detection of these objects is therefore still consistent with this prediction, and hence with the small-scale predictions of the ΛCDM model.

For more optimistic assumptions according to the dark matter profile and the WIMP scenario, the absence of promising candidates allows placing mass and distance limits on nearby DM subhalos, in principle. However, such bounds strongly depend on various model parameters.

VHE follow-up observations with current (H.E.S.S.-II, MAGIC-II, and VERITAS) and planned (CTA) imaging atmospheric Cherenkov telescopes offer promising opportunities of constraining the nature of candidate sources further. The high photon numbers collected with the large effective areas of IACTs would result in more precise positional and spectral parameters. As briefly discussed in Section 4.3.3, VHE follow-up observations also provide a unique tool for searching for a blazar-related source population with an additional emission component at GeV to TeV energies. It should be emphasized in this manner, that the existence of unknown source populations (with a small spatial anisotropy) is favored by observations of the overall diffuse gamma-ray background emission (Cuoco *et al.* 2012). Note that appropriate selection cuts to find such sources in the *Fermi*-LAT catalogs would be similar to the ones employed to find DM subhalo candidates.

This study has clearly established the need for multi-wavelength (optical, UV, and X-ray) monitoring campaigns of candidate sources. Ultimately, a detection of variability in different wavelength bands including the high-energy band would both confirm the multi-wavelength associations and categorize an unassociated gamma-ray source to originate from an AGN. Therefore, densely sampled multi-wavelength light curves are of considerable interest. Additional spectroscopic optical observations offer a promising method to determine the redshifts of these sources.

Annihilating dark matter also emits charged particles, which would lead to synchrotron emission and inverse-Compton radiation if the subhalo is embedded in (e.g., Galactic) magnetic fields and (e.g., stellar) photon fields. This results in very faint diffuse radio and X-ray halos (Baltz & Wai 2004; Colafrancesco *et al.* 2007; Jeltema & Profumo 2008), which might potentially be resolvable with next-generation high-sensitivity instruments. In combination with the gamma-ray characteristics, this establishes a unique multi-wavelength signature which can ultimately be used to discriminate DM subhalos from conventional astrophysical sources.

Outlook. The first *Fermi*-LAT catalog of sources above 10 GeV (1FHL; Paneque *et al.* 2013) will soon provide a very useful tool for future candidate searches. However, catalog searches for DM subhalo candidates are likely biased by catalog requirements for detection, in combination with common standard analysis setups (energy range, spectral fitting, etc.). Forthcoming activities using high-sensitivity data sets could address these issues with complementary methods, such as dedicated analyses for high-energy photon clusters.

In the near future, higher sensitivity in the HE regime will significantly enlarge the observable horizon for DM subhalos. For instance, $\mathcal{O}(5)$ subhalos are anticipated in the 10-year *Fermi*-LAT data set. Improvements through generically longer *Fermi*-LAT observations will be further increased by optimized event selection and event reconstruction algorithms (Pass 8; Atwood *et al.* 2013). These imply a better background-rejection efficiency, a smaller PSF, and a larger acceptance increased by ∼25% towards high energies. Potential successors of *Fermi*-LAT such as GAMMA-400 might improve source localization and spectroscopy.

Future searches for DM subhalos may be complemented by next-generation optical sky surveys, presumably providing sufficient sensitivity for the discovery of a population of ultra-faint satellites with a comparably low surface brightness (see Section 2.3.5). Such galaxies are predicted to be hosted by DM subhalos with comparably low masses.

In the light of diffuse radio halos anticipated around dark matter overdensities in Galactic environments, we conducted radio observations of the nearby dwarf spheroidal galaxy UMa II at 4.8 GHz with the single-dish Effelsberg 100 m radio telescope in the year 2012 (Lobanov *et al.* 2011a). UMa II has been identified to be amongst the dSphs with best detection prospects, expecting an extended radio halo with a peak flux of up to 1.8 mJy/beam. Radio images of the galaxy with a diameter of $\sim 40'$ have been produced from high-quality maps in both intensity and polarization, containing ∼15 h of data. The corresponding noise level of the images is ∼450 μJy/beam (total intensity) and ∼300 μJy/beam (polarized intensity), respectively. High-level analysis of the map will enable the search for diffuse radio emission. Apart from promising astrophysical implications, a non-detection will give rise to competitive constraints of the self-annihilation cross section of dark matter.

7.2 The imprint of dark matter in the diffuse gamma-ray background

Summary. Both a population of conventional high energy gamma-ray sources and the overall distribution of annihilating WIMP dark matter produce specific signatures in the angular anisotropy spectrum of the diffuse gamma-ray background. With a simplified Monte-Carlo approach, the sensitivity of current and future ground-based Cherenkov telescopes for measuring such signals in the anisotropy power spectrum of the extragalactic DGB above 100 GeV has been investigated.

The range of angular scales (i.e., multipoles) accessible with IACTs is limited by the field of view, constraining the sensitivity at large angular scales (low multipoles), and the point-spread function, suppressing the power spectrum at small angular scales (high multipoles). Typical characteristics of IACTs allow the observation of angular scales between ∼0.2° and ∼2°, corresponding to multipoles between ∼100 and ∼1 000. A sufficiently high signal-to-noise ratio requires the suppression of both the hadronic and leptonic cosmic-ray backgrounds with a good gamma-hadron separation. The development of a feasible gamma-electron separation would additionally suppress the electron background, which provides a significant contribution at low energies.

In particular, measurements of the small-scale power spectrum may permit isolating a contribution of annihilating dark matter to the DGB. The sensitivity of planned CTA setups is sufficient for detecting a gamma-ray flux contribution from dark matter to the extragalactic DGB down to ∼10% (at 95% confidence level), considering energies above 300 GeV and a single-target observation of 1 000 h. However, a more realistic data sample will contain various different pointings. It has been shown that a stacking of data from multiple targets (with a total exposure similar to the single-target observation) worsens the sensitivity by a factor of ∼ 2 only, i.e., to ∼20% for ten fields with an exposure of 100 h each. Note that this result implies that even for CTA the sensitivity is not cosmic-variance limited.

Conclusions. The sensitivity to the dark matter contribution can be expressed in terms of the velocity-averaged dark matter self-annihilation cross section $\langle\sigma_\mathrm{A} v\rangle$. Assuming an overall cosmological distribution of dark matter halos including a population of DM subhalos, the resulting sensitivity reaches cross sections smaller than the one compatible with a thermal WIMP scenario $\langle\sigma_\mathrm{A} v\rangle = 3\times10^{-26}\,\mathrm{cm}^3\,\mathrm{s}^{-1}$, for WIMP masses below ∼200 GeV. In the case of a non-detection, achievable constraints would thus be comparable to the most sensitive measurements currently pursued.

The search for small-scale anisotropies with IACTs will complement anisotropy measurements with *Fermi*-LAT data. Although current IACTs are inferior to CTA in terms of sensitivity, searches in current data sets would already provide competitive constraints on the population properties of astrophysical very-high energy gamma-ray emitters. Furthermore, investigating current data will support the development of the detailed analysis approach required for future studies.

Outlook. The CTA observatory is foreseen to be built in the near future (> 2015). In the light of indirect dark matter searches, complementary methods are required, investigating different data sets. The compelling sensitivity and the multi-purpose applicability of the suggested method will make it a prime objective for science data analyses.

7.3 The case for WISPs – hidden U(1) gauge bosons

Summary. Recent data from particle accelerators such as the LHC raise doubts in supersymmetric models such as the cMSSM. Various extensions of the Standard Model also predict a class of light particles such as WISPs, which can even provide a completely different kind of particle dark matter. Popular WISP candidates include axions, ALPs, and hidden photons.

Weak kinetic mixing of hidden photons with ordinary photons gives rise to flavor oscillations that would imply energy-dependent modifications of astrophysical spectra. It has been demonstrated in this thesis that ultra-light hidden photons with masses below $\sim 10^{-14}\,\mathrm{eV}$ may influence the broad-band spectra of compact Galactic and extragalactic radio sources. This enables dedicated searches with radio telescopes. A non-detection of a hidden-photon signal would lead to constraints in a yet unexplored region of the hidden-photon parameter space.

Photon propagation in intergalactic and galactic environments depends on the refractive properties of the ambient plasma density, which leads to an effective mass of the propagating photon. Accordingly, photon – hidden-photon oscillations are affected by the propagation environments, giving rise to exponential damping or resonant amplification of the hidden-photon signal under favorable conditions. In addition to this, de-coherence effects related to the photon production and detection processes can result in vanishing oscillations over large propagation distances.

Radio observations of Galactic supernova remnants and distant radio-loud AGN in the frequency range between 30 MHz and 1 400 GHz are, in principle, sensitive to resolving photon – hidden-photon oscillations for hidden-photon masses between $\sim 10^{-19}$ eV and $\sim 10^{-12}$ eV. Propagation effects, which depend on the line-of-sight, constrain the lower resolvable mass to $\sim 10^{-17}$ eV, considering photon propagation through large intervening cosmic voids. Decoherence effects do not severely restrict the achievable upper mass bound. Conservative estimates show that current facilities such as ALMA, the Effelsberg 100-m single-dish antenna, JVLA, and LOFAR, the SKA precursors ASKAP and MeerKAT, and the planned SKA provide the instrumental bandwidth and resolution to constrain mixing angles down to $\sim 10^{-3}$ in the mass range mentioned above.

The achievable sensitivity of radio observations can be significantly improved with the development of broad-band receivers enabling in-band measurements within a bandwidth of 1 GHz. With an accurate bandpass calibration, the limits on the mixing angle can be lowered by at least one order of magnitude.

Conclusions. With such measurements, the parameter space of hidden photons can be investigated in the ultra-light mass range, where no measurements have previously been made. This would provide an important contribution to the search of beyond-SM physics.

Outlook. Based upon this study, investigations of absolute flux density measurements made for the primary radio astronomy calibrator sources Cas A, Tau A, Vir A, and Cyg A have begun. To complement the data and extend their sensitivity, the authors of Publication IV recently took radio data for a selection of eight compact radio-loud AGN with the Effelsberg 100-m radio telescope (Lobanov *et al.* 2011b). We aim for in-band searches of periodic oscillations using a total bandwidth of 100 MHz centered on the observing frequency of 4.8 GHz. The selected setup, covering a total observation time of $\sim$12 h, will enable us to probe for hidden photons with a mixing angle down to $\sim 10^{-3}$.

Appendix A

Units, Notation, and Conventions

If not otherwise stated, equations are given in natural units $\hbar = c = 1$, where $\hbar$ denotes the reduced Planck constant and c the speed of light. In this system, $[\text{length}] = [\text{time}] = [\text{energy}]^{-1} = [\text{mass}]^{-1}$ holds. Therefore, particle masses are usually given in units of energy.

In general, physical constants and values of physical quantities are expressed referring to the common unit systems, i.e., the International System of Units (SI), the CGS system, or specifically defined astrophysical units (see Beringer *et al.* 2012 for details). Transformation rules among different units and the numerical values of physical constants are listed in the afore-mentioned reference as well. Prefixes are adopted from the SI system. For microscopic quantities, energy is often given in electron-volts (eV) or the CGS unit "erg", where $1\,\text{eV} = 1.602\,176\,565(35) \times 10^{-19}\,\text{J}$ and $1\,\text{erg} = 10^{-7}\,\text{J}$.

4-vectors and tensors. Lorentz indices are denoted with small Greek subscripts or superscripts, e.g., $\mu = 0, 1, 2, 3$. The metric of Minkowski space is given by

$$g_{\mu\nu} = \text{diag}(-1, +1, +1, +1)\,. \tag{A.1}$$

The sign conventions used in the field equations of general relativity follow the definitions by Misner, Thorne & Wheeler (1973). The spacetime metric raises and lowers Lorentz indices of 4-vectors and tensors such as $x_\mu = g_{\mu\nu} x^\nu$ and $y^\mu = g^{\mu\nu} y_\nu$. The sum convention for Lorentz indices is used.

Appendix B

Supplementary Information

B.1 Publication II

B.1.1 Spectral fits

For reference, the spectra fit to the 24-month *Fermi*-LAT data of 2FGL J0031.0+0724, 2FGL J0143.6–5844, 2FGL J0305.0–1602, 2FGL J0338.2+1306, and 2FGL J1410.4+7411 are shown in Fig. B.1. In the individual subfigures, the spectral fits of power laws with exponential cutoff are compared to the cataloged data, including the cataloged power-law fit.

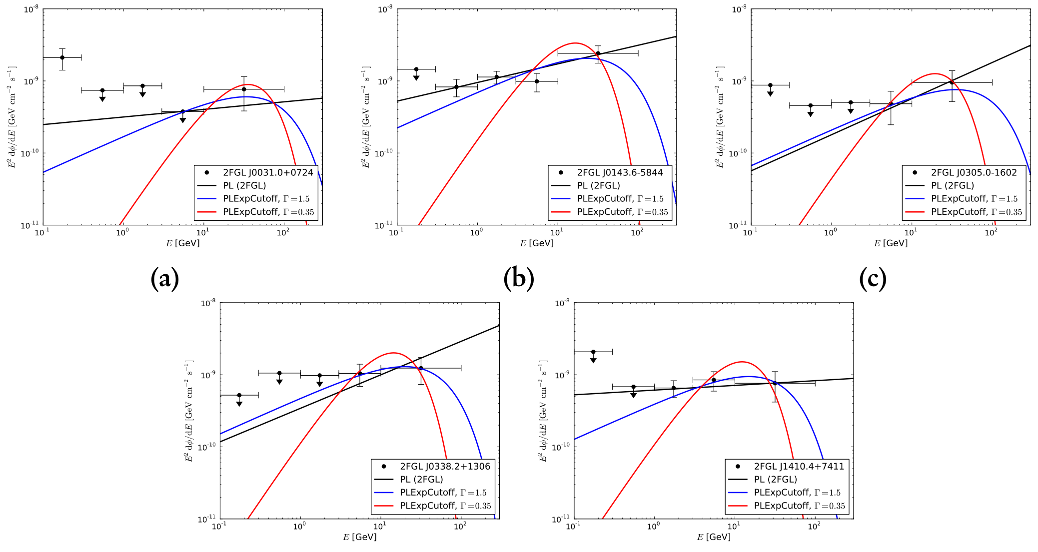

(a) (b) (c)

(d) (e)

Figure B.1: Spectral fits following a power law with exponential cutoff (PLExpCutoff), compared to the data points and power-law (PL) fit (black solid line) reported in the 2FGL catalog. Black arrows denote upper limits (95% CL). The power-law index of the PLExpCutoff fit was fixed to $\Gamma = 1.5$ (blue solid line) and $\Gamma = 0.35$ (red solid line), respectively. The subfigures consider the sources selected in Publication II.

B.1.2 Variability

The following plots in Fig. B.2 show the normalized cumulative light curves of high-energy photons detected with *Fermi*-LAT from 2FGL J0031.0+0724, 2FGL J0143.6–5844, 2FGL J0305.0–1602, 2FGL J0338.2+1306, and 2FGL J1410.4+7411, in comparison to the corresponding normalized cumulative exposure distributions. The hypothesis of a temporally constant source was tested with an (unbinned) Kolmogorov-Smirnov test (Press *et al.* 2007), where $p(D > D_{\text{max}})$ represents the probability that the two distributions have been statistically drawn from the same underlying distribution function, i.e., $p(D > D_{\text{max}})$ is the probability for steady gamma-ray emission.[1]

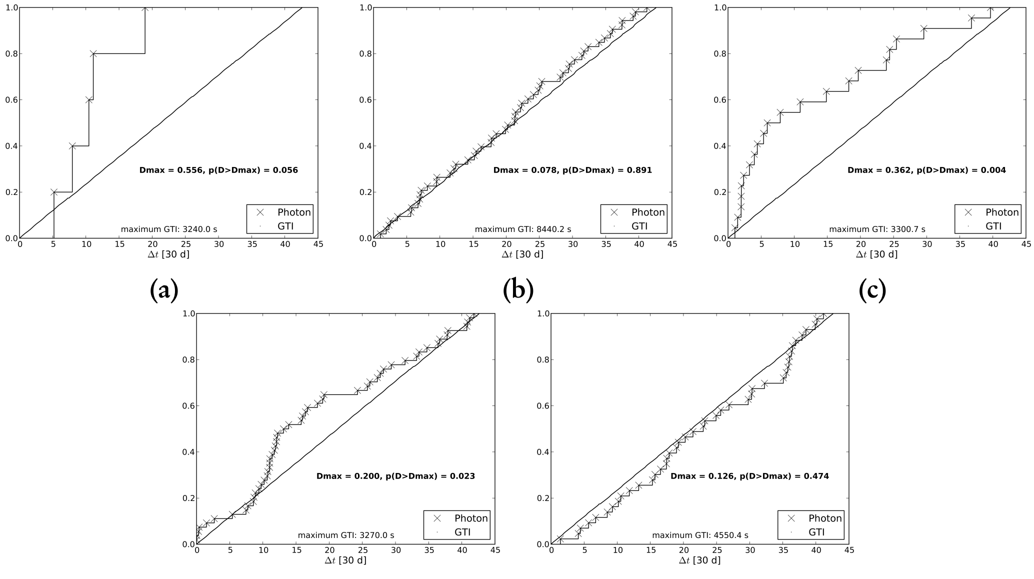

(a) **(b)** **(c)**

(d) **(e)**

Figure B.2: Most constraining normalized cumulative light curves of high-energy photons (black crosses) from **(a)** 2FGL J0031.0+0724 (10–300 GeV), **(b)** 2FGL J0143.6–5844 (3–300 GeV), **(c)** 2FGL J0305.0–1602 (3–300 GeV), **(d)** 2FGL J0338.2+1306 (3–300 GeV), and **(e)** 2FGL J1410.4+7411 (3–300 GeV), drawn from the 42-month *Fermi*-LAT data. The time from observation start is denoted by Δt. The subfigures include the corresponding cumulative exposure curves, derived from the good-time-interval (GTI) lengths (black dots). The temporal uncertainty of the exposure curve is smaller than the maximum GTI value. Temporal variability was tested with a Kolmogorov-Smirnov test, where $p(D > D_{\text{max}})$ is the probability of a constant source.

B.1.3 Angular extent

A likelihood-ratio test was applied to test the hypothesis of angularly extended gamma-ray emission. The likelihood-ratio is defined by $\lambda_r = \mathscr{L}_0/\mathscr{L}_1$, where the total likelihoods for the null hypothesis ($\mathscr{L}_0$) and alternative hypothesis ($\mathscr{L}_1$) are given by the likelihood function $L(\theta_{\text{s}})$ defined in Publication II, Section 3.4:

$$\mathscr{L}_0 = \exp\left[-L(\theta_{\text{s}}^{\text{T}})/2\right], \quad \text{and} \quad \mathscr{L}_1 = \exp\left[-L(\theta_{\text{s}})/2\right]. \tag{B.1}$$

---

[1] D_{max} denotes the *maximum* vertical distance between the curves, whereof the probability $p(D > D_{\text{max}})$ can be calculated from (see, e.g., Press *et al.* 2007 for details).

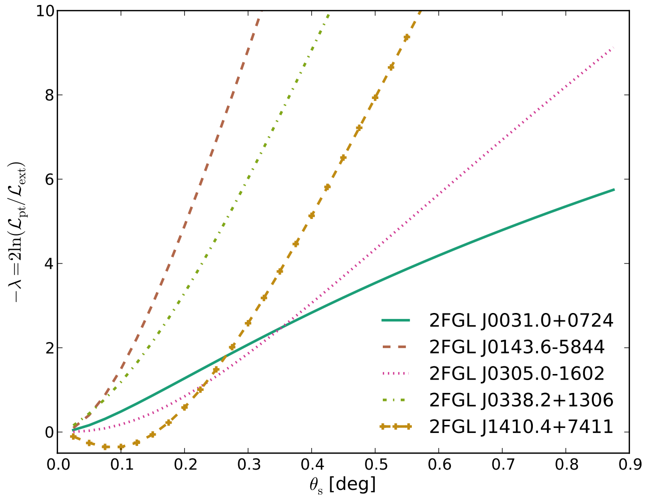

Figure B.3: Distributions of the likelihood-ratio $-\lambda$ for sources discussed in Publication II, as function of the characteristic angular source extent θ_{s}. The intrinsic intensity profile is assumed to follow a line-of-sight integrated squared NFW profile.

In the null hypothesis, the value of the parameter θ_{s} is fixed to $\theta_{\mathrm{s}}^{\mathrm{T}}$. Applying the theorem of Wilks (1938), in the null hypothesis the quantity $\lambda = -2\ln\lambda_r$ is distributed as a chi-square distribution with one degree of freedom (e.g., Press *et al.* 2007), apart from terms of $\mathcal{O}(1/\sqrt{N})$. Here, N denotes the number of photon counts.

Fig. B.3 shows the distributions of $2\ln\lambda_r$ as function of the characteristic angular source extension θ_{s}, considering the sources discussed in Publication II. The plotted distributions refer to the null hypothesis $\mathscr{L}_{\mathrm{pt}}$ of a point-like source (i.e., $\theta_{\mathrm{s}}^{\mathrm{T}} \to 0$), in comparison to the alternative hypothesis $\mathscr{L}_{\mathrm{ext}}$ of an extended source.

B.2 Thermal emission component

Fig. B.4 shows the SEDs of the considered candidate sources as presented in Fig. 4.2 in Section 4.3. The SEDs additionally include the thermal emission component expected from a standard giant elliptical BL-Lac host galaxy with an absolute R-band magnitude $M_R = -22.9^{\mathrm{m}} \pm 0.5^{\mathrm{m}}$. The assumed redshifts correspond to the lower limits determined in Section 4.3.1. For 2FGL J0143.6–5844 and 2FGL J0305.0–1602 the thermal emission outshines the infrared flux reported in the 2MASS catalog. However, a thermal component can consistently explain the infrared emission (2MASS) and the low-state B-band flux (USNO $B1$) of 2FGL J0338.2+1306.

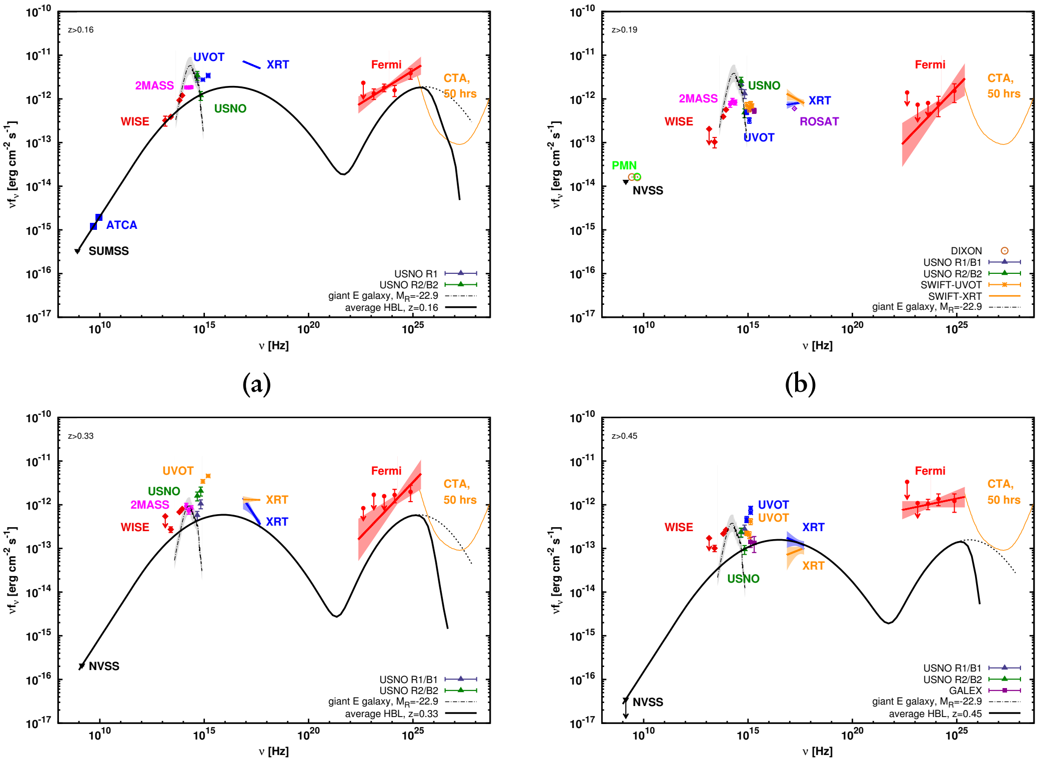

(a) (b)

(c) (d)

Figure B.4: SEDs of **(a)** 2FGL J0143.6–5844, **(b)** 2FGL J0305.0–1602, **(c)** 2FGL J0338.2+1306, and **(d)** 2FGL J1410.4+7411, as shown in Fig. 4.2 in Section 4.3. The SEDs include the thermal emission spectrum expected from a standard giant elliptical BL-Lac host galaxy ($M_R = -22.9^{\mathrm{m}}$) in the redshifts corresponding to the lower limits determined in Table 4.1. The thermal spectrum is denoted with the black dot-dashed line, peaking at $\sim 10^{14}$ Hz. The gray-shaded area corresponds to a scatter of 0.5^{m} in the brightness of the galaxy.

B.3 *Swift*-XRT data

Table B.1 (below) lists the spectral fit parameters of X-ray sources detected in the celestial vicinity of the *Fermi*-LAT sources discussed in Publication I and Publication II.

B.4 X-ray spectral fits

Fig. B.5 shows the binned count spectra of the X-ray associations to the selected *Fermi*-LAT sources. The spectra were fit with a power-law model corrected for Galactic absorption.

B.5 *Swift*-UVOT counterparts

Table B.2 lists the UV counterparts of the X-ray sources associated to the candidate *Fermi*-LAT sources, see Section 4.3.4.

Target ID	Name SWIFT	σ_{90} [arcsec]	S/N	N_{H} [$10^{20}\,\mathrm{cm}^{-2}$]	$f^{\mathrm{abs}}(0.3–2\,\mathrm{keV})$ [$10^{-13}\,\mathrm{erg\,cm^{-2}\,s^{-1}}$]	ϕ_0 [$10^{-4}\,\mathrm{keV^{-1}\,cm^{-2}\,s^{-1}}$]	Γ	$C_{\mathrm{stat}}/\mathrm{dof}$	P_C	$f^{\mathrm{unabs}}(0.3–2\,\mathrm{keV})$ [$10^{-13}\,\mathrm{erg\,cm^{-2}\,s^{-1}}$]
41265	J003017.8+072142	5	5.3	3.64	$0.56^{+0.15}_{-0.12}$	$0.23^{+0.05}_{-0.05}$	$1.70^{+0.30}_{-0.29}$	7.8/5	0.45	$0.67^{+0.17}_{-0.16}$
	J003029.9+072013	5	5.1	3.63	$0.32^{+0.10}_{-0.10}$	$0.13^{+0.04}_{-0.04}$	$0.73^{+0.27}_{-0.31}$	11.7/5	0.14	$0.36^{+0.11}_{-0.09}$
	J003119.5+072455†	5	6.5	3.60	$2.57^{+0.46}_{-0.40}$	$1.01^{+0.15}_{-0.14}$	$2.22^{+0.22}_{-0.23}$	8.7/9	0.80	$3.27^{+0.59}_{-0.57}$
47130	J003030.0+072004	5	5.0	3.63	$0.55^{+0.13}_{-0.13}$	$0.23^{+0.09}_{-0.08}$	$0.95^{+0.34}_{-0.40}$	10.4/5	0.34	$0.63^{+0.23}_{-0.21}$
	J003113.1+073143	5	5.9	3.57	$1.10^{+0.23}_{-0.19}$	$0.45^{+0.08}_{-0.07}$	$1.87^{+0.27}_{-0.28}$	4.5/7	0.92	$1.34^{+0.29}_{-0.27}$
	J003119.9+072452†	4	10.4	3.60	$3.43^{+0.39}_{-0.36}$	$1.23^{+0.12}_{-0.11}$	$2.58^{+0.16}_{-0.16}$	26.8/19	0.43	$4.54^{+0.54}_{-0.51}$
41274	J014229.0–584553	5	7.4	2.13	$3.03^{+0.50}_{-0.48}$	$1.21^{+0.20}_{-0.18}$	$1.56^{+0.23}_{-0.22}$	9.9/10	0.80	$3.37^{+0.61}_{-0.56}$
	J014347.3–584551†	4	47.4	2.04	$100.02^{+2.58}_{-2.53}$	$35.76^{+0.81}_{-0.80}$	$2.20^{+0.03}_{-0.03}$	125.3/145	0.92	$115.10^{+3.06}_{-3.03}$
	J014410.1–584042	6	4.1	2.03	$0.86^{+0.22}_{-0.22}$	$0.32^{+0.09}_{-0.08}$	2.00	2.2/3	0.84	$0.97^{+0.28}_{-0.24}$
41286	J030514.9–160818†	4	13.1	3.62	$12.18^{+1.14}_{-1.06}$	$5.03^{+0.42}_{-0.40}$	$1.92^{+0.12}_{-0.12}$	26.9/30	0.89	$14.98^{+1.48}_{-1.43}$
49995	J030515.8–160818†	4	8.6	3.62	$15.32^{+2.17}_{-1.81}$	$5.96^{+0.74}_{-0.68}$	$2.26^{+0.23}_{-0.23}$	16.7/12	0.59	$19.55^{+2.86}_{-2.71}$
47147	J033828.9+130211†	4	15.4	15.30	$12.45^{+0.95}_{-0.96}$	$8.14^{+0.66}_{-0.63}$	$2.01^{+0.11}_{-0.11}$	23.2/21	0.59	$24.82^{+2.54}_{-2.46}$
41292	J033829.2+130217†	5	6.5	15.30	$5.65^{+1.02}_{-0.87}$	$3.68^{+0.59}_{-0.54}$	$2.73^{+0.31}_{-0.32}$	6.1/7	0.79	$14.58^{+3.51}_{-3.39}$
	J033840.4+130722	5	4.4	15.20	$1.00^{+0.22}_{-0.21}$	$0.65^{+0.15}_{-0.13}$	2.00	3.2/4	0.74	$1.99^{+0.46}_{-0.40}$
47219	J141234.8+741153†	5	5.4	2.35	$2.33^{+0.55}_{-0.46}$	$0.85^{+0.16}_{-0.15}$	$2.21^{+0.29}_{-0.28}$	11.1/5	0.73	$2.74^{+0.63}_{-0.58}$
41402	J141235.2+741153†	5	4.8	2.35	$1.41^{+0.37}_{-0.32}$	$0.56^{+0.13}_{-0.12}$	$1.81^{+0.36}_{-0.39}$	5.3/3	0.63	$1.62^{+0.43}_{-0.40}$

Table B.1: List of X-ray sources detected with *Swift*-XRT within a radius of $\lesssim 13'$ around the candidate *Fermi*-LAT sources investigated in Publication I and II. The table is sorted by right ascension. The X-ray sources associated to the *Fermi*-LAT sources are marked with a dagger symbol (†). Besides a revision of Table 11 in Publication II, the table contains additional data sets of the considered regions, taken in temporal epochs before or after the data samples analyzed in Publication II (cf., Table 4.2 in Section 4.3). All data were analyzed with the improved analysis method of Publication II, along with the same calibration files. An energy threshold of 0.3 keV was used for spectral fitting, reducing systematic uncertainties (Godet *et al.* 2009). The notation of the table is chosen as of Table 11 in Publication II. The column P_C additionally lists the goodness-of-fit (p-value) of the C-statistic. The p-value was obtained with Monte-Carlo simulations, using the *goodness* command implemented in *Xspec*.

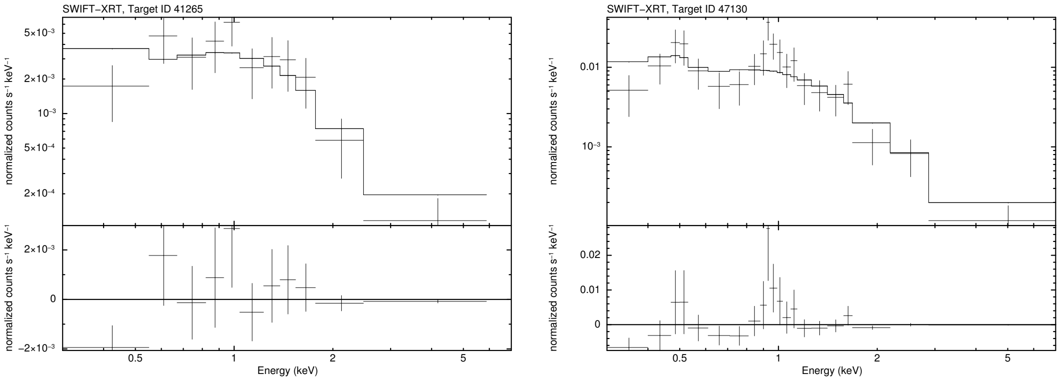

(a) 2FGL J0031.0+0724, 2010

(b) 2FGL J0031.0+0724, 2012

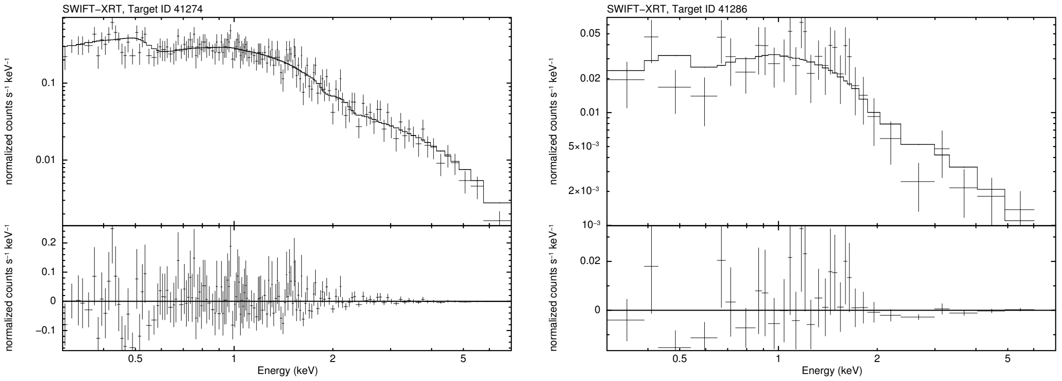

(c) 2FGL J0143.6–5844, 2010

(d) 2FGL J0305.0–1602, 2011

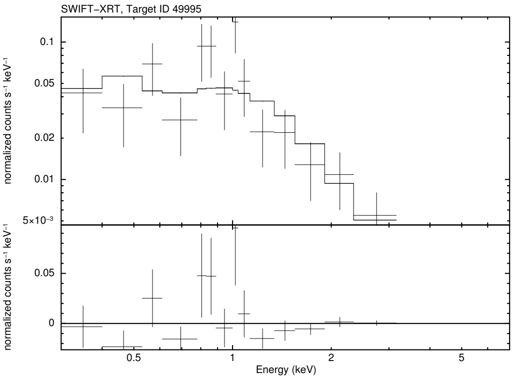

(e) 2FGL J0305.0–1602, 2013

Figure B.5: X-ray count spectra of the X-ray associations to the *Fermi*-LAT sources selected in the publications. The spectra are sorted by the source's right ascension and by the observational epoch. A power law corrected for Galactic absorption has been used for spectral fitting, choosing an energy threshold of 0.3 keV.

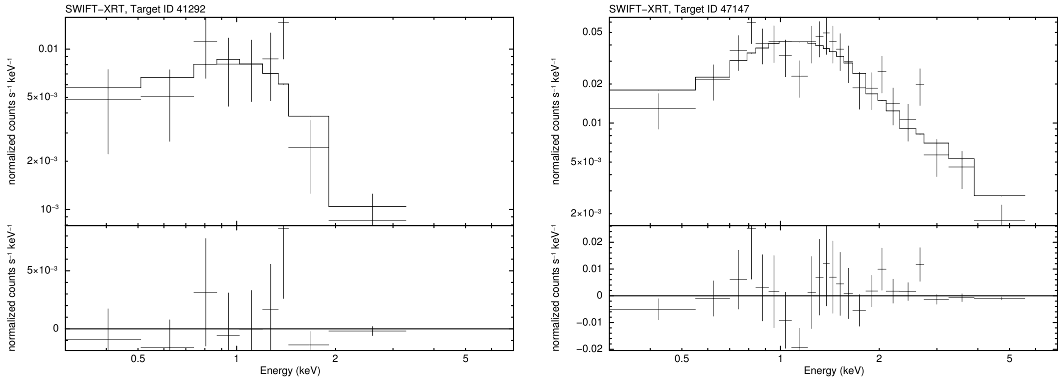

(f) 2FGL J0338+1306, 2010

(g) 2FGL J0338+1306, 2012

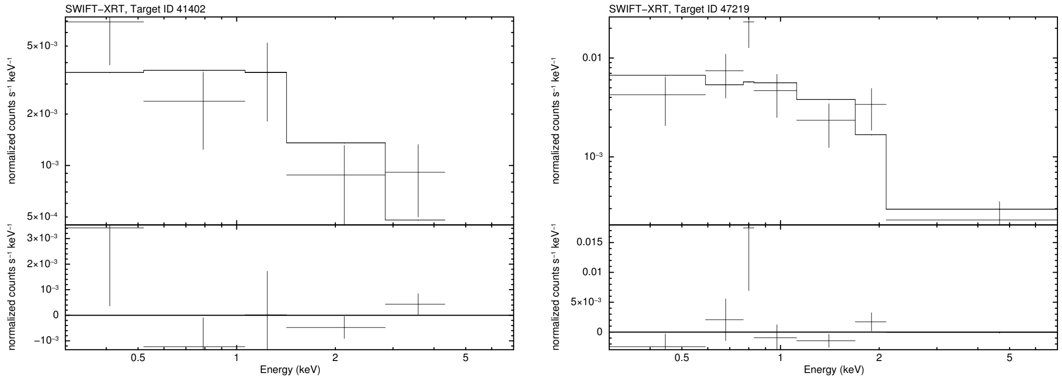

(h) 2FGL J1410.4+7411, 2011

(i) 2FGL J1410.4+7411, 2012

Figure B.5 continued.

Table B.2: X-ray and UV associations of the candidate *Fermi* sources selected in Publication I and II. The sources are sorted by right ascension in ascending order. Spectral parameters of the X-ray associations are listed in Table B.1. UV associations have been detected with *Swift*-UVOT, see Section 4.3.4 for details. Apart from the positions of the X-ray and UV source (SWIFT JHHMMSS.s±DDMMSS), the table lists the signal-to-noise ratios S/N, exposures, and AB-magnitudes m for all UVOT filters (UVW2,UVM2,UVW1,U,B,V) which have been used for the observations. If $S/N < 5$, m is interpreted as upper limit. Each entry corresponds to data of one observation (flagged by a single *Swift* observation ID). The data of all exposures within one observation have been summed.

Target ID	XRT name SWIFT	UVOT name SWIFT	Filter	S/N	Exposure [ks]	m
47130	J003119.9+072452	J003119.7+072453	UVM2	11.5	470.3	$19.66^{m} \pm 0.10^{m}_{stat} \pm 0.03^{m}_{sys}$
			UVW1	41.9	4537.2	$19.38^{m} \pm 0.03^{m}_{stat} \pm 0.03^{m}_{sys}$
			U	38.6	3004.9	$18.75^{m} \pm 0.04^{m}_{stat} \pm 0.02^{m}_{sys}$
41274	J014347.3–584551	J014347.3–584550	UVW2	59.3	1696.5	$18.19^{m} \pm 0.03^{m}_{stat} \pm 0.03^{m}_{sys}$
			UVW2	36.0	658.0	$18.25^{m} \pm 0.04^{m}_{stat} \pm 0.03^{m}_{sys}$
			U	86.1	2025.1	$17.76^{m} \pm 0.03^{m}_{stat} \pm 0.02^{m}_{sys}$
41286	J030514.9–160818	J030515.0–160816	UVW2	3.6	50.8	> 20.31
			UVW1	7.0	366.2	$20.58^{m} \pm 0.16^{m}_{stat} \pm 0.03^{m}_{sys}$
			U	9.1	363.0	$19.76^{m} \pm 0.12^{m}_{stat} \pm 0.02^{m}_{sys}$
			U	21.1	1405.6	$19.69^{m} \pm 0.06^{m}_{stat} \pm 0.02^{m}_{sys}$
49995	J030515.8–160818	J030515.0–160816	UVW2	9.6	343.3	$20.15^{m} \pm 0.12^{m}_{stat} \pm 0.03^{m}_{sys}$
			UVM2	7.6	270.6	$19.92^{m} \pm 0.14^{m}_{stat} \pm 0.03^{m}_{sys}$
			UVW1	6.6	171.0	$19.92^{m} \pm 0.17^{m}_{stat} \pm 0.03^{m}_{sys}$
			U	6.2	85.4	$19.36^{m} \pm 0.18^{m}_{stat} \pm 0.02^{m}_{sys}$
			B	3.9	85.4	> 19.13
			V	2.6	85.4	> 18.71
47147	J033828.9+130211	J033829.2+130215	UVW2	18.0	2640.6	$20.60^{m} \pm 0.06^{m}_{stat} \pm 0.03^{m}_{sys}$
			U	11.1	679.7	$19.29^{m} \pm 0.10^{m}_{stat} \pm 0.02^{m}_{sys}$
47219	J141234.8+741153	J141235.7+741158	UVM2	10.7	376.1	$19.64^{m} \pm 0.10^{m}_{stat} \pm 0.03^{m}_{sys}$
			UVM2	16.7	1151.2	$19.90^{m} \pm 0.07^{m}_{stat} \pm 0.03^{m}_{sys}$
			U	6.8	237.0	$19.70^{m} \pm 0.16^{m}_{stat} \pm 0.02^{m}_{sys}$
			U	10.3	321.1	$19.78^{m} \pm 0.11^{m}_{stat} \pm 0.02^{m}_{sys}$
41402	J141235.2+741153	J141235.7+741158	UVM2	6.5	327.2	$20.40^{m} \pm 0.17^{m}_{stat} \pm 0.03^{m}_{sys}$
			UVW1	5.7	534.9	$20.94 \pm 0.19_{stat} \pm 0.03_{sys}$
			U	10.3	1384.9	$20.52^{m} \pm 0.11^{m}_{stat} \pm 0.02^{m}_{sys}$
			U	10.3	1438.6	$20.49^{m} \pm 0.11^{m}_{stat} \pm 0.02^{m}_{sys}$

Appendix C

Observational Proposal

C.1 ToO request for observation of 1FGL J0030.7+0724 with *Swift*-XRT

The following Target-of-Opportunity (ToO) request was submitted via the Astrophysics Research Knowledgebase (ARK; see `https://heasarc.gsfc.nasa.gov/ark/`), provided by NASA's High Energy Astrophysics Science Archive Research Center (HEASARC).

Date	08 November, 2010
Target	1FGL J0030.7+0724
Urgency	Low Urgency
Source Position	RA: 7.6775 deg DEC: 7.4025 deg Error: 5 arcmin Epoch: J2000
Info	14.4 hrs from the Sun
Source Type or Description	Other: Counterpartless Fermi Source
Redshift	Unknown
Observation Most Critical to your Science Goals	Spectroscopy
Instrument Most Critical to your Science Goals	XRT (0.2–10 keV)
Source Brightness	XRT – (0.2–10 keV): 2.83E-2

Requested Observation:

Observation Type	Single Observation
Total Exposure Time	10 000 s
Exposure Time Justification	The requested observation aims at a detection and appropriate spectroscopy of an extended X-ray source (flux level 10^{-12} erg/cm^2/s), see scientific justification.
XRT Mode	Photon Counting (PC)
UVOT Filters	Default (Filter of the day)

Scientific Justification:

Structure formation within a LCDM-Universe predicts the presence of dark-matter (DM) clumps (subhalos) hosted by Milky Way-like galaxies. If DM is composed of heavy self-annihilating or decaying particles, these clumps are (expected to be) visible in the gamma-ray band as counterpartless, faint, non-variable, and possibly extended objects. Recent searches in the Fermi data reveal (at least) one promising candidate which is already listed in the first year's catalogue as 1FGL J0030.7+0724. The observed faint and steady high-energy flux can plausibly be explained by DM combined with a moderately enhanced annihilation cross section. Our analysis of available archival Fermi data favors a moderate extension of the source (0.1 deg), strengthening a dark matter origin. Multi-wavelength searches in the uncertainty area of the Fermi source (5 arcmin) have yielded no likely counterpart (e.g., Blazars, FSRQs, or pulsars) in the radio, optical, and X-ray bands. However, many DM scenarios predict X-ray fluxes at similar level of the gamma-ray flux ($10^{-12}\,\mathrm{erg\,cm^{-2}\,s^{-1}}$), generated by synchrotron emitting electrons. The positional uncertainty area was covered by ROSAT exhibiting no X-ray detection, but the corresponding exposure time (170 s) is insufficient to exclude an extended X-ray source of the predicted level. The source is currently observed with MAGIC and H.E.S.S. at very high energy gamma-rays. We propose X-ray follow-up observations with Swift's XRT carried out during the same epoch as ongoing VHE observations in the next month. The proposed observation is sufficient to detect an X-ray counterpart of 1FGL J0030.7+0724 and clarify the origin of the gamma-ray emission.

C.2 NOT service application

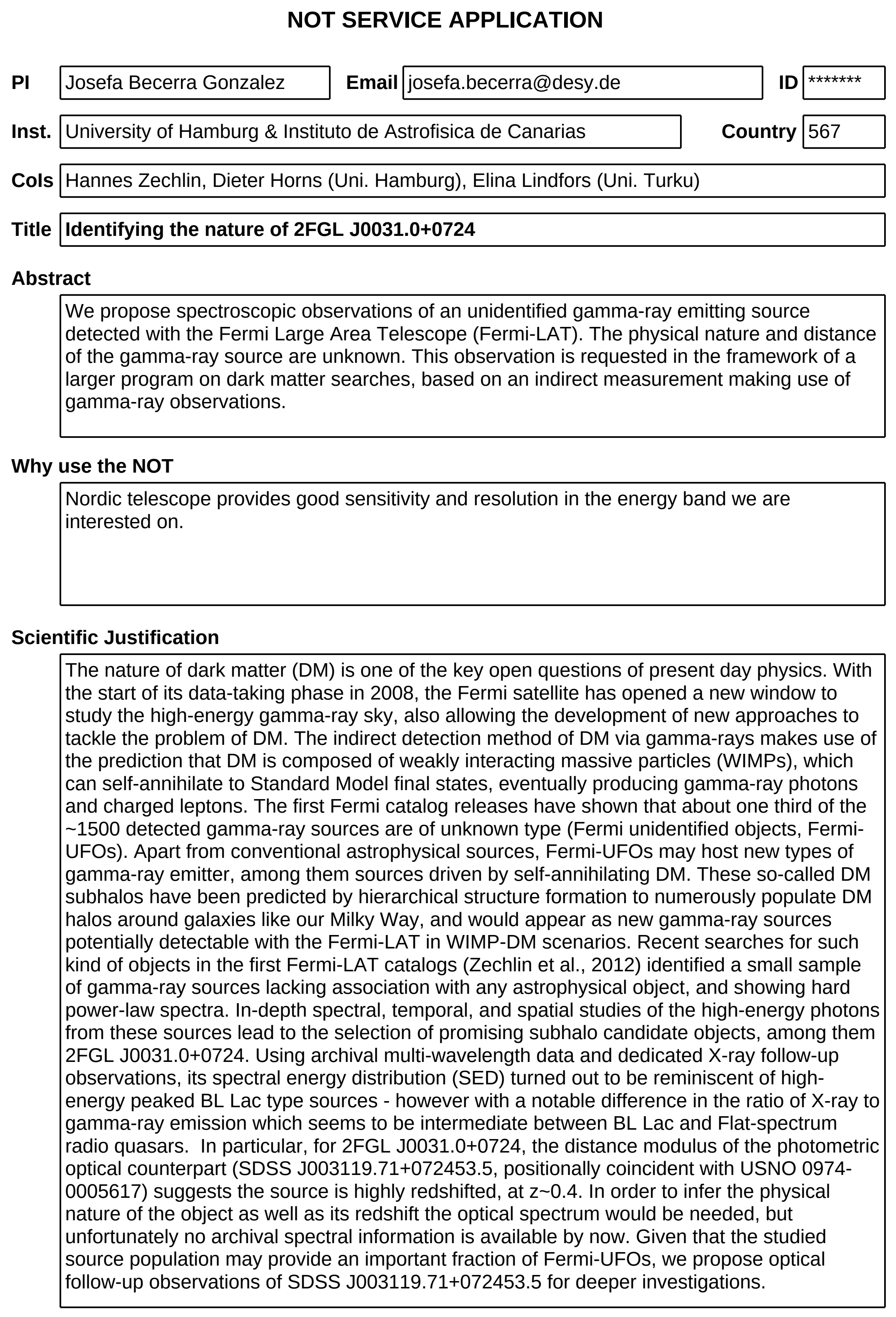

NOT SERVICE APPLICATION

PI	Josefa Becerra Gonzalez	**Email**	josefa.becerra@desy.de	**ID**	*******
Inst.	University of Hamburg & Instituto de Astrofisica de Canarias			**Country**	567

CoIs Hannes Zechlin, Dieter Horns (Uni. Hamburg), Elina Lindfors (Uni. Turku)

Title **Identifying the nature of 2FGL J0031.0+0724**

Abstract

We propose spectroscopic observations of an unidentified gamma-ray emitting source detected with the Fermi Large Area Telescope (Fermi-LAT). The physical nature and distance of the gamma-ray source are unknown. This observation is requested in the framework of a larger program on dark matter searches, based on an indirect measurement making use of gamma-ray observations.

Why use the NOT

Nordic telescope provides good sensitivity and resolution in the energy band we are interested on.

Scientific Justification

The nature of dark matter (DM) is one of the key open questions of present day physics. With the start of its data-taking phase in 2008, the Fermi satellite has opened a new window to study the high-energy gamma-ray sky, also allowing the development of new approaches to tackle the problem of DM. The indirect detection method of DM via gamma-rays makes use of the prediction that DM is composed of weakly interacting massive particles (WIMPs), which can self-annihilate to Standard Model final states, eventually producing gamma-ray photons and charged leptons. The first Fermi catalog releases have shown that about one third of the ~1500 detected gamma-ray sources are of unknown type (Fermi unidentified objects, Fermi-UFOs). Apart from conventional astrophysical sources, Fermi-UFOs may host new types of gamma-ray emitter, among them sources driven by self-annihilating DM. These so-called DM subhalos have been predicted by hierarchical structure formation to numerously populate DM halos around galaxies like our Milky Way, and would appear as new gamma-ray sources potentially detectable with the Fermi-LAT in WIMP-DM scenarios. Recent searches for such kind of objects in the first Fermi-LAT catalogs (Zechlin et al., 2012) identified a small sample of gamma-ray sources lacking association with any astrophysical object, and showing hard power-law spectra. In-depth spectral, temporal, and spatial studies of the high-energy photons from these sources lead to the selection of promising subhalo candidate objects, among them 2FGL J0031.0+0724. Using archival multi-wavelength data and dedicated X-ray follow-up observations, its spectral energy distribution (SED) turned out to be reminiscent of high-energy peaked BL Lac type sources - however with a notable difference in the ratio of X-ray to gamma-ray emission which seems to be intermediate between BL Lac and Flat-spectrum radio quasars. In particular, for 2FGL J0031.0+0724, the distance modulus of the photometric optical counterpart (SDSS J003119.71+072453.5, positionally coincident with USNO 0974-0005617) suggests the source is highly redshifted, at z~0.4. In order to infer the physical nature of the object as well as its redshift the optical spectrum would be needed, but unfortunately no archival spectral information is available by now. Given that the studied source population may provide an important fraction of Fermi-UFOs, we propose optical follow-up observations of SDSS J003119.71+072453.5 for deeper investigations.

Technical Description

The most probable emission lines present in the spectra are Lyman alpha (1215 A), MgII (2798 A), OII (3727 A), Hbeta (4861 A), OIII (5007 A), Halpha (6563 A) and NII (6584 A) in emission and CaII (3934 A), G band (4305 A) and MgI (5173 A) in absorption. Although the redshift is unknown, z~0.4 has been estimated (as discussed above). Therefore, we would like to optimize the range 4000-7000 A without fringes using grism 7. In case of FSRQs the optical spectra show strong emission lines, while the BL Lac objects emission lines are weaker. From previous successful spectroscopic searches (e.g. Sbarufatti et al. 2008), it was demonstrated that a high signal to noise ratio is needed for BL Lacs, and we see that we need at least S/N~100 per resolution element. With grism 7, this means S/N per pixel to be at least 44. Making use of the exposure time calculator for a source of magnitude 18.63, airmass 1.3, extinction 0.05, sky brightness gray, we estimated a observing time of 5 exposures of 2800 s, which can be adapted accordingly with the observations conditions.

Instrument Configuration

{ALFOSC}{Spectro-long-slit}{grism=7}
{ALFOSC}{Spectro-long-slit}{width=1"}

Targets

Source	RA (deg)	Dec (deg)	Magnitude (R-band)
SDSS J003119.71+072453.5	7.832121	+7.414878	18.63

Max Seeing Any **Weather** Clear **Moon** Any **Total Time** 14000 sec

C.3 Follow-up observations on the dark matter clump candidate 1FGL J0030.7+0724 with H.E.S.S.

H.-S. Zechlin[1], D. Horns[1], D. Elsässer[1,2], S. Januschek[1], N. Nguyen[1], B. Opitz[1]

[1] Universität Hamburg, Inst. f. Experimentalphysik, Luruper Chaussee 149, D-22761 Hamburg, Germany
[2] Universität Würzburg, D-97074 Würzburg, Germany

March 31, 2010

Abstract. *We propose a follow-up observation of the dark matter clump candidate in the Fermi source catalogue J0030.7+0724. This object does not have any counterpart at other wavelengths, is not variable, and has a hard spectrum (it is only detected significantly in the energy range above 10 GeV). Given the uncertainties on photon index and normalization, the extrapolated flux in the HESS energy range turns out to be between 1% and 70% of the Crab nebula's flux. With a 10 h exploratory exposure in the coming season (July–November), we anticipate a possible detection. In the case of a hint of a signal ($S \geq 3\sigma$), a secondary pointing of at least 10 h would then allow us to constrain the energy spectrum and improve the positional uncertainty. A detection of a line or a cutoff could reveal the origin of this dark source.*

C.3.1 Introduction

Assuming that the dominant amount of matter building up the entire Universe is dark (non-baryonic), results from numerical N-body simulations of structure formation (e.g., Aquarius and Via Lactea II, see Springel *et al.* 2008a; Diemand *et al.* 2008a) indicate that the dark halo surrounding a Milky-Way-like galaxy is built up of a smooth dark matter distribution and a non-negligible amount of virialized dark matter substructures (also called *clumps*). By today only a small number (approx. 23) of dwarf galaxies – which probably can be identified with dark matter clumps – are known and it may be assumed that most of the clumps do not contain any baryonic matter. Within the canonical model, dark matter could consist of a (new) massive elementary particle ($m_\chi = \mathcal{O}(100)\mathrm{GeV}$; WIMP) which can be self-annihilating and will reproduce the measured relic density if $\langle \sigma_\mathrm{A} v \rangle = 3 \times 10^{-26}\,\mathrm{cm}^3\,\mathrm{s}^{-1}$. The final states of the self-annihilation process lead to the emission of photons with energies within the HE/VHE band. Estimates show that – depending on the model/cross section – the *Fermi*-LAT experiment could be able to detect gamma-rays from dark matter annihilation of substructures within its planned operation phase (Pieri *et al.* 2011; Januschek 2010). To determine the (probably high) WIMP mass and the properties of dark matter, measurements in the VHE band and, therefore, by ground-based Cherenkov telescopes are essential. Combining all data it could be possible to unravel the nature of dark matter and the existence of substructures (*missing satellites problem*) with further observations.

C.3.2 Observational proposal

Recently, the *Fermi*-LAT Collaboration has published the First *Fermi*-LAT Source Catalog (1FGL) containing 1 451 detected gamma-ray sources ($> 4\sigma$), based on the analysis of the first 11 months of data (Abdo *et al.* 2010b). The sources are characterized in an energy range between 100 MeV and 100 GeV. In order to single out possible clump candidates we have scanned the catalogue[1] for unassociated, steady[2] gamma-ray point sources detected in the energy band between 10 GeV and 100 GeV. We have also constrained the candidate's locations to high galactic latitudes $|b_{\rm II}| > 20°$ in order to avoid confusion with conventional Galactic sources. A total of twelve unidentified sources (listed in Table C.1) pass the cuts. A more detailed breakdown of the applied cuts and cut efficiencies compared with identified AGN is listed in Table C.3.

Name	Ra (J2000)	Dec (J2000)	$\sigma_{\rm pos}$ [arcmin]	Spectral Index	$E_{\rm pivot}$ [MeV]	Energy Flux [10^{-11} erg cm^{-2}s^{-1}]
1FGL J0051.4–6242	00 51 29.6	−62 42 23	2.4	1.68 ± 0.12	2822.93	1.75 ± 0.46
1FGL J0143.9–5845	01 43 56.5	−58 45 42	3.0	1.95 ± 0.18	2151.91	1.44 ± 0.42
1FGL J0335.5–4501	03 35 31.2	−45 01 54	2.4	2.12 ± 0.17	1402.51	1.45 ± 0.37
1FGL J0614.1–3328	06 14 10.9	−33 28 43	1.2	1.93 ± 0.03	958.03	11.16 ± 0.60
1FGL J2134.5–2130	21 34 33.5	−21 30 21	3.0	1.92 ± 0.17	2346.57	1.12 ± 0.34
1FGL J0022.2–1850	00 22 16.5	−18 50 49	6.0	1.56 ± 0.14	4298.54	1.29 ± 0.38
1FGL J2146.6–1345	21 46 41.3	−13 45 13	3.0	1.82 ± 0.16	3173.25	1.51 ± 0.45
1FGL J0848.6+0504	08 48 41.1	+05 04 50	5.4	1.24 ± 0.35	12074.89	1.03 ± 0.46
1FGL J0030.7+0724	00 30 42.6	+07 24 09	3.0	1.68 ± 0.35	6705.91	1.03 ± 0.39
1FGL J1323.1+2942	13 23 06.1	+29 42 22	1.8	1.97 ± 0.12	1740.33	1.53 ± 0.38
1FGL J1754.3+3212	17 54 19.7	+32 12 07	2.4	2.09 ± 0.09	1223.00	2.61 ± 0.37
1FGL J2329.2+3755	23 29 12.1	+37 55 53	1.2	1.61 ± 0.17	5648.06	1.73 ± 0.47

Table C.1: Ordered by declination: unidentified, steady gamma-ray (point-)sources at high Galactic latitudes which are detected in the 10–100 GeV band can be found in the 1FGL catalogue. The table lists the name of the source, the position in equatorial coordinates (J2000.0), the uncertainty (68% CL) of the position, and the parameters of a power-law fit to the data. In the last column, the energy flux integrated between 100 MeV and 100 GeV is provided (Abdo *et al.* 2010b).

The differential energy flux $E^2\,{\rm d}N/{\rm d}E$ of all sources is shown in Figure C.2. Additionally, the best-fit power law is indicated. By extrapolation of the given power-law fit (Table C.1) we calculate the expected flux in the H.E.S.S. sensitivity range (between 400 GeV and 10 TeV). The uncertainties of the extrapolation are estimated by varying both the normalization and the photon index at the pivot energy $E_{\rm pivot}$. The resulting highest/lowest flux values are listed in per-centages of the Crab flux (Table C.2).

Given that the source identification procedure of the 1FGL catalogue does not include all available source catalogues to identify possible associations, we carried out a further search[3] for possible counterparts within the positional uncertainty of a source. Considering the positional uncertainty within the 68% confidence level, one source with no counterpart (1FGL J0030.7+0724) and two sources with galaxies inside the uncertainty area (1FGL J0335.5-4501, 1FGL J2329.2+3755) have been found[4]. Concerning the investigated dark matter scenario the other sources which have a possible counterpart detected in the radio or X-ray band can be discarded. Additional searches inside the 95%-region provide associations: For 1FGL J0030.7+0724 we find a faint radio source (NVSS J003030+072132,

---

[1] See also `http://fermi.gsfc.nasa.gov/ssc/data/access/lat/1yr_catalog/` for details.

[2] The cut on the variability excludes all sources with a probability to be steady < 1%.

[3] See `http://nedwww.ipac.caltech.edu/`

[4] Due to the curved spectrum (see Figure C.2) we reject the source 1FGL J0614.1-3328 for possible TeV observations and, therefore, it is not included in the following discussion.

Name	Possible Counterparts	Possible Counterparts	Flux [Crab]		
1FGL	68% CL	95% CL	low	mean	high
J0051.4–6242	2×G (20^{m}), QSO (17^{m})		11%	27%	65%
J0143.9–5845	RadioS, G (20^{m}), G (19^{m}), G (13^{m})		1%	3.8%	14%
J0335.5–4501	G (18^{m}), G (19^{m})	XrayS (ROSAT, dist. $3.8'$)	0.3%	1.3%	4.6%
J0614.1–3328	3EG J0616-3310, EGR J0615-3308		44%	57%	72%
J2134.5–2130	RadioS, 6×G (20^{m})		1%	4%	13%
J0022.2–1850	27×G, 2×RadioS		12%	33%	90%
J2146.6–1345	RadioS, XrayS, 4×G (20^{m})		3.3%	10%	30%
J0848.6+0504	G's, *'s, XrayS's, VisS's, RadioS's		9%	77%	624%
J0030.7+0724	–	RadioS (NVSS, dist. $3.9'$, 3.8 mJy @ 1.4 GHz)	**0.9%**	**8.1%**	**69%**
J1323.1+2942	G's, *'s, RadioS's, VisS's		1.7%	4.3%	10%
J1754.3+3212	RadioS		1.8%	3.6%	7.2%
J2329.2+3755	G (14^{m})	RadioS (NVSS, dist. $1.68'$, 20.4 mJy), XrayS (ROSAT, dist. $1.68'$)	9.1%	29%	87%

Table C.2: Multi-wavelength catalogue searches reveal possible counterparts for the sources not listed in the 1FGL catalogue. Possible counterparts within the 68% confidence level (CL) uncertainty area around the source are listed, for selected sources the search was broadened to the 95% CL. Note that the angle given in the third column means the distance of the source from the nominal *Fermi* position. The last three columns show the extrapolated flux for H.E.S.S. within the error bands of the power-law fit.

3.8 mJy @ 1.4 GHz) which is 3.9 arcmin away from the *Fermi* position. Since the probability for such a radio source lying in the uncertainty area by chance is $\approx 70\%$ and the distance between the Fermi position and the radio source is high this association is probably not real.

We therefore propose to observe the *Fermi* source 1FGL J0030.7+0724 for at least 10 h between July and November, when favorable zenith angles can be reached ($< 35°$). If the achieved significance will be $\geq 3\sigma$, we propose additional 10 h of observation. Details on the visibility of the source are shown in Figure C.1.

C.3.3 Impact of the observations

The general concept of performing VHE follow-up observations on hard spectrum *Fermi* sources has led to a number of newly discovered VHE AGN. The approach followed here, however, aims at singling out a dark/unidentified source at high Galactic latitude which would be consistent with a gamma-ray source powered by self-annihilating dark matter in a clump in the Galactic halo. As a caveat, it should be noted that the proposed object could be in fact an AGN. When comparing the cut efficiencies of the AGN sample with the unidentified source sample, they are similar (5% vs. 11%) – indicating that the two populations share general properties. It should be noted, however, that all *Fermi* identified AGN have radio counterparts which exceed 20 mJy, while the source proposed here has no counterpart (at the level of a few mJy sensitivity) in the 1σ error box. Typically, HE

Cut	Unidentified	AGN
—	671	693
$\lvert b_{\mathrm{II}} \rvert > 20°$	249 (100%)	539 (100%)
$\mathrm{var} < 23$	241 (96.8%)	372 (69.0%)
detection 10 — 100 GeV	12 (4.8%)	58 (10.8%)

Table C.3: Cuts applied for the search of possible clump candidates. The number of unidentified sources is compared to the number of AGN passing the cuts. Note that the cuts are cumulative, i.e., that each cut includes all cuts from above. The Galactic latitude is denoted by b_{II}, $\mathrm{var} < 23$ corresponds to a probability for a source to be steady > 1%, and the last cut assures the detection of a source in the energy bin $E \in [10; 100]\,\mathrm{GeV}$.

AGN have X-ray counterparts (mostly ROSAT detections) – for this dark source, no X-ray counterpart candidate exists. Even if the faint (3.8 mJy) radio source is indeed associated with the gamma-ray source, it would be revealing to search and find VHE gamma-rays from this dark object. This may be a new type of gamma-ray emitting AGN. The source location will be constrained to a smaller region by the VHE observations providing a better handle on the identification with multi-wavelength follow-up observations.

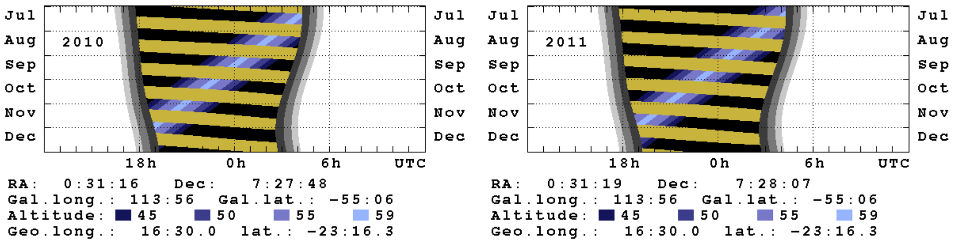

(a) 1FGL J0030.7+0724, Year 2010 **(b)** 1FGL J0030.7+0724, Year 2011

Figure C.1: Visibility of the Fermi source 1FGL J0030.7+0724 from the H.E.S.S. site during the years **(a)** 2010 and **(b)** 2011. From "Visibility of astronomical objects during darkness" by K. Bernlöhr.

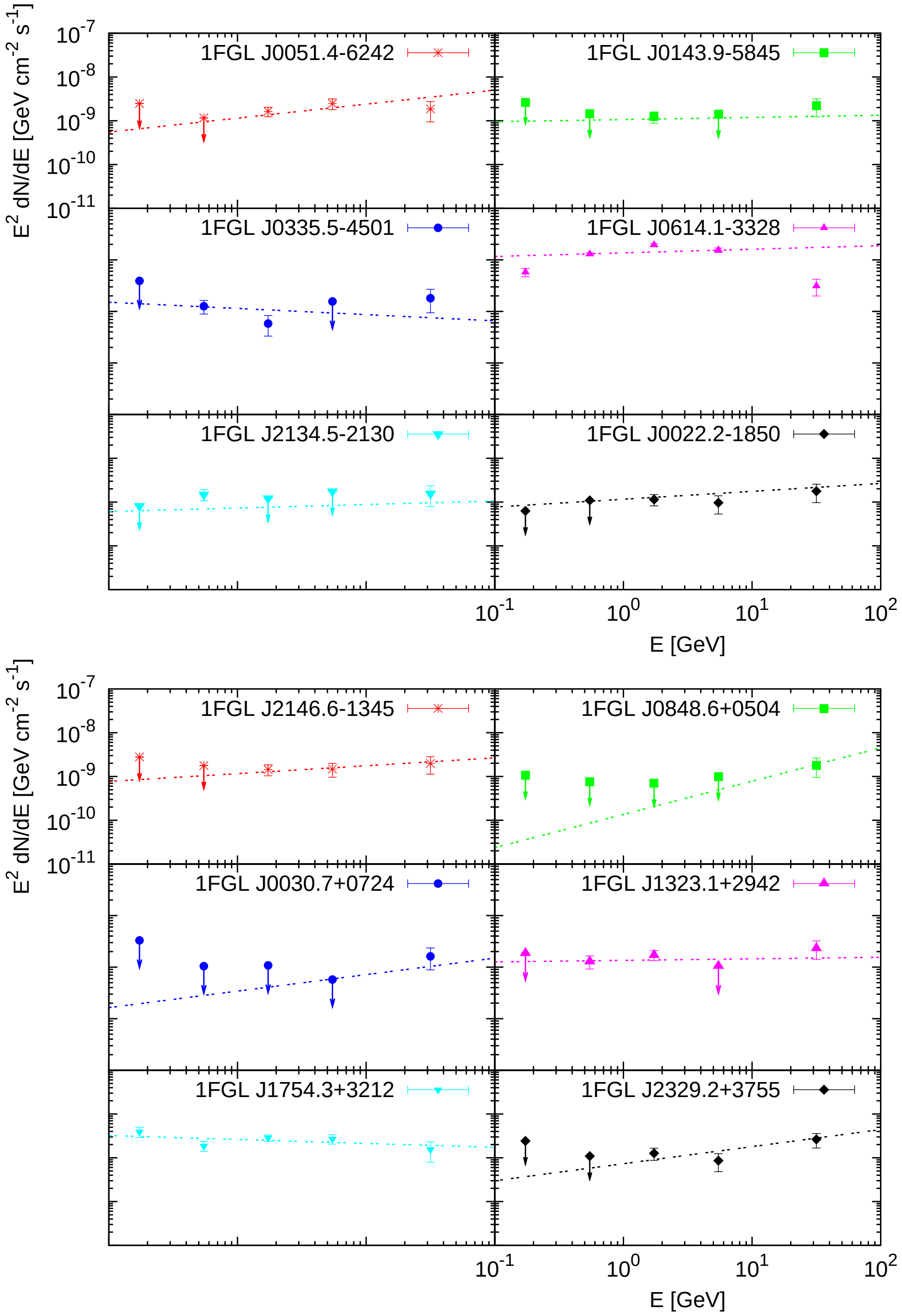

Figure C.2: Differential flux of the twelve 1FGL sources discussed in the text. Additionally, the best-fit power law is shown.

C.4 Reproposal for follow-up observations on the dark matter clump candidate 1FGL J0030.7+0724 with H.E.S.S.

H.-S. Zechlin[1], D. Horns[1], M. V. Fernandes[1], B. Giebels[2], N. Nguyen[1], B. Opitz[1]

[1] Universität Hamburg, Inst. f. Experimentalphysik, Luruper Chaussee 149, D-22761 Hamburg, Germany

[2] Laboratoire Leprince-Ringuet, École polytechnique, CNRS/IN2P3, Palaiseau, France

October 8, 2010

C.4.1 Observational proposal

The proposal 2010-1a "Follow-up observations on a dark matter clump candidate: 1FGL J0030.7+0724" had been presented at this years H.E.S.S.'s annual spring meeting in Hamburg and discussed within the Observation Committee (OC). Based on a working group decision (Astroparticle-WG) further progress on the properties and interpretation of the source was posted in an "Update on Follow-up observations on a dark matter clump candidate: 1FGL J0030.7+0724" (2010-1b) in September 2010. Furthermore, the analysis of the Fermi data presented below has been cross-checked by B. Giebels, obtaining similar results. Sequentially, the OC has decided to grant 15 h of observation within the period *p2010-10*.

Due to bad weather conditions during the beginning of October no observations have been applied by today. Accordingly, if the observations cannot be finished within the ongoing season, we propose to take the remaining observations within the upcoming season. In the case of a hint of a signal ($S \geq 3\sigma$), a secondary pointing of at least 10 h would allow us to constrain the energy spectrum and improve the positional uncertainty.

C.4.2 Source properties and interpretation

In the following, a summary of the current status of the analysis of the *Fermi* data, the update on the MWL analysis, and the interpretation of the source as a DM clump is attached, as given in the "Update on Follow-up observations on a dark matter clump candidate: 1FGL J0030.7+0724" (2010-1b). Furthermore, consequences of the source's possible AGN nature will be discussed. For an overview of the proposal's basic idea, conclusion, and source-visibility the reader is referred to the original proposal 2010-1a.

The public Fermi dataset on 1FGL J0030.7+0724 has been analyzed up to May 2010, using the standard public version of the Fermi Science Tools (v9r15p2, IRFs: P6_V3) with an unbinned likelihood analysis. We have reproduced the cataloged values for the spectral fit (see Table C.4). The average flux over the entire dataset has decreased by a factor of ≈ 1.5 with respect to the first eleven months (Table C.4 and Figure C.3). However, given the limited number of photons (six), no strong conclusion on the spectral shape or variability is possible. Within the errors the photon index remains stable. With respect to the 1yr-catalog the best-fit position shifts by $\approx 1.2'$, the radius of the 95% confidence level error circle is $\approx 5'$. The galactic foreground as well as the extragalactic background at $(l, b) = (113.96, -55.11)$ deg are negligible with respect to the source's signal, with an expected number of photons below one within the considered region of 0.5 deg.

From the power-law fit to the *Fermi* data the extrapolated flux for H.E.S.S. is calculated above 300 GeV, see Table C.5. Note that this is done assuming maximum anti-correlation between the errors of N_0 and Γ.

Dataset	Ra (J2000)	Dec (J2000)	N_0 $[10^{-15}\,\mathrm{MeV}^{-1}\,\mathrm{cm}^{-2}\,\mathrm{s}^{-1}]$	Spectral Index	E_{pivot} [MeV]
11 months	00 30 42.6	+07 24 09	14.00 ± 4.75	1.68 ± 0.35	6705.91
21 months	00 30 47.5	+07 24 20	9.89 ± 3.21	1.64 ± 0.31	6705.91

Table C.4: Comparison of spectral and positional properties of 1FGL J0030.7+0724 between the data published in the catalog (11 months) and the analysis of the 21-month dataset.

Name	Possible Counterparts	Possible Counterparts	$\phi(>300\,\mathrm{GeV})$ [Crab]		
	68% CL	95% CL	low	mean	high
1FGL J0030.7+0724	–	RadioS (NVSS, dist. 5′, 3.8 mJy @ 1.4 GHz)	0.8%	5.4%	35%

Table C.5: Multi-wavelength catalogue searches reveal possible counterparts for the sources not listed in the 1FGL catalog. Possible counterparts within the 68% and 95% confidence level (CL) uncertainty area around the source are listed. Note that the angular distance of 5′ given in the third column means the distance of the source from the *Fermi* position. The last three columns show the extrapolated flux for H.E.S.S. within the error-bands of the power-law fit, $\phi(>300\,\mathrm{GeV})$.

For interpretational purposes, we have also searched for a possible extension of the source by examining the likelihood-ratio between the likelihoods for an extended and a point source. This reveals a best fit source extension of $\Theta_{\mathrm{src}} = 0.11\,\mathrm{deg}$ and an upper limit (3σ) of $\Theta_{\mathrm{src}}^{99\%} \leq 0.43\,\mathrm{deg}$. Note that the final calibration of the *Fermi* point-spread function (PSF) may lead to a different result[5].

Further investigations have also been carried out to search possible (conventional) counterparts such as blazars. The faint radio source (NVSS J003030+072132, 3.8 mJy @ 1.4 GHz) is located within the 95% confidence level region, but no convincing counterpart for 1FGL J0030.7+0724 as well as for the radio source has been found at other wavelengths. We applied extensive searches in the optical and infrared databases USNO B1.0, SDSS, and 2MASS. Further searches are ongoing, maybe accompanied by follow-up proposals. The area of 1FGL J0030.7+0724 contains no detected X-ray source (ROSAT, see proposal).

In order to interpret the source as a possible DM clump an in-depth modeling has been carried out. We point out that, apart from the dependence on the subhalo model and the annihilation channel, this study relies only on the integrated source flux between 10 GeV and 100 GeV, $\phi_{\mathrm{src}}(10-100\,\mathrm{GeV})$ (published in the catalog or given by our analysis, respectively), its extension $\Theta_{\mathrm{src}}^{99\%}$, and its position (l, b) in the Galaxy.

The main result of this modeling is that the required boost factor $b = \langle\sigma_{\mathrm{A}} v\rangle / \langle\sigma_{\mathrm{A}} v\rangle_0$ is not larger than $b \geq 30 - 100\,(100 - 300)$ for a subhalo of mass $M_{\mathrm{clump}} = 10^6\,(10^4)\,\mathrm{M}_{\odot}$, depending on the assumed annihilation channel, i.e., $\tau^+\tau^-$ $(m_\chi = 150\,\mathrm{GeV})$ and W^+W^- $(m_\chi = 500\,\mathrm{GeV})$ for this case. The distance of such an object should be larger than $D_{\mathrm{min}} \geq 5\,(1)\,\mathrm{kpc}$. For comparison with the simple power-law extrapolations, in Table C.6 the expected *minimum* flux for H.E.S.S., $\phi(>300\,\mathrm{GeV})$, is listed in fractional Crab units (for the hadronic channels W^+W^- and $b\bar{b}$, and leptophilic channel $\tau^+\tau^-$). Note that the

---

[5] According to the calibration notes, the PSF at high energies is underestimated systematically.

DM model	$m_\chi = 500\,\mathrm{GeV}$		$m_\chi = 1\,\mathrm{TeV}$	
	b	$\phi(>300\,\mathrm{GeV})\,[\mathrm{Crab}]$	b	$\phi(>300\,\mathrm{GeV})\,[\mathrm{Crab}]$
W^+W^-	104	0.02 %	244	0.2 %
$b\overline{b}$	70	0.0006 %	152	0.04 %
$\tau^+\tau^-$	302	0.9 %	1529	9.1 %

Table C.6: The expected *minimum* flux for H.E.S.S., $\phi(>300\,\mathrm{GeV})$, in fractional Crab units as a function of the annihilation channel, the neutralino mass m_χ, and the required minimum boost factor b (which is also a function of m_χ).

required boost is also a function of the DM-particle mass.

The observed *Fermi* index is also compatible with a very hard AGN spectrum, such as those found for PG 1553 or 1ES 1440+122, but with a much fainter flux. Interestingly, the photon indexes found in the 1FGL catalog appear to not get any harder than the canonical index of 1.5 used as a constraint in some EBL studies, so constraining the VHE part of the hardest Fermi sources is important if this source turns out to be a blazar. VHE spectra can be estimated using a Franceschini EBL model and, provided the intrinsic spectrum extends up to the TeV range, the estimated flux is similar to the above mentioned one for nearby sources down to 0.1% Crab at $z = 0.2$. Any non-detection will yield a lower limit on the redshift of the source, which will be pushed farther out with increasing exposure, and provided the above assumption which is valid for many TeV blazars (Abdo *et al.* 2009b).

Note added: Due to subsequent improvements of the modeling, the interpretation of 1FGL J0030.7+0724 presented here differs from the final modeling reported in Publication I.

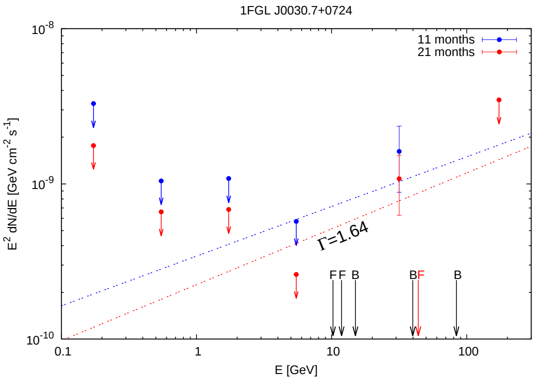

Figure C.3: Spectrum of 1FGL J0030.7+0724. The arrows indicate the energy of each photon measured between 10 GeV and 100 GeV, as well as the corresponding conversion type.

Bibliography

Aad, G., Abajyan, T., Abbott, B., *et al.* 2012a. Combined search for the Standard Model Higgs boson in pp collisions at s=7TeV with the ATLAS detector. Phys. Rev. D, **86**(3), 032003. ATLAS Collaboration.

Aad, G., Abbott, B., Abdallah, J., *et al.* 2012b. Combined search for the Standard Model Higgs boson using up to 4.9 fb^{-1} of pp collision data at s=7 TeV with the ATLAS detector at the LHC. *Physics Letters B*, **710**, 49–66. ATLAS Collaboration.

Aad, G., Abajyan, T., Abbott, B., *et al.* 2012c. Further search for supersymmetry at s=7TeV in final states with jets, missing transverse momentum, and isolated leptons with the ATLAS detector. Phys. Rev. D, **86**(9), 092002. ATLAS Collaboration.

Aad, G., Abajyan, T., Abbott, B., *et al.* 2012d. Search for supersymmetry in events with large missing transverse momentum, jets, and at least one tau lepton in 7 TeV proton-proton collision data with the ATLAS detector. *European Physical Journal C*, **72**, 2215. ATLAS Collaboration.

Aad, G., Abajyan, T., Abbott, B., *et al.* 2013a. Search for Dark Matter Candidates and Large Extra Dimensions in Events with a Photon and Missing Transverse Momentum in pp Collision Data at s=7TeV with the ATLAS Detector. *Physical Review Letters*, **110**(1), 011802. ATLAS Collaboration.

Aad, G., Abajyan, T., Abbott, B., *et al.* 2013b. Search for squarks and gluinos with the ATLAS detector in final states with jets and missing transverse momentum using 4.7fb^{-1} of s=7TeV proton-proton collision data. Phys. Rev. D, **87**(1), 012008. ATLAS Collaboration.

Aaij, R., Abellan Beteta, C., Adametz, A., *et al.* 2012. Strong Constraints on the Rare Decays $B_s^0 \to \mu^+\mu^-$ and $B^0 \to \mu^+\mu^-$. *Physical Review Letters*, **108**(23), 231801.

Aalseth, C. E., Barbeau, P. S., Colaresi, J., *et al.* 2011. Search for an Annual Modulation in a p-Type Point Contact Germanium Dark Matter Detector. *Physical Review Letters*, **107**(14), 141301.

Abate, A., Aldering, G., Allen, S., *et al.* 2012. Large Synoptic Survey Telescope: Dark Energy Science Collaboration. *arXiv:1211.0310*.

Abazajian, K. N., Agrawal, P., Chacko, Z., & Kilic, C. 2010. Conservative constraints on dark matter from the Fermi-LAT isotropic diffuse gamma-ray background spectrum. J. Cosmology Astropart. Phys., **11**, 41.

Abbasi, R., Abdou, Y., Abu-Zayyad, T., *et al.* 2011. Search for dark matter from the Galactic halo with the IceCube Neutrino Telescope. Phys. Rev. D, **84**(2), 022004. IceCube Collaboration.

Abbasi, R., Abdou, Y., Abu-Zayyad, T., *et al.* 2012a. Multiyear search for dark matter annihilations in the Sun with the AMANDA-II and IceCube detectors. Phys. Rev. D, **85**(4), 042002. IceCube Collaboration.

Abbasi, R., Abdou, Y., Ackermann, M., *et al.* 2012b. Search for Neutrinos from Annihilating Dark Matter in the Direction of the Galactic Center with the 40-String IceCube Neutrino Observatory. *arXiv:1210.3557*. IceCube Collaboration.

Abdo, A. A., Ackermann, M., Ajello, M., *et al.* 2009a. Fermi Large Area Telescope Measurements of the Diffuse Gamma-Ray Emission at Intermediate Galactic Latitudes. *Physical Review Letters*, **103**(25), 251101. Fermi-LAT Collaboration.

ABDO, A. A., ACKERMANN, M., AJELLO, M., *et al.* 2009b. Fermi Observations of TeV-Selected Active Galactic Nuclei. ApJ, **707**, 1310–1333. Fermi-LAT Collaboration.

ABDO, A. A., ACKERMANN, M., AJELLO, M., *et al.* 2009c. Measurement of the Cosmic Ray $e^{+}+e^{-}$ Spectrum from 20GeV to 1TeV with the Fermi Large Area Telescope. *Physical Review Letters*, **102**(18), 181101. Fermi-LAT Collaboration.

ABDO, A. A., ACKERMANN, M., AJELLO, M., *et al.* 2010a. Constraints on cosmological dark matter annihilation from the Fermi-LAT isotropic diffuse gamma-ray measurement. J. Cosmology Astropart. Phys., **4**, 14. Fermi-LAT Collaboration.

ABDO, A. A., ACKERMANN, M., AJELLO, M., *et al.* 2010b. Fermi Large Area Telescope First Source Catalog. ApJS, **188**, 405–436. Fermi-LAT Collaboration.

ABEYSEKARA, A. U., AGUILAR, J. A., AGUILAR, S., *et al.* 2012. On the sensitivity of the HAWC observatory to gamma-ray bursts. *Astroparticle Physics*, **35**, 641–650.

ABRAMOWSKI, A., ACERO, F., AHARONIAN, F., *et al.* 2011a. H.E.S.S. constraints on dark matter annihilations towards the sculptor and carina dwarf galaxies. *Astroparticle Physics*, **34**, 608–616. H.E.S.S. Collaboration.

ABRAMOWSKI, A., ACERO, F., AHARONIAN, F., *et al.* 2011b. H.E.S.S. Observations of the Globular Clusters NGC 6388 and M15 and Search for a Dark Matter Signal. ApJ, **735**, 12. H.E.S.S. Collaboration.

ABRAMOWSKI, A., ACERO, F., AHARONIAN, F., *et al.* 2011c. Search for a Dark Matter Annihilation Signal from the Galactic Center Halo with H.E.S.S. *Physical Review Letters*, **106**(16), 161301. H.E.S.S. Collaboration.

ABRAMOWSKI, A., ACERO, F., AHARONIAN, F., *et al.* 2013. Search for Photon-Linelike Signatures from Dark Matter Annihilations with H.E.S.S. *Physical Review Letters*, **110**(4), 041301. H.E.S.S. Collaboration.

ACCIARI, V. A., ARLEN, T., AUNE, T., *et al.* 2010. VERITAS Search for VHE Gamma-ray Emission from Dwarf Spheroidal Galaxies. ApJ, **720**, 1174–1180. VERITAS Collaboration.

ACKERMANN, M., AJELLO, M., ALLAFORT, A., *et al.* 2010a. Constraints on dark matter annihilation in clusters of galaxies with the Fermi large area telescope. J. Cosmology Astropart. Phys., **5**, 25. Fermi-LAT Collaboration.

ACKERMANN, M., AJELLO, M., ATWOOD, W. B., *et al.* 2010b. Fermi LAT observations of cosmic-ray electrons from 7 GeV to 1 TeV. Phys. Rev. D, **82**(9), 092004. Fermi-LAT Collaboration.

ACKERMANN, M., AJELLO, M., ATWOOD, W. B., *et al.* 2010c. Searches for cosmic-ray electron anisotropies with the Fermi Large Area Telescope. Phys. Rev. D, **82**(9), 092003. Fermi-LAT Collaboration.

ACKERMANN, M., AJELLO, M., ALBERT, A., *et al.* 2011. Constraining Dark Matter Models from a Combined Analysis of Milky Way Satellites with the Fermi Large Area Telescope. *Physical Review Letters*, **107**(24), 241302. Fermi-LAT Collaboration.

ACKERMANN, M., AJELLO, M., ALBERT, A., *et al.* 2012a. Fermi LAT search for dark matter in gamma-ray lines and the inclusive photon spectrum. Phys. Rev. D, **86**(2), 022002. Fermi-LAT Collaboration.

ACKERMANN, M., AJELLO, M., ALLAFORT, A., *et al.* 2012b. Measurement of Separate Cosmic-Ray Electron and Positron Spectra with the Fermi Large Area Telescope. *Physical Review Letters*, **108**(1), 011103. Fermi-LAT Collaboration.

ACKERMANN, M., AJELLO, M., ALBERT, A., *et al.* 2012c. The Fermi Large Area Telescope on Orbit: Event Classification, Instrument Response Functions, and Calibration. ApJS, **203**, 4. Fermi-LAT Collaboration.

ACKERMANN, M., AJELLO, M., ALBERT, A., *et al.* 2013. Search for Gamma-ray Spectral Lines with the Fermi Large Area Telescope and Dark Matter Implications. *arXiv:1305.5597.* Fermi-LAT Collaboration.

ACTIS, M., AGNETTA, G., AHARONIAN, F., *et al.* 2011. Design concepts for the Cherenkov Telescope Array CTA: an advanced facility for ground-based high-energy gamma-ray astronomy. *Experimental Astronomy*, **32**, 193–316. The CTA Consortium.

ADE, P. A. R., AGHANIM, N., ARMITAGE-CAPLAN, C., *et al.* 2013a. Planck 2013 results. I. Overview of products and scientific results. *arXiv:1303.5062*. Planck Collaboration.

ADE, P. A. R., AGHANIM, N., ARMITAGE-CAPLAN, C., *et al.* 2013b. Planck 2013 results. XVI. Cosmological parameters. *arXiv:1303.5076*. Planck Collaboration.

ADE, P. A. R., AGHANIM, N., ARMITAGE-CAPLAN, C., *et al.* 2013c. Planck 2013 Results. XXIV. Constraints on primordial non-Gaussianity. *arXiv:1303.5084*. Planck Collaboration.

ADRIÁN-MARTINEZ, S., SAMARAI, I. A., ALBERT, A., *et al.* 2013. First Search for Dark Matter Annihilation in the Sun Using the ANTARES Neutrino Telescope. *arXiv:1302.6516*. ANTARES Collaboration.

ADRIANI, O., BARBARINO, G. C., BAZILEVSKAYA, G. A., *et al.* 2009. An anomalous positron abundance in cosmic rays with energies 1.5-100GeV. Nature, **458**, 607–609.

ADRIANI, O., BARBARINO, G. C., BAZILEVSKAYA, G. A., *et al.* 2011. Cosmic-Ray Electron Flux Measured by the PAMELA Experiment between 1 and 625 GeV. *Physical Review Letters*, **106**(20), 201101.

AGUILAR, M., ALBERTI, G., ALPAT, B., *et al.* 2013. First Result from the Alpha Magnetic Spectrometer on the International Space Station: Precision Measurement of the Positron Fraction in Primary Cosmic Rays of 0.5–350 GeV. *Phys. Rev. Lett.*, **110**, 141102. AMS Collaboration.

AHARONIAN, F., AKHPERJANIAN, A. G., AYE, K.-M., *et al.* 2004. Very high energy gamma rays from the direction of Sagittarius A*. A&A, **425**, L13–L17. H.E.S.S. Collaboration.

AHARONIAN, F., AKHPERJANIAN, A. G., BAZER-BACHI, A. R., *et al.* 2006a. Discovery of very-high-energy γ-rays from the Galactic Centre ridge. Nature, **439**, 695–698. H.E.S.S. Collaboration.

AHARONIAN, F., AKHPERJANIAN, A. G., BAZER-BACHI, A. R., *et al.* 2006b. HESS Observations of the Galactic Center Region and Their Possible Dark Matter Interpretation. *Physical Review Letters*, **97**(22), 221102. H.E.S.S. Collaboration.

AHARONIAN, F., AKHPERJANIAN, A. G., BAZER-BACHI, A. R., *et al.* 2006c. Observations of the Crab nebula with HESS. A&A, **457**, 899–915. H.E.S.S. Collaboration.

AHARONIAN, F., AKHPERJANIAN, A. G., BARRES DE ALMEIDA, U., *et al.* 2008a. Energy Spectrum of Cosmic-Ray Electrons at TeV Energies. *Physical Review Letters*, **101**(26), 261104. H.E.S.S. Collaboration.

AHARONIAN, F., AKHPERJANIAN, A. G., BAZER-BACHI, A. R., *et al.* 2008b. Observations of the Sagittarius dwarf galaxy by the HESS experiment and search for a dark matter signal. *Astroparticle Physics*, **29**, 55–62. H.E.S.S. Collaboration.

AHARONIAN, F., AKHPERJANIAN, A. G., DE ALMEIDA, U. B., *et al.* 2009a. A Search for a Dark Matter Annihilation Signal Toward the Canis Major Overdensity with H.E.S.S. ApJ, **691**, 175–181. H.E.S.S. Collaboration.

AHARONIAN, F., AKHPERJANIAN, A. G., ANTON, G., *et al.* 2009b. Probing the ATIC peak in the cosmic-ray electron spectrum with H.E.S.S. A&A, **508**, 561–564. H.E.S.S. Collaboration.

AHARONIAN, F., AKHPERJANIAN, A. G., BAZER-BACHI, A. R., *et al.* 2010. Erratum to "Observations of the Sagittarius dwarf galaxy by the HESS experiment and search for a dark matter signal" [Astropart. Phys. 29(1) (2008) 55-62]. *Astroparticle Physics*, **33**, 274–275. H.E.S.S. Collaboration.

AHARONIAN, F., KHANGULYAN, D., & MALYSHEV, D. 2012. Cold ultrarelativistic pulsar winds as potential sources of galactic gamma-ray lines above 100 GeV. A&A, **547**, A114.

AHMED, Z., AKERIB, D. S., ARMENGAUD, E., *et al.* 2011. Combined limits on WIMPs from the CDMS and EDELWEISS experiments. Phys. Rev. D, **84**(1), 011102.

AHN, K., & SHAPIRO, P. R. 2005. Formation and evolution of self-interacting dark matter haloes. MNRAS, **363**, 1092–1110.

AIHARA, H., ALLENDE PRIETO, C., AN, D., *et al.* 2011a. Erratum: "The Eighth Data Release of the Sloan Digital Sky Survey: First Data from SDSS-III" (2011, ApJS, 193, 29). ApJS, **195**, 26.

AIHARA, H., ALLENDE PRIETO, C., AN, D., *et al.* 2011b. The Eighth Data Release of the Sloan Digital Sky Survey: First Data from SDSS-III. ApJS, **193**, 29.

AKIMOV, D. Y., ARAÚJO, H. M., BARNES, E. J., *et al.* 2012. WIMP-nucleon cross-section results from the second science run of ZEPLIN-III. *Physics Letters B*, **709**, 14–20.

ALBERT, J., ALIU, E., ANDERHUB, H., *et al.* 2006. Observation of Gamma Rays from the Galactic Center with the MAGIC Telescope. ApJ, **638**, L101–L104. MAGIC Collaboration.

ALBERT, J., ALIU, E., ANDERHUB, H., *et al.* 2008a. Upper Limit for γ-Ray Emission above 140 GeV from the Dwarf Spheroidal Galaxy Draco. ApJ, **679**, 428–431.

ALBERT, J., ALIU, E., ANDERHUB, H., *et al.* 2008b. VHE γ-Ray Observation of the Crab Nebula and its Pulsar with the MAGIC Telescope. ApJ, **674**, 1037–1055. MAGIC Collaboration.

ALEKSIĆ, J., ANTONELLI, L. A., ANTORANZ, P., *et al.* 2010. MAGIC Gamma-ray Telescope Observation of the Perseus Cluster of Galaxies: Implications for Cosmic Rays, Dark Matter, and NGC 1275. ApJ, **710**, 634–647. MAGIC Collaboration.

ALEKSIĆ, J., ALVAREZ, E. A., ANTONELLI, L. A., *et al.* 2011. Searches for dark matter annihilation signatures in the Segue 1 satellite galaxy with the MAGIC-I telescope. J. Cosmology Astropart. Phys., **6**, 35. MAGIC Collaboration.

ALIU, E., ANDERHUB, H., ANTONELLI, L. A., *et al.* 2009. Upper Limits on the VHE Gamma-Ray Emission from the Willman 1 Satellite Galaxy with the Magic Telescope. ApJ, **697**, 1299–1304. MAGIC Collaboration.

ALIU, E., ARLEN, T., AUNE, T., *et al.* 2011. Detection of Pulsed Gamma Rays Above 100 GeV from the Crab Pulsar. *Science*, **334**, 69. VERITAS Collaboration.

ALIU, E., ARCHAMBAULT, S., ARLEN, T., *et al.* 2012. VERITAS deep observations of the dwarf spheroidal galaxy Segue 1. Phys. Rev. D, **85**(6), 062001. VERITAS Collaboration.

AMENOMORI, M., BI, X. J., CHEN, D., *et al.* 2009. Multi-TeV Gamma-Ray Observation from the Crab Nebula Using the Tibet-III Air Shower Array Finely Tuned by the Cosmic Ray Moon's Shadow. ApJ, **692**, 61–72.

AMORISCO, N. C., & EVANS, N. W. 2012. Dark matter cores and cusps: the case of multiple stellar populations in dwarf spheroidals. MNRAS, **419**, 184–196.

AN, H., POSPELOV, M., & PRADLER, J. 2013. New stellar constraints on dark photons. *arXiv:1302.3884*.

ANDERSON, L., AUBOURG, E., BAILEY, S., *et al.* 2012. The clustering of galaxies in the SDSS-III Baryon Oscillation Spectroscopic Survey: baryon acoustic oscillations in the Data Release 9 spectroscopic galaxy sample. MNRAS, **427**, 3435–3467.

ANGLOHER, G., BAUER, M., BAVYKINA, I., *et al.* 2012. Results from 730 kg days of the CRESST-II Dark Matter search. *European Physical Journal C*, **72**, 1971.

APPELQUIST, T., CHENG, H.-C., & DOBRESCU, B. A. 2001. Bounds on universal extra dimensions. Phys. Rev. D, **64**(3), 035002.

APRILE, E., ALFONSI, M., ARISAKA, K., *et al.* 2012. Dark Matter Results from 225 Live Days of XENON100 Data. *Physical Review Letters*, **109**(18), 181301. XENON100 Collaboration.

ARCHAMBAULT, S., BEHNKE, E., BHATTACHARJEE, P., *et al.* 2012. Constraints on low-mass WIMP interactions on ^{19}F from PICASSO. *Physics Letters B*, **711**, 153–161.

ARIAS, P., CADAMURO, D., GOODSELL, M., *et al.* 2012. WISPy cold dark matter. J. Cosmology Astropart. Phys., **6**, 13.

ARIK, M., AUNE, S., BARTH, K., *et al.* 2011. Search for Sub-eV Mass Solar Axions by the CERN Axion Solar Telescope with He3 Buffer Gas. *Physical Review Letters*, **107**(26), 261302.

ARKANI-HAMED, N., DIMOPOULOS, S., & DVALI, G. 1998. The hierarchy problem and new dimensions at a millimeter. *Physics Letters B*, **429**, 263–272.

ARMENGAUD, E., AUGIER, C., BENOÎT, A., *et al.* 2011. Final results of the EDELWEISS-II WIMP search using a 4-kg array of cryogenic germanium detectors with interleaved electrodes. *Physics Letters B*, **702**, 329–335. EDELWEISS Collaboration.

ASZTALOS, S. J., CAROSI, G., HAGMANN, C., *et al.* 2010. SQUID-Based Microwave Cavity Search for Dark-Matter Axions. *Physical Review Letters*, **104**(4), 041301. ADMX Collaboration.

ATKINS, R., BENBOW, W., BERLEY, D., *et al.* 2004. TeV Gamma-Ray Survey of the Northern Hemisphere Sky Using the Milagro Observatory. ApJ, **608**, 680–685.

ATWOOD, W., ALBERT, A., BALDINI, L., *et al.* 2013. Pass 8: Toward the Full Realization of the Fermi-LAT Scientific Potential. *In: 2012 Fermi Symposium proceedings - eConf C121028*. arXiv:1303.3514, Fermi-LAT Collaboration.

ATWOOD, W. B., ABDO, A. A., ACKERMANN, M., *et al.* 2009. The Large Area Telescope on the Fermi Gamma-Ray Space Telescope Mission. ApJ, **697**, 1071–1102. Fermi-LAT Collaboration.

BAAK, M., GOEBEL, M., HALLER, J., *et al.* 2012a. The electroweak fit of the standard model after the discovery of a new boson at the LHC. *European Physical Journal C*, **72**, 2205.

BAAK, M., GOEBEL, M., HALLER, J., *et al.* 2012b. Updated status of the global electroweak fit and constraints on new physics. *European Physical Journal C*, **72**, 2003.

BABCOCK, H. W. 1939. The rotation of the Andromeda Nebula. *Lick Observatory Bulletin*, **19**, 41–51.

BÄHRE, R., DÖBRICH, B., DREYLING-ESCHWEILER, J., *et al.* 2013. Any light particle search II – Technical Design Report. *Journal of Instrumentation*, **8**, 9001.

BALTZ, E. A., & WAI, L. 2004. Diffuse inverse Compton and synchrotron emission from dark matter annihilations in galactic satellites. Phys. Rev. D, **70**(2), 023512.

BALTZ, E. A., TAYLOR, J. E., & WAI, L. L. 2007. Can Astrophysical Gamma-Ray Sources Mimic Dark Matter Annihilation in Galactic Satellites? ApJ, **659**, L125–L128.

BAND, D. L., & GRINDLAY, J. E. 1985. The synchrotron-self-Compton process in spherical geometries. I - Theoretical framework. ApJ, **298**, 128–146.

BARBIERI, R., GREGOIRE, T., & HALL, L. J. 2005. Mirror World at the Large Hadron Collider. *arXiv:hep-ph/0509242*.

BECHERINI, Y., & PUNCH, M. 2012. Performance of HESS-II in multi-telescope mode with a multi-variate analysis. *Pages 741–744 of: 5th International Meeting on High Energy Gamma-Ray Astronomy, July 9–13, 2012, Heidelberg, Germany*. AIP Conf. Proc., vol. 1505. H.E.S.S. Collaboration.

BECHTLE, P., BRINGMANN, T., DESCH, K., *et al.* 2012. Constrained supersymmetry after two years of LHC data: a global view with Fittino. *Journal of High Energy Physics*, **6**, 98.

BEGEMAN, K. G., BROEILS, A. H., & SANDERS, R. H. 1991. Extended rotation curves of spiral galaxies - Dark haloes and modified dynamics. MNRAS, **249**, 523–537.

BEHNKE, E., BEHNKE, J., BRICE, S. J., *et al.* 2012. First dark matter search results from a 4-kg CF_3I bubble chamber operated in a deep underground site. Phys. Rev. D, **86**(5), 052001.

BEKENSTEIN, J. D. 2010. *Modified gravity as an alternative to dark matter*. Cambridge University Press. Page 99.

BÉLANGER, G., KAKIZAKI, M., & PUKHOV, A. 2011. Dark matter in UED: the role of the second KK level. J. Cosmology Astropart. Phys., **2**, 9.

BEREZINSKY, V., DOKUCHAEV, V., & EROSHENKO, Y. 2003. Small-scale clumps in the galactic halo and dark matter annihilation. Phys. Rev. D, **68**(10), 103003.

BEREZINSKY, V., DOKUCHAEV, V., & EROSHENKO, Y. 2006. Destruction of small-scale dark matter clumps in the hierarchical structures and galaxies. Phys. Rev. D, **73**(6), 063504.

BERGSTRÖM, L., ULLIO, P., & BUCKLEY, J. H. 1998. Observability of gamma rays from dark matter neutralino annihilations in the Milky Way halo. *Astroparticle Physics*, **9**, 137–162.

BERGSTRÖM, L., BERTONE, G., BRINGMANN, T., *et al.* 2009. Gamma-ray and radio constraints of high positron rate dark matter models annihilating into new light particles. Phys. Rev. D, **79**(8), 081303.

BERGSTRÖM, L., BERTONE, G., CONRAD, J., FARNIER, C., & WENIGER, C. 2012. Investigating gamma-ray lines from dark matter with future observatories. J. Cosmology Astropart. Phys., **11**, 25.

BERINGER, J., ARGUIN, J.-F., BARNETT, R. M., *et al.* 2012. Review of Particle Physics. Phys. Rev. D, **86**(1), 010001. `http://pdg.lbl.gov/`.

BERNABEI, R., BELLI, P., CAPPELLA, F., *et al.* 2008. First results from DAMA/LIBRA and the combined results with DAMA/NaI. *European Physical Journal C*, **56**, 333.

BERTONE, G. 2010a. *Particle Dark Matter : Observations, Models and Searches*. Cambridge University Press.

BERTONE, G. 2010b. The moment of truth for WIMP dark matter. Nature, **468**, 389–393.

BERTONE, G., HOOPER, D., & SILK, J. 2005. Particle dark matter: evidence, candidates and constraints. Phys. Rep., **405**, 279–390.

BERTONE, G., BUCHMÜLLER, W., COVI, L., & IBARRA, A. 2007. Gamma-rays from decaying dark matter. J. Cosmology Astropart. Phys., **11**, 3.

BINNEY, J., & TREMAINE, S. 2008. *Galactic Dynamics: Second Edition*. Princeton University Press, NJ, USA.

BLUMENTHAL, G. R., FABER, S. M., FLORES, R., & PRIMACK, J. R. 1986. Contraction of dark matter galactic halos due to baryonic infall. ApJ, **301**, 27–34.

BODE, P., OSTRIKER, J. P., & TUROK, N. 2001. Halo Formation in Warm Dark Matter Models. ApJ, **556**, 93–107.

BOJOWALD, M. 2008. Loop Quantum Cosmology. *Living Reviews in Relativity*, **11**, 4.

BOJOWALD, M., & PAILY, G. M. 2012. A no-singularity scenario in loop quantum gravity. *Classical and Quantum Gravity*, **29**(24), 242002.

BOND, J. R., KOFMAN, L., & POGOSYAN, D. 1996. How filaments of galaxies are woven into the cosmic web. Nature, **380**, 603–606.

BORLA TRIDON, D., COLIN, P., COSSIO, L., *et al.* 2011. Measurement of the cosmic electron spectrum with the MAGIC telescopes. *Page 43 of: 32nd International Cosmic Ray Conference, August 11-18, 2011, Beijing, China*. Vol. 6 OG1: Cosmic Ray Origin and Galactic Phenomena. arXiv:1110.4008.

BORM, K. 2010 (Aug.). *Research on a Possible Dark Matter Substructure within the Galactic Halo*. Bachelor's thesis, Universität Hamburg, Hamburg, Germany.

BORRIELLO, E., CUOCO, A., & MIELE, G. 2009. Radio constraints on dark matter annihilation in the galactic halo and its substructures. Phys. Rev. D, **79**(2), 023518.

BÖTTCHER, M., DERMER, C. D., & FINKE, J. D. 2008. The Hard VHE γ-Ray Emission in High-Redshift TeV Blazars: Comptonization of Cosmic Microwave Background Radiation in an Extended Jet? ApJ, **679**, L9–L12.

BOYLAN-KOLCHIN, M., BULLOCK, J. S., & KAPLINGHAT, M. 2011. Too big to fail? The puzzling darkness of massive Milky Way subhaloes. MNRAS, **415**, L40–L44.

BOYLAN-KOLCHIN, M., BULLOCK, J. S., & KAPLINGHAT, M. 2012. The Milky Way's bright satellites as an apparent failure of ΛCDM. MNRAS, **422**, 1203–1218.

BRADAČ, M., CLOWE, D., GONZALEZ, A. H., *et al.* 2006. Strong and Weak Lensing United. III. Measuring the Mass Distribution of the Merging Galaxy Cluster 1ES 0657-558. ApJ, **652**, 937–947.

BRADAČ, M., ALLEN, S. W., TREU, T., *et al.* 2008. Revealing the Properties of Dark Matter in the Merging Cluster MACS J0025.4-1222. ApJ, **687**, 959–967.

BRINGMANN, T. 2009. Particle models and the small-scale structure of dark matter. *New Journal of Physics*, **11**(10), 105027.

BRINGMANN, T. 2011. *Dark Matter - Lecture Notes.*
`http://www.desy.de/~troms/teaching/SoSe11/index.html.`

BRINGMANN, T., & SALATI, P. 2007. Galactic antiproton spectrum at high energies: Background expectation versus exotic contributions. Phys. Rev. D, **75**(8), 083006.

BRINGMANN, T., & WENIGER, C. 2012. Gamma ray signals from dark matter: Concepts, status and prospects. *Physics of the Dark Universe*, **1**, 194–217.

BRINGMANN, T., BERGSTRÖM, L., & EDSJÖ, J. 2008. New gamma-ray contributions to supersymmetric dark matter annihilation. *Journal of High Energy Physics*, **1**, 49.

BRINGMANN, T., HUANG, X., IBARRA, A., VOGL, S., & WENIGER, C. 2012. Fermi LAT search for internal bremsstrahlung signatures from dark matter annihilation. J. Cosmology Astropart. Phys., **7**, 54.

BROWN, T. M., TUMLINSON, J., GEHA, M., *et al.* 2012. The Primeval Populations of the Ultra-faint Dwarf Galaxies. ApJ, **753**, L21.

BRUN, P., DELAHAYE, T., DIEMAND, J., *et al.* 2009. Cosmic ray lepton puzzle in the light of cosmological N-body simulations. Phys. Rev. D, **80**(3), 035023.

BRYAN, G. L., & NORMAN, M. L. 1998. Statistical Properties of X-Ray Clusters: Analytic and Numerical Comparisons. ApJ, **495**, 80–99.

BUCHMUELLER, O., CAVANAUGH, R., DE ROECK, A., *et al.* 2007. Prediction for the lightest Higgs boson mass in the CMSSM using indirect experimental constraints. *Physics Letters B*, **657**, 87–94.

BUCHMUELLER, O., CAVANAUGH, R., CITRON, M., *et al.* 2012. The CMSSM and NUHM1 in light of 7 TeV LHC, $B_s \to \mu^+\mu^-$ and XENON100 data. *European Physical Journal C*, **72**, 2243.

BUCHMÜLLER, W., COVI, L., HAMAGUCHI, K., *et al.* 2007. Gravitino dark matter in R-parity breaking vacua. *Journal of High Energy Physics*, **3**, 37.

BUCHMÜLLER, W., IBARRA, A., SHINDOU, T., *et al.* 2009. Probing gravitino dark matter with PAMELA and Fermi. J. Cosmology Astropart. Phys., **9**, 21.

BULLOCK, J. S. 2010. Notes on the Missing Satellites Problem. *arXiv:1009.4505*.

BULLOCK, J. S., KOLATT, T. S., SIGAD, Y., *et al.* 2001. Profiles of dark haloes: evolution, scatter and environment. MNRAS, **321**, 559–575.

BULLOCK, J. S., STEWART, K. R., KAPLINGHAT, M., *et al.* 2010. Stealth Galaxies in the Halo of the Milky Way. ApJ, **717**, 1043–1053.

BURGESS, C. P., POSPELOV, M., & TER VELDHUIS, T. 2001. The Minimal Model of nonbaryonic dark matter: a singlet scalar. *Nuclear Physics B*, **619**, 709–728.

BURKERT, A. 1995. The Structure of Dark Matter Halos in Dwarf Galaxies. ApJ, **447**, L25.

CADAMURO, D., & REDONDO, J. 2012. Cosmological bounds on pseudo Nambu-Goldstone bosons. J. Cosmology Astropart. Phys., **2**, 32.

CALDERONE, G., GHISELLINI, G., COLPI, M., & DOTTI, M. 2013. Black hole mass estimate for a sample of radio-loud narrow-line Seyfert 1 galaxies. MNRAS, **431**, 210–239.

CALORE, F., DI MAURO, M., & DONATO, F. 2013. Updated constraints on WIMP dark matter annihilation into gamma-rays. *arXiv:1303.3284*.

CAPALBI, M., PERRI, M., SAIJA, B., *et al.* 2005. *The SWIFT XRT Data Reduction Guide. Version 1.2.* ASI Science Data Center and HEASARC.
`http://swift.gsfc.nasa.gov/docs/swift/analysis/xrt_swguide_v1_2.pdf`.

CARLSON, E., HOOPER, D., LINDEN, T., & PROFUMO, S. 2013. Testing the dark matter origin of the WMAP-Planck haze with radio observations of spiral galaxies. J. Cosmology Astropart. Phys., **7**, 26.

CARROLL, S. M. 1997. Lecture Notes on General Relativity. *arXiv:gr-qc/9712019*.

CARROLL, S. M., PRESS, W. H., & TURNER, E. L. 1992. The cosmological constant. ARA&A, **30**, 499–542.

CATENA, R., & ULLIO, P. 2010. A novel determination of the local dark matter density. J. Cosmology Astropart. Phys., **8**, 4.

CHANG, J., ADAMS, J. H., AHN, H. S., *et al.* 2008. An excess of cosmic ray electrons at energies of 300-800GeV. Nature, **456**, 362–365.

CHATRCHYAN, S., KHACHATRYAN, V., SIRUNYAN, A. M., *et al.* 2013a. Search for new physics in final states with a lepton and missing transverse energy in pp collisions at the LHC. Phys. Rev. D, **87**(7), 072005. CMS Collaboration.

CHATRCHYAN, S., KHACHATRYAN, V., SIRUNYAN, A. M., *et al.* 2013b. Study of the Mass and Spin-Parity of the Higgs Boson Candidate via Its Decays to Z Boson Pairs. *Physical Review Letters*, **110**(8), 081803. CMS Collaboration.

CHENG, H.-C., MATCHEV, K. T., & SCHMALTZ, M. 2002. Radiative corrections to Kaluza-Klein masses. Phys. Rev. D, **66**(3), 036005.

CHERNYAKOVA, M., MALYSHEV, D., AHARONIAN, F. A., *et al.* 2011. The High-energy, Arcminute-scale Galactic Center Gamma-ray Source. ApJ, **726**, 60.

CIRELLI, M., FORNENGO, N., & STRUMIA, A. 2006. Minimal dark matter. *Nuclear Physics B*, **753**, 178–194.

CIRELLI, M., PANCI, P., & SERPICO, P. D. 2010. Diffuse gamma ray constraints on annihilating or decaying Dark Matter after Fermi. *Nuclear Physics B*, **840**, 284–303.

CIRELLI, M., CORCELLA, G., HEKTOR, A., *et al.* 2011. PPPC 4 DM ID: a poor particle physicist cookbook for dark matter indirect detection. J. Cosmology Astropart. Phys., **3**, 51.

CIRELLI, M., CORCELLA, G., HEKTOR, A., *et al.* 2012. Erratum: PPPC 4 DM ID: a poor particle physicist cookbook for dark matter indirect detection. J. Cosmology Astropart. Phys., **10**.

CLOWE, D., GONZALEZ, A., & MARKEVITCH, M. 2004. Weak-Lensing Mass Reconstruction of the Interacting Cluster 1E 0657-558: Direct Evidence for the Existence of Dark Matter. ApJ, **604**, 596–603.

CLOWE, D., BRADAČ, M., GONZALEZ, A. H., *et al.* 2006. A Direct Empirical Proof of the Existence of Dark Matter. ApJ, **648**, L109–L113.

CLOWE, D., MARKEVITCH, M., BRADAČ, M., *et al.* 2012. On Dark Peaks and Missing Mass: A Weak-lensing Mass Reconstruction of the Merging Cluster System A520. ApJ, **758**, 128.

CMS COLLABORATION. 2012a. Combined results of searches for the standard model Higgs boson in pp collisions at s=7 TeV. *Physics Letters B*, **710**, 26–48.

CMS COLLABORATION. 2012b. Search for supersymmetry in events with b-quark jets and missing transverse energy in pp collisions at 7 TeV. Phys. Rev. D, **86**(7), 072010.

CMS COLLABORATION. 2013a. Search for new physics in events with opposite-sign leptons, jets, and missing transverse energy in pp collisions at s=7 TeV. *Physics Letters B*, **718**, 815–840.

CMS COLLABORATION. 2013b. Search for supersymmetry in events with photons and low missing transverse energy in pp collisions at s=7 TeV. *Physics Letters B*, **719**, 42–61.

CMS COLLABORATION. 2013c. Search for supersymmetry in final states with missing transverse energy and 0, 1, 2, or ≥ 3 b-quark jets in 7 TeV pp collisions using the variable α_T. *Journal of High Energy Physics*, **1**, 77.

COLAFRANCESCO, S., PROFUMO, S., & ULLIO, P. 2006. Multi-frequency analysis of neutralino dark matter annihilations in the Coma cluster. A&A, **455**, 21–43.

COLAFRANCESCO, S., PROFUMO, S., & ULLIO, P. 2007. Detecting dark matter WIMPs in the Draco dwarf: A multiwavelength perspective. Phys. Rev. D, **75**(2), 023513.

COLE, S., PERCIVAL, W. J., PEACOCK, J. A., *et al.* 2005. The 2dF Galaxy Redshift Survey: power-spectrum analysis of the final data set and cosmological implications. MNRAS, **362**, 505–534.

COLLESS, M., DALTON, G., MADDOX, S., *et al.* 2001. The 2dF Galaxy Redshift Survey: spectra and redshifts. MNRAS, **328**, 1039–1063.

CUOCO, A., KOMATSU, E., & SIEGAL-GASKINS, J. M. 2012. Joint anisotropy and source count constraints on the contribution of blazars to the diffuse gamma-ray background. Phys. Rev. D, **86**(6), 063004.

D'AMICO, G., KAMIONKOWSKI, M., & SIGURDSON, K. 2009. Dark Matter Astrophysics. *arXiv:0907.1912*.

DE NAUROIS, M., & ROLLAND, L. 2009. A high performance likelihood reconstruction of γ-rays for imaging atmospheric Cherenkov telescopes. *Astroparticle Physics*, **32**, 231–252.

DI BERNARDO, G., EVOLI, C., GAGGERO, D., *et al.* 2011. Implications of the cosmic ray electron spectrum and anisotropy measured with Fermi-LAT. *Astroparticle Physics*, **34**, 528–538.

DI CINTIO, A., KNEBE, A., LIBESKIND, N. I., *et al.* 2011. Too small to succeed? Lighting up massive dark matter subhaloes of the Milky Way. MNRAS, **417**, L74–L78.

DI CINTIO, A., KNEBE, A., LIBESKIND, N. I., *et al.* 2013. Size matters: the non-universal density profile of subhaloes in SPH simulations and implications for the Milky Way's dSphs. MNRAS, **431**, 1220–1229.

DIEMAND, J., & MOORE, B. 2011. The Structure and Evolution of Cold Dark Matter Halos. *Advanced Science Letters*, **4**, 297–310.

DIEMAND, J., MOORE, B., & STADEL, J. 2004. Convergence and scatter of cluster density profiles. MNRAS, **353**, 624–632.

DIEMAND, J., MOORE, B., & STADEL, J. 2005. Earth-mass dark-matter haloes as the first structures in the early Universe. Nature, **433**, 389–391.

DIEMAND, J., KUHLEN, M., & MADAU, P. 2007a. Dark Matter Substructure and Gamma-Ray Annihilation in the Milky Way Halo. ApJ, **657**, 262–270.

Diemand, J., Kuhlen, M., & Madau, P. 2007b. Formation and Evolution of Galaxy Dark Matter Halos and Their Substructure. ApJ, **667**, 859–877.

Diemand, J., Kuhlen, M., Madau, P., *et al.* 2008a. Clumps and streams in the local dark matter distribution. Nature, **454**, 735–738.

Diemand, J., Kuhlen, M., & Madau, P. 2008b. Erratum: "Formation and Evolution of Galaxy Dark Matter Halos and Their Substructure". ApJ, **679**, 1680–1683.

Dietrich, J. P., Werner, N., Clowe, D., *et al.* 2012. A filament of dark matter between two clusters of galaxies. Nature, **487**, 202–204.

Dixon, R. S. 1970. A Master List of Radio Sources. ApJS, **20**, 1–503.

Dobler, G., Finkbeiner, D. P., Cholis, I., *et al.* 2010. The Fermi Haze: A Gamma-ray Counterpart to the Microwave Haze. ApJ, **717**, 825–842.

Donato, F., Maurin, D., Brun, P., *et al.* 2009. Constraints on WIMP Dark Matter from the High Energy PAMELA $\overline{p}/p$ Data. *Physical Review Letters*, **102**(7), 071301.

Doro, M., Conrad, J., Emmanoulopoulos, D., Sànchez-Conde, M. A., Barrio, J. A., Birsin, E., Bolmont, J., Brun, P., Colafrancesco, S., Connell, S. H., Contreras, J. L., Daniel, M. K., Fornasa, M., Gaug, M., Glicenstein, J. F., González-Muñoz, A., Hassan, T., Horns, D., Jacholkowska, A., Jahn, C., Mazini, R., Mirabal, N., Moralejo, A., Moulin, E., Nieto, D., Ripken, J., Sandaker, H., Schwanke, U., Spengler, G., Stamerra, A., Viana, A., Zechlin, H.-S., Zimmer, S., & CTA Consortium. 2013. Dark matter and fundamental physics with the Cherenkov Telescope Array. *Astroparticle Physics*, **43**(Mar.), 189–214.

Drake, A. J., Djorgovski, S. G., Mahabal, A., *et al.* 2009. First Results from the Catalina Real-Time Transient Survey. ApJ, **696**, 870–884.

Ehret, K., Frede, M., Ghazaryan, S., *et al.* 2010. New ALPS results on hidden-sector lightweights. *Physics Letters B*, **689**, 149–155.

Einasto, J. 1965. On the Construction of a Composite Model for the Galaxy and on the Determination of the System of Galactic Parameters. *Trudy Astrofizicheskogo Instituta Alma-Ata*, **5**, 87–100.

Einstein, A. 1916. Die Grundlage der allgemeinen Relativitätstheorie. *Annalen der Physik*, **354**, 769–822.

Eisenstein, D. J., Zehavi, I., Hogg, D. W., *et al.* 2005. Detection of the Baryon Acoustic Peak in the Large-Scale Correlation Function of SDSS Luminous Red Galaxies. ApJ, **633**, 560–574.

Eke, V. R., Cole, S., & Frenk, C. S. 1996. Cluster evolution as a diagnostic for Omega. MNRAS, **282**, 263–280.

Eke, V. R., Navarro, J. F., & Steinmetz, M. 2001. The Power Spectrum Dependence of Dark Matter Halo Concentrations. ApJ, **554**, 114–125.

El-Zant, A., Shlosman, I., & Hoffman, Y. 2001. Dark Halos: The Flattening of the Density Cusp by Dynamical Friction. ApJ, **560**, 636–643.

Ellis, J., Hagelin, J. S., Nanopoulos, D. V., Olive, K., & Srednicki, M. 1984. Supersymmetric relics from the big bang. *Nuclear Physics B*, **238**, 453–476.

Essig, R., Sehgal, N., & Strigari, L. E. 2009. Bounds on cross sections and lifetimes for dark matter annihilation and decay into charged leptons from gamma-ray observations of dwarf galaxies. Phys. Rev. D, **80**(2), 023506.

Evans, J. L., Churchill, C. W., Murphy, M. T., *et al.* 2013. The Redshift Distribution of Intervening Weak Mg II Quasar Absorbers and a Curious Dependence on Quasar Luminosity. ApJ, **768**, 3.

EVRARD, A. E., MACFARLAND, T. J., COUCHMAN, H. M. P., *et al.* 2002. Galaxy Clusters in Hubble Volume Simulations: Cosmological Constraints from Sky Survey Populations. ApJ, **573**, 7–36.

FALOMO, R., BERSANELLI, M., BOUCHET, P., & TANZI, E. G. 1993. The optical to near-infrared emission of BL Lac objects - Simultaneous observations. AJ, **106**, 11–27.

FARRAR, G. R., & ROSEN, R. A. 2007. A New Force in the Dark Sector? *Physical Review Letters*, **98**(17), 171302.

FELDMAN, G. J., & COUSINS, R. D. 1998. Unified approach to the classical statistical analysis of small signals. Phys. Rev. D, **57**, 3873–3889.

FELIZARDO, M., GIRARD, T. A., MORLAT, T., *et al.* 2012. Final Analysis and Results of the Phase II SIMPLE Dark Matter Search. *Physical Review Letters*, **108**(20), 201302.

FERMI, E. 1949. On the Origin of the Cosmic Radiation. *Physical Review*, **75**, 1169–1174.

FINKBEINER, D. P. 2004. Microwave Interstellar Medium Emission Observed by the Wilkinson Microwave Anisotropy Probe. ApJ, **614**, 186–193.

FINKBEINER, D. P., SU, M., & WENIGER, C. 2013. Is the 130 GeV line real? A search for systematics in the Fermi-LAT data. J. Cosmology Astropart. Phys., **1**, 29.

FORNENGO, N., LINEROS, R., REGIS, M., & TAOSO, M. 2012a. Cosmological radio emission induced by WIMP Dark Matter. J. Cosmology Astropart. Phys., **3**, 33.

FORNENGO, N., LINEROS, R. A., REGIS, M., & TAOSO, M. 2012b. Galactic synchrotron emission from WIMPs at radio frequencies. J. Cosmology Astropart. Phys., **1**, 5.

FRENK, C. S. 1986. Galaxy clustering and the dark-matter problem. *Royal Society of London Philosophical Transactions Series A*, **320**, 517–541.

FUNK, S., & HINTON, J. A. 2013. Comparison of Fermi-LAT and CTA in the region between 10-100 GeV. *Astroparticle Physics*, **43**, 348–355. for the CTA Consortium.

GARDNER, J. P., MATHER, J. C., CLAMPIN, M., *et al.* 2006. The James Webb Space Telescope. Space Sci. Rev., **123**, 485–606.

GEHRELS, N. 2010. The Joint Dark Energy Mission (JDEM) Omega. *arXiv:1008.4936*.

GELLER, M. J., & HUCHRA, J. P. 1989. Mapping the universe. *Science*, **246**, 897–903.

GERINGER-SAMETH, A., & KOUSHIAPPAS, S. M. 2011. Exclusion of Canonical Weakly Interacting Massive Particles by Joint Analysis of Milky Way Dwarf Galaxies with Data from the Fermi Gamma-Ray Space Telescope. *Physical Review Letters*, **107**(24), 241303.

GERINGER-SAMETH, A., & KOUSHIAPPAS, S. M. 2012. Dark matter line search using a joint analysis of dwarf galaxies with the Fermi Gamma-ray Space Telescope. Phys. Rev. D, **86**(2), 021302.

GNEDIN, O. Y., & PRIMACK, J. R. 2004. Dark Matter Profile in the Galactic Center. *Physical Review Letters*, **93**(6), 061302.

GNEDIN, O. Y., & ZHAO, H. 2002. Maximum feedback and dark matter profiles of dwarf galaxies. MNRAS, **333**, 299–306.

GNEDIN, O. Y., KRAVTSOV, A. V., KLYPIN, A. A., & NAGAI, D. 2004. Response of Dark Matter Halos to Condensation of Baryons: Cosmological Simulations and Improved Adiabatic Contraction Model. ApJ, **616**, 16–26.

GODET, O., BEARDMORE, A. P., ABBEY, A. F., *et al.* 2009. Modelling the spectral response of the Swift-XRT CCD camera: experience learnt from in-flight calibration. A&A, **494**, 775–797.

GONDOLO, P., & SILK, J. 1999. Dark Matter Annihilation at the Galactic Center. *Physical Review Letters*, **83**, 1719–1722.

GOVERNATO, F., BROOK, C., MAYER, L., *et al.* 2010. Bulgeless dwarf galaxies and dark matter cores from supernova-driven outflows. Nature, **463**, 203–206.

GRASSO, D., PROFUMO, S., STRONG, A. W., *et al.* 2009. On possible interpretations of the high energy electron-positron spectrum measured by the Fermi Large Area Telescope. *Astroparticle Physics*, **32**, 140–151.

GRCEVICH, J., & PUTMAN, M. E. 2009. H I in Local Group Dwarf Galaxies and Stripping by the Galactic Halo. ApJ, **696**, 385–395.

GRCEVICH, J., & PUTMAN, M. E. 2010. Erratum: "H I in Local Group Dwarf Galaxies and Stripping by the Galactic Halo" (2009, ApJ, 696, 385). ApJ, **721**, 922.

GREEN, A. M., HOFMANN, S., & SCHWARZ, D. J. 2005. The first WIMPy halos. J. Cosmology Astropart. Phys., **8**, 3.

GRIEST, K., & KAMIONKOWSKI, M. 1990. Unitarity limits on the mass and radius of dark-matter particles. *Physical Review Letters*, **64**, 615–618.

GRIFFITH, M. R., WRIGHT, A. E., BURKE, B. F., & EKERS, R. D. 1994. The Parkes-MIT-NRAO (PMN) surveys. 3: Source catalog for the tropical survey ($-29^\circ < \delta < 9^\circ.5$). ApJS, **90**, 179–295.

GUNN, J. E., LEE, B. W., LERCHE, I., *et al.* 1978. Some astrophysical consequences of the existence of a heavy stable neutral lepton. ApJ, **223**, 1015–1031.

HALL, L. J., RUDERMAN, J. T., & VOLANSKY, T. 2013. A Cosmological Upper Bound on Superpartner Masses. *arXiv:1302.2620*.

HARRISON, E. R. 1970. Fluctuations at the Threshold of Classical Cosmology. Phys. Rev. D, **1**, 2726–2730.

HEATH, D. J. 1977. The growth of density perturbations in zero pressure Friedmann-Lemaitre universes. MNRAS, **179**, 351–358.

HEKTOR, A., RAIDAL, M., & TEMPEL, E. 2012. Fermi-LAT gamma-ray signal from Earth Limb, systematic detector effects and their implications for the 130 GeV gamma-ray excess. *arXiv:1209.4548*.

HEKTOR, A., RAIDAL, M., & TEMPEL, E. 2013. Evidence for Indirect Detection of Dark Matter from Galaxy Clusters in Fermi γ-Ray Data. ApJ, **762**, L22.

HODGE, J. A., KARIM, A., SMAIL, I., *et al.* 2013. An ALMA Survey of Submillimeter Galaxies in the Extended Chandra Deep Field South: Source Catalog and Multiplicity. ApJ, **768**, 91.

HOGG, D. W., BALDRY, I. K., BLANTON, M. R., & EISENSTEIN, D. J. 2002. The K correction. *arXiv:astro-ph/0210394*.

HOOPER, D., & LINDEN, T. 2011. Origin of the gamma rays from the Galactic Center. Phys. Rev. D, **84**(12), 123005.

HOOPER, D., & LINDEN, T. 2012. Are lines from unassociated gamma-ray sources evidence for dark matter annihilation? Phys. Rev. D, **86**(8), 083532.

HOOPER, D., & SLATYER, T. R. 2013. Two Emission Mechanisms in the Fermi Bubbles: A Possible Signal of Annihilating Dark Matter. *arXiv:1302.6589*.

HOOPER, D., & XUE, W. 2013. Possibility of Testing the Light Dark Matter Hypothesis with the Alpha Magnetic Spectrometer. *Physical Review Letters*, **110**(4), 041302.

HOOPER, D., FINKBEINER, D. P., & DOBLER, G. 2007. Possible evidence for dark matter annihilations from the excess microwave emission around the center of the Galaxy seen by the Wilkinson Microwave Anisotropy Probe. Phys. Rev. D, **76**(8), 083012.

HOOPER, D., BELIKOV, A. V., JELTEMA, T. E., *et al.* 2012. The isotropic radio background and annihilating dark matter. Phys. Rev. D, **86**(10), 103003.

HORNS, D. 2005. TeV γ-radiation from Dark Matter annihilation in the Galactic center. *Physics Letters B*, **607**, 225–232.

HORNS, D. 2008. High-(Energy)-Lights - The Very High Energy Gamma-Ray Sky. *Reviews in Modern Astronomy*, **20**, 167.

HORNS, D., & MEYER, M. 2012. Indications for a pair-production anomaly from the propagation of VHE gamma-rays. J. Cosmology Astropart. Phys., **2**, 33.

HORNS, D., MACCIONE, L., MEYER, M., MIRIZZI, A., *et al.* 2012a. Hardening of TeV gamma spectrum of active galactic nuclei in galaxy clusters by conversions of photons into axionlike particles. Phys. Rev. D, **86**(7), 075024.

HORNS, D., MACCIONE, L., MIRIZZI, A., & RONCADELLI, M. 2012b. Probing axionlike particles with the ultraviolet photon polarization from active galactic nuclei in radio galaxies. Phys. Rev. D, **85**(8), 085021.

HORNS, D., JAECKEL, J., LINDNER, A., LOBANOV, A., REDONDO, J., & RINGWALD, A. 2013. Searching for WISPy cold dark matter with a dish antenna. J. Cosmology Astropart. Phys., **4**, 16.

HU, W., & DODELSON, S. 2002. Cosmic Microwave Background Anisotropies. ARA&A, **40**, 171–216.

HUBBLE, E. 1929. A Relation between Distance and Radial Velocity among Extra-Galactic Nebulae. *Proceedings of the National Academy of Science*, **15**, 168–173.

HUBBLE, E., & HUMASON, M. L. 1931. The Velocity-Distance Relation among Extra-Galactic Nebulae. ApJ, **74**, 43.

HUMPHREY, P. J., LIU, W., & BUOTE, D. A. 2009. χ^2 and Poissonian Data: Biases Even in the High-Count Regime and How to Avoid Them. ApJ, **693**(Mar.), 822–829.

IBARRA, A., & WILD, S. 2013. Prospects of antideuteron detection from dark matter annihilations or decays at AMS-02 and GAPS. J. Cosmology Astropart. Phys., **2**, 21.

IMMLER, S., STILL, M., BOYD, P., *et al.* 2008. *The SWIFT UVOT Software Guide. Version 2.2.* NASA/GSFC — Swift Science Center.
`http://swift.gsfc.nasa.gov/docs/swift/analysis/UVOT_swguide_v2_2.pdf`.

ISERN, J., GARCÍA-BERRO, E., TORRES, S., & CATALÁN, S. 2008. Axions and the Cooling of White Dwarf Stars. ApJ, **682**, L109–L112.

IZOTOV, Y. I., CHAFFEE, F. H., FOLTZ, C. B., *et al.* 1999. Helium Abundance in the Most Metal-deficient Blue Compact Galaxies: I ZW 18 and SBS 0335-052. ApJ, **527**, 757–777.

JAECKEL, J. 2013. A force beyond the Standard Model - Status of the quest for hidden photons. *In: Proceedings for the "Dark Forces at Accelerators" workshop, October 16-19, 2012.* arXiv:1303.1821.

JAECKEL, J., & RINGWALD, A. 2010. The Low-Energy Frontier of Particle Physics. *Annual Review of Nuclear and Particle Science*, **60**, 405–437.

JANUSCHEK, S. 2010 (Mar.). *Analyse zur Detektierbarkeit von Substrukturen Dunkler Materie-Halos mit dem Fermi-LAT-Experiment.* Diploma thesis, Universität Hamburg, Hamburg, Germany.

JASCHEK, C., & JASCHEK, M. 1995. *The Behavior of Chemical Elements in Stars.* Cambridge University Press, UK.

JEANS, J. H. 1902. The Stability of a Spherical Nebula. *Royal Society of London Philosophical Transactions Series A*, **199**, 1–53.

JELTEMA, T. E., & PROFUMO, S. 2008. Searching for Dark Matter with X-Ray Observations of Local Dwarf Galaxies. ApJ, **686**, 1045–1055.

JELTEMA, T. E., & PROFUMO, S. 2012. Dark matter detection with hard X-ray telescopes. MNRAS, **421**, 1215–1221.

JUNGMAN, G., KAMIONKOWSKI, M., & GRIEST, K. 1996. Supersymmetric dark matter. Phys. Rep., **267**, 195–373.

KAMIONKOWSKI, M., & LIDDLE, A. R. 2000. The Dearth of Halo Dwarf Galaxies: Is There Power on Short Scales? *Physical Review Letters*, **84**, 4525–4528.

KANE, G. L., KOLDA, C., ROSZKOWSKI, L., & WELLS, J. D. 1994. Study of constrained minimal supersymmetry. Phys. Rev. D, **49**, 6173–6210.

KATARZYŃSKI, K., SOL, H., & KUS, A. 2001. The multifrequency emission of Mrk 501. From radio to TeV gamma-rays. A&A, **367**, 809–825.

KAUFFMANN, G., WHITE, S. D. M., & GUIDERDONI, B. 1993. The Formation and Evolution of Galaxies Within Merging Dark Matter Haloes. MNRAS, **264**, 201.

KINMAN, T. D. 1959. Globular clusters, III. An analysis of the cluster radial velocities. MNRAS, **119**, 559.

KLYPIN, A., GOTTLÖBER, S., KRAVTSOV, A. V., & KHOKHLOV, A. M. 1999a. Galaxies in N-Body Simulations: Overcoming the Overmerging Problem. ApJ, **516**, 530–551.

KLYPIN, A., KRAVTSOV, A. V., VALENZUELA, O., & PRADA, F. 1999b. Where Are the Missing Galactic Satellites? ApJ, **522**, 82–92.

KOMATSU, E., SMITH, K. M., DUNKLEY, J., *et al.* 2011. Seven-year Wilkinson Microwave Anisotropy Probe (WMAP) Observations: Cosmological Interpretation. ApJS, **192**, 18.

KOWALSKI, M., RUBIN, D., ALDERING, G., *et al.* 2008. Improved Cosmological Constraints from New, Old, and Combined Supernova Data Sets. ApJ, **686**, 749–778.

KROUPA, P. 2012. The Dark Matter Crisis: Falsification of the Current Standard Model of Cosmology. PASA, **29**, 395–433.

KUHLEN, M. 2010. The Dark Matter Annihilation Signal from Dwarf Galaxies and Subhalos. *Advances in Astronomy*, **2010**.

KUHLEN, M., GUEDES, J., PILLEPICH, A., MADAU, P., & MAYER, L. 2013. An Off-center Density Peak in the Milky Way's Dark Matter Halo? ApJ, **765**, 10.

KUZIO DE NARAY, R., & SPEKKENS, K. 2011. Do Baryons Alter the Halos of Low Surface Brightness Galaxies? ApJ, **741**, L29.

LAHA, R., NG, K. C. Y., DASGUPTA, B., & HORIUCHI, S. 2013. Galactic Center radio constraints on gamma-ray lines from dark matter annihilation. Phys. Rev. D, **87**(4), 043516.

LANDONI, M., FALOMO, R., TREVES, A., *et al.* 2013. ESO Very Large Telescope Optical Spectroscopy of BL Lacertae Objects. IV. New Spectra and Properties of the Full Sample. AJ, **145**, 114.

LARSON, D., DUNKLEY, J., HINSHAW, G., *et al.* 2011. Seven-year Wilkinson Microwave Anisotropy Probe (WMAP) Observations: Power Spectra and WMAP-derived Parameters. ApJS, **192**, 16.

LEBEDEV, O., & RAMOS-SÁNCHEZ, S. 2010. The NMSSM and string theory. *Physics Letters B*, **684**(Feb.), 48–51.

LEE, B. W., & WEINBERG, S. 1977. Cosmological lower bound on heavy-neutrino masses. *Physical Review Letters*, **39**, 165–168.

LIFSHITZ, E. 1946. On the Gravitational stability of the expanding universe. *Journal of Physics (USSR)*, **10**, 116.

LINDEN, T., & PROFUMO, S. 2012. Exploring the Nature of the Galactic Center γ-Ray Source with the Cherenkov Telescope Array. ApJ, **760**, 23.

LOBANOV, A. P., BECK, R., ZECHLIN, H.-S., OPITZ, B., & HORNS, D. 2011a. *Dark Matter Annihilation in the Halo of Dwarf Spheroidal Galaxy UMa II*. Effelsberg Proposal 58-11.

LOBANOV, A. P., HORNS, D., & ZECHLIN, H.-S. 2011b. *In-band searches for hidden photon signal at 4.8 GHz*. Effelsberg Proposal 105-11.

LOBANOV, A. P., ZECHLIN, H.-S., & HORNS, D. 2013. Astrophysical searches for a hidden-photon signal in the radio regime. Phys. Rev. D, **87**(6), 065004.

LONGAIR, M. S. 2008. *Galaxy Formation*. Springer, Berlin.

LOVELL, M. R., EKE, V., FRENK, C. S., *et al.* 2012. The haloes of bright satellite galaxies in a warm dark matter universe. MNRAS, **420**, 2318–2324.

LYNDEN-BELL, D. 1967. Statistical mechanics of violent relaxation in stellar systems. MNRAS, **136**, 101.

MADAU, P., KUHLEN, M., DIEMAND, J., *et al.* 2008. Fossil Remnants of Reionization in the Halo of the Milky Way. ApJ, **689**, L41–L44.

MARTIN, S. P. 1998. A Supersymmetry Primer. *Page 1 of:* KANE, G. L. (ed), *Perspectives on Supersymmetry*.

MASHCHENKO, S., WADSLEY, J., & COUCHMAN, H. M. P. 2008. Stellar Feedback in Dwarf Galaxy Formation. *Science*, **319**, 174–.

MATEO, M., OLSZEWSKI, E. W., PRYOR, C., *et al.* 1993. The Carina dwarf spheroidal galaxy - How dark is it? AJ, **105**, 510–526.

MEADE, P., PAPUCCI, M., STRUMIA, A., & VOLANSKY, T. 2010. Dark Matter interpretations of the e excesses after FERMI. *Nuclear Physics B*, **831**, 178–203.

MERLE, A. 2013. keV Neutrino Model Building. *arXiv:1302.2625*.

MERRITT, D. 2004. Evolution of the Dark Matter Distribution at the Galactic Center. *Physical Review Letters*, **92**(20), 201304.

MERTEN, J., COE, D., DUPKE, R., *et al.* 2011. Creation of cosmic structure in the complex galaxy cluster merger Abell 2744. MNRAS, **417**, 333–347.

MEYER, M., HORNS, D., & ZECHLIN, H.-S. 2010. The Crab Nebula as a standard candle in very high-energy astrophysics. A&A, **523**(Nov.), A2.

MEYER, M., RAUE, M., MAZIN, D., & HORNS, D. 2012. Limits on the extragalactic background light in the Fermi era. A&A, **542**, A59.

MEYER, M., HORNS, D., & RAUE, M. 2013. First lower limits on the photon-axion-like particle coupling from very high energy gamma-ray observations. Phys. Rev. D, **87**(3), 035027.

MILGROM, M. 1983a. A modification of the Newtonian dynamics - Implications for galaxies. ApJ, **270**, 371–389.

MILGROM, M. 1983b. A Modification of the Newtonian Dynamics - Implications for Galaxy Systems. ApJ, **270**, 384.

MILGROM, M. 1983c. A modification of the Newtonian dynamics as a possible alternative to the hidden mass hypothesis. ApJ, **270**, 365–370.

MIRABAL, N. 2013. The dark knight falters. MNRAS, **429**, L109–L113.

MIRIZZI, A., REDONDO, J., & SIGL, G. 2009a. Constraining resonant photon-axion conversions in the early universe. J. Cosmology Astropart. Phys., **8**, 1.

MIRIZZI, A., REDONDO, J., & SIGL, G. 2009b. Microwave background constraints on mixing of photons with hidden photons. J. Cosmology Astropart. Phys., **3**, 26.

MISNER, C. W., THORNE, K. S., & WHEELER, J. A. 1973. *Gravitation*. W. H. Freeman and Co., San Francisco, USA.

MONET, D. G., LEVINE, S. E., CANZIAN, B., *et al.* 2003. The USNO-B Catalog. AJ, **125**, 984–993.

MOORE, B., GOVERNATO, F., QUINN, T., STADEL, J., & LAKE, G. 1998. Resolving the Structure of Cold Dark Matter Halos. ApJ, **499**, L5.

MOORE, B., GHIGNA, S., GOVERNATO, F., *et al.* 1999. Dark Matter Substructure within Galactic Halos. ApJ, **524**, L19–L22.

MORSELLI, A., CANADAS, B., & VITALE, V. 2010. The Indirect Search for Dark Matter from the centre of the Galaxy with the Fermi LAT. *arXiv:1012.2292*, Dec. Fermi-LAT Collaboration.

MOSKALENKO, I. V., PORTER, T. A., & STRONG, A. W. 2006. Attenuation of Very High Energy Gamma Rays by the Milky Way Interstellar Radiation Field. ApJ, **640**, L155–L158.

NATH, P., NELSON, B., DAVOUDIASL, H., *et al.* 2010. The Hunt for New Physics at the Large Hadron Collider. *Nuclear Physics B Proceedings Supplements*, **200**, 185–417.

NAVARRO, J. F., FRENK, C. S., & WHITE, S. D. M. 1997. A Universal Density Profile from Hierarchical Clustering. ApJ, **490**, 493.

NAVARRO, J. F., HAYASHI, E., POWER, C., *et al.* 2004. The inner structure of ΛCDM haloes - III. Universality and asymptotic slopes. MNRAS, **349**, 1039–1051.

NAVARRO, J. F., LUDLOW, A., SPRINGEL, V., *et al.* 2010. The diversity and similarity of simulated cold dark matter haloes. MNRAS, **402**, 21–34.

NESTI, F., & SALUCCI, P. 2013. The Dark Matter halo of the Milky Way, AD 2013. J. Cosmology Astropart. Phys., **7**, 16.

NGUYEN, N., HORNS, D., & BRINGMANN, T. 2012. AstroFit: An Interface Program for Exploring Complementarity in Dark Matter Research. *arXiv:1202.1385*.

NIELSEN, N. M., CHURCHILL, C. W., KACPRZAK, G. G., & MURPHY, M. T. 2013. MAGIICAT I. The Mg II Absorber-Galaxy Catalog. ApJ, **776**, 114.

NOLAN, P. L., ABDO, A. A., ACKERMANN, M., *et al.* 2012. Fermi Large Area Telescope Second Source Catalog. ApJS, **199**, 31. Fermi-LAT Collaboration.

OKABE, N., & UMETSU, K. 2008. Subaru Weak Lensing Study of Seven Merging Clusters: Distributions of Mass and Baryons. PASJ, **60**, 345.

OKUN, L. B. 1982. The limits of electrodynamics – Paraphotons. *Zhurnal Eksperimentalnoi i Teoreticheskoi Fiziki*, **83**, 892–898.

OORT, J. H. 1932. The force exerted by the stellar system in the direction perpendicular to the galactic plane and some related problems. Bull. Astron. Inst. Netherlands, **6**, 249.

OSTERBROCK, D. E., FULBRIGHT, J. P., MARTEL, A. R., *et al.* 1996. Night-Sky High-Resolution Spectral Atlas of OH and O2 Emission Lines for Echelle Spectrograph Wavelength Calibration. PASP, **108**, 277.

PANEQUE, D., BALLET, J., BURNETT, T., *et al.* 2013. The First Fermi-LAT Catalog of Sources Above 10 GeV. *In: 2012 Fermi Symposium proceedings - eConf C121028*. arXiv:1304.4153.

PAPUCCI, M., & STRUMIA, A. 2010. Robust implications on dark matter from the first FERMI sky γ map. J. Cosmology Astropart. Phys., **3**, 14.

PARRENT, J. T., THOMAS, R. C., FESEN, R. A., *et al.* 2011. A Study of Carbon Features in Type Ia Supernova Spectra. ApJ, **732**, 30.

PEACOCK, J. A., COLE, S., NORBERG, P., *et al.* 2001. A measurement of the cosmological mass density from clustering in the 2dF Galaxy Redshift Survey. Nature, **410**, 169–173.

PECCEI, R. D., & QUINN, H. R. 1977. CP conservation in the presence of pseudoparticles. *Physical Review Letters*, **38**, 1440–1443.

PENZIAS, A. A., & WILSON, R. W. 1965. A Measurement of Excess Antenna Temperature at 4080 Mc/s. ApJ, **142**, 419–421.

PERLMUTTER, S., ALDERING, G., GOLDHABER, G., *et al.* 1999. Measurements of Omega and Lambda from 42 High-Redshift Supernovae. ApJ, **517**, 565–586.

PETERSON, B. M. 1997. *An Introduction to Active Galactic Nuclei.* Cambridge University Press, Cambridge, NY, USA.

PETROV, L., MAHONY, E. K., EDWARDS, P. G., *et al.* 2013. Australia Telescope Compact Array observations of Fermi unassociated sources. MNRAS, **432**, 1294–1302.

PETTINI, M., ZYCH, B. J., MURPHY, M. T., *et al.* 2008. Deuterium abundance in the most metal-poor damped Lyman alpha system: converging on $\Omega_{b,0}h^2$. MNRAS, **391**, 1499–1510.

PIERI, L., LAVALLE, J., BERTONE, G., & BRANCHINI, E. 2011. Implications of high-resolution simulations on indirect dark matter searches. Phys. Rev. D, **83**(2), 023518.

POGGIANTI, B. M. 1997. K and evolutionary corrections from UV to IR. A&AS, **122**, 399–407.

POOLE, T. S., BREEVELD, A. A., PAGE, M. J., *et al.* 2008. Photometric calibration of the Swift ultraviolet/optical telescope. MNRAS, **383**, 627–645.

PORTER, T. A., MOSKALENKO, I. V., STRONG, A. W., *et al.* 2008. Inverse Compton Origin of the Hard X-Ray and Soft Gamma-Ray Emission from the Galactic Ridge. ApJ, **682**, 400–407.

PORTER, T. A., JOHNSON, R. P., & GRAHAM, P. W. 2011. Dark Matter Searches with Astroparticle Data. ARA&A, **49**, 155–194.

PRESS, W. H., & SCHECHTER, P. 1974. Formation of Galaxies and Clusters of Galaxies by Self-Similar Gravitational Condensation. ApJ, **187**, 425–438.

PRESS, W. H., TEUKOLSKY, S. A., VETTERLING, W. T., & FLANNERY, B. P. 2007. *Numerical Recipes: The Art of Scientific Computing*. 3rd edn. Cambridge University Press.

PRIMACK, J. R. 2012. Triumphs and tribulations of ΛCDM, the double dark theory. *Annalen der Physik*, **524**, 535–544.

RAFFELT, G. G. 1996. *Stars as laboratories for fundamental physics: the astrophysics of neutrinos, axions, and other weakly interacting particles*. University of Chicago Press.

RAGOZZINE, B., CLOWE, D., MARKEVITCH, M., *et al.* 2012. Weak-lensing Results for the Merging Cluster A1758. ApJ, **744**, 94.

RANDALL, L., & SUNDRUM, R. 1999. Large Mass Hierarchy from a Small Extra Dimension. *Physical Review Letters*, **83**, 3370–3373.

RANDALL, S. W., MARKEVITCH, M., CLOWE, D., *et al.* 2008. Constraints on the Self-Interaction Cross Section of Dark Matter from Numerical Simulations of the Merging Galaxy Cluster 1E 0657-56. ApJ, **679**, 1173–1180.

REDONDO, J. 2008. Helioscope bounds on hidden sector photons. J. Cosmology Astropart. Phys., **7**, 8.

REGIS, M., & ULLIO, P. 2008. Multiwavelength signals of dark matter annihilations at the Galactic center. Phys. Rev. D, **78**(4), 043505.

RIEGER, F. M., DE ONA-WILHELMI, E., & AHARONIAN, F. A. 2013. TeV Astronomy. *arXiv:1302.5603*.

RIESS, A. G., FILIPPENKO, A. V., CHALLIS, P., *et al.* 1998. Observational Evidence from Supernovae for an Accelerating Universe and a Cosmological Constant. AJ, **116**, 1009–1038.

RINGWALD, A. 2012. Exploring the role of axions and other WISPs in the dark universe. *Physics of the Dark Universe*, **1**, 116–135.

RIPKEN, J., CUOCO, A., ZECHLIN, H.-S., CONRAD, J., & HORNS, D. 2012. The sensitivity of Cherenkov telescopes to dark matter and astrophysically induced anisotropies in the diffuse gamma-ray background. J. Cosmology Astropart. Phys., *in revision*, Nov. arXiv:1211.6922.

ROMING, P. W. A., KENNEDY, T. E., MASON, K. O., *et al.* 2005. The Swift Ultra-Violet/Optical Telescope. Space Sci. Rev., **120**, 95–142.

RUBIN, V. C., & FORD, JR., W. K. 1970. Rotation of the Andromeda Nebula from a Spectroscopic Survey of Emission Regions. ApJ, **159**, 379.

SBARUFATTI, B., TREVES, A., & FALOMO, R. 2005. Imaging Redshifts of BL Lacertae Objects. ApJ, **635**, 173–179.

SCHERRER, R. J., & TURNER, M. S. 1986. On the relic, cosmic abundance of stable, weakly interacting massive particles. Phys. Rev. D, **33**, 1585–1589.

SCHLEGEL, D. J., FINKBEINER, D. P., & DAVIS, M. 1998. Maps of Dust Infrared Emission for Use in Estimation of Reddening and Cosmic Microwave Background Radiation Foregrounds. ApJ, **500**, 525.

SCHMALTZ, M., & TUCKER-SMITH, D. 2005. Little Higgs Theories. *Annual Review of Nuclear and Particle Science*, **55**, 229–270.

SCHNEIDER, P. 2006. *Extragalactic Astronomy and Cosmology*. Springer, Berlin.

SCHWARZ, M. 2012. Solar Hidden Photon Search. *Page 129 of: 7th Patras Workshop on Axions, WIMPs and WISPs (PATRAS 2011).* arXiv:1111.5797.

SERVANT, G., & TAIT, T. M. P. 2003. Is the lightest Kaluza-Klein particle a viable dark matter candidate? *Nuclear Physics B*, **650**, 391–419.

SHAW, L. D., WELLER, J., OSTRIKER, J. P., & BODE, P. 2007. The Bound Mass of Substructures in Dark Matter Halos. ApJ, **659**, 1082–1095.

SHAW, M. S., ROMANI, R. W., COTTER, G., *et al.* 2013. Spectroscopy of the Largest Ever γ-Ray-selected BL Lac Sample. ApJ, **764**, 135.

SIKIVIE, P. 2010. Dark Matter Axions. *International Journal of Modern Physics A*, **25**, 554–563.

SIMON, J. D., & GEHA, M. 2007. The Kinematics of the Ultra-faint Milky Way Satellites: Solving the Missing Satellite Problem. ApJ, **670**, 313–331.

SMOOT, G. F., BENNETT, C. L., KOGUT, A., *et al.* 1992. Structure in the COBE differential microwave radiometer first-year maps. ApJ, **396**, L1–L5.

SOFUE, Y., & RUBIN, V. 2001. Rotation Curves of Spiral Galaxies. ARA&A, **39**, 137–174.

SOUCAIL, G. 2012. Dark matter distribution in the merging cluster Abell 2163. A&A, **540**, A61.

SPEKKENS, K., MASON, B. S., AGUIRRE, J. E., & NHAN, B. 2013. A Deep Search for Extended Radio Continuum Emission from Dwarf Spheroidal Galaxies: Implications for Particle Dark Matter. ApJ, **773**, 61.

SPERGEL, D. N., & STEINHARDT, P. J. 2000. Observational Evidence for Self-Interacting Cold Dark Matter. *Physical Review Letters*, **84**, 3760–3763.

SPRINGEL, V., & FARRAR, G. R. 2007. The speed of the 'bullet' in the merging galaxy cluster 1E0657-56. MNRAS, **380**, 911–925.

SPRINGEL, V., WHITE, S. D. M., JENKINS, A., *et al.* 2005. Simulations of the formation, evolution and clustering of galaxies and quasars. Nature, **435**, 629–636.

SPRINGEL, V., FRENK, C. S., & WHITE, S. D. M. 2006. The large-scale structure of the Universe. Nature, **440**, 1137–1144.

SPRINGEL, V., WHITE, S. D. M., FRENK, C. S., *et al.* 2008a. Prospects for detecting supersymmetric dark matter in the Galactic halo. Nature, **456**, 73–76.

SPRINGEL, V., WANG, J., VOGELSBERGER, M., *et al.* 2008b. The Aquarius Project: the subhaloes of galactic haloes. MNRAS, **391**, 1685–1711.

STRIGARI, L. E. 2013. Galactic searches for dark matter. Phys. Rep., **531**, 1–88.

STRIGARI, L. E., BULLOCK, J. S., KAPLINGHAT, M., *et al.* 2008. A common mass scale for satellite galaxies of the Milky Way. Nature, **454**, 1096–1097.

SU, M., & FINKBEINER, D. P. 2012a. Double Gamma-ray Lines from Unassociated Fermi-LAT Sources. *arXiv:1207.7060.*

SU, M., & FINKBEINER, D. P. 2012b. Strong Evidence for Gamma-ray Line Emission from the Inner Galaxy. *arXiv:1206.1616.*

SUNYAEV, R. A., & ZELDOVICH, I. B. 1980. Microwave background radiation as a probe of the contemporary structure and history of the universe. ARA&A, **18**, 537–560.

TANAKA, T., ABE, K., HAYATO, Y., *et al.* 2011. An Indirect Search for Weakly Interacting Massive Particles in the Sun Using 3109.6 Days of Upward-going Muons in Super-Kamiokande. ApJ, **742**, 78. Super-Kamiokande Collaboration.

TAVANI, M., BARBIELLINI, G., ARGAN, A., *et al.* 2008. The AGILE space mission. *Nuclear Instruments and Methods in Physics Research A*, **588**, 52–62.

TEGMARK, M., BLANTON, M. R., STRAUSS, M. A., *et al.* 2004. The Three-Dimensional Power Spectrum of Galaxies from the Sloan Digital Sky Survey. ApJ, **606**, 702–740.

TEMPEL, E., HEKTOR, A., & RAIDAL, M. 2012. Fermi 130 GeV gamma-ray excess and dark matter annihilation in sub-haloes and in the Galactic centre. J. Cosmology Astropart. Phys., **9**, 32.

THE CTA CONSORTIUM. 2013. Seeing the High-Energy Universe with the Cherenkov Telescope Array - The Science Explored with the CTA. *Astroparticle Physics*, **43**, 1–356.

THOMPSON, H. M. A., KEENAN, F. P., DUFTON, P. L., *et al.* 2008. Iron abundances from optical FeIII absorption lines in B-type stellar spectra. MNRAS, **383**, 729–740.

TISSERAND, P., LE GUILLOU, L., AFONSO, C., *et al.* 2007. Limits on the Macho content of the Galactic Halo from the EROS-2 Survey of the Magellanic Clouds. A&A, **469**, 387–404. EROS-2 Collaboration.

TLUCZYKONT, M., HAMPF, D., HORNS, D., *et al.* 2011. The ground-based large-area wide-angle γ-ray and cosmic-ray experiment HiSCORE. *Advances in Space Research*, **48**, 1935–1941.

TLUCZYKONT, M., HORNS, D., HAMPF, D., *et al.* 2012. HiSCORE: A new detector for astroparticle and particle physics beyond 10 TeV. *Nuclear Instruments and Methods in Physics Research A*, **692**, 246–249.

TLUCZYKONT, M., HAMPF, D., EINHAUS, U., *et al.* 2013. The HiSCORE experiment and its potential for gamma-ray astronomy. *Journal of Physics Conference Series*, **409**(1), 012120.

TOLLERUD, E. J., BULLOCK, J. S., STRIGARI, L. E., & WILLMAN, B. 2008. Hundreds of Milky Way Satellites? Luminosity Bias in the Satellite Luminosity Function. ApJ, **688**, 277–289.

TONRY, J. L., SCHMIDT, B. P., BARRIS, B., *et al.* 2003. Cosmological Results from High-z Supernovae. ApJ, **594**, 1–24.

TORII, S., YAMAGAMI, T., TAMURA, T., *et al.* 2008. High-energy electron observations by PPB-BETS flight in Antarctica. *arXiv:0809.0760.*

TRIDON, D. B., SCHWEIZER, T., GOEBEL, F., *et al.* 2010. The MAGIC-II gamma-ray stereoscopic telescope system. *Nuclear Instruments and Methods in Physics Research A*, **623**, 437–439. MAGIC Collaboration.

TYSON, J. A., KOCHANSKI, G. P., & DELL'ANTONIO, I. P. 1998. Detailed Mass Map of CL 0024+1654 from Strong Lensing. ApJ, **498**, L107.

ULLIO, P., & BERGSTRÖM, L. 1998. Neutralino annihilation into a photon and a Z boson. Phys. Rev. D, **57**, 1962–1971.

VAN BIBBER, K., & CAROSI, G. 2013. Status of the ADMX and ADMX-HF experiments. *In: 8th Patras Workshop on Axions, WIMPs and WISPs, Chicago, IL, USA, 2012.* arXiv:1304.7803.

VERTONGEN, G., & WENIGER, C. 2011. Hunting dark matter gamma-ray lines with the Fermi LAT. J. Cosmology Astropart. Phys., **5**, 27.

VINCENT, P. 2005. H.E.S.S. Phase II. *Page 163 of: 29th International Cosmic Ray Conference, August 3–10, 2005, Pune, India*, vol. 5. H.E.S.S. Collaboration.

VOGEL, J. K., AVIGNONE, F. T., CANTATORE, G., *et al.* 2013. IAXO - The International Axion Observatory. *In: 8th Patras Workshop on Axions, WIMPs and WISPs, Chicago, IL, USA, 2012.* arXiv:1302.3273.

WAGNER, A., RYBKA, G., HOTZ, M., *et al.* 2010. Search for Hidden Sector Photons with the ADMX Detector. *Physical Review Letters*, **105**(17), 171801.

WALKER, M. G., & PEÑARRUBIA, J. 2011. A Method for Measuring (Slopes of) the Mass Profiles of Dwarf Spheroidal Galaxies. ApJ, **742**, 20.

WALKER, M. G., MATEO, M., OLSZEWSKI, E. W., *et al.* 2009. A Universal Mass Profile for Dwarf Spheroidal Galaxies? ApJ, **704**, 1274–1287.

WALKER, M. G., MATEO, M., OLSZEWSKI, E. W., *et al.* 2010. Erratum: "A Universal Mass Profile For Dwarf Spheroidal Galaxies?" (2009, ApJ, 704, 1274). ApJ, **710**, 886–890.

WALKER, M. G., COMBET, C., HINTON, J. A., *et al.* 2011. Dark Matter in the Classical Dwarf Spheroidal Galaxies: A Robust Constraint on the Astrophysical Factor for γ-Ray Flux Calculations. ApJ, **733**, L46.

WANG, J., FRENK, C. S., NAVARRO, J. F., *et al.* 2012. The missing massive satellites of the Milky Way. MNRAS, **424**, 2715–2721.

WEINBERG, M. D., & KATZ, N. 2007. The bar-halo interaction - II. Secular evolution and the religion of N-body simulations. MNRAS, **375**, 460–476.

WEINBERG, S. 1972. *Gravitation and Cosmology: Principles and Applications of the General Theory of Relativity.* Wiley-VCH.

WENIGER, C. 2012. A tentative gamma-ray line from Dark Matter annihilation at the Fermi Large Area Telescope. J. Cosmology Astropart. Phys., **8**, 7.

WILKS, S. S. 1938. The Large-Sample Distribution of the Likelihood Ratio for Testing Composite Hypotheses. *Ann. Math. Statist.*, **9**(1), 60–62.

WILLMAN, B. 2010. In Pursuit of the Least Luminous Galaxies. *Advances in Astronomy*, **2010**.

WOLF, J., MARTINEZ, G. D., BULLOCK, J. S., *et al.* 2010. Accurate masses for dispersion-supported galaxies. MNRAS, **406**, 1220–1237.

YEE, H. K. C., & OKE, J. B. 1978. Photoelectric spectrophotometry of radio galaxies. ApJ, **226**, 753–769.

YORK, D. G., ADELMAN, J., ANDERSON, JR., J. E., *et al.* 2000. The Sloan Digital Sky Survey: Technical Summary. AJ, **120**, 1579–1587. SDSS Collaboration.

ZACKRISSON, E., & RIEHM, T. 2010. Gravitational Lensing as a Probe of Cold Dark Matter Subhalos. *Advances in Astronomy*, **2010**.

ZECHLIN, H.-S. 2009 (Feb.). *Einschränkung der Mischungsparameter verborgener Photonen durch Analyse sehr hochenergetischer Gamma-Spektren des Krebsnebels.* Diploma thesis, Universität Hamburg, Hamburg, Germany.
`http://www.iexp.uni-hamburg.de/groups/astroparticle/de/forschung/zechlin_diplom.pdf`.

ZECHLIN, H.-S., & HORNS, D. 2012. Unidentified sources in the Fermi-LAT second source catalog: the case for DM subhalos. J. Cosmology Astropart. Phys., **11**(Nov.), 50.

ZECHLIN, H.-S., HORNS, D., & REDONDO, J. 2008 (Dec.). New Constraints on Hidden Photons using Very High Energy Gamma-Rays from the Crab Nebula. *Pages 727–730 of:* AHARONIAN, F. A., HOFMANN, W., & RIEGER, F. (eds), *4th International Meeting on High Energy Gamma-Ray Astronomy*. AIP Conference Proceedings, vol. 1085.

ZECHLIN, H.-S., FERNANDES, M. V., ELSAESSER, D., & HORNS, D. 2011. Dark matter subhalos as Fermi gamma-ray sources and first candidates in the 1FGL catalog. *In: 2011 Fermi Symposium proceedings - eConf C110509*. arXiv:1110.6868.

ZECHLIN, H.-S., FERNANDES, M. V., ELSÄSSER, D., & HORNS, D. 2012. Dark matter subhaloes as gamma-ray sources and candidates in the first Fermi-LAT catalogue. A&A, **538**(Feb.), A93.

ZELDOVICH, Y. B. 1972. A hypothesis, unifying the structure and the entropy of the Universe. MNRAS, **160**, 1P.

ZELDOVICH, YA.B., KLYPIN, A.A., KHLOPOV, M. YU., & CHECHETKIN, V.M. 1980. Astrophysical constraints on the mass of heavy stable neutral leptons. *Sov.J.Nucl.Phys.*, **31**, 664–669.

ZEMP, M., DIEMAND, J., KUHLEN, M., *et al.* 2009. The graininess of dark matter haloes. MNRAS, **394**, 641–659.

ZENTNER, A. R., & BULLOCK, J. S. 2003. Halo Substructure and the Power Spectrum. ApJ, **598**, 49–72.

ZHA, M., & LHAASO COLLABORATION. 2012. Status of the large high altitude air shower observatory project. *Nuclear Instruments and Methods in Physics Research A*, **692**, 77–82.

ZWICKY, F. 1933. Die Rotverschiebung von extragalaktischen Nebeln. *Helvetica Physica Acta*, **6**, 110–127.

Personal Acknowledgments

Many people have been involved in my professional and private life over the past years to whom I would like to thank for their assistance, advice, love, and support.

First, I owe a special thanks to my supervisor Prof. Dieter Horns for teaching me the way how to pursue scientific work, for giving me the freedom and support to develop my projects in my own way, for his never ending enthusiasm, optimism, and confidence in me, and for the warm working atmosphere in his group for Astroparticle Physics at the University of Hamburg. Special thanks also to my collaborators and colleagues Josefa Becerra, Jonathan Biteau, Alessandro Cuoco, Dominik Elsässer, Milton Fernandes, and Joachim Ripken for all their contributions to the success of this work, a great collaboration, and many helpful discussions. A special thanks is dedicated to Andrei Lobanov, for our joint efforts and many valuable discussions on our hidden-photon projects, for a great time at the Effelsberg observatory and my stays at the MPIfR in Bonn. Furthermore, I would like to acknowledge the past conveners of the Astroparticle Working Group of the H.E.S.S. Collaboration, Agnieszka Jacholkowski and Ullrich Schwanke, for their constant efforts in supporting the observation of DM subhalo candidates with H.E.S.S. I would also like to thank all my institutional colleagues at the University of Hamburg and DESY, whose list of names would be too long to mention here.

I am grateful to JProf. Alessandro Mirizzi for co-refereeing this thesis. A special thanks also to Prof. Marcus Brüggen and Prof. Günter Sigl for refereeing my defense.

Especially, I would like to thank Nelly Nguyen for her constant support in my questions on English grammar and her excellent suggestions for phrasing. For proof-reading I also thank Carmelo Evoli, Kristopher Healey, Götz Heinzelmann, and Dieter Horns for their valuable comments.

A warm thanks to our students Katharina Borm, Frederike Jäger, Stefanie Januschek, and Marco Prüser for their work and for a great working atmosphere.

My PhD time would not have been such a pleasant one without all my colleagues in the Astroparticle Group at Hamburg University. In particular, it was a pleasure for me to work with Tanja Kneiske, Martin Raue, and Martin Tluczykont: thanks for all the valuable skills you taught me, for answering so many small and big questions, and all the fun we had together. A special thanks to my long-term officemates Nelly Nguyen and Björn Opitz for the great and fruitful times we spent together. I really enjoyed a lot of professional and personal discussions with Attila Abramowski, Milton Fernandes, Max Kastendieck, Andreas Maurer, Manuel Meyer, Alexander Gewering-Peine, and Franziska Spies.

My stay at the H.E.S.S. site in Namibia would not have been the same without Aldée Charbonnier, Frikkie van Greunen, Albert Jahnke, Maveipi Kandjii, and Eben Tjingaete. Thanks for the great time.

Finally, I would like to thank all my friends and my family for their never ending encouragement, inspiration, and all the love and support.

Without all of them, this work would not have been possible.

List of Publications

Publications with peer review process

1. Lobanov, A. P., Zechlin, H.-S., Horns, D. (2013). Astrophysical searches for a hidden-photon signal in the radio regime. Phys. Rev. D, 87(6), 065004
2. Zechlin, H.-S., Horns, D. (2012). Unidentified sources in the Fermi-LAT second source catalog: the case for DM subhalos. J. Cosmology Astropart. Phys., 11, 50.
3. Doro, M., et al. (including Zechlin, H.-S.) (2013). Dark matter and fundamental physics with the Cherenkov Telescope Array. Astroparticle Physics, 43, 189-214.
4. Zechlin, H.-S., Fernandes, M. V., Elsaesser, D., Horns, D. (2012). Dark matter subhaloes as gamma-ray sources and candidates in the first Fermi-LAT catalogue. A&A, 538, A93.
5. Meyer, M., Horns, D., Zechlin, H.-S. (2010). The Crab Nebula as a standard candle in very high-energy astrophysics. A&A, 523, A2.
6. Abramowski, A., Gillessen, S., Horns, D., Zechlin, H.-S. (2010). Locating the very high energy source in the Galactic Centre with milliarcsecond accuracy. MNRAS, 402, 1342.
7. Co-author of 31 H.E.S.S. Collaboration papers published in peer-reviewed journals from June 2010 to June 2013.

Submitted publications with peer review process

1. Ripken, J., Cuoco, A., Zechlin, H.-S., Conrad, J., Horns, D. (2012). The sensitivity of Cherenkov telescopes to dark matter and astrophysically induced anisotropies in the diffuse gamma-ray background. Submitted to J. Cosmology Astropart. Phys., in revision. arXiv:1211.6922

Publications without peer review process

1. Zechlin, H.-S., Fernandes, M. V., Elsaesser, D., Horns, D. (2011). Dark matter subhalos as Fermi gamma-ray sources and first candidates in the 1FGL catalog. Proceedings of the 2011 Fermi Symposium - eConf C110509 at Rome, Italy. arXiv:1110.6868
2. Meyer, M., Horns, D., Zechlin, H.-S. (2009). Cross Calibration of Imaging Air Cherenkov Telescopes with Fermi. Proceedings of the 2009 Fermi Symposium - eConf Proceedings C091122 at Washington D.C., USA. arXiv:0912.3754
3. Ripken, J., Conrad, J., Horns, D., Zechlin, H.-S. (2009). Update on Dark Matter in the Galactic Centre with H.E.S.S. Proceedings of the 31st ICRC at Łódź, Poland.
4. Raue, M., Behera, B., Charbonnier, A., Giebels, B., Hauser, M., Kosack, K., Punch, M., Zechlin, H.-S. (2009). H.E.S.S. discovers VHE emission from the Fermi LAT source PKS 0447-439. The Astronomer's Telegram, 2350, 1.
5. Zechlin, H.-S., Horns, D., Redondo, J. (2008). New Constraints on Hidden Photons using Very High Energy Gamma-Rays from the Crab Nebula. Proceedings of the 4th International Meeting on High Energy Gamma-Ray Astronomy at Heidelberg, Germany. AIP Conference Proceedings, Volume 1085, pp. 727-730.

Diploma thesis

Zechlin, H.-S. (2009). Einschränkung der Mischungsparameter verborgener Photonen durch Analyse sehr hochenergetischer Gamma-Spektren des Krebsnebels. Diploma thesis, Universität Hamburg, Hamburg, Germany.
`http://www.iexp.uni-hamburg.de/groups/astroparticle/de/forschung/zechlin_diplom.pdf`